

Cooperative (De-)Hydrogenation of Small Molecules

Dissertation

zur Erlangung des mathematisch-naturwissenschaftlichen Doktorgrades

„Doctor rerum naturalium“

der Georg-August-Universität Göttingen

im Promotionsprogramm „Catalysis for Sustainable Synthesis“

der Georg-August University School of Science (GAUSS)

vorgelegt von

Arne Glüer

aus Herford

Göttingen, 2018

Betreuungsausschuss

Prof. Dr. Sven Schneider

Institut für Anorganische Chemie, Georg-August-Universität Göttingen

Prof. Dr. Franc Meyer

Institut für Anorganische Chemie, Georg-August-Universität Göttingen

Prof. Dr. Guido Clever

Fakultät für Chemie und Chemische Biologie, Technische Universität Dortmund

Mitglieder der Prüfungskommission

Referent: **Prof. Dr. Sven Schneider**

Institut für Anorganische Chemie, Georg-August-Universität Göttingen

Korreferent: **Prof. Dr. Franc Meyer**

Institut für Anorganische Chemie, Georg-August-Universität Göttingen

Weitere Mitglieder der Prüfungskommission:

Prof. Dr. Dietmar Stalke

Institut für Anorganische Chemie, Georg-August-Universität Göttingen

Prof. Dr. Manuel Alcarazo

Institut für Organische und Biomolekulare Chemie, Georg-August-Universität Göttingen

Priv.-Doz. Dr. Alexander Breder

Institut für Organische und Biomolekulare Chemie, Georg-August-Universität Göttingen

Dr. Michael John

Institut für Anorganische Chemie, Georg-August-Universität Göttingen

Danksagung

Zu aller erst danke ich Prof. Dr. Sven Schneider für die Betreuung meiner Promotion inklusive vieler anregender Gespräche über meine Forschung, durch die ich viel gelernt habe. Danke auch für die interessanten Forschungsthemen und die Freiheit, sie eigenständig anzugehen.

Des Weiteren danke ich Prof. Dr. Franc Meyer und Prof. Dr. Guido Clever dafür, dass sie sich bereit erklärt haben, Teil meines Betreuungsausschusses zu sein und Prof. Dr. Franc Meyer für die Übernahme des Korreferats. Außerdem danke ich Prof. Dr. Dietmar Stalke, Prof. Dr. Manuel Alcarazo, Priv.-Doz. Dr. Alexander Breder sowie Dr. Michael John für ihr Engagement in der Prüfungskommission.

Michael gilt zusätzlich besonderer Dank für seine vielfältige kompetente Hilfe bei jeglichen Problemen rund um die NMR Spektroskopie. Danke für ausführliche Erklärungen und die Möglichkeit, selber Spektren aufzunehmen und kleinere Probleme eigenständig zu beheben.

Genauso bedanke ich mich bei Ralf Schöne, der ebenfalls stets ein offenes Ohr für Fragen zu Spektrenaufnahme und -interpretation hatte, sowie der gesamten NMR Abteilung für die gute Zusammenarbeit.

Ebenso danke ich dem Analytischen Labor für die Aufnahme von Elementaranalysen und der Massenabteilung für die Aufnahme von Massenspektren. Danke auch an die Mitarbeiter der Werkstätten, die mit Raffinesse einige Spezialaufträge umgesetzt haben.

Des Weiteren danke ich Prof. Dr. Max C. Holthausen, Dr. Martin Diefenbach, Moritz Förster, Julia I. Schweizer, Umut S. Karaca, Prof. Dr. Jörn Schmedt auf der Günne und Vinicius R. Celinski für die fruchtbaren Kooperationen.

Dank gilt auch Christian Würtele und Christian Volkmann für die Aufnahme und Auswertung von Röntgenstrukturdaten.

Danke an Thorben Böhnisch, Mike Schütze und Thomas Kothe für ihren Einsatz als CaSuS-Koordinatoren und die Organisation vieler Exkursionen, Kurse und Konferenzen, die ich sehr genossen habe.

Außerdem danke ich meinen Bachelorstudenten und Forschungspraktikanten Bastian Schlusshass, Balthasar Rauschendorfer und Christian Bartling für die Unterstützung im Labor.

Besonderer Dank gilt dem gesamten Arbeitskreis für die freundliche, hilfsbereite Atmosphäre und die tolle Zeit! Ich danke Jenni Meiners für das Anlernen im Arbeitskreis und meinen Laborkollegen Christoph Schiwiek, Jan Hufschmidt, Katja Yuzik-Klimova, Lukas Alig und Max Fritz für gute Zusammenarbeit, wissenschaftliche Diskussionen und entspannte Pausen.

Für das Korrekturlesen der Dissertation danke ich Max Fritz, Lukas Alig, Sebastian Nestke, Christian Volkmann, Thorben Schulte und Christine Schiewer.

Meinem Liebling Tine danke ich für die bedingungslose Unterstützung in allen Lebenslagen und für das Bereichern meines Lebens durch die harmonische Beziehung.

Meinen Eltern, Schwestern, Paten und dem Rest meiner Familie danke ich dafür, dass sie aus mir den Menschen gemacht haben, der ich bin und meinen Freunden für die vielen schönen Stunden!

Eidesstattliche Erklärung

Hiermit erkläre ich, dass ich die beigefügte Dissertation selbstständig verfasst und keine anderen als die angegebenen Hilfsmittel genutzt habe. Die aus anderen Quellen direkt oder indirekt übernommenen Daten und Konzepte sind unter Angabe des Literaturzitats gekennzeichnet.

Ich versichere außerdem, dass ich die beigefügte Dissertation nur in diesem und keinem anderen Promotionsverfahren eingereicht habe und, dass diesem Promotionsverfahren keine endgültig gescheiterten Promotionsverfahren vorausgegangen sind.

Arne Glüer

List of Abbreviations

[AB ₀]	starting concentration of AB
[M] ⁺	molecular ion peak
°C	degree(s) celsius
a.u.	arbitrary units
AB	ammonia borane
approx.	approximately
BARF ₄ ⁻	[(3,5-(CF ₃) ₂ -C ₆ H ₃) ₄ B] ⁻
BCDB	B-(cyclodiborazanyl)amine-borane
BCTB	B-(cyclotriborazanyl)amine-borane
BDE	bond dissociation energy at standard conditions
br	broad
BZ	borazine
c	concentration
calc	calculated value
CDB	cyclodiaminoborane
cf.	confer (compare)
conv.	conversion
CTB	cyclotriaminoborane
Cy	cyclohexyl
d	day(s)
d	doublet (in the context of NMR spectroscopy)
DBU	1,8-diazabicyclo[5.4.0.]undec-7-ene
dcpe	(1,2-bis(dicyclohexylphosphino)ethane
DFT	density functional theory
DMF	<i>N,N</i> -dimethylformamide
DMSO	dimethylsulfoxide
dppe	1,2-bis(diphenylphosphino)ethane
DSC	differential scanning calorimetry
DTA	differential thermal analysis
e.g.	example given
eq	equivalents
Et	ethyl
<i>et al.</i>	et alii (and others)
exp	experimental value
g	gram
h	hour(s)
HMBC	heteronuclear multiple bond correlation

List of Abbreviations

HPLC	high pressure/performance liquid chromatography
<i>HPNP^{Pr}</i>	<i>HN{CH₂CH₂(P^{Pr})₂}</i> ₂
Hz	hertz
I	intensity
i.e.	id est (that is to say)
<i>in vacuo</i>	with reduced pressure
<i>i</i> Pr	<i>iso</i> -propyl
K	Kelvin
kcal	1000 calories
l	liquid
L	liter(s)
L	ligand (in molecules)
LIFDI	liquid injection field desorption ionization
ln	natural logarithm
lut	2,6-lutidine
m	mass
m	multiplet (in the context of NMR spectroscopy)
M	metal
M	molar (mol/L)
<i>m/z</i>	mass to charge ratio
max	maximum
Me	methyl
mg	milligram(s)
MHz	megahertz
min	minute(s)
min.	minimal
mL	milliliter(s)
MLC	metal-ligand cooperation
mmol	milimole(s)
mol	mole
MQ-MAS NMR	multiple quantum magic-angle spinning nuclear magnetic resonance
MS	mass spectrometry
<i>n</i> -hex	<i>n</i> -hexane
NMR	nuclear magnetic resonance
OTf ⁻	triflate (trifluoromethanesulfonate, CF ₃ SO ₃ ⁻)
p	pentet
PAB	polyaminoborane
PBZ	polyborazylene

Ph	phenyl
$pK_{a,MeCN}$	negative decadic logarithm of the acidity constant in acetonitrile
POCOP	μ^3 -1,3-(OP <i>t</i> Bu) ₂ C ₆ H ₃
ppm	parts per million
q	quartet
r.t.	room temperature
ref.	reference
rxn.	reaction
s	second(s)
s	singlet (in the context of NMR spectroscopy)
sept	septett
t	time
t	triplet (in the context of NMR spectroscopy)
<i>t</i> Bu	<i>tert</i> -butyl
TEM	transmission electron microscope
TGA	thermogravimetric analysis
THF	tetrahydrofuran
THF- <i>d</i> ₈	Octadeuterotetrahydrofuran
TM	transition metal
TMB	1,2,4,5-tetramethylbenzene
TMS	trimethylsilyl
TOF	turnover frequency
TON	turnover number
v_0	initial rate
VB ^{Pr}	2,8,9-Triisopropyl-2,5,8,9-tetraaza-1-phospha-bicyclo[3.3.3]undecane
vide supra	see above
vs.	versus
vt	virtual triplet
WCA	weakly coordinating anion
ΔG°	standard Gibbs free energy
$\Delta G_{H^-}^\circ$	standard Gibbs free energy for hydride release (thermodynamic hydricity)
ΔG^\ddagger	Gibbs free energy of activation
ΔG_R°	Gibbs free energy of the given reaction at standard conditions
ΔH_R°	enthalpy of the given reaction at standard conditions
ΔS_R°	entropy of the given reaction at standard conditions
δ	chemical shift
μ L	microliter(s)
μ mol	micromole(s)

Table of Contents

1	INTRODUCTION	1
1.1	PNP Pincer Complexes	2
1.1.1	Cooperativity in PNP Pincer Complexes	3
1.1.2	Ruthenium and Iron PNP Pincer Complexes in Catalysis	4
1.2	Ammonia Borane Dehydrogenation	6
1.2.1	Thermal Ammonia Borane Dehydrocoupling	7
1.2.2	Transition Metal Catalyzed Ammonia Borane Dehydrocoupling	8
1.2.2.1	Selected Precious Metal Complexes for Ammonia Borane Dehydrocoupling	10
1.2.2.2	Iron Complexes for Ammonia Borane Dehydrocoupling	12
1.3	Hydrogenolysis of Halosilanes and Silyl Triflates	15
1.3.1	Conventional Routes to Organosilanes	15
1.3.2	Hydrogenolysis of Halosilanes	16
1.3.3	Hydrogenolysis of Silyl Triflates	17
1.4	Lessons from Hydrogenation of CO₂ to Formate by Iron Complexes	18
1.4.1	PNP Pincer Ligands for CO ₂ Hydrogenation	20
1.4.2	Tetradentate Phosphine Ligands for CO ₂ Hydrogenation	25
1.4.3	Conclusions for Design of Catalysts for Chlorosilane/Silyl Triflate Hydrogenolysis	28
2	OBJECTIVES	29
3	AMMONIA BORANE DEHYDROCOUPLING	31
3.1	Introduction	31
3.2	Results and Discussion	32
3.3	Summary	39
4	HYDROGENOLYSIS OF CHLOROSILANES	41
4.1	Introduction	41
4.2	Results and Discussion	42
4.3	Summary	48

Table of Contents

5	HYDROGENOLYSIS OF SILYL TRIFLATES	49
5.1	Introduction	49
5.2	Results and Discussion	50
5.2.1	Attempted Hydrogenolysis of Silyl Sulfonic Acids	56
5.2.2	Side note on the Purity of 2,6-Lutidine	58
5.3	Summary	60
6	CONCLUSION	61
7	EXPERIMENTAL PART	63
7.1	General Methods	63
7.2	Experimental Part for Ammonia Borane Dehydrocoupling	65
7.2.1	Synthetic Procedures.....	65
7.2.1.1	Catalytic Protocol	65
7.2.1.2	Mercury Poisoning Experiment	65
7.2.1.3	Dehydrocoupling with Ruthenium Catalyst 9	65
7.2.1.4	Catalysis with added Amine	66
7.2.2	Spectroscopic Examinations.....	67
7.2.2.1	Solid State NMR of PAB	67
7.2.2.2	NMR Examination of Catalytic Runs.....	67
7.2.2.3	Aminoborane Trapping	68
7.2.2.4	Catalyst Deactivation	69
7.3	Experimental Part for Hydrogenolysis of Chlorosilanes and Silyl Triflates	72
7.3.1	Synthetic Procedures.....	72
7.3.1.1	Synthesis of Me ₂ SiOTf ₂	72
7.3.1.2	Synthesis of Me ₃ SiOSO ₂ Me.....	72
7.3.1.3	Synthesis of (HPNP ^{iPr})RuH(OTf)CO (90).....	72
7.3.1.4	Synthesis of (MePNP ^{Pr})RuH(OTf)CO (92)	73
7.3.2	Catalytic Protocols	74
7.3.2.1	General Catalytic Protocol for Hydrogenolysis of Chlorosilanes	74
7.3.2.2	General Catalytic Protocol for Hydrogenolysis of Pure Silyl Triflates	74
7.3.2.3	General Catalytic Protocol for Hydrogenolysis of Silyl Chloride/Triflate Mixtures	74
7.3.3	Spectroscopic Characterizations	75
7.3.3.1	Reaction of Me ₃ SiCl and (HPNP ^{Pr})Ru(H) ₂ CO (82).....	75

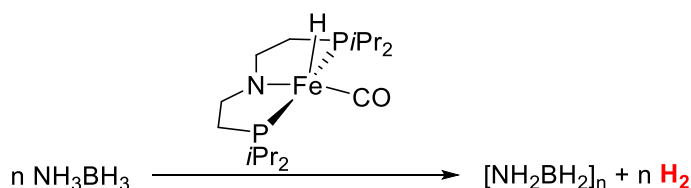
7.3.3.2	Reaction of Me_3SiOTf and $(\text{HPNP}^{\text{Pr}})\text{Ru}(\text{H})_2\text{CO}$ (82).....	75
7.3.3.3	Reaction of $\text{Me}_3\text{SiOSO}_2\text{Me}$ and $(\text{HPNP}^{\text{Pr}})\text{Ru}(\text{H})_2\text{CO}$ (82)	75
7.3.3.4	Reaction of $(\text{HPNP}^{\text{Pr}})\text{RuH}(\text{OTf})\text{CO}$ (90) with NEt_3 under H_2 Atmosphere	76
7.3.3.5	Reaction of $(\text{HPNP}^{\text{Pr}})\text{RuH}(\text{Cl})\text{CO}$ (87) and VB^{Pr} under H_2 Atmosphere.....	76
7.3.3.6	Reaction of $(\text{HPNP}^{\text{Pr}})\text{RuH}(\text{Cl})\text{CO}$ (87) with NaBARF_4	76
7.3.3.7	Characterization of $[\text{Me}_3\text{SiNEt}_3]\text{BARF}_4$	77
7.3.3.8	Catalytic Hydrogenolysis of Chlorosilanes with NEt_3 as Base.....	78
7.3.3.9	Catalytic Hydrogenolysis of Silyl Triflates with NEt_3 as Base	78
7.3.3.10	Catalytic Hydrogenolysis of Silyl Triflates with 2,6-Lutidine as Base	79
7.3.3.11	Catalytic Run with 2 eq 2,6-Lutidine	80
7.3.3.12	Attempted Hydrogenolysis of $\text{Me}_3\text{SiOSO}_2\text{Me}$	81
7.3.3.13	Comproportionation equilibrium of Me_2SiCl_2 and $\text{Me}_2\text{SiOTf}_2$ to $\text{Me}_2\text{SiClOTf}$	82
7.3.3.14	Reaction of Lutidinium Triflate with Me_2SiClH to Silyl Triflates and H_2	84
8	STRUCTURES	85
8.1	Structures of Complexes	85
8.2	Structures other Compounds.....	89
9	APPENDIX – CRYSTAL STRUCTURES.....	91
9.1	Single-Crystal Structure Analysis of $(\text{HPNP}^{\text{Pr}})\text{RuH}(\text{OTf})\text{CO}$ (90).....	91
9.2	Single-Crystal Structure Analysis of $(\text{MePNP}^{\text{Pr}})\text{RuH}(\text{OTf})\text{CO}$ (92)	99
9.3	Single-Crystal Structure Analysis of $(\text{HPNP}^{\text{Pr}})\text{RuH}(\text{OSO}_2\text{Me})\text{CO}$ (94)	107
9.4	Single-Crystal Structure Analysis of $[(\text{HPNP}^{\text{Pr}})\text{RuH}(\text{lut})\text{CO}]\text{OTf}$ (95).....	115
10	REFERENCES	125

1 Introduction

Hydrogenation and dehydrogenation reactions are intrinsically atom economic, thus constituting important transformations for chemical industry and synthetic chemists.^[1–4] (De-)hydrogenation reactions typically do not proceed spontaneously but require a catalyst. Precious metal complexes often show high catalytic activity as they can activate H₂ via reversible oxidative addition / reductive elimination. In the last decades, bifunctional complexes capable of metal ligand cooperation (MLC) became increasingly popular especially for the hydrogenation of polar bonds due to their exceptionally high activity and stability. Additionally, MLC enabled efficient hydrogenation with base metal catalysts that do not commonly undergo oxidative addition / reductive elimination.^[5,6]

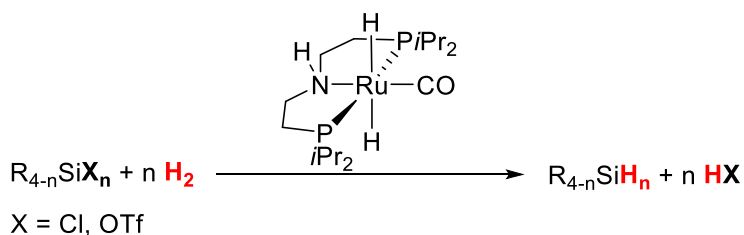
In this thesis, bifunctional iron and ruthenium catalysts are investigated with regard to their ability to catalyze (de-)hydrogenation reactions of inorganic substrates. Emphasis will be put on the understanding of mechanistic principles in order to optimize reaction conditions and extract general guidelines for catalyst design. Two main topics can be identified:

- 1) Ammonia borane dehydrocoupling (i.e. dehydrogenation and subsequent B-N coupling) mediated by a bifunctional iron catalyst (chapter 3).



Scheme 1.1 Ammonia borane dehydrocoupling.

- 2) Hydrosilane synthesis via chlorosilane and silyl triflate hydrogenolysis (i.e. cleavage of Si-Cl or Si-OTf bond with dihydrogen) mediated by a bifunctional ruthenium catalyst (chapter 4 and 5).



Scheme 1.2 Hydrogenolysis of chlorosilanes and silyl triflates.

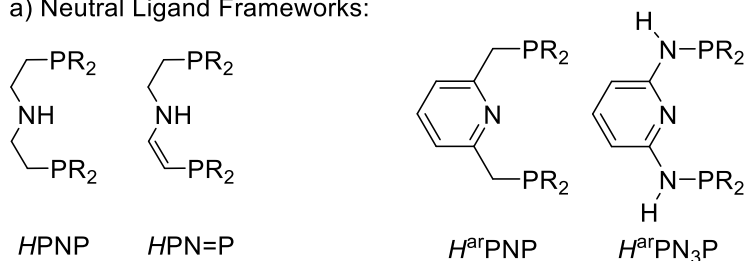
1 Introduction

1.1 PNP Pincer Complexes

PNP pincer ligands are tridentate ligands that coordinate a metal center via two phosphorous and one nitrogen atom in a meridional fashion.^[1,7] Two important classes differing in the N-donating unit can be distinguished: i) aliphatic secondary (and tertiary) amine and ii) aromatic pyridine based PNP ligands (Figure 1.1). Notably, the bite angle of aliphatic amine pincer ligands is larger than for aromatic PNP complexes, rendering the metal center less exposed to incoming substrates. However, steric properties can be easily tuned by change of substituents on phosphorous.^[8] For example, bulky *tert*-butyl (*t*Bu) substituents are predominantly used in pyridine based PNP catalysts, while less bulky *iso*-propyl (*i*Pr), cyclohexyl (Cy) or phenyl (Ph) moieties are rather used for aliphatic PNP catalysts. Electronic properties can be tuned by additional substituents on the pyridine ring or modification of the linker that connects the phosphorous donors to the central pyridine ring (for aromatic PNP ligands).^[9] Additionally, dehydrogenation of the backbone in aliphatic PNP complexes considerably weakens the N-donor strength by delocalization of the N p electrons into the π -system. In contrast, deprotonation strongly increases the donating abilities of PNP ligands by significant π -contribution (Figure 1.1b).

PNP pincer ligands form thermally robust complexes and can stabilize metals in unusual oxidation states or low coordination numbers.^[8] Decomposition of PNP complexes for example via partial ligand dissociation (hemilability) or complete ligand loss (mostly for 3d metals) is only occasionally observed.^[10,11] Consequently they have been employed as persistent catalysts in a variety of transformations.^[8,12]

a) Neutral Ligand Frameworks:



b) Anionic Ligand Frameworks:

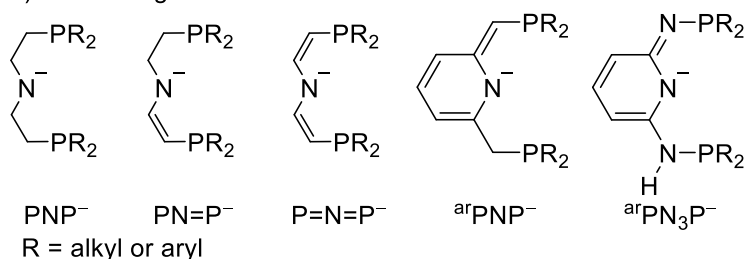
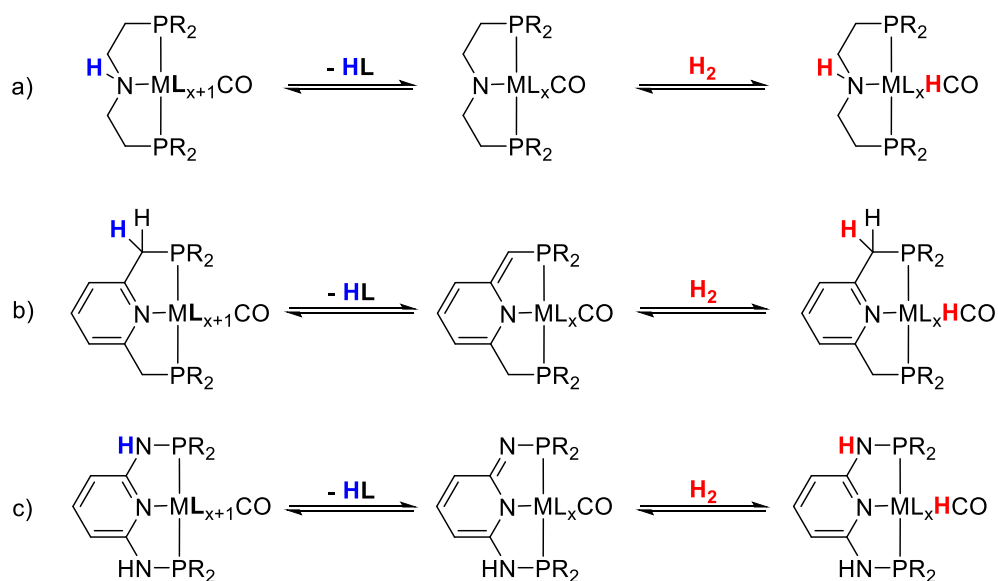


Figure 1.1 Overview of aliphatic (left) and aromatic (right) ligand frameworks relevant for this thesis.

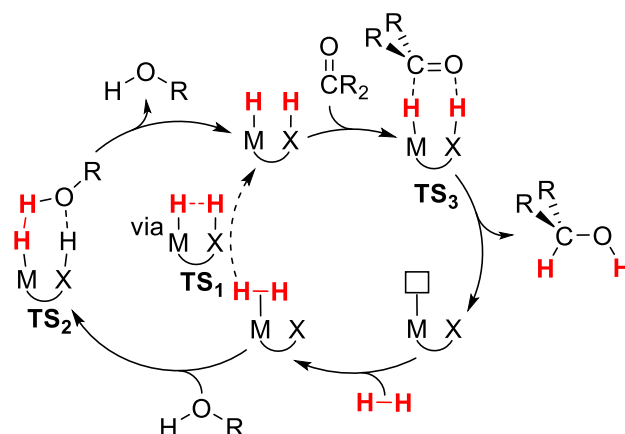
1.1.1 Cooperativity in PNP Pincer Complexes

Several slightly varying definitions for metal-ligand cooperation (MLC) are discussed in literature.^[5,13–15] For this thesis, the broad definition by Grützmacher *and coworkers* will be used: “A cooperating ligand in a metal complex can be defined as one that actively participates in the substrate activation. The chemical structure of the ligand can remain intact during the catalytic process (substrate activation via hydrogen bonding) or undergo a reversible transformation (protonation/deprotonation, reorganization of a π -system, or electron transfer to/from the metal).”^[13,14] MLC by definition is a synergistic process leading to improved catalysis. Sometimes, however, a cooperating ligand leads to decreased catalytic activity, e.g. by resting state overstabilization by hydrogen bonds. This phenomenon is termed “counterproductive MLC” in this thesis. MLC often plays an important role in (especially polar) bond activation processes due to the presence of both an acidic (metal) and a basic site (e.g. nitrogen or carbon). For example, stoichiometric experiments show that H_2 heterolysis can occur along the metal-nitrogen bond in aliphatic PNP pincer complexes (1,2-addition, Scheme 1.3a) or via a more distant basic site in pyridine based PNP pincer complexes (1,3-addition accompanied by aromatization/dearomatization of the pyridine ring, Scheme 1.3b/c).^[5]



Scheme 1.3 Metal-ligand cooperativity with aliphatic secondary amine based (a) and aromatic pyridine based (b, c) PNP complexes. R = *t*Bu, *i*Pr, Cy, Ph.

These findings might tempt to propose a transition state in which H_2 is coordinated directly along the M-N unit such as in **TS₁** (Scheme 1.4). However, computational evaluation suggests that hydrogen bond donors/acceptors (e.g. an alcoholic solvent, a product, a catalyst or traces of water) catalyze H_2 heterolysis, leading to a transition state similar to **TS₂** under most catalytic conditions.^[16] The resulting hydride-NH complex may subsequently transfer both the hydridic and protic hydrogens to a substrate in a concerted fashion via **TS₃** or stepwise depending on catalyst and substrate.^[16]



Scheme 1.4 Cooperative mechanism for ketone hydrogenation with two possible pathways for H₂ heterolysis.^[16]

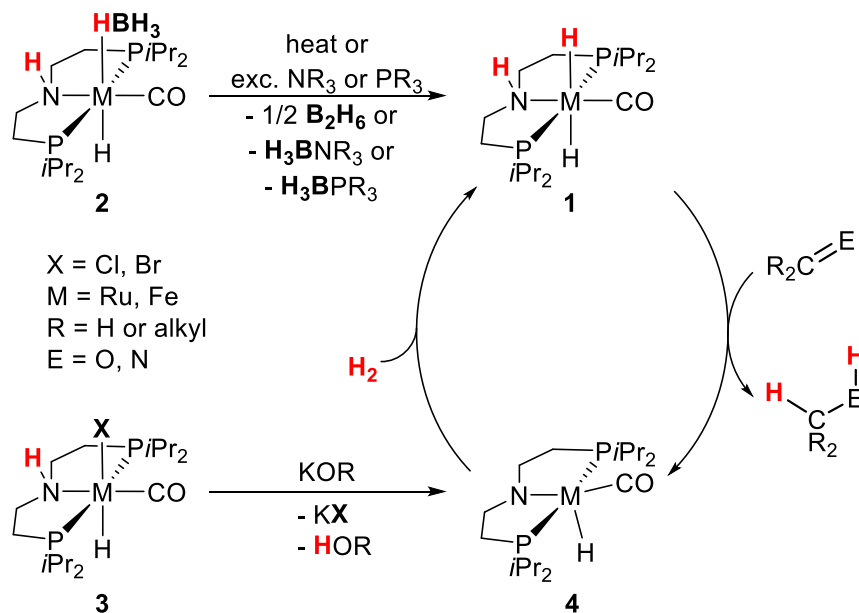
Importantly, MLC allows the metal to retain its oxidation state throughout the catalytic cycle. Consequently, transformations that traditionally involved multi-electron steps such as oxidative addition or reductive elimination are enabled for metals preferring single electron reactivity such as 3d metals.^[5]

A common test to estimate the role of MLC in aliphatic PNP complexes is to methylate the N-donor to the respective tertiary amine and compare its activity to the parent secondary amine complex. Owing to lack of MLC, tertiary amine catalysts were generally classified inferior to secondary amine systems.^[17,18] However, the opposite is found e.g. in the hydrogenation of CO₂ and carbonate to formate, where in fact the tertiary amine species is *superior* in terms of activity and stability to its secondary amine congener, suggesting counterproductive MLC (see chapter 1.4.1).^[19–21] Resting state overstabilization by hydrogen bonding of the substrate to the N-H moiety and additional unproductive reaction pathways were held accountable for inferior activity of the secondary amine catalysts.

1.1.2 Ruthenium and Iron PNP Pincer Complexes in Catalysis

Group 8 PNP metal complexes have been used as catalysts for a wide range of hydrogenation and dehydrogenation reactions of polar substrates (aldehydes, ketones, esters, amides, imines, nitriles, polarized C=C double bonds, N-heterocycles, formic acid, CO₂, alcohols, ammonia borane).^[6,12,18,22–28] Iron based catalysts are of special interest due to the high abundance and low cost/toxicity of the metal, but are still outperformed by analogous ruthenium complexes in most transformations.^[4] Specifically, *trans*-dihydride complexes show remarkable reactivity in hydrogenation and (acceptorless) dehydrogenation of polar substrates.^[12,29] This is attributed to their high thermodynamic M-H hydricities^[30] (i.e. low $\Delta G^{\circ}_{\text{H}^-}$ values, $\Delta G^{\circ}_{\text{H}^-}$: $\text{L}_n\text{M}-\text{H} \rightarrow \text{L}_n\text{M}^+ + \text{H}^-$) that arise from the strong *trans*-influence of hydride ligands.^[18] Additionally, the kinetic *trans*-effect facilitates hydride transfer. Hydride and proton transfer from *trans*-dihydride complex **1** to a polar substrate such as ketones gives pentacoordinate amido species **4**, which subsequently adds H₂ heterolytically to reform dihydride **1** and close a catalytic cycle (Scheme 1.5).^[6,18,24] Commonly used

precatalysts are tetrahydridoborate complexes **2** or hydride halide complexes **3**. BH_3 abstraction from **2** by heat or treatment with excess amines/phosphines gives active dihydride catalyst **1**. Alternatively, HCl elimination from **3** by strong alkoxide/hydroxide bases gives pentacoordinate amido complex **4** which heterolytically adds H_2 to give dihydride **1**.^[31,32]



Scheme 1.5 Precatalyst activation and general catalytic cycle for hydrogenation of polar double bonds with aliphatic Fe and Ru PNP pincer complexes.

1 Introduction

1.2 Ammonia Borane Dehydrogenation

As fossil fuels are running out, renewable energy sources such as wind- or solar power increase in popularity. However, these energy sources are not evenly distributed throughout the day and mostly inapplicable for mobile use. Conventional batteries suffer small energy densities, thus limiting their use to a relatively small scale. Storage of energy in chemical bonds makes higher energy densities accessible and can be conducted easily on large scales. Ammonia borane (AB, NH_3BH_3) contains 19.6 wt% H_2 enabling high gravimetric and volumetric energy densities (Figure 1.2).^[33]

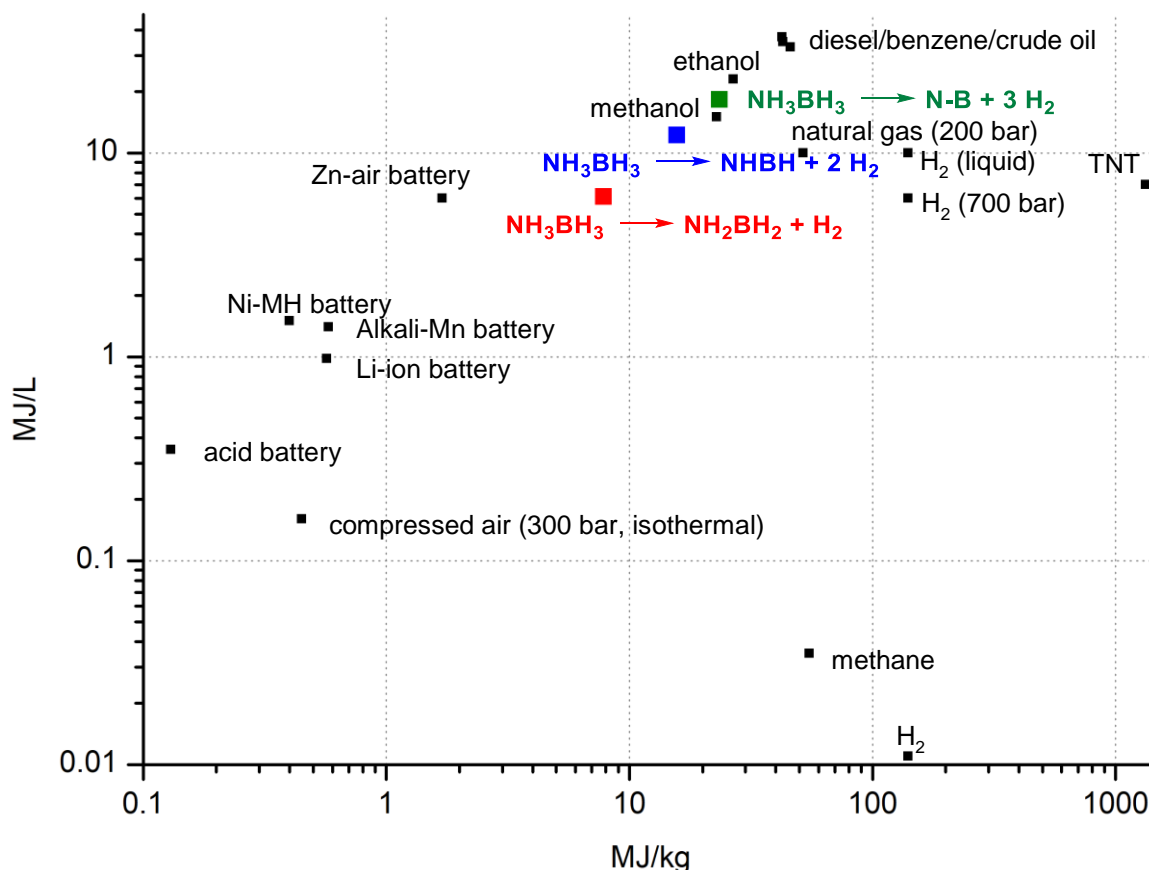


Figure 1.2 Volumetric (y-axis) and gravimetric (x-axis) energy densities.

Yet, in contrast to explosive H_2 , it is a white solid that can be safely stored under air at room temperature.^[33] AB is relatively stable with respect to hydrolysis in neutral or basic aqueous solution, however, it readily hydrolyzes in acidic solution. The mechanism can be rationalized as electrophilic substitution in which the acid coordinates to the nitrogen to replace BH_3 which is readily hydrolyzed to boronic acid with concomitant formation of H_2 (Figure 1.3a).^[34] However, given the thermodynamic stability of B-O bonds (BDE (bond dissociation energy) = $193 \text{ kcal mol}^{-1}$),^[35] the reverse reaction to AB is highly unfavored rendering any hydrolytic dehydrogenation of AB unsuitable for reversible hydrogen storage.

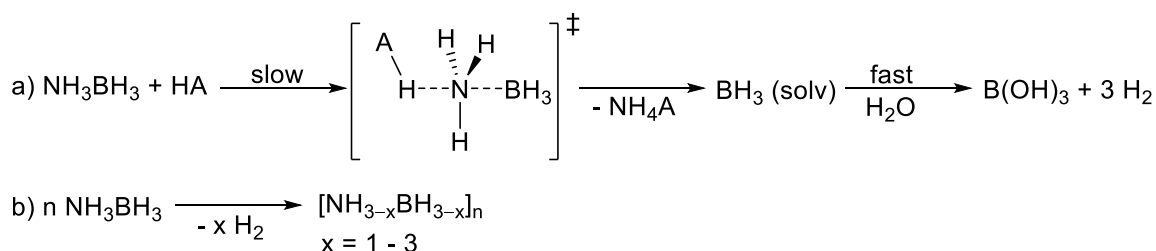
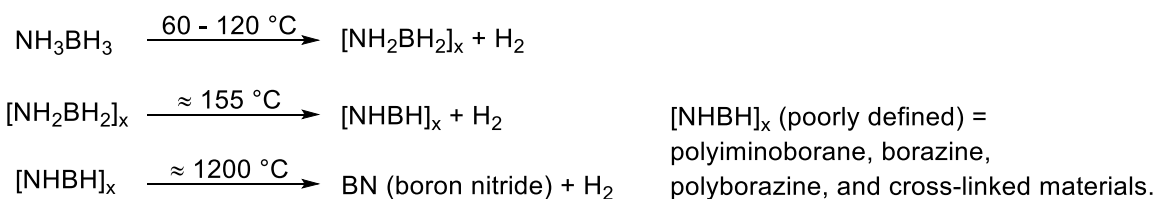


Figure 1.3 a) Mechanism of Brønsted acid catalyzed hydrolysis of ammonia borane. b) General equation for AB dehydrocoupling.

As an alternative, dehydrocoupling of ammonia borane (Figure 1.3b) has been studied in detail and will be discussed in the following chapters.^[33,36] While thermal dehydrocoupling (see chapter 1.2.1) is difficult to control, catalysis (see chapter 1.2.2) offers in principal control over the extent of H₂ release and the oligomer/polymer microstructures. Thus, investigations of AB dehydrocoupling might not only be interesting in terms of H₂ storage but also offer routes to new B-N polymeric materials.^[37,38]

1.2.1 Thermal Ammonia Borane Dehydrocoupling

Solid ammonia borane can be dehydrogenated thermally in a stepwise process, releasing one equivalent H₂ after the other as revealed by differential thermal analysis (DTA), thermogravimetric analysis (TGA) and differential scanning calorimetry (DSC) experiments.^[33] With high DTA heating rates (10 °C/min), melting may be observed (112 °C) prior to hydrogen release (starting at 117 °C).^[39] However, an isothermal study of AB stability indicated slow hydrogen loss already at 60 °C albeit with a half-life of weeks.^[40] The product after loss of dihydrogen is not soluble solvents such as dimethyl sulfoxide (DMSO), *N,N*-dimethyl formamide (DMF) or tetrahydrofuran (THF), thus hampering its characterization.^[41,42] It is generally referred to as polyaminoborane (PAB, $[\text{NH}_2\text{BH}_2]_x$), but most likely contains borazinylic residues as well as cyclic and crosslinked structures when obtained thermally. PAB becomes unstable around 155 °C to release another equivalent of hydrogen to give (poly)iminoboranes $[\text{NHBH}]_x$ and cross-linked materials that are mostly poorly defined (Scheme 1.6). The third molecule of dihydrogen is released at much higher temperatures around 1200 °C with concomitant formation of boron nitride.^[33]



Scheme 1.6 Stepwise thermal decomposition of ammonia borane.^[33]

As release of the 2nd and 3rd equivalent of H₂ is strongly exothermic, regeneration protocols are complex.^[43-46] On the contrary, release of the 1st equivalent H₂ is calculated to be only slightly exothermic ($\text{NH}_3\text{BH}_3 (\text{s}) \rightarrow [\text{H}_2\text{BNH}_2]_x + \text{H}_2 (\text{g})$; $\Delta H_R^\circ = -1.6 \text{ kcal mol}^{-1}$), making it the most

1 Introduction

promising candidate for reversible hydrogen release.^[47] However, as DSC studies of solid AB conducted under high pressures (up to 600 bar) of dihydrogen did not give evidence of reversible hydrogen loss, solvation might to be crucial to shift the equilibrium via intermolecular interactions.^[33] Nevertheless, rehydrogenation of AB spent fuel was not achieved by now.

1.2.2 Transition Metal Catalyzed Ammonia Borane Dehydrocoupling

Depending on the nature of the catalyst, 1 to 2.5 equivalents H_2 can be liberated from AB leading to polyaminoborane (PAB), cyclodiaminoborane (CDB), cyclotriaminoborane (CTB), B-(cyclodiborazanyl)amine-borane (BCDB), B-(cyclotriborazanyl)amine-borane (BCTB), borazine (BZ) or polyborazylene (PBZ, Figure 1.4). It is important to note that BCTB *tetramer* was mistaken for BCDB *trimer* by Baker *and coworkers* in pioneering studies (2008).^[48] Until they corrected their assignment in 2015,^[49] several publications describe the formation of BCDB following Baker's original assignment, leaving uncertainty about the accuracy of these reports.

Depending on the extent of H_2 release and the products obtained, two classes of catalysts are distinguished: i) Type I catalysts release one eq H_2 and form mainly PAB. ii) Type II catalysts release > 2 eq H_2 and form (P)BZ parallel with CDB, CTB and BCDB/BCTB.

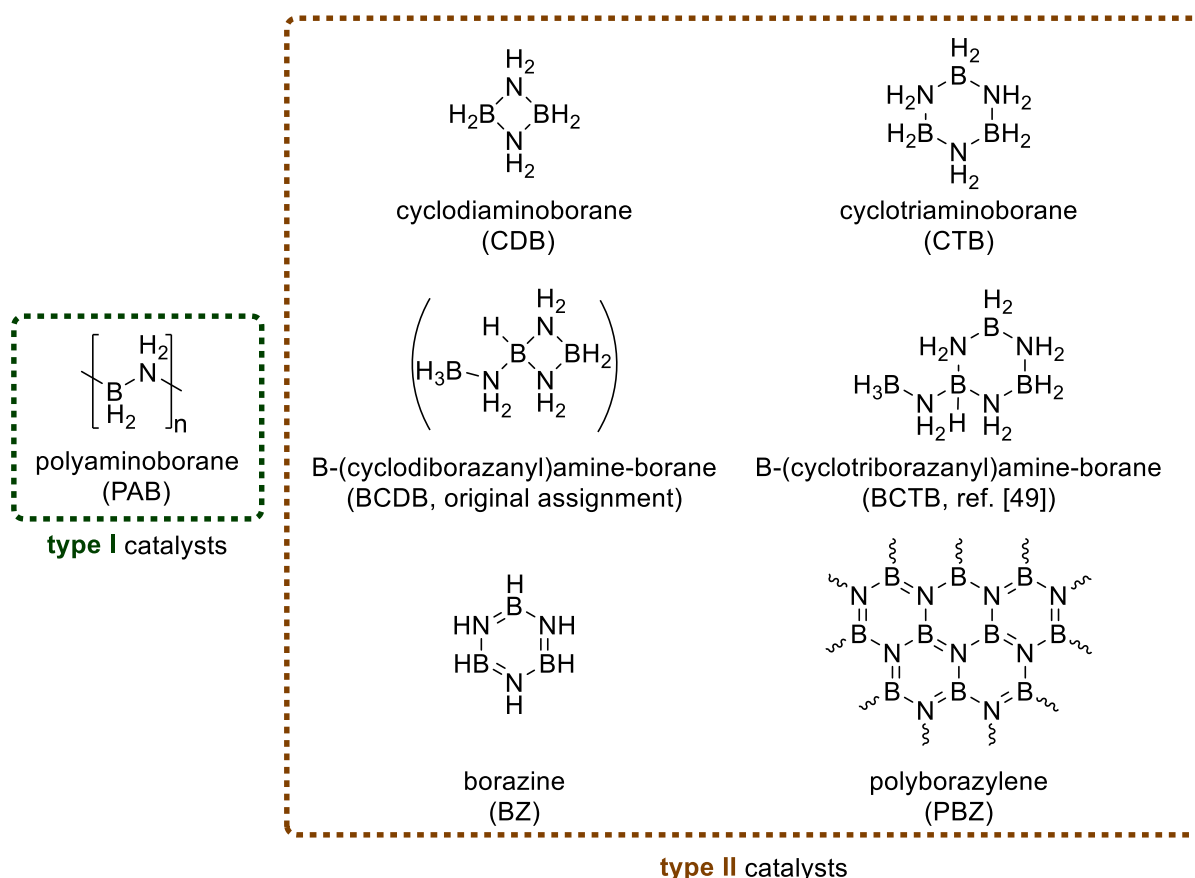


Figure 1.4 Possible products of metal catalyzed AB dehydrocoupling with type I catalysts (release of 1 eq H_2) and type II catalysts (release of ≥ 2 eq H_2). Several publications report BCDB as product, however later studies indicate that it was incorrectly assigned and is in fact tetramer BCTB.

AB is a polar molecule with protic and hydridic hydrogens. Activation may occur on either of these moieties or both simultaneously. For example, metal hydrides can coordinate to protic hydrogens, whereas metal vacancies or (in case of bifunctional catalysts) protons on a ligand can interact with hydridic hydrogens (Figure 1.5).^[36]

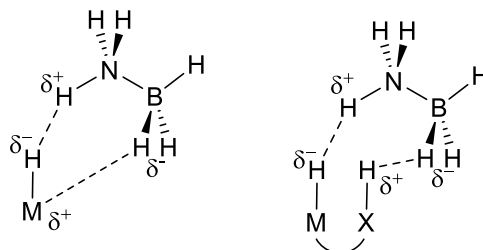
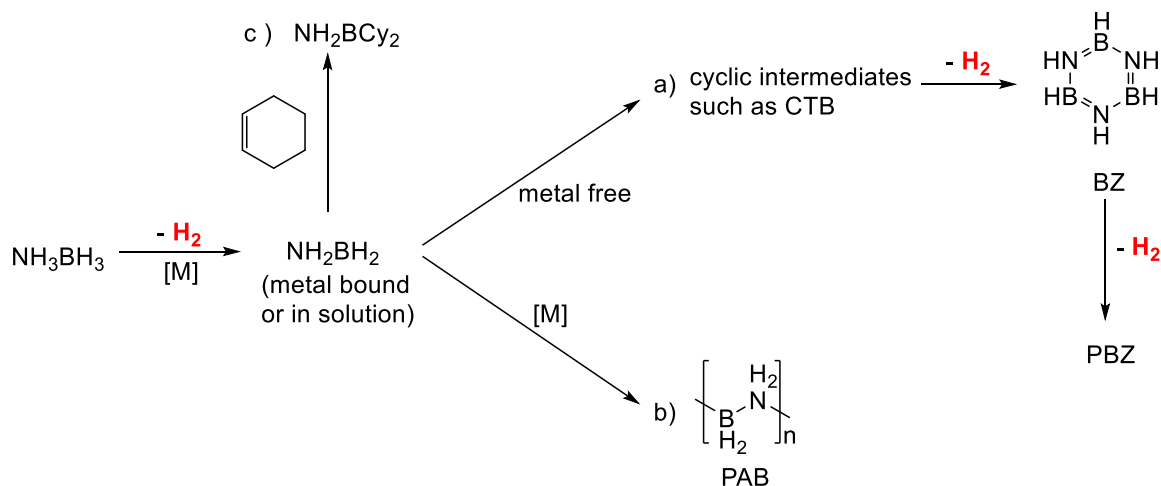


Figure 1.5 Simultaneous activation of N-H and B-H bonds by a metal hydride complex with a vacant coordination side (left) and a bifunctional catalyst (right).^[36]

In any case, molecular hydrogen may be released after hydrogen bonding of a protic and a hydridic hydrogen. The residual NH_2BH_3 or BH_2NH_3 moiety may either be stabilized by hydrogen bonding to a ligand (proton or hydride)^[17] or by coordination to the metal to form amido-/boryl complexes ($\text{M-NH}_2\text{BH}_3$ / $\text{M-BH}_2\text{NH}_3$), respectively.^[36] Subsequent loss of another equivalent of H_2 generates aminoborane (NH_2BH_2), which is either released into solution or still coordinated to the metal/ligand.



Scheme 1.7 Pathways for formation of a) (P)BZ and b) PAB from AB. c) Formation of $\text{H}_2\text{N-BCy}_2$ by trapping of free $\text{H}_2\text{N=BH}_2$ with cyclohexene.

It is commonly believed that PAB formation (type I catalysts, vide supra) proceeds via metal bound NH_2BH_2 , while P(BZ) is obtained from metal-free oligomerization of free NH_2BH_2 (generated by type II catalysts) (Scheme 1.7).^[48,50–54] However, NH_2BH_2 is only stable below $-150\text{ }^\circ\text{C}$ ^[55] and has not been observed spectroscopically during AB dehydrocoupling, necessitating indirect evidence by trapping experiments e.g. with cyclohexene.^[36] Detection of hydroboration product $\text{H}_2\text{N-BCy}_2$ upon addition of cyclohexene is regarded indicative of free NH_2BH_2 .^[48] However, it was argued that no hydroboration is expected if NH_2BH_2 is consumed by a faster follow-up reaction, e.g. polymerization.^[17] Interestingly, *N*-methylated NMe_2BH_2 is more stable, thus serving as model for

1 Introduction

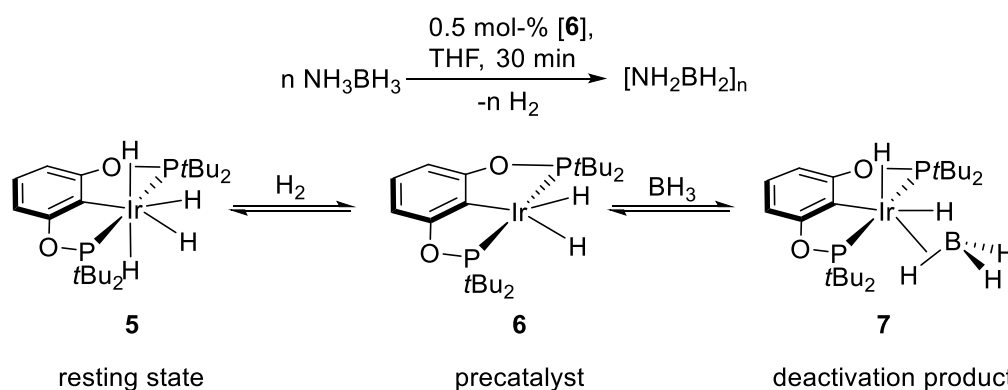
mechanistic investigations. For example, it was observed as intermediate in the dehydrocoupling of NHMe_2BH_3 ^[56,57] and as ligand in metal complexes.^[58,59]

1.2.2.1 Selected Precious Metal Complexes for Ammonia Borane Dehydrocoupling

Precious metal based complexes have been extensively used for catalytic dehydrocoupling of amine boranes.^[33,36] Two classes of intensively studied catalysts will be presented here as they are most relevant for this thesis: I) Iridium POCOP pincer complex $[(\text{POCOP}^{\text{tBu}})\text{Ir}(\text{H}_2)]$ (POCOP = μ^3 -1,3-(OPtBu_2) $_2\text{C}_6\text{H}_3$, **6**) and II) Ruthenium PNP pincer complexes $[(\text{PNP}^{\text{Pr}})\text{Ru}(\text{H})\text{PMe}_3]$ (**8**) and $[(\text{HPNP}^{\text{Pr}})\text{Ru}(\text{H})_2\text{PMe}_3]$ (**9**).

I) Ir POCOP Pincer Complex **6** for Ammonia Borane Dehydrocoupling

In pioneering work, Goldberg, Heinekey *and coworkers* reported the dehydrocoupling of ammonia borane^[60] and methylamine-boranes^[61] using Brookhart's iridium POCOP pincer complex **6**. Later, computational evaluation shed light on dehydrogenation^[62] of AB to NH_2BH_2 and subsequent polymerization^[52] to PAB. AB dehydrocoupling proceeded at room temperature within 30 min at low catalyst loadings (0.5 mol-%). Formation of iridium tetrahydride complex **5** in the initial phase of catalysis was indicated by NMR spectroscopy as might be expected due to the tendency of **6** to oxidatively add H_2 (Scheme 1.8).^[63] Alternatively, **5** was proposed as direct product from reaction of **6** and AB with concomitant formation of NH_2BH_2 by computational evaluation.^[62] As catalysis progressed, borane adduct **7**^[64] accumulated. Therefore, **7** was synthesized/characterized independently by reaction of **6** and BH_3 in THF and tested for AB dehydrocoupling. Negligible activity was observed, establishing **7** as deactivation product.

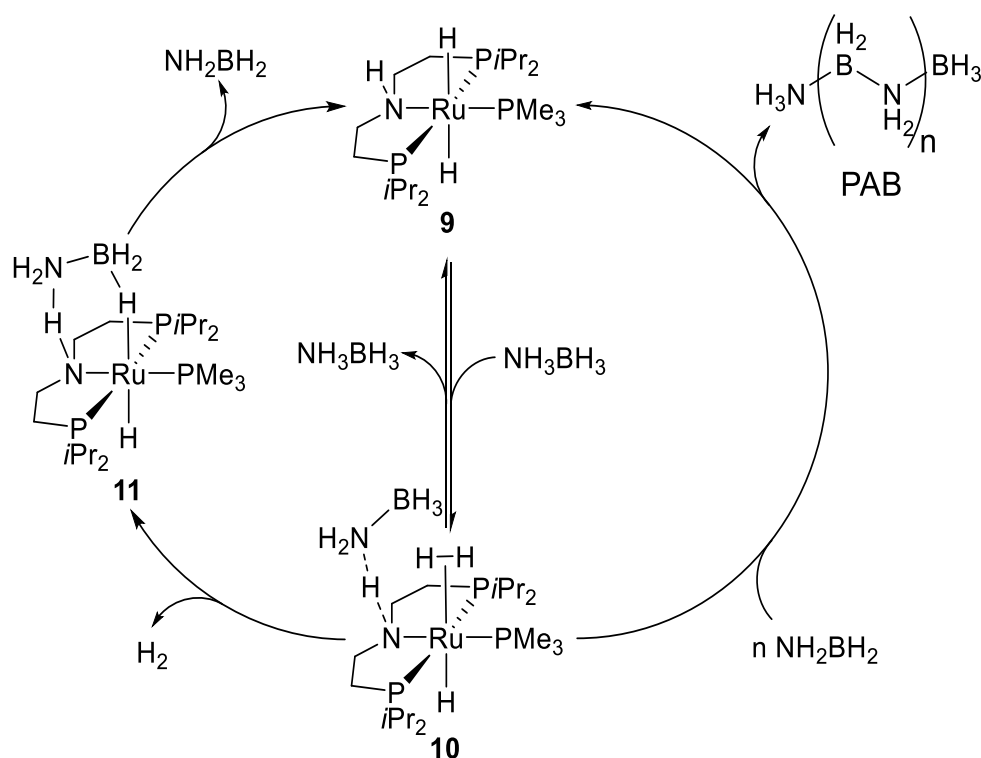


Scheme 1.8 Top: AB dehydrocoupling mediated by **6**. Bottom: Stoichiometric experiments relevant for catalysis.^[60]

II) Ruthenium PNP Pincer Complexes **8** and **9** for Ammonia Borane Dehydrocoupling

Schneider *and coworkers* employed remarkably active ruthenium PNP pincer complexes $[(\text{PNP}^{\text{Pr}})\text{Ru}(\text{H})\text{PMe}_3]$ (**8**) and $[(\text{HPNP}^{\text{Pr}})\text{Ru}(\text{H})_2\text{PMe}_3]$ (**9**) for amine borane dehydrocoupling, including AB dehydrocoupling to PAB (1.1 eq H_2) at room temperature with low catalyst loading (0.1 - 0.01 mol-%).^[17,65,66] Even though these catalysts are closely related and can be interconverted by reversible H_2 addition/elimination, they operate via different mechanism as

evidenced by kinetic studies and characterization of the obtained PAB polymers. The mechanism of dehydrogenation with **9** was investigated in detail including kinetic analysis, isotopic labeling and computational evaluation and can be divided in i) AB dehydrogenation to NH_2BH_2 (Scheme 1.9, left) and ii) metal catalyzed B-N coupling (Scheme 1.9, right).^[17] AB dehydrogenation is initialized by transfer of a N-H proton of ammonia borane to the hydride ligand of **9** upon formation of dihydrogen complex **10** with a residual NH_2BH_3 moiety stabilized by hydrogen bonding to the pincer N-H. Subsequent loss of the H_2 ligand gives **11**, a formal adduct of NH_2BH_2 and **9**, which releases aminoborane upon regeneration of **9**. B-N coupling also proceeds via key intermediate **10**, but requires NH_2BH_2 , which is attacked on the BH_2 terminus of the nucleophilic nitrogen of the formal NH_2BH_3 moiety in **10**.



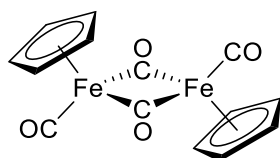
Scheme 1.9 Proposed mechanistic cycles for AB dehydrogenation to aminoborane (left) and B-N coupling to PAB (right).

The mechanistic proposal involves MLC via hydrogen bonding to the N-H of the ligand. Thus, the methylated analogon of complex **9** was synthesized and tested as a catalyst. Indeed, N-methylated compound $[(\text{MePNP}^{\text{Pr}})\text{Ru}(\text{H})_2\text{PMe}_3]$ (**12**) was less active by two orders of magnitude, demonstrating the importance of MLC for efficient AB dehydrocoupling with this system. Additionally, the mechanistic proposal involves the liberation of NH_2BH_2 into solution. However, a trapping experiment with cyclohexene did not give hydroboration product NH_2BCy_2 and borazine formation is only observed in small amounts. These findings were rationalized with rapid B-N coupling compared to slow hydroboration of cyclohexene and metal free oligomerization of NH_2BH_2 to BZ.

1 Introduction

1.2.2.2 Iron Complexes for Ammonia Borane Dehydrocoupling

Up to now, there are only a handful of reports for ammonia borane dehydrocoupling mediated by well-defined iron catalysts. Manners *and coworkers* reported iron carbonyl complex $[\text{CpFe}(\text{CO})_2]_2$ (**13**; 5 mol-%) for photocatalytic amine borane dehydrocoupling,^[67] including ammonia borane dehydrocoupling.^[68] After 3 h at 20 °C (95 % conversion) the B-(cyclotriborazanyl)amine-borane tetramer BCTB^a was observed as major product (62%) together with borazine (33%).



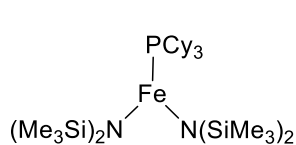
13

Products:

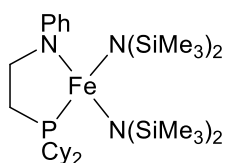
- BZ
- BCDB (original assignment)
- BCTB (ref. [49])

Figure 1.6 Iron catalyst reported by Manners and coworkers for photocatalytic AB dehydrocoupling.^[68]

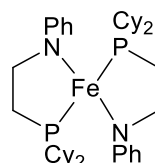
Baker *and coworkers* reported a series of iron complexes **14** - **16** as precatalysts for AB dehydrocoupling to mainly (P)BZ, BCTB^a and CTB (1.2 - 1.7 eq H₂) at 60 °C (5 mol-%).^[69] In contrast, similar complex **17** affords PAB (1 eq H₂) and operates at a much faster rate with identical catalyst loading. Unfortunately, mechanistic investigations are hindered by decomposition of the complexes to Fe(0) nanoparticles as indicated by black precipitates.



14



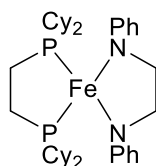
15



16

Products:

- (P)BZ
- CTB
- BCDB (original assignment)
- BCTB (ref. [49])



17

Product:

- PAB

Figure 1.7 Iron (pre)catalysts reported by Baker *and coworkers* for AB dehydrocoupling.^[69]

Similarly, Morris *and coworkers* found degradation of tetradentate complexes **18** - **22** to Fe(0) nanoparticles upon exposure to a AB solution.^[70] Interestingly, similar nanoparticles (ca. 4 nm by transition electron microscope, TEM) with comparable activity were generated from commercially available Fe²⁺ sources and substoichiometric amounts of PNNP ligand. The nanoparticles are extremely active (2.5 mol-% Fe) at 22 °C with a TOF of up to 3.66 s⁻¹ for production of BZ, PBZ and unidentified (NH₂BH₂)_n products (up to 1.8 eq H₂).

^a Previously assigned as B-(cyclodiborazanyl)amine-borane *trimer* BCDB. However, later studies suggest that it is correctly assigned as B-(cyclotriborazanyl)amine-borane *tetramer* BCTB.^[49]

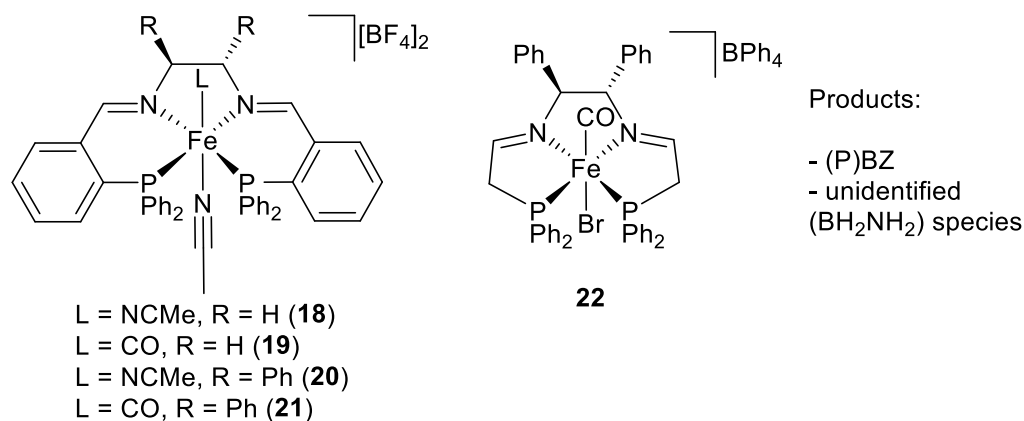


Figure 1.8 Iron precatalysts reported by Morris *and coworkers* for Fe(0) nanoparticle mediated dehydrocoupling of AB.^[70]

On the contrary, homogeneous amine borane dehydrocoupling was reported by Grützmacher *and coworkers* using low-valent iron mono-diazadiene complexes (Figure 1.9) as evidenced by poisoning experiments with 0.1 eq $\text{P}(\text{OMe})_3$ per iron.^[71] The reasoning behind such experiments is that substoichiometric amounts (in this case 0.1 eq) of phosphine would coordinate to the catalyst and shut down activity of only 10% of the catalysts. On the contrary, heterogeneous catalysts would completely lose their activity as they possess much less active sites due to agglomeration to nanoparticles. Ammonia borane dehydrocoupling to polyaminoborane with (pre)catalyst **23** (5 mol-%) proceeds in 5 h at 23 °C in THF and toluene equally well. On the contrary, activity of **24** is strongly solvent dependent with low activity in THF (12 % conversion after 2.5 h) and high activity in toluene (77 % conversion after 1.5 h).

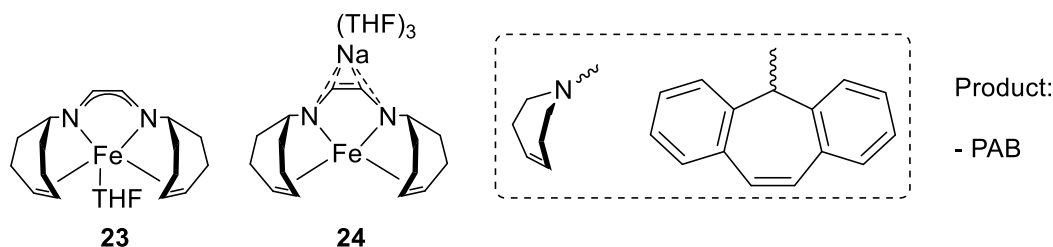


Figure 1.9 Iron (pre)catalysts for Ammonia borane dehydrocoupling to polyaminoborane reported by Grützmacher *and coworkers*.^[71]

The first iron pincer catalysts for dehydrocoupling of AB were reported by Guan *and coworkers* in 2014 and subjected to mechanistic evaluation by experimental^[72] and computational^[73] means. Complexes **25** - **27** do not operate at r.t. but require heating to 60 °C to release up to 2.5 eq H_2 upon generation of BZ, PBZ, CTB and BCTB^b. It should be noted that thermal decomposition of AB also takes place at 60 °C in a THF/diglyme mixture but slower and with a maximum of 1.3 eq H_2 after 50 h. Mechanistic studies suggest that dissociation of phosphine *trans* to the hydride generates the active species. As this process is accelerated by transition from **25** over **26** to **27**, the activity is

^b Previously assigned as B-(cyclodiborazanyl)amine-borane trimer BCDB. However, later studies suggest that it is correctly assigned as B-(cyclotriborazanyl)amine-borane *tetramer* BCTB.^[49]

1 Introduction

increasing accordingly with **27** being most active (2.5 eq H₂ after 20 h at 60 °C and 5 mol-% catalyst).

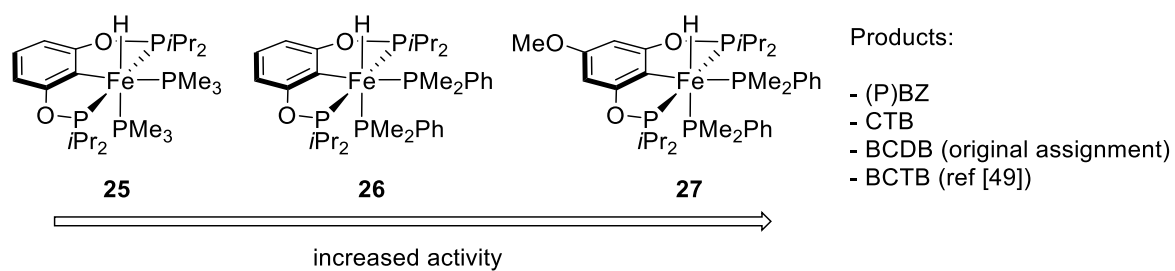


Figure 1.10 Iron precatalysts reported by Guan *and coworkers* for AB dehydrocoupling.

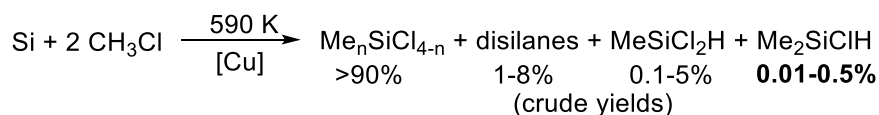
1.3 Hydrogenolysis of Halosilanes and Silyl Triflates

Results of this chapter have been published recently (A. Glüer, J. I. Schweizer, U. S. Karaca, C. Würtele, M. Diefenbach, M. C. Holthausen, S. Schneider, *Inorg. Chem.* **2018**, *57*, 13822) and parts of this work have been adapted from this publication with permission from ACS.^[74] Copyright 2018 American Chemical Society.

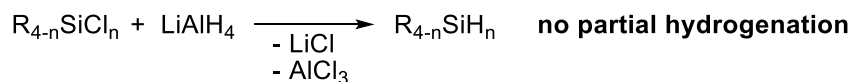
1.3.1 Conventional Routes to Organosilanes

Organohydrosilanes are important reagents for olefin hydrosilylation^[75–78] and other applications such as C-H bond silylation,^[79,80] desulfurization of fuels,^[81] or dehydrogenative oligo/polysilane formation.^[82,83] (Organo)hydrochlorosilane building blocks $\text{SiH}_x\text{Cl}_y\text{R}_z$ enable the orthogonal synthesis of branched polysiloxanes and self-healing silicones by sequential polycondensation and cross-linking via hydrosilylation as used e.g. for the fabrication of release coatings, moldings and adhesives.^[84–87] Some of these precursors, like MeSiCl_2H , are conveniently obtained as a byproduct of the Müller-Rochow process. However, Me_2SiClH synthesis suffers from low crude yields (0.01 - 0.5 %, Scheme 1.10a) and challenging separation procedures, necessitating alternative synthetic routes to hydro(chloro)silanes from chlorosilanes.^[88]

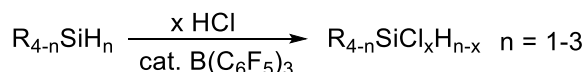
a) Müller-Rochow Process:



b) Reduction with LiAlH_4 :



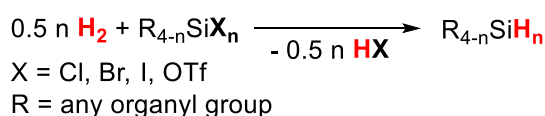
c) (Partial) Chlorination of Hydrosilanes:



Scheme 1.10 Conventional routes to hydrosilanes and hydrochlorosilanes.

Hydrosilanes are prepared on industrial scale by salt metathesis from chlorosilanes with LiAlH_4 (Scheme 1.10b). Besides the low atom economy that is associated with the use of complex hydride reagents, this approach is not commonly applicable for the synthesis of hydrochlorosilanes due to overreduction. Recently, the selective synthesis of chlorohydrosilanes was achieved by chlorination of hydrosilanes using HCl as chloride source and $\text{B(C}_6\text{F}_5)_3$ as catalyst (Scheme 1.10c).^[89] However, the reverse reaction, i.e. hydrogenolysis of chlorosilanes would arguably be much more desirable as chlorosilanes constitute optimal substrates due to their low and already established large scale production in the Müller-Rochow process (Scheme 1.10a). Alternatively, any progress in the production of organohydrosilanes via H_2 heterolysis (such as hydrogenolysis of silyl triflates) is highly desired (Scheme 1.11).

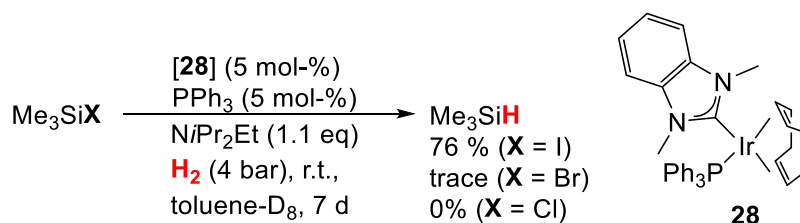
1 Introduction



Scheme 1.11 Silane synthesis from chlorosilanes or derivatives via H₂ heterolysis is highly desirable.

1.3.2 Hydrogenolysis of Halosilanes

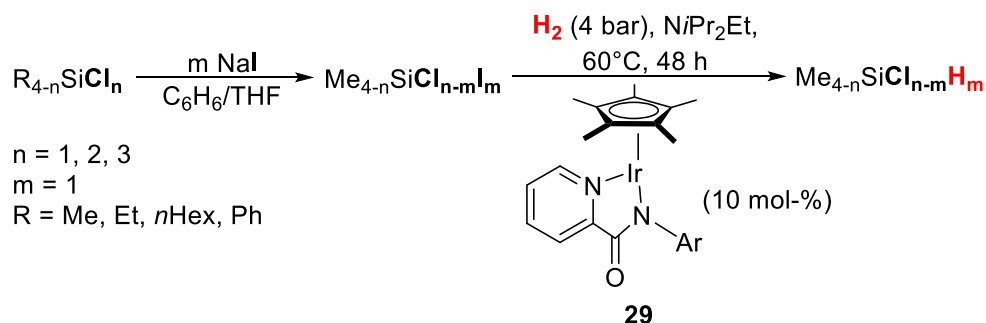
Examples of halosilane hydrogenolysis are scarce with only two reports by Shimada *and coworkers*. In 2017, hydrogenolysis of Me₃SiI with a variant of Crabtree's iridium catalyst **28** and NiPr₂Et as base was reported (Scheme 1.12). Me₃SiBr and Me₃SiCl were not converted under the same conditions. Upon change to the stronger base DBU (1,8-Diazabicyclo[5.4.0]undec-7-ene; pK_{a,MeCN} ([H-DBU]⁺) = 24.34),^[90] Me₃SiBr was hydrogenated in 21 % yield while Me₃SiCl only gave stoichiometric amounts of Me₃SiH (7 %).



Scheme 1.12 Shimada's first catalytic system for the hydrogenolysis of halosilanes.

The trend Si-I > Si-Br > Si-Cl is also found in the second (very recent) report of Shimada and coworkers.^[91] With iridium catalyst **29** (10 mol-%) and NiPr₂Et as base, Me₃SiI is readily hydrogenated, while Me₃SiBr only gives stoichiometric amounts of Me₃SiH (11 %). Again, change of base to DBU enables Me₃SiBr hydrogenolysis (80 % Me₃SiH) but fails for Me₃SiCl.

Interestingly, chlorosilanes can be hydrodechlorinated in a two-step process. Firstly, Me₃SiCl is converted to Me₃SiI by mixing with NaI in benzene/THF, presumably precipitating NaCl as driving force. Secondly, **29** (10 mol-%), H₂ and NiPr₂Et are added and the mixture heated to 60 °C for 2 d to obtain Me₃SiH in 84 % spectroscopic yield (Scheme 1.13).

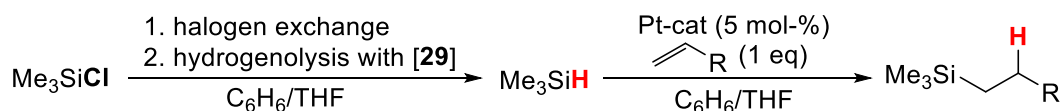


Scheme 1.13 Two-step one-pot hydrogenolysis of chlorosilanes via iodides. Mixed hydrochlorosilanes are also available via this route.

Similarly, other phenyl and alkylchlorosilanes are hydrogenated in spectroscopic yields of

49 – 78 %. Isolated yields were only 6 – 7 percentage points lower. Importantly, semihydrogenolysis of dichloro- and trichlorosilanes was achieved by treatment with only one eq NaI and subsequent hydrogenolysis of the chloriodosilane. Me_2SiClH (61 %), $(n\text{Hex})\text{MeSiClH}$ (57 %), Ph_2SiClH (71 %) and PhSiCl_2H (64 %) were accessible via this route.^c

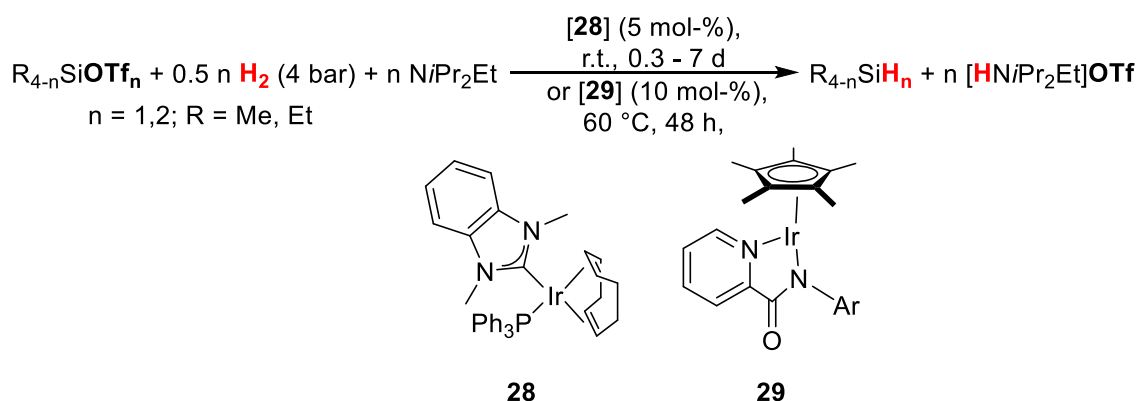
Additionally, one-pot hydrosilylation of olefins was performed with *in situ* generated Me_3SiH . For this purpose, an olefin (1-octene, ethyl-3-butenolate, styrene or 4-methoxy-styrene) and a platinum based hydrosilylation catalyst (5 mol-%) was added to the mixture after generation of Me_3SiH from Me_3SiCl . Hydrosilylation products were obtained in 58 – 78 % isolated yield with good anti-Markovnikov selectivity.



Scheme 1.14 One pot hydrosilylation of olefins with *in situ* generated Me_3SiH from Me_3SiCl reported by Shimada *and coworkers*.^[91]

1.3.3 Hydrogenolysis of Silyl Triflates

Shimada *and coworkers* performed two-step hydrogenolysis of chlorosilanes by intermediate conversion to iododisilanes and subsequent hydrogenolysis (chapter 1.3.2). Similarly, chlorosilanes can be converted to silyl triflates by neat reaction with HOTf (HCl as only byproduct), thus providing a better leaving group for hydrogenolysis.^[92,93] However, silyl triflate hydrogenolysis remains scarce with the only explicit reports published recently by Shimada *and coworkers* using iridium complexes **28** and **29** at high catalysts loadings of 5 or 10 mol-%, respectively.^[91,94] Additionally, the yield for hydrogenolysis of dimethylsilyl triflate $\text{Me}_2\text{SiOTf}_2$ is low (53%) and the reaction slow (1 week). Most importantly, they did not report about the formation of chlorohydrosilanes such as Me_2SiClH .



Scheme 1.15 Catalytic systems of Shimada *and coworkers* for silyl triflate hydrogenolysis.^[91,94]

^c spectroscopic yields (determined by ^1H NMR spectroscopy) are given.

1.4 Lessons from Hydrogenation of CO₂ to Formate by Iron Complexes

Results of this chapter have been published as review article ([A. Glüer, S. Schneider, *J. Organomet. Chem.* 2018, 861, 159](#)) and parts of this work have been adapted from this publication with permission from Elsevier.^[95] Copyright 2018 Elsevier.

The catalytic reactions attempted in this thesis (ammonia borane dehydrocoupling and hydrogenolysis of chlorosilanes/silyl triflates) are challenging as indicated by the fact that hydrogenolysis of halosilanes and silyl triflates was reported for the first time just recently^[91,94] and ammonia borane dehydrocoupling by base metal catalysts suffers high catalyst loading (typically 5 mol-%), reaction temperatures (typically 60 °C) and/or photochemical activation. In contrast, reversible hydrogenation of CO₂ was investigated in great detail, allowing for remarkable high turnover numbers (TONs) and turnover frequencies (TOFs) for hydrogen release (TON > 900000, TOF > 190000 h⁻¹)^[10] and formate production (TON ≈ 60000, TOF ≈ 20000 h⁻¹).^[19] Albeit not related on first sight, hydrogenation of CO₂ and hydrogenolysis of chlorosilanes/silyl triflates exhibits remarkable parallels. For example, the initial step of catalysis, i.e. hydride transfer to CO₂ and chlorosilanes (with concomitant chloride loss) is thermochemically challenging as indicated by the thermodynamic hydricity of formate ($\Delta G^{\circ}_{\text{H}^-} = 44 \text{ kcal mol}^{-1}$)^[30] on the one hand and the difference in Si-Cl and Si-H bond dissociation energies (BDE (Si-Cl) – BDE (Si-H) = 100 kcal mol⁻¹ – 70 kcal mol⁻¹ = 30 kcal mol⁻¹)^[35] on the other hand. These steps of high thermodynamic cost are alleviated by stabilization of protons by neutralization with base later in the catalytic cycle. Similar considerations can be made for silyl triflates. Accordingly, recent progress in the hydrogenation of CO₂ with iron complexes is reviewed in the following chapter.

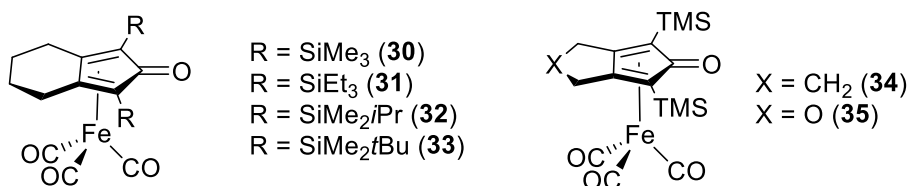
Reduction of CO₂ is still a challenging process as it is both thermodynamically stable (Gibbs free energy of formation, $\Delta_f G = -94.26 \text{ kcal mol}^{-1}$) and chemically inert (no overall dipole moment).^[96] On the other hand, CO₂ has two very polar bonds that account for both a strongly electropositive carbon center and two electronegative oxygen atoms. Consequently, the conversion of CO₂ needs both a catalyst and energy, which can be supplied in form of high energetic molecules such as H₂. In principal, hydrogenation of CO₂ can lead to several products such as formic acid, formaldehyde, methanol, methane, dimethyl ether and even higher hydrocarbons.^[96] Despite recent progress in iron catalyzed methanol production (not discussed here),^[97] coordination chemists have mainly been successful in developing catalysts that afford formic acid (or formate).

Hydrogenation of CO₂ to formic acid is endothermic ($\Delta H_{\text{R}}^{\circ} = +3.5 \text{ kcal mol}^{-1}$ in the gas phase^[98]), thus needing additional driving force. Besides high CO₂/H₂ pressures, base (typically tertiary amine) is utilized to generate extra driving force via deprotonation, thus shifting the equilibrium towards formate (Table 1.1). Subsequent reactions with the solvent or additives may then yield formate esters or formamides.

Table 1.1 Thermochemical data for CO₂ hydrogenation to several products (at 25 °C).^[99]

	ΔG_R° [kcal/mol]	ΔH_R° [kcal/mol]	ΔS_R° [cal/(molK)]
CO ₂ (g) + H ₂ (g) → HCO ₂ H (g)	10	3.5	-23
CO ₂ (g) + H ₂ (g) → HCO ₂ H (l)	7.9	-7.5	-51
CO ₂ (g) + H ₂ (g) + NH ₃ (aq) → HCO ₂ ⁻ (aq) + NH ₄ ⁺ (aq)	-2.3	-20	-60
CO ₂ (aq) + H ₂ (aq) + NH ₃ (aq) → HCO ₂ ⁻ (aq) + NH ₄ ⁺ (aq)	-8.5	-14	-19
CO ₂ (aq) + H ₂ (aq) → CO (aq) + H ₂ O (l)	2.6	2.6	-0.2
CO ₂ (aq) + 3 H ₂ (aq) → MeOH (l) + H ₂ O (l)	-19	-25	-21
CO ₂ (aq) + 4 H ₂ (aq) → CH ₄ (l) + 2 H ₂ O (l)	-46	-55	-30
CO ₂ (aq) + H ₂ (aq) + MeOH (l) → HCO ₂ Me (l) + H ₂ O (l)	-1.3	-3.7	-8.0
CO ₂ (aq) + H ₂ (aq) + NHMe ₂ (aq) → HCONMe ₂ (l) + H ₂ O (l)	-0.2	-8.7	-28

The relatively high solubility of CO₂ in water (0.033 mol/L at 25 °C under 1 bar CO₂) renders transformations in aqueous solution attractive. The CO₂ hydration constant is low ($[\text{H}_2\text{CO}_3]/[\text{CO}_2] = 1.70 \cdot 10^{-3}$) and uncatalyzed equilibrium formation is relatively slow. However, H₂CO₃ is a weak acid ($\text{p}K_{\text{a}1} = 3.6$ at 25 °C) which further complicates the picture, as the nature of the reactive species (CO₂ or bicarbonate) can depend on pH, temperature and CO₂ partial pressure. Laurenzy et al. examined aqueous CO₂ to formate hydrogenation with a molecular ruthenium phosphine catalyst.^[100] The rate dependence on pH and HCO₃⁻ concentration suggests that bicarbonate is the substrate rather than CO₂. Notably, most iron catalysts discussed here hydrogenate both CO₂ and carbonate. The first examples of iron based CO₂ hydrogenation catalysts have been reported in the 1980s, however, their reactivity can barely be regarded catalytic, as turnover numbers (TONs) higher than 6 have not been observed for the formation of alkyl formates even under harsh conditions.^[101,102] No progress was made until 2003 when Jessop reported a “High-Pressure Combinatorial Screening of Homogeneous Catalysts” for the hydrogenation of carbon dioxide by which he found combinations of FeCl₃ and either PPh₃, dppe (1,2-bis(diphenylphosphino)ethane) or dcpe (1,2-bis(dicyclohexylphosphino)ethane) in DMSO (dimethylsulfoxide) catalytically active in the formation of formate with TONs of 20, 23 and 113 respectively.^[103] It took until 2010 to discover Fe(PNP) pincer complexes^[19,104–106] (Chapter 1.4.1) and iron complexes ligated by tetradentate phosphine ligands^[107–111] (Chapter 1.4.2) with remarkable catalytic activities and TONs in the range of 10² to 10⁵. Additionally, air and moisture tolerant piano stool complexes **30** - **33** and **34** - **35** based on Knölker’s complex were also found to be catalytically active with moderate TONs around 50 to 400 (Figure 1.11).^[112] Computations support a mechanism with hydride transfer to CO₂ and rate determining, water/methanol assisted deprotonation of an intermediate H₂-complex.^[113] Interestingly, recent computational work predicts promising kinetics for CO₂ to methanol hydrogenation using Knölker-type catalysts.^[114]

Figure 1.11 Knölker-type iron piano stool catalysts for CO₂ hydrogenation.^[112]

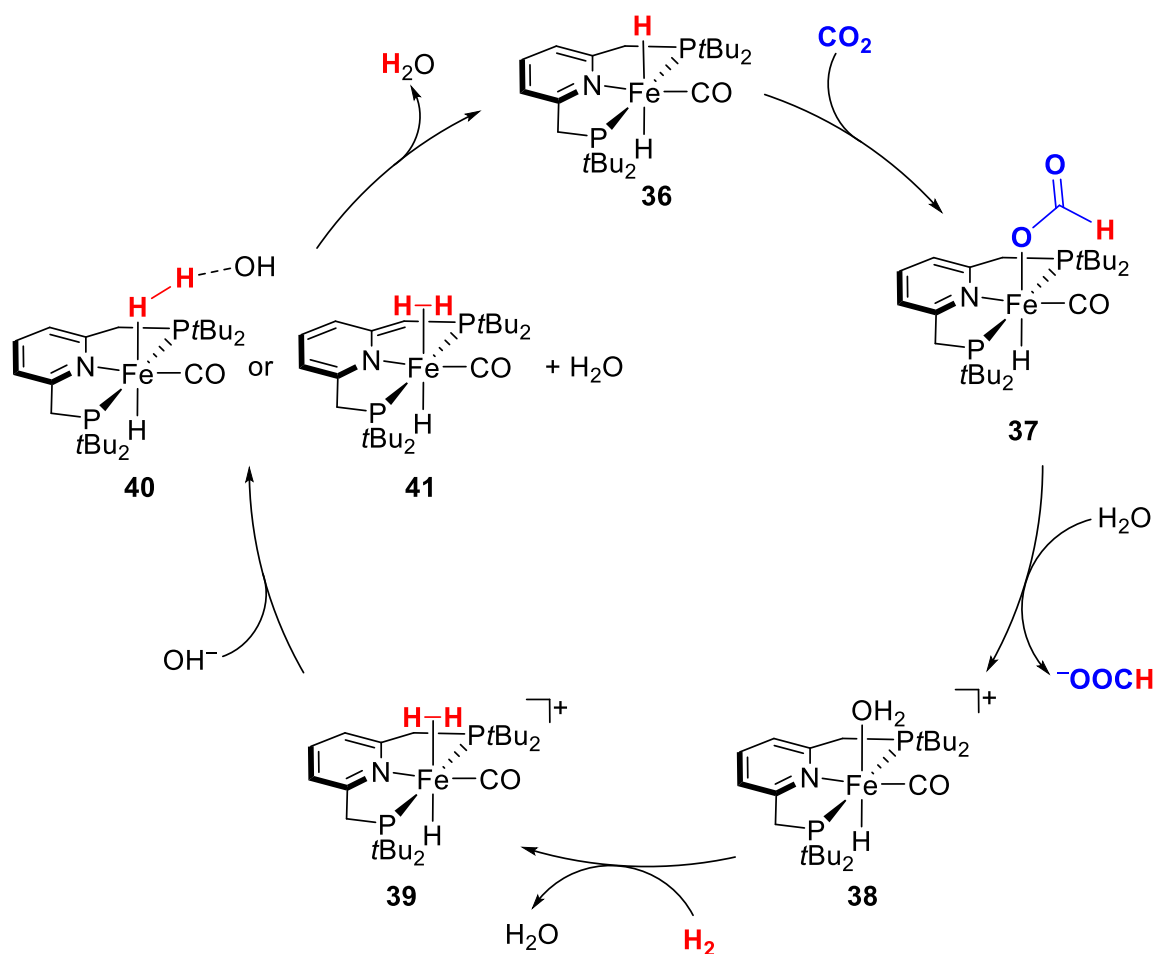
1 Introduction

1.4.1 PNP Pincer Ligands for CO₂ Hydrogenation

Only a handful of iron based pincer complexes are known to catalyze the hydrogenation of CO₂ or carbonate (CO₂ dissolved in H₂O).^[19,104–106] Two types of iron PNP complexes can be distinguished: Milstein-type aromatic pyridine (or pyrazine) based systems^[104–106] and aliphatic secondary (and tertiary) amine based systems.^[19] Yet, some generalizations can be made:

- 1) Like the iron co-factors of the hydrogenase enzymes,^[115,116] all catalysts carry additional CO auxiliary ligands. The strong π -accepting carbonyl ligand maintains a low-spin electronic configuration throughout the catalytic cycle, which might be a prerequisite for hydrogen activation.
- 2) The proposed mechanisms consist of all-iron(II) cycles. MLC reactivity might be instrumental for heterolytic H₂ activation. However, concerted outer-sphere H⁺/H⁻ transfer of a hydride ligand and a ligand proton to CO₂, as often proposed for the hydrogenation of organic carbonyl compounds, is not found. This is a direct consequence of the endothermicity of formic acid formation from H₂ and CO₂, which requires additional base for turnover. As a kinetic argument, CO₂ activation by outer-sphere hydride attack at the carbon atom is accompanied by bending of the two oxygen atoms away from the catalyst, hampering proton transfer.
- 3) The active species that undergo hydride transfer to CO₂ carry strong-field ligands in *trans*-position to the hydride, e.g. another hydride or CO. Such configurations foster high Fe–H hydricities (i.e. low $\Delta G^{\circ}_{\text{H}^-}$ values) as a prerequisite for nucleophilic CO₂ attack. The success of the meridionally binding, rigid pincer ligands in CO₂ hydrogenation catalysis might to a considerable extent rely on the stabilization of these configurations.

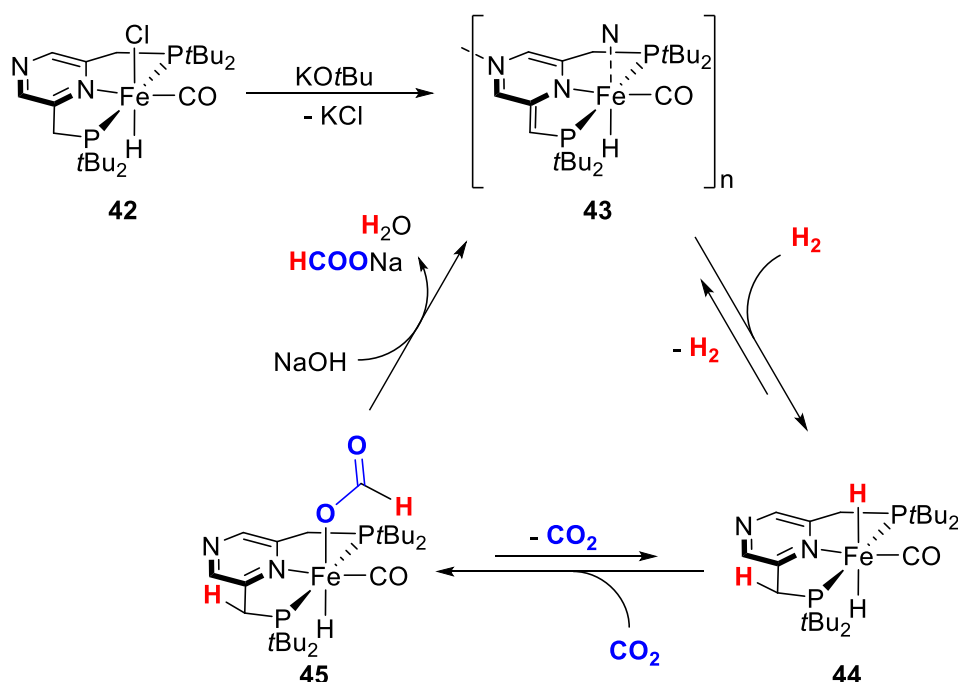
In 2011 Milstein *and Coworkers* reported the catalytic hydrogenation of CO₂ and carbonate to formate at low pressures by pyridine based dihydride pincer complex **36** at low pressures (< 10 bar total pressure; Scheme 1.16).^[104] Moderate activity (maximal turnover frequency, TOF_{max} = 156 after 5h at 80°C) and stability (TON_{max} = 800) is observed in a mixture of water and THF (10:1).



Scheme 1.16 Mechanistic proposal for CO₂ hydrogenation by dihydride complex **36**.^[104]

Although bifunctional activation of CO₂ is well known,^[5,22,117,118] stoichiometric experiments^[104] and calculations^[119] indicate that CO₂ is not activated via MLC but rather directly attacked by a metal bound hydride (“normal insertion”), leading to formate complex **37** after fast rearrangement (Scheme 1.16). Formate is released via substitution by a water molecule from the solvent leading to water complex **38**, which in turn can be substituted by dihydrogen to form complex **39**. Subsequent deprotonation of **38** might occur either directly on the dihydrogen ligand (**40**) or on the pincer backbone (**41**) with subsequent heterolytic 1,3-addition of dihydrogen via MLC to regenerate dihydride **36**, closing the catalytic cycle.

1 Introduction



Scheme 1.17 Mechanistic proposal for CO₂ hydrogenation by precatalyst **42**.^[106]

Recently, the slightly modified iron pincer complex **42** was reported which is pyrazine- instead of pyridine based (Scheme 1.17)^[106]. This system keeps the possibility of MLC through aromatization/dearomatization but has the additional possibility to coordinate metals via the nitrogen atom in 4-position of the aromatic ring. In fact, upon deprotonation of **42**, the backbone is dearomatized and oligomeric complex **43** is formed by coordination of the nitrogen atoms in 4-position of the pyrazine ring to another coordinatively unsaturated iron center (Scheme 1.17). Dearomatized oligomeric complex **43** (18-electron, six coordinate) is a masked 16-electron, five-coordinate hydride-CO species and (prepared *in situ* from **42** in H₂O/THF 10:1) a catalyst for hydrogenation of CO₂ and carbonate to formate. Its performance is comparable to the previously described pyridine-based system with a TON_{max} of 388 and 149 for CO₂^d and sodium carbonate^e hydrogenation, respectively.

It was shown that dearomatized **43** reacts with dihydrogen via 1,3-addition to form dihydride complex **44** which can insert CO₂ into the hydride-iron bond yielding formate complex **45**. Most likely, **45** is deprotonated at the pincer backbone and releases formate to regenerate dearomatized **43**, closing the catalytic cycle. Alternatively, formation of **43** can be skipped by a mechanism analogous to the one proposed for the related pyridine-based catalyst **36** (vide supra). In that case, **45** would release formate by substitution with H₂O, which in turn would be substituted by dihydrogen. Subsequent deprotonation would regenerate dihydride **44**, closing the catalytic cycle. However, catalysis with pyrazine-based **42** was shown to proceed also in the absence of water (albeit with a lower TON).^[106]

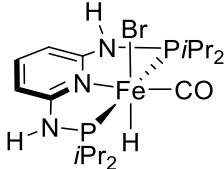
Another modification of Milstein's pyridine based pincer catalysts was introduced by Kirchner *and*

^d 16 h, 80 °C **42** (0.9 M); p(H₂) = 6.3 bar; p(CO₂) = 3.3 bar; c(NaOH) = 4 mol/L

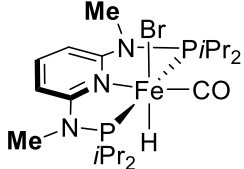
^e 16 h, 45 °C, HCO₃Na (9 M); **42** (0.9 M); KOtBu (1.1 M); p(H₂) = 6.5 bar; NaOH (4 mol/L)

coworkers, i.e. exchange of the methylene linker with NR (R = H, Me) groups.^[120–126] Iron complex **46** (Table 1.2) catalyzes both CO₂ and HCO₃⁻ hydrogenation in alkaline H₂O/THF (4:1) with TONs of 1220 (80 °C, 80 bar, 21 h) and 1964 (80 °C, 90 bar, 24 h), respectively.^[105] No catalytic turnover was observed in EtOH with DBU as base, which was attributed to consumption of catalytically active dihydrides by the solvent.^[105] Backbone *N*-methylation increases the stability and enables a high TON ≈ 10000 under the same conditions (Table 1.2).

Table 1.2 Solvent dependence for CO₂ hydrogenation with catalysts **46** and **47**.



46



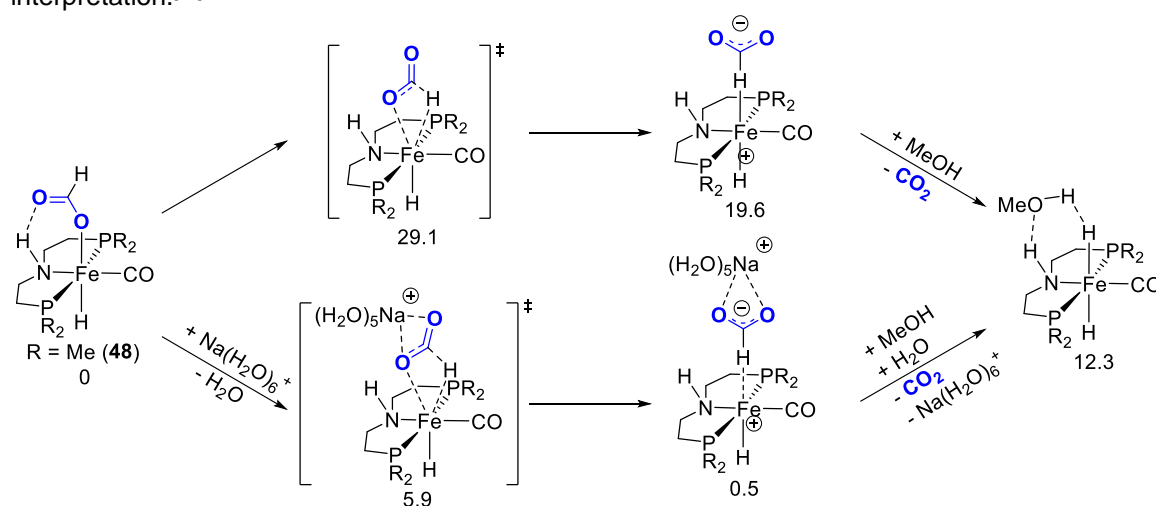
47

H ₂ O/THF, NaOH ^a	TON = 1220	TON = 680
EtOH, DBU ^b	TON = 0	TON = 9840
THF, DBU ^a	TON = 0	TON = 0

^a 80 °C, 80 bar total pressure, 21h, catalyst:base = 1:1250.

^b 80 °C, 80 bar total pressure, 21h, catalyst:base = 1:10000.

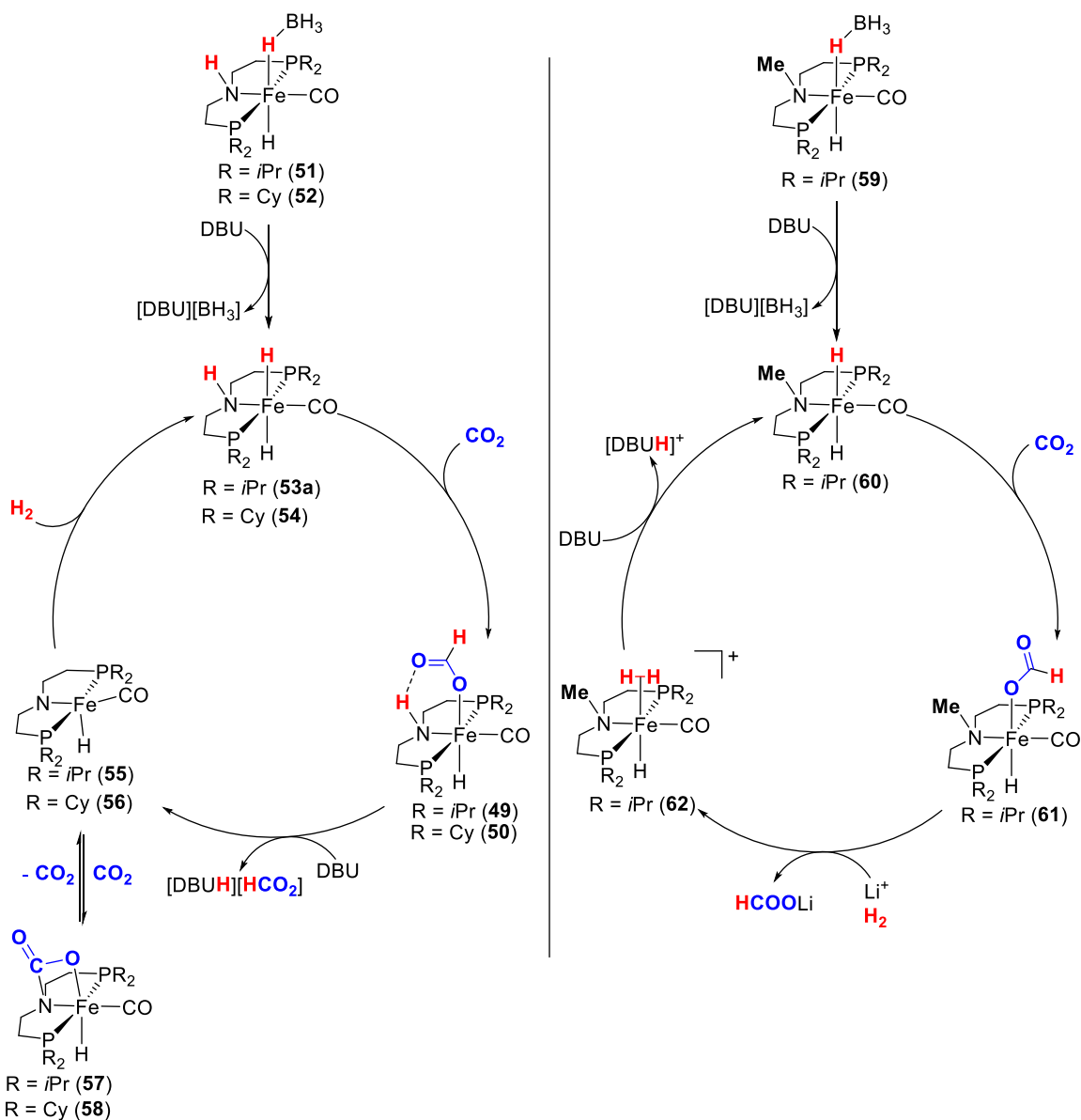
In contrast to Kirchner's catalyst, Lewis acid (LA) co-catalysts decisively improve the catalytic performance of aliphatic PNP pincer catalysts. Hazari, Schneider *and coworkers* initially reported unprecedented activities in hydrogen release (TOF > 190000 h⁻¹, TON > 900000) for formic acid dehydrogenation with formate catalysts of type **48** (Scheme 1.18, R = *i*Pr, Cy) and significantly increased catalytic performance by LA co-catalysts, e.g. 10 mol-% LiBF₄.^[10] This observation was rationalized with acceleration of turnover limiting CO₂-loss by LA coordination to the formate ligand. DFT computations for methanol reforming to H₂ and CO₂ with this catalyst support this interpretation.^[26]



Scheme 1.18 Computed relative energies (in kcal mol⁻¹) of formate extrusion for a Me-truncated model in the presence of Lewis acid (bottom) and without additive (top).^[26]

1 Introduction

The secondary and tertiary aliphatic PNP pincer ligands were also utilized in iron catalyzed CO₂ hydrogenation to formate (Scheme 1.19) and formamides.^[19,20] As for the reverse reaction, Bernskoetter, Hazari, and coworkers found a significant increase in activity by LA addition. As for dehydrogenation, the “Lewis acid-effect” was attributed to acceleration of turnover limiting formate rearrangement. An unusual dependence of the activity on the ligand was also observed. Deprotonation or hydrogen bonding of the secondary amine ligand *H*N(CH₂CH₂PR₂)₂ potentially enables MLC reactivity,^[7] which is blocked for the tertiary amine ligand *Me*N(CH₂CH₂PR₂)₂. As a consequence, the latter ligand was shown to be inferior, e.g. for ruthenium catalyzed ammonia borane dehydropolymerization.^[17,42] However, the contrary was found for iron catalyzed CO₂ and carbonate hydrogenation to formate.^[19] Methylated precatalyst **59** exhibited far superior catalytic performance (TON_{24h} = 42350, TOF_{1h} = 18050 h⁻¹) over **51** (TON_{24h} = 1500, TOF_{1h} = 680 h⁻¹) under identical conditions (69 bar, 80 °C, catalyst:DBU:LiOTf = 1:79600:10500). As for Milstein’s catalyst, CO₂ insertion was proposed after *in situ* formation of *trans*-dihydrides **53a/60**. In case of the secondary amine catalyst, this step is followed by turnover limiting formate release upon deprotonation, which is hampered by intramolecular formate hydrogen bonding with the pincer ligand. Furthermore, the authors found that the isolable, five-coordinate amido intermediate **55** forms an off-cycle equilibrium with carbamate **57**. Hence, the inferior catalytic performance was attributed to formate complex overstabilization and inhibition by carbamate formation, i.e. counterproductive MLC in this case. Interestingly, Lewis acids also facilitate formate extrusion from the tertiary amine complex **61** via stabilization of anionic formate. The TON (60000) and TOF (20000 h⁻¹) reported for precatalyst **59**/LiOTf currently define the benchmark for earth abundant metal CO₂ hydrogenation catalysis.^[19]



Scheme 1.19 Mechanistic proposals for the two classes of aliphatic PNP iron catalysts. *Left*: Secondary amine PNP ligand. *Right*: More efficient tertiary amine PNP ligand.

1.4.2 Tetradentate Phosphine Ligands for CO₂ Hydrogenation

Concurrent with the aforementioned Fe(PNP) pincer catalysts, tetradentate ligands with mostly phosphorous donors were employed to stabilize iron complexes for CO₂ and carbonate hydrogenation at relatively high pressures (total pressure: 30 – 90 bar). All catalysts form formate as initial product, however further transformation to formyl esters and amides is possible in the presence of alcoholic solvents or secondary amine, respectively.^[108,109,111] The proposed mechanisms exhibit similarities with the pincer catalysts discussed above:

- 1) The catalytic cycles are comprised of all-iron(II) mechanisms with heterolytic H₂ activation.
- 2) CO₂ activation proceeds via insertion into a Fe–H bond. Hence, the hydricities of the active iron hydride catalyst species are predictors for efficient catalysis.^[30,109,127]
- 3) The reaction is strongly solvent dependent. Protic solvents are preferable for CO₂/HCO₃[–]

1 Introduction

hydrogenation, while aprotic solvents are favored for reverse formic acid dehydrogenation. The influence of solvation was examined computationally by DFT giving a more detailed picture.^[128] Protic solvents with high dielectric constant (e.g. MeOH) can overstabilize bicarbonate. This in turn hampers deprotonation of the Fe-H₂ complex, therefore slowing down H₂ heterolysis. In contrast, non-protic solvents with low dielectric constant (e.g. THF) overstabilize the resulting iron hydride, which also slows down catalysis. Hence, a volcano-type plot results for effective activation energy vs. bicarbonate free enthalpy of solvation. Consequently, low polarity protic (e.g. ^tBuOH) or high polarity non-protic solvents (e.g. DMSO) perform best.

Beller *and coworkers* reported the use of tris(2-(diarylphosphino)ethyl)phosphine (^{et}PP₃) based complex **63** and tris(2-(diarylphosphino)aryl)phosphine (^{ar}PP₃) based iron precatalyst **72** (Figure 1.12).^[108,111] Additionally, Laurency *and coworkers* recently modified complex **63** with three sulfonate groups, enabling catalysis in neat water at room temperature.^[129] Peters *and coworkers* found related ^{ar}XP₃ based precatalysts (X = Si, C, BPh) **66** - **71** to be less active under identical conditions and Gonsalvi *and coworkers* utilized slightly different P₄ based precatalysts **64/65** (Figure 1.12).^[107,109]

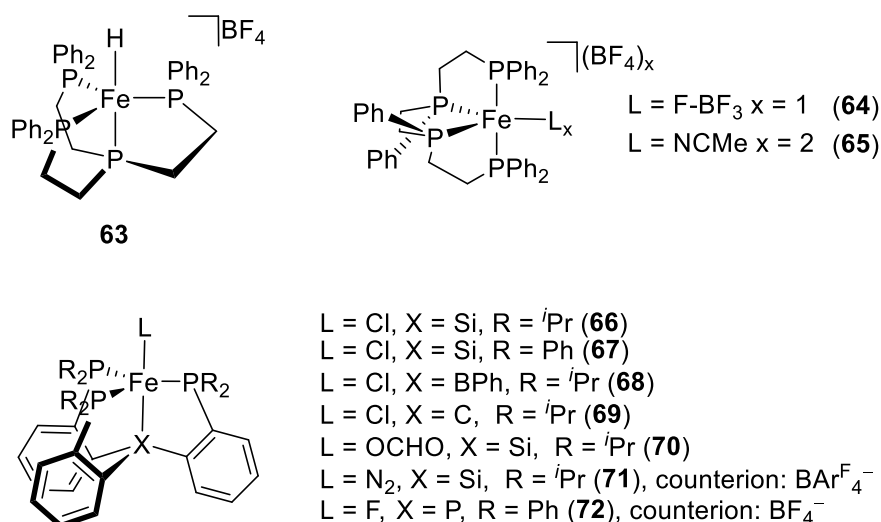
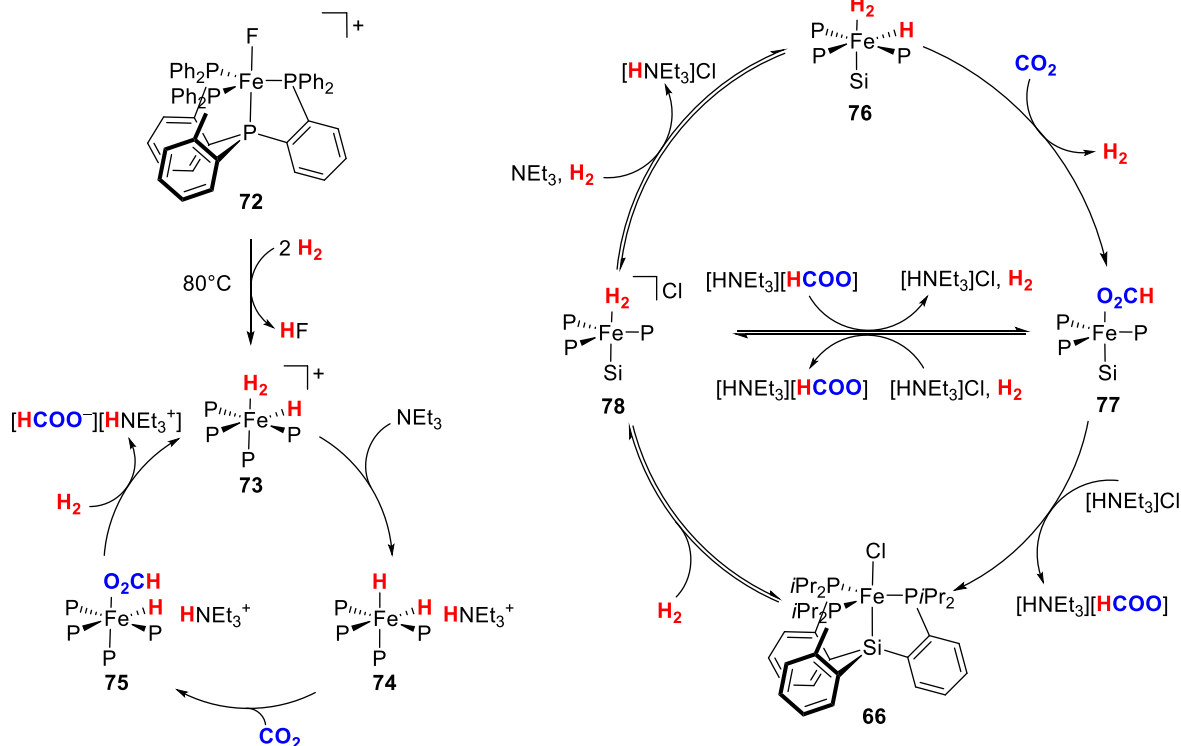


Figure 1.12 XP₃ (right) and P₄ (left) based (pre)catalysts for hydrogenation of CO₂ and carbonate (Gonsalvis Complexes **64/65** were not tested for catalytic CO₂ hydrogenation and Peters systems **66** - **71** were not tested for carbonate hydrogenation).

For example, with methanol as solvent and NEt₃ as base (**63**: 90 bar CO₂/H₂ 2:1; **72**: 60 bar CO₂/H₂ 1:1, 60 bar), Beller *and coworkers* obtained methylformate (**63**: TON = 292; **72**: TON = 1692) as main product after 20 h at 100 °C, whereas DMF (*N,N*-Dimethylmethanamide) was formed in 70 % yield when HNEt₂ was added to the reaction mixture (**63**: TON = 727; **72**: TON = 2329).^[108,111]

Their mechanistic proposal involves activation of precatalyst **72** with H₂ upon loss of HF to form the active hydride-dihydrogen complex **73**. Deprotonation by NEt₃ gives dihydride complex **74** which is stabilized by the generated conjugate acid HNEt₃⁺ (Scheme 1.20). Subsequent attack of CO₂ on

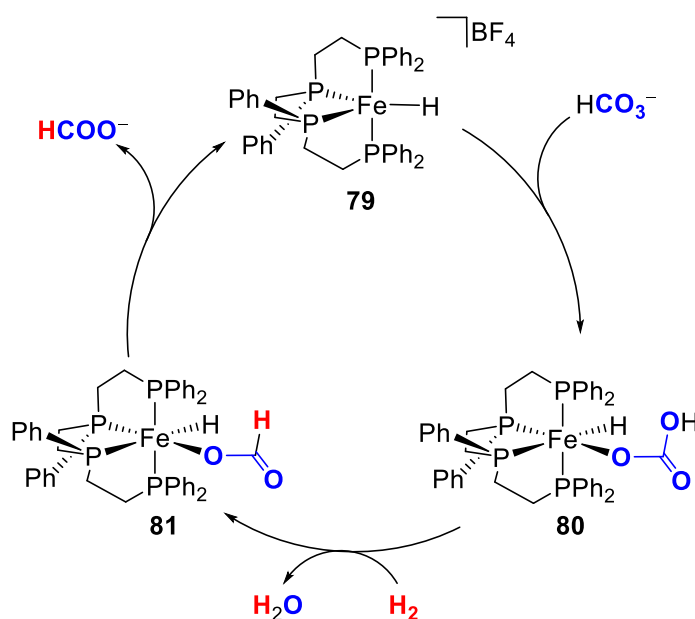
the hydride ligand and formal insertion into the M-H bond yields formate complex **75** which releases formic acid upon substitution with H_2 . Calculations suggest that HNEt_3^+ facilitates formate release by formation of an acid-base complex^[130] (Similarly, Bernskoetter, Hazari *and* *Coworkers* facilitated formate release by addition of Lewis acids such as Li^+ ; see Chapter 1.4.1).



Scheme 1.20 Mechanistic proposals for Beller's PP_3 system (left) and Peters' less active XP_3 system ($\text{X} = \text{Si}$).

Even though, superficially, Peters' XP_3 system ($\text{X} = \text{Si}, \text{C}, \text{BPh}$) seems to be closely related to Beller's PP_3 system, it is less active (TONs = 27 - 200) and the mechanism for CO_2 hydrogenation with **66** as catalyst differs. XP_3 dihydride-hydride complex **76** is not charged contrary to analogous PP_3 complex **73**, thus deprotonation of **76** would result in an anionic dihydride complex which is likely to be very unstable. Hence, an alternative mechanism was suggested where dihydride-hydride **76** reacts with CO_2 directly under H_2 loss to give formate complex **77**. This might form cationic dihydrogen complex **78** either directly by formate for H_2 substitution or via chloro complex **66**. Additionally, Peters *and coworkers* report that choice of solvent (MeOH) is critical as no reaction occurred in neat THF, again highlighting the importance of polar, protic solvents in phosphinoiron CO_2 hydrogenation catalysis.^[109,131]

Gonsalvi *and coworkers* utilized neutral tetraphosphine ligands.^[107] The precatalysts **64/65** hydrogenate bicarbonate (0.1 mol-% catalyst) in MeOH/propylene carbonate at 80 °C and 30 bar H_2 with a TON of 620 (**64**) and 780 (**65**), respectively, after 24h. Mechanistic studies suggest hydride **79** as key intermediate as it coordinates HCO_3^- to a vacant site to form hydride carbonate **80** (Scheme 1.21). Subsequent reaction with H_2 yields hydride formate complex **81** under elimination of water. Dissociation of formate regenerates hydride **79**, closing the catalytic cycle.



Scheme 1.21 Mechanistic proposal for Gonsalvis P_4 based catalyst for HCO_3^- hydrogenation.^[107]

1.4.3 Conclusions for Design of Catalysts for Chlorosilane/Silyl Triflate Hydrogenolysis

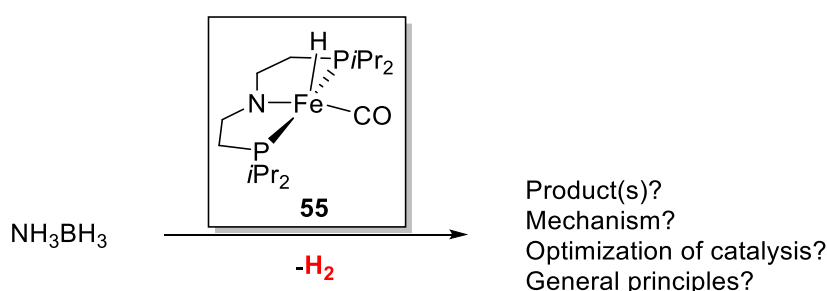
Aliphatic PNP pincer complexes **51** and **59** constitute highly active base metal precatalysts for CO_2 hydrogenation (chapter 1.4.1),^[19] suggesting that the PNP pincer platform is suitable for the hydrogenolysis of chlorosilanes and silyl triflates due to the similarities discussed above. N-methylation increased activity of CO_2 hydrogenation, because resting state over-stabilization by hydrogen bonding of formate to the N-H proton was prevented. Nevertheless, H_2 activation might be facilitated by MLC. Consequently, the effect of N-methylation should be investigated when polar or ionic leaving groups (such as triflate) are expected. It is important to note that iron catalyzed CO_2 hydrogenation requires strongly hydridic metal hydrides to facilitate the initial hydride transfer to the substrate. High thermodynamic hydricities are obtained using strong *trans*-ligands such as hydrides, suggesting the *trans*-dihydride motif for thermochemically challenging hydride transfer, e.g. to chlorosilanes.^[30] The catalytic cycles for CO_2 hydrogenation are comprised of outer-sphere all-iron(II) mechanisms. Strong-field ligands such as CO are employed to lock the metal in the low-spin state and avoid energetic penalty by reorganization. To ensure that no high spin species complicate the picture in chlorosilane/silyl triflate hydrogenolysis, ruthenium is targeted instead of iron due to higher ligand field splitting. Literature known complex *trans*- $[(\text{HPNP}^{\text{Pr}})\text{Ru}(\text{H}_2)\text{CO}]$ (**82**, $\text{HPNP} = \text{HN}(\text{CH}_2\text{CH}_2\text{P}^{\text{Pr}}\text{R}_2)_2$) fits to all requirements discussed above and is an isolable solid unlike other dihydrides such as $[(\text{HPNP})\text{Ru}(\text{H})_2\text{PMe}_3]$ (**9**) or $[(\text{HPNP}^{\text{Pr}})\text{Fe}(\text{H}_2)\text{CO}]$ (**53**).^[10,65] Additionally, it is active in CO_2 hydrogenation, proving its ability to transfer hydrides to challenging substrates.^[132,133]

2 Objectives

Two main objectives of this thesis can be differentiated:

1) Ammonia borane dehydrocoupling mediated by a base metal pincer complex.

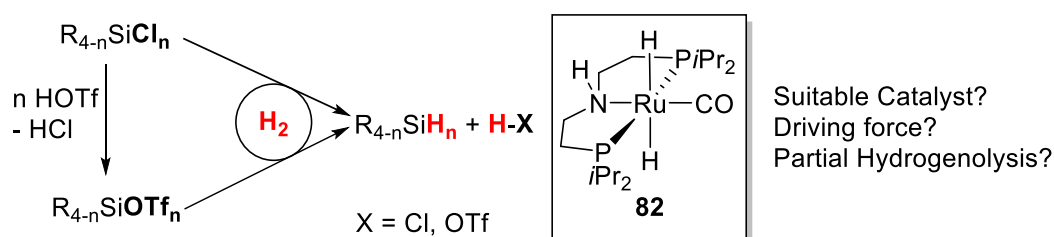
Ammonia borane is a potential H₂ storage material and precursor to B-N polymeric materials.^[33,36,38,66] Bifunctional precious metal pincer complexes are among the most active ammonia borane dehydrocoupling catalysts,^[17,36,65] but bifunctional base metal complexes for this transformation are rare (chapter 1.2).^[72] Thus, iron pincer complex **55** is targeted as potential catalyst for ammonia borane dehydrocoupling (Scheme 2.1). Subsequently, mechanistic studies are to be conducted in order to optimize reaction conditions. If possible, general principles for catalyst design may be extracted.



Scheme 2.1 Complex **55** is targeted as catalyst for ammonia borane dehydrocoupling.

2) Silane synthesis via H₂ heterolysis.

Most organohydrosilanes are conventionally obtained using stoichiometric amounts of metal hydrides such as LiAlH₄, producing large amounts of metal-containing waste.^[134] Thus, utilization of H₂ as (atom)economic reducing agent is highly desirable. Organochlorosilanes constitute optimal substrates for Si-Cl hydrogenolysis as they are produced on large scale and low cost.^[88] However, direct organochlorosilane hydrogenolysis remains elusive, due to its endergonicity.^[89] Thus, initial studies should aim to understand the thermochemistry of this reaction and find ways to add driving force to facilitate turnover. As an alternative, chlorosilanes can be converted to silyl triflates by reaction with triflic acid and subsequently tested for hydrogenolysis. Potent bifunctional ruthenium hydrogenation catalyst **82** is targeted as potential catalyst to extend its scope to both chlorosilane and silyl triflate hydrogenolysis. Special emphasis will be put on selectivity to possibly obtain valuable partially hydrogenated products such as Me₂SiClH or Me₂SiHOTf.



Scheme 2.2 Complex **82** is targeted as catalyst for hydrogenolysis of chlorosilanes/silyl triflates.

3 Ammonia Borane Dehydrocoupling

Results of this chapter have been published ([A. Glüer](#), M. Förster, V. R. Celinski, J. Schmedt auf der Günne, M. C. Holthausen, S. Schneider, *ACS Catal.* **2015**, 5, 7214) and parts of this work have been adapted from this publication with permission from ACS.^[42] Copyright 2015 American Chemical Society.

3.1 Introduction

Dehydrocoupling of ammonia borane (NH_3BH_3 , AB) has received considerable attention for H_2 storage/transfer and for the selective formation of B-N polymeric materials (see chapter 1.2). Protocols on the regeneration of dehydrogenation products such as borazine (BZ), polyborazylene (PBZ) or polyaminoborane (PAB) further fueled this interest.^[43–46] Several catalysts for AB dehydrocoupling were reported and particularly some homogeneous 2nd and 3rd row transition metal transition catalysts showed remarkably high activity and selectivity.^[36,135,136] In contrast, only a few well-defined base metal catalysts were examined (see chapter 1.2.2.2 for a comprehensive overview over molecular iron catalysts for AB dehydrocoupling).^[68–72,137–139] Importantly, they generally suffer from much lower turnover numbers (TON) and frequencies (TOF), hence requiring high catalyst loading (typically 5 mol-%), reaction temperatures (typically 60°C), and/or photochemical activation. Recently reported bifunctional ruthenium catalysts [(PNP)Ru(H)PMe₃] (**8**) and [(HPNP)Ru(H)₂PMe₃] (**9**, HPNP = $\text{HN}(\text{CH}_2\text{CH}_2\text{P}i\text{Pr}_2)_2$) demonstrated efficient AB dehydrocoupling at room temperature enabled by metal-ligand cooperation (MLC; see chapter 1.2.2.1). The similar iron complex [(PNP)Fe(H)CO] (**55**) and related PNP hydrides were successfully utilized by several groups as catalysts in challenging de-/hydrogenation reactions of organic substrates.^[10,140–144] Thus, **55** was targeted as potential catalyst for AB dehydrocoupling.

3 Ammonia Borane Dehydrocoupling

3.2 Results and Discussion

Iron complex [(PNP)Fe(H)CO] (**55**, HPNP = HN(CH₂CH₂P*i*Pr₂)₂) catalyzes the release of one equivalent H₂ from ammonia borane (AB) at room temperature without additional activation, such as base or irradiation with unprecedented high catalytic activities (TOF = 30 h⁻¹) for base metal catalysts.^[68–72,137–139] Full conversion is obtained with catalyst loadings as low as 0.5 mol-%. Furthermore, the TON_{max} is strongly dependent on catalyst loading, e.g. rising from around 80 (0.1 mol-% **55**) to 200 (0.5 mol-% **55**), respectively (Figure 3.1). This observation suggests that catalysis scales with a higher order in Fe concentration than catalyst deactivation.

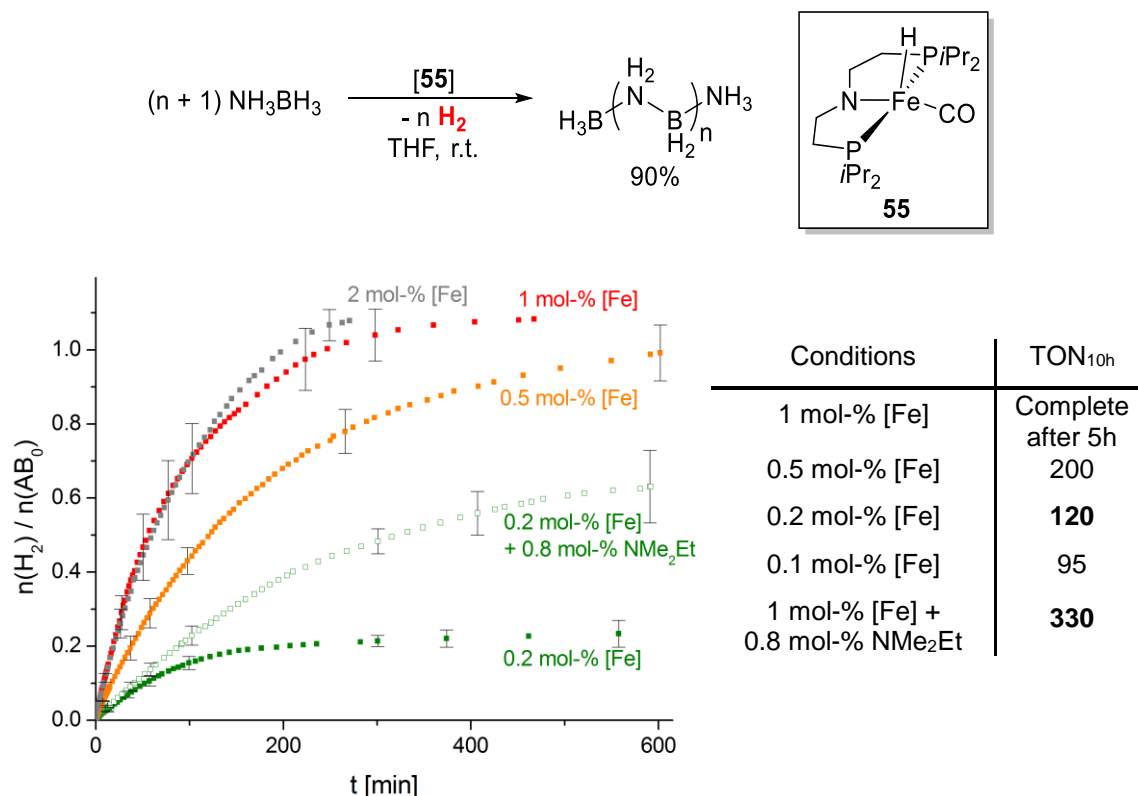


Figure 3.1 Top: AB dehydrocoupling to PAB mediated by iron catalyst **55** (top). Bottom: Time conversion plots of AB ($c_0 = 0.54$ M) dehydrogenation in THF catalyzed by **55** (left) and table with corresponding TONs after 10 h (right).

Concomitant with H₂ evolution, a white insoluble material is obtained as main product (ca. 90%). The ¹¹B MQ-MAS NMR spectrum (Figure 3.2; recorded and interpreted by Vicinius R. Celinski and Jörn Schmedt auf der Günne from the University of Siegen)^[42] strongly resembles that of PAB obtained with catalyst **9**.^[17] The main signal at $\delta_{\text{iso}} = -10.6$ ppm (second order quadrupolar effect parameter (SOQE) = 1.5 MHz) is assigned to boron atoms in the main chain and low intensity signals at $\delta_{\text{iso}} = -21.4$ ppm (SOQE = 1.1 MHz) and $\delta_{\text{iso}} = -20.8$ ppm (SOQE = 1.4 MHz) to BH₃ end groups. The small SOQE (0.5 MHz) of a minor signal at $\delta_{\text{iso}} = 1.5$ ppm indicates a symmetrical environment, and the chemical shift is in agreement with four nitrogen substituents around boron.^[145] This signal is therefore assigned to B(NH₂)₄ moieties that link the polymer chains. Notably, the same signals were found for catalysts **6**, **8** and **9**.^[17,66]

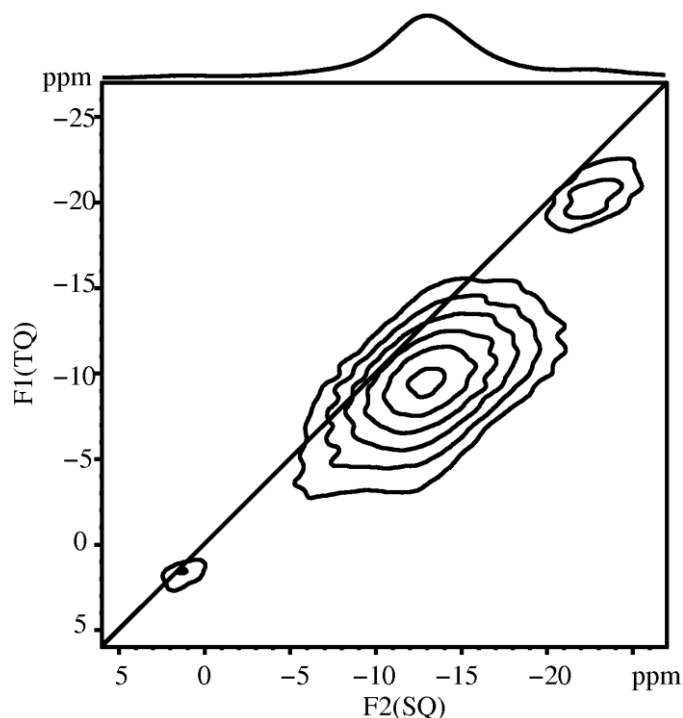


Figure 3.2 ^{11}B MAS NMR sheared triple-quantum filtered MQMAS spectrum of PAB obtained from AB dehydrocoupling with catalyst **55** (measured and interpreted by Vinicius R. Celinski and Jörn Schmedt auf der Günne).^[42]

Besides PAB, small amounts of borazine (BZ, $\text{B}_3\text{N}_3\text{H}_6$, $\delta_{1\text{B}} = +30.7$ ppm), polyborazylene (PBZ, $\text{B}_3\text{N}_3\text{H}_{x<6}$, $\delta_{1\text{B}} = +27.8$ ppm), cyclotriaminoborane (CTB, $\text{B}_3\text{N}_3\text{H}_6$, $\delta_{1\text{B}} = -10.9$ ppm), cyclodiaminoborane (CDB, $\text{B}_2\text{N}_2\text{H}_4$, $\delta_{1\text{B}} = -11.7$ ppm) and B-(cyclotriborazanyl)amine-borane (BCTB, $\text{H}_3\text{BNH}_2\text{-}cyclo\text{-B}_3\text{N}_3\text{H}_{11}$, $\delta_{1\text{B}} = -5.8, -11.7, -24.7$ ppm) are detected in solution by ^{11}B NMR spectroscopy.^[49] Hence, the formation of BZ and PBZ account for the slightly higher yield in H_2 than 1 equivalent. According to experimental and theoretical studies, these products can be attributed to metal-free oligomerization of transient, free aminoborane.^[48,50,51,53,54] The release of $\text{H}_2\text{N=BH}_2$ as intermediate was confirmed by the observation of $\text{H}_2\text{NB}(\text{C}_6\text{H}_{11})_2$ upon dehydrogenation in the presence of cyclohexene.^[48,53] Note, that release of free aminoborane is generally associated with catalysts that produce (P)BZ instead of PAB.^[146]

Initial rate kinetic examinations revealed that hydrogen release exhibits first order rate dependence both in catalyst and in AB ($v_0 = k [\mathbf{55}] [\text{AB}]$, $k = 4.6 \text{ M}^{-1}\text{s}^{-1}$; Figure 3.3), as previously found for catalyst **9** ($k = 24 \text{ M}^{-1}\text{s}^{-1}$).

3 Ammonia Borane Dehydrocoupling

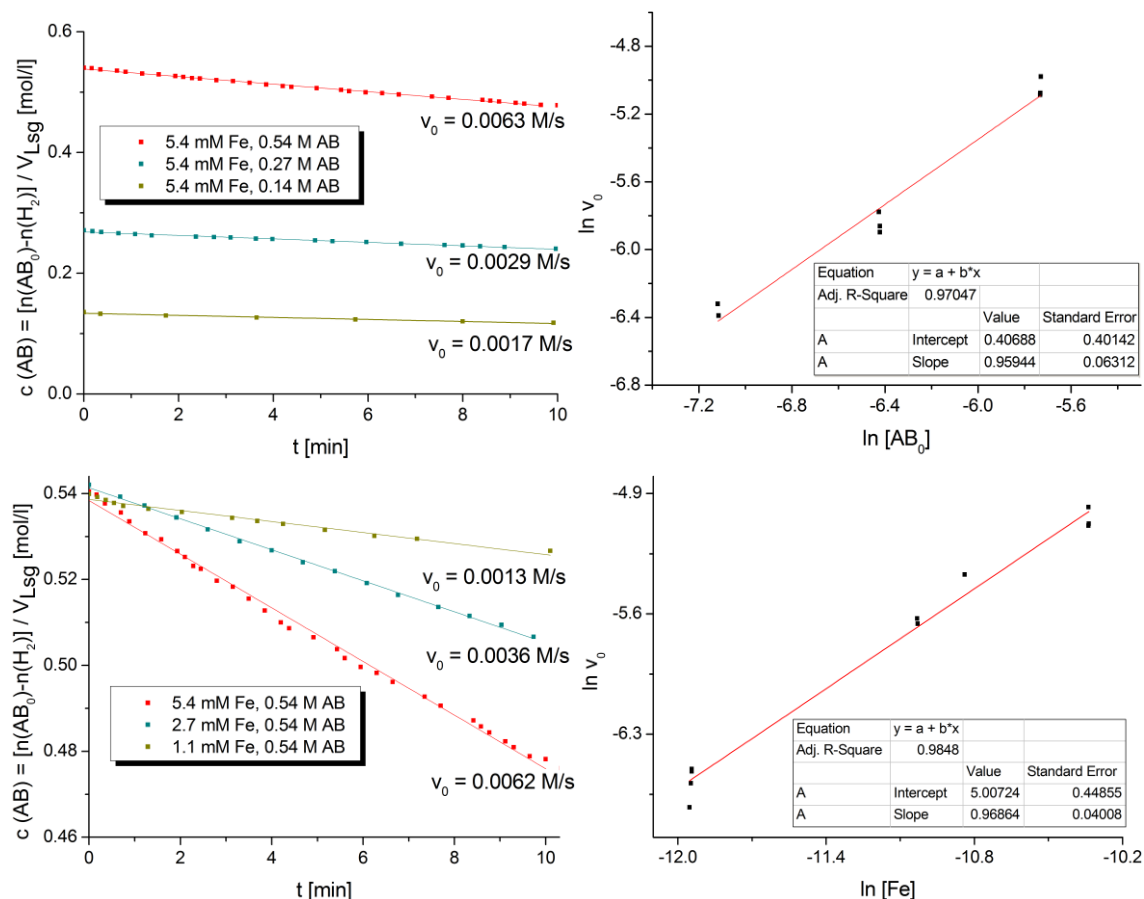


Figure 3.3 Top: Representative initial rate plots for catalyst **55** at varying AB concentrations (left) and rate dependence on AB concentration (right, $k = 4.7 \text{ M}^{-1}\text{s}^{-1}$). Bottom: Representative initial rate plots for catalyst **55** at varying catalyst concentrations (left) and rate dependence on catalyst concentration ($k = 4.6 \text{ M}^{-1}\text{s}^{-1}$).

No induction period is observed. Furthermore, the solution retains a yellow color during catalysis and addition of mercury leaves the reaction rate unchanged. These results point towards homogeneous catalysis.^{f,[147]}

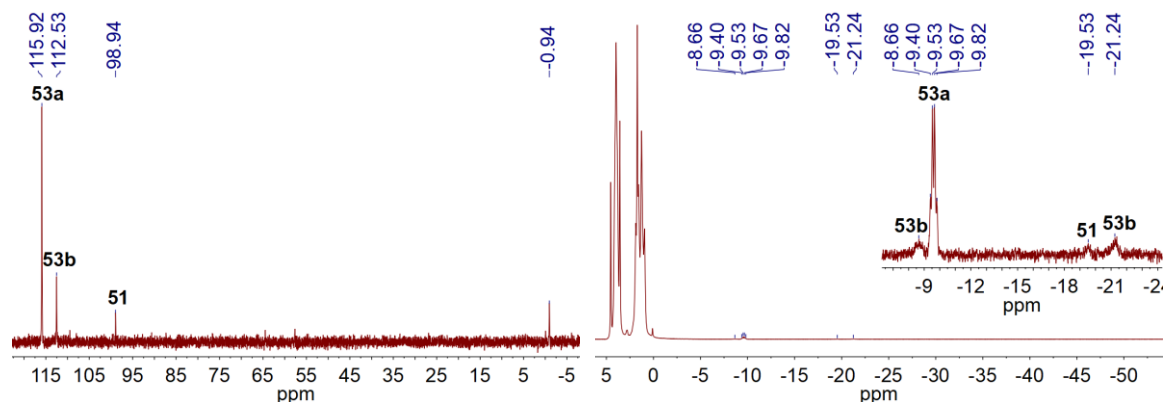


Figure 3.4 $^{31}\text{P}\{^1\text{H}\}$ (left) and ^1H NMR spectrum (right) of a typical catalytic run ($\text{THF-}d_8$).

^f Some recent studies indicate that the mercury test might be unreliable, particularly for Fe.^[147] However, all poisoning studies are to be interpreted with care. For example, NMe_2Et , i.e. a typical substoichiometric poisoning test reagent, in fact *improves* performance for the present catalyst.

3 Ammonia Borane Dehydrocoupling

The dihydrides *trans*- and *cis*-[(*HPNP*)Fe(H)₂CO] (**53a/b**),^[10] are detected by NMR spectroscopy as main iron species during catalysis, presumably representing the resting state (Figure 3.4). Further mechanistic details are obtained from DFT computations for the PMe₂-truncated model system (Figure 3.5, conducted by Moritz Förster supervised by Max C. Holthausen from the University of Frankfurt).^{9,[42]} Formation of dihydride **53a**^{Me} from **55**^{Me} and AB is exergonic by 9.2 kcal mol⁻¹ with an effective kinetic barrier of $\Delta G^\ddagger = 22.5$ kcal mol⁻¹. From here, the lowest free energy pathway starts with proton transfer from the substrate to the hydride ligand via the loose AB adduct **83**^{Me}, which also includes the turnover limiting transition state (**TS**¹) of the catalytic cycle. The resulting aminoborate anion is stabilized by hydrogen bonding with the PNP ligand. Subsequent H₂ loss is irreversible ($\Delta G^\circ = -20.6$ kcal mol⁻¹) with a minute free energy barrier ($\Delta G^\ddagger = 2.2$ kcal mol⁻¹). Final loss of aminoborane from bridging hydride **86**^{Me} is thermoneutral and readily feasible ($\Delta G^\ddagger = 5.4$ kcal mol⁻¹). Hence, the computational analysis is in agreement with the second order rate law and the observation of **53a** as resting state. Furthermore, MLC cooperation is indicated by stabilizing of intermediates **83** - **86** via hydrogen bridging with the pincer ligand.

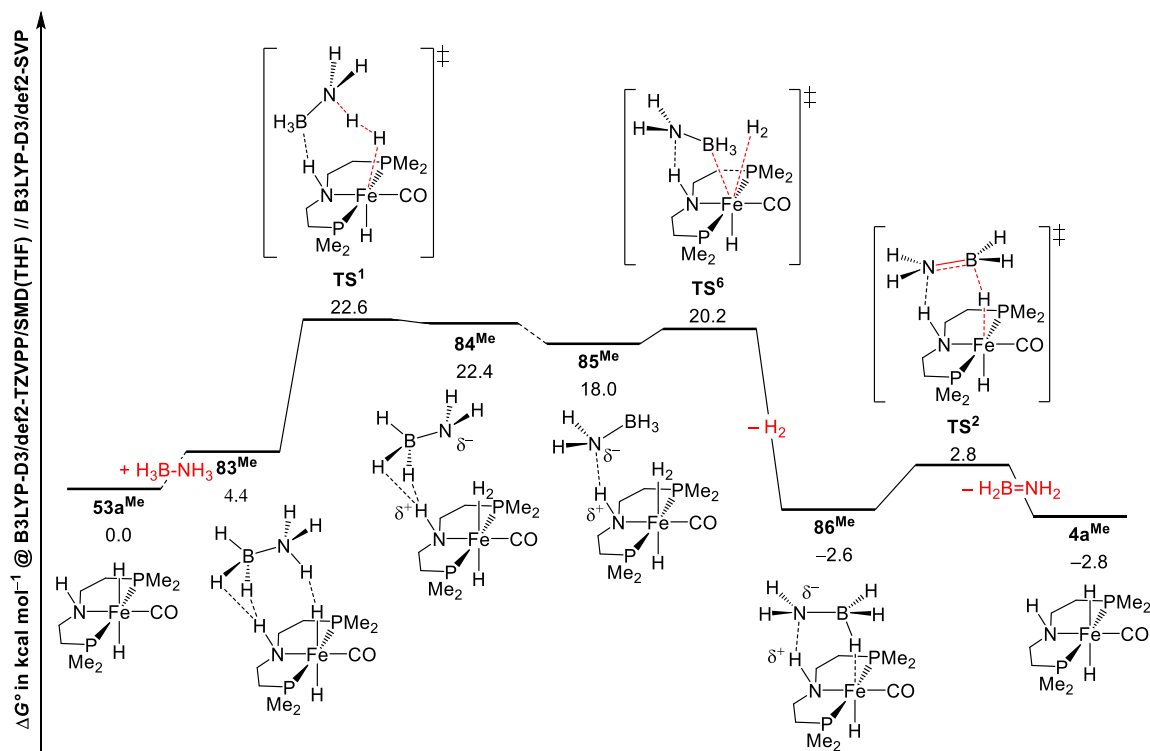


Figure 3.5 Computed lowest free-energy pathway for AB dehydrogenation to aminoborane starting from resting-state model **53a**^{Me} by Moritz Förster supervised by Max C. Holthausen from the University of Frankfurt (B3LYP-D3/def2-TZVP/SMD(THF)// B3LYP-D3/def2-SVP).^[42]

NMR analysis of the residue of catalytic runs with incomplete substrate conversion (0.2 mol-% **55**) reveals the formation of borate complex [(*HPNP*)FeH(BH₄)CO] (**51**) (Figure 7.6).^[148]

Thus, **51** was prepared and tested in catalysis. Its activity (9% conversion after 11h @ 1 mol-%

⁹ @ B3LYP-D3/def2-TZVP/SMD(THF)//B3LYP-D3/def2-SVP level of theory. Reported Gibbs free energies were calculated at standard conditions (T = 298.15 K, p = 1 atm).

3 Ammonia Borane Dehydrocoupling

[cat], 0.54 M AB in an NMR tube) is 1 - 2 orders of magnitude lower than for catalyst **55** (100% conversion after <11h under identical conditions) and will thus be referred to as catalyst deactivation product.^h To understand the mechanism of catalyst deactivation, *in situ* prepared **53a/b** was mixed with BH_3NMe_3 under H_2 atmosphere. No reaction was observed indicating that BH_3 -transfer from parent AB or from PAB end-groups, is unlikely. In search of the BH_3 source, AB dehydrogenation with **55** (1 mol-%) was monitored by ^{11}B NMR spectroscopy (Figure 3.6). Prior to the observation of BZ ($\delta_{11\text{B}} = +30.7$ ppm, d, $^1J_{\text{BH}} = 133$ Hz) and subsequently PBZ ($\delta_{11\text{B}} = +25$ ppm, br), a peak at $\delta_{11\text{B}} = 27.9$ ppm (d, $^1J_{\text{BH}} = 125$ Hz) is detected. This signal can be assigned to diaminoborane, $\text{HB}(\text{NH}_2)_2$.^[46,149]

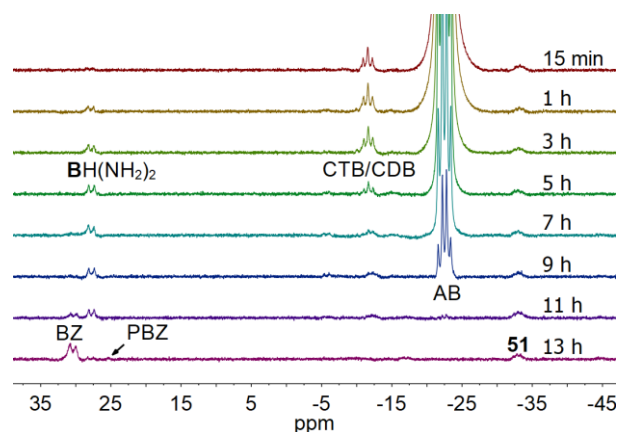


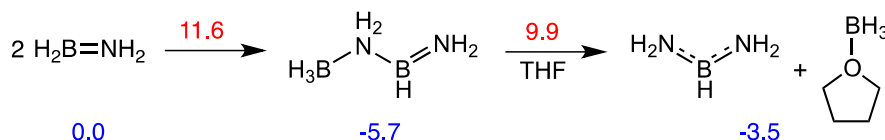
Figure 3.6 *In situ* ^{11}B NMR spectra in $\text{THF}-d_8$ during catalysis ($c_0(\text{AB})=0.54$ M; 1 mol-% **55**; AB: ammonia borane, BZ: borazine, PBZ: polyborazylene, CTB: cyclotriaminoborane, CDB: cyclodiaminoborane, BCTB: B-(cyclotriborazanyl)amine-borane).

Notably, more stable *N,N*-dimethylaminoborane, $\text{HB}(\text{NMe}_2)_2$, is generally observed during $\text{Me}_2\text{HN}-\text{BH}_3$ dehydrodimerization with several catalysts but the mechanistic implications were not addressed.^[66,70,150–154] Paul *and co-workers* recently proposed in a theoretical study that the uncatalyzed rearrangement of $\text{H}_2\text{B}=\text{NH}_2$ towards $\text{BH}_3(\text{THF})$ and $\text{HB}(\text{NH}_2)_2$ is exergonic with low kinetic barriers (Scheme 3.1).^[53] Hence, the spectroscopic observation of $\text{HB}(\text{NH}_2)_2$ provides indirect evidence that this pathway offers a source for free borane which leads to catalyst deactivation.ⁱ Importantly, the formation of borates also accounts for the deactivation of other heterogeneous and homogeneous catalysts.^[60,72,155,156]

^h Despite its low activity for AB dehydrocoupling, **51** was employed as catalyst for dehydrocoupling of methylamine borane.^[178]

ⁱ Free $\text{BH}_3(\text{THF})$ also reacts with AB to the diborane $\text{NH}_2\text{B}_2\text{H}_5$ upon loss of H_2 . Subsequently, the diborazane $\text{NH}_3\text{BH}_2\text{NH}_2\text{BH}_3$ is formed with NH_3 which provides a pathway for decay of free borane besides catalyst deactivation.^[179]

3 Ammonia Borane Dehydrocoupling



Scheme 3.1 Computed mechanism by Malakar *et al.* for the rearrangement of aminoborane (ΔG° and ΔG^\ddagger in kcal/mol).^[53]

This proposed pathway for catalyst deactivation also suggests that trapping of free borane could improve catalyst lifetime. Accordingly, the addition of less than 1 mol-% NMe₂Et (**55**/NMe₂Et/AB = 1/4/500) results in a TON (330) three times higher compared with pure **55** (TON = 120, Figure 3.1). Addition of NMe₂Et after catalyst deactivation has no effect on TON indicating that the formation of **51** is irreversible.^j Furthermore, the performance of our previously reported Ru catalyst could similarly be improved: Addition of amine (**9**/NMe₂Et/AB = 1/80/10000) also raises the TON by a factor of three compared with the absence of amine (Figure 3.7, left). Additionally, a preliminary (not reproduced) experiment with Iridium catalyst ^tBu(POCOP)IrH₂ (**6**, ^tBuPOCOP = κ^3 -C₆H₃-2,6-[OP(^tBu)₂]₂) indicated a TON (1600) 11 times higher in the presence of amine (**6**/NMe₂Et/AB = 5/80/10000) compared with pure **6** (Figure 3.7 right).

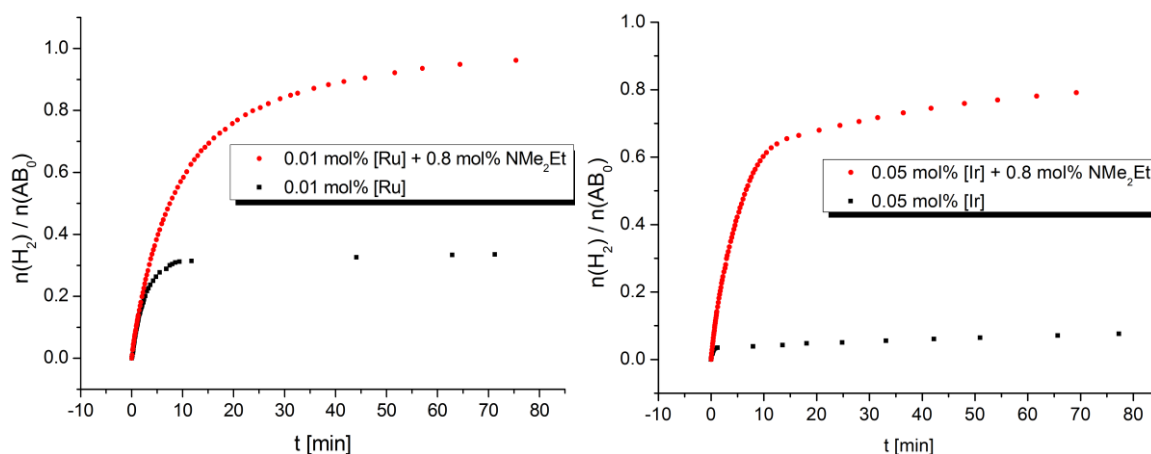


Figure 3.7 Time conversion plots of AB (0.54 M) dehydrocoupling with catalyst **9** (left) and **6** (right) with and without amine.

To shed light on the effect of added amine, *in situ* ³¹P{¹H} NMR monitoring of a catalytic run was performed. In the control experiment (0.2 mol-% **55**, 0.54 M AB) without amine, the amount of deactivation product **51** gradually increases, accompanied with a decline of **53a/b**, until it is virtually the only phosphorous species after 12 h (Figure 3.8 left). On the contrary, an identical catalytic run with additional amine (0.8 mol-%) confirmed that buildup of **51** is much slower and the dihydrides **53a/b** remain the main species after 13 h (Figure 3.8 right).

^j Excess NR₃/PR₃ or heat is required to abstract BH₃ from **51**.^[31,32]

3 Ammonia Borane Dehydrocoupling

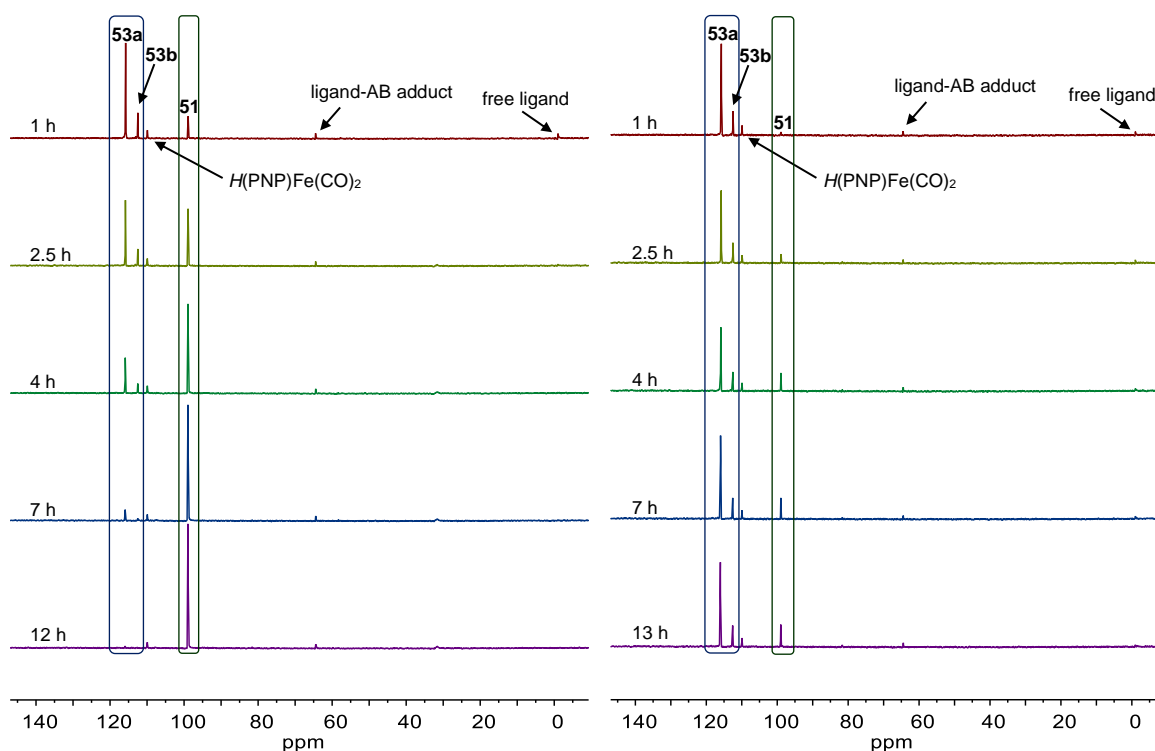
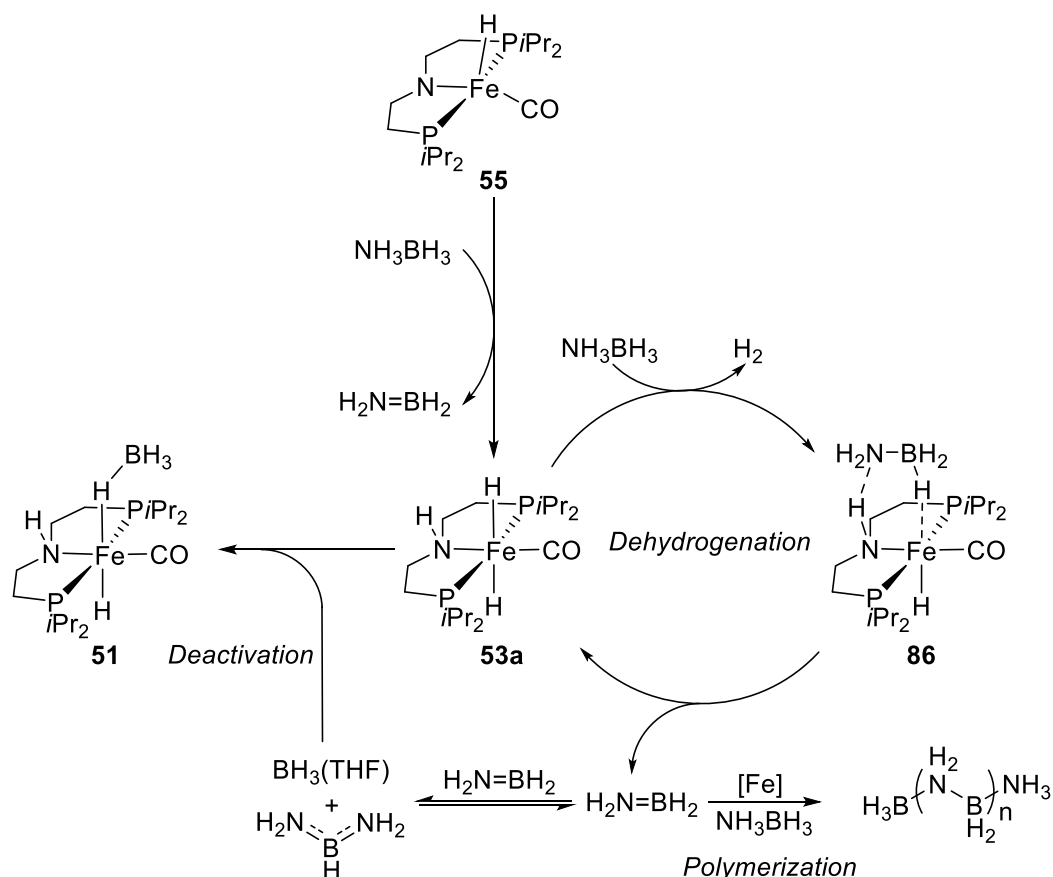


Figure 3.8 *In situ* $^{31}\text{P}\{^1\text{H}\}$ NMR monitoring of a catalytic run (0.2 mol-% **55**, 0.54 M AB) (left) and additionally 0.8 mol-% NMe_2Et (right).

The catalyst deactivation pathway also indicates further insight into the dehydrocoupling mechanism. A general question for catalysts that release free aminoborane upon AB dehydrogenation is whether aminoborane polymerization is also metal-catalyzed. Recent computational studies suggest that besides BH_3 formation (Scheme 3.1),^[53] metal free oligomerization of free aminoborane^[51,157] also proceeds through initial, irreversible dimerization of two aminoboranes to $\text{H}_3\text{B}-\text{NH}_2-\text{BH}=\text{NH}_2$. Therefore, higher catalyst loadings (hence higher aminoborane steady-state concentrations) should equally accelerate both routes for aminoborane decay and, consequently, catalyst deactivation should also become more rapid. However, in contrast higher TONs are found at higher catalyst loading (see above). Additionally, a run at extremely high catalyst loadings (11 mol-%, 0.54 M AB) did not show formation of **51** at all (chapter 7.2.2.2.2). These results suggest that polymerization is also iron catalyzed and that the aminoborane steady-state concentration therefore doesn't increase with higher catalyst loading, ultimately leading to higher TON.

3.3 Summary

The results discussed above can be summarized within a simple mechanistic model (Scheme 3.2). Resting state **53a** dehydrogenates AB to H_2 and $H_2B=NH_2$, as evidenced by trapping with cyclohexene. AB dehydrogenation possibly proceeds via an aminoborane complex (**86**), as was previously proposed for ruthenium catalyst **9**.^[17] Furthermore, the qualitative rationalization of pathways leading to transient aminoborane formation and polymerization vs. catalyst deactivation to borate complex **51** suggests that B–N bond formation is also metal catalyzed, as was previously proposed for Ru catalyst **9** based on computational results.^[17]



Scheme 3.2 Proposed mechanism for AB dehydrogenation, polymerization and catalyst deactivation with catalyst **55**.

Importantly, based on this model the TON for AB dehydrocoupling with **55** could be raised by a factor of 3 upon simply adding substoichiometric amounts of amine, leading to unprecedented TON and TOF for a well-defined base metal catalyst. This effect is attributed to trapping of free BH_3 , delaying catalyst deactivation through irreversible formation of borates. Similarly, the TON of ruthenium and iridium complexes **9** and **6** could be increased by a factor of 3 and 11 respectively. Given that BH_3 poisoning was also found for other heterogeneous and homogeneous catalysts for AB dehydrocoupling,^[72,155,156] this result might be more general in nature.

3 Ammonia Borane Dehydrocoupling

4 Hydrogenolysis of Chlorosilanes

Results of this chapter have been published recently (A. Glüer, J. I. Schweizer, U. S. Karaca, C. Würtele, M. Diefenbach, M. C. Holthausen, S. Schneider, *Inorg. Chem.* **2018**, *57*, 13822) and parts of this work have been adapted from this publication with permission from ACS.^[74] Copyright 2018 American Chemical Society.

4.1 Introduction

Organohydrosilanes are important reagents for olefin hydrosilylation^[75–78] and other applications such as C-H bond silylation,^[79,80] desulfurization of fuels,^[81] or dehydrogenative oligo/polysilane formation.^[82,83] Hydrosilanes are commonly obtained from chlorosilanes via reaction with stoichiometric amounts of strong reducing agents such as LiAlH₄, producing large amounts of metal containing waste.^[134] Thus, hydrogenolysis of cheap chlorosilanes using H₂ as (atom)economic hydrogen source is highly desirable (see chapter 1.3.1).

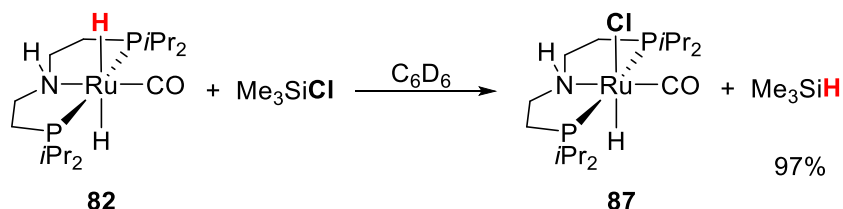
As discussed in chapter 1.3.2 and 1.3.3, ease of halosilane hydrogenolysis shows a trend, i.e. Si-I > Si-Br > Si-Cl. It is believed that thermodynamic reasons are accountable, as Si-X bond dissociation energies follow the same trend (BDE (Si-I) = 58 kcal mol⁻¹, BDE (Si-Br) = 86 kcal mol⁻¹, BDE (Si-Cl) = 100 kcal mol⁻¹). Consequently, hydrogenolysis of chlorosilanes is strongly endergonic (e.g. Me₃SiCl + H₂ → Me₃SiH + HCl Δ_RG_{calc} = 22.2 kcal mol⁻¹)^[89] thus necessitating additional driving force, e.g. by neutralization of protons with base or precipitation of chlorides as a salt. However, amine based bases do not deliver enough driving force to facilitate hydrogenolysis (Me₃SiCl + H₂ → Me₃SiH + [NMe₃H]Cl; ΔG_R^o = 11.9 kcal mol⁻¹), explaining Shimada's failure in direct chlorosilane hydrogenolysis (see chapter 1.3.2).^[91,94] Therefore, first attempts were directed on the utilization of stronger non-nucleophilic bases. Subsequently, chloride precipitation (as NaCl) with NaBAR^F₄ (BAR^F₄⁻ = [(3,5-(CF₃)₂-C₆H₃)₄B]⁻) was successfully evaluated to add additional driving force. Interestingly, Shimada *and coworkers* had a similar idea at the same time using NaI as chloride abstractor (see chapter 1.3.2).^[91]

The considerably higher Si-Cl (~100 kcal mol⁻¹) vs. Si-H (~69 kcal mol⁻¹) bond dissociation energy indicates that hydride vs. chloride metathesis is a thermochemically challenging step,^[35] necessitating transition metal hydride catalysts of high M-H hydricity (i.e. low ΔG^o_{H-} values, ΔG^o_{H-:} L_nM-H → L_nM⁺ + H⁻) as indicated e.g. by their capability to hydrogenate CO₂ to formate (ΔG^o_{H-} (HCO₂⁻) = 44 kcal mol⁻¹ in MeCN).^[30] As Ru-MACHO-type precatalysts (HPNPR)^RRuH(Cl)CO (HPNPR = HN(CH₂CH₂PR₂)₂) show high activities in CO₂ hydrogenation,^[132] this class of complexes was tested for their activity in chlorosilane hydrogenolysis.

4 Hydrogenolysis of Chlorosilanes

4.2 Results and Discussion

An initial stoichiometric experiment showed that the *trans*-dihydride species $[(\text{HPNP}^{\text{Pr}})\text{Ru}(\text{H}_2)\text{CO}]$ (**82**) readily reacts with Me_3SiCl to the corresponding hydrosilane in 97 % yield (Scheme 4.1), also demonstrating favorable kinetics for hydride transfer with this catalyst class.



Scheme 4.1 Stoichiometric hydride transfer of **82** with Me_3SiCl to Me_3SiH and concomitant formation of **87**.

However, HCl elimination and H_2 heterolysis from the resulting ruthenium chloro complex **87** requires strong bases like alkaline metal hydroxides, alkoxides or amides which all proved incompatible with chlorosilane substrates. As computational evaluation indicates strong endergonicity for trimethylchlorosilane hydrogenolysis with a weaker base like NMe_3 ($\text{Me}_3\text{SiCl} + \text{H}_2 \rightarrow \text{Me}_3\text{SiH} + [\text{NMe}_3\text{H}]\text{Cl}$; $\Delta G_{\text{R}}^\circ = 11.9 \text{ kcal/mol}$), Verkade's "superbase" 2,8,9-Triisopropyl-2,5,8,9-tetraaza-1-phosphabicyclo[3,3,3]undecane (VB^{Pr}), one of the strongest non-nucleophilic neutral bases known to date ($\text{p}K_{\text{a,MeCN}}([\text{H-VB}^{\text{Pr}}]^+) = 33.63$)^[158] was evaluated. Indeed, when **87** was reacted with VB^{Pr} in C_6D_6 under H_2 atmosphere (9 bar), 8 % and 13 % of **82** was formed after 3 h and 22 h, respectively, as evidenced by $^{31}\text{P}(\text{ig})$ NMR (Figure 4.1).^k

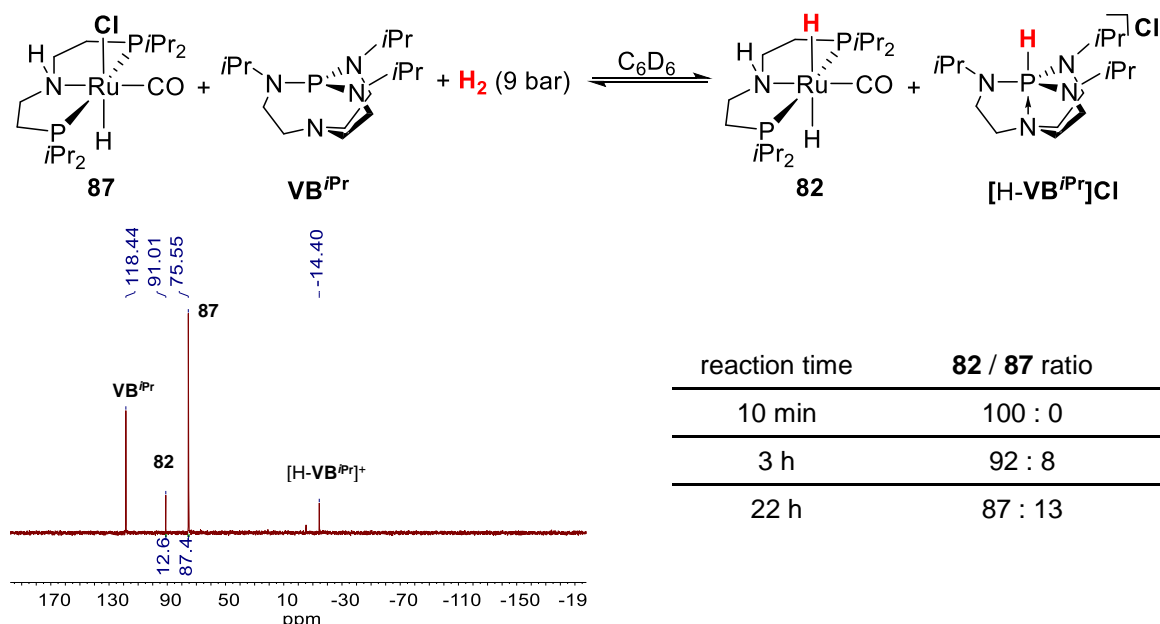
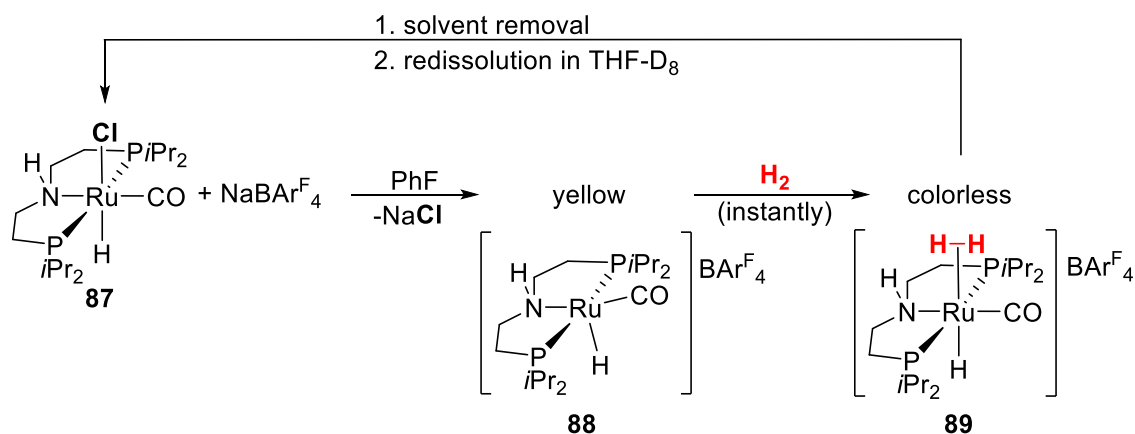


Figure 4.1 $^{31}\text{P}(\text{ig})$ NMR spectrum (bottom left) of the reaction (top) of **87** with VB^{Pr} and H_2 after 22 h. Right: Ratios of **82** and **87** at different reaction times derived by $^{31}\text{P}(\text{ig})$ NMR.

^k An analogous experiment in THF-d_6 confirmed the establishment of an equilibrium as the **82** : **87** ratio after 1 d and 1 week were identical (14:86).

As stoichiometric H/Cl exchange of **82** with Me_3SiCl is exergonic (vide supra), the overall reaction $\text{Me}_3\text{SiCl} + \text{H}_2 + \text{VB}^{\text{iPr}} \rightarrow \text{Me}_3\text{SiH} + [\text{VB}^{\text{iPr}}]\text{Cl}$ is either roughly thermoneutral or exergonic. However, catalytic attempts to hydrogenate Me_3SiCl failed in both C_6D_6 and PhF with pressures of 9 and 4 bar respectively, presumably due to slow conversion of **87** to active **82**. Additionally, chloride would accumulate during catalysis, thus shifting the equilibrium to **87**. Thus, *in situ* chloride precipitation was evaluated as a synthetic strategy to add additional driving force. Addition of NaBARF_4 to complex **87** in PhF as solvent results in the formation of new species by NMR spectroscopy accompanied by precipitation of a white solid (NaCl ; Scheme 4.2). Its spectral features ($^{31}\text{P}\{^1\text{H}\}$ and ^1H NMR) as well as its LIFDI mass spectrum (chapter 7.3.3.6) closely resemble that of $[(\text{HPNP}^{\text{iPr}})\text{RuH}(\text{CO})]\text{BF}_4$ as reported by Beller *and coworkers* which can exist as *syn* and *anti* isomer (orientation of the N-H proton with respect to the hydride).^[159]

The existence of a vacant site on corresponding BARF_4 -complex **88** is backed up by the finding that addition of H_2 results in immediate disappearance of the color and new signals in the $^{31}\text{P}\{^1\text{H}\}$ NMR spectrum. Furthermore, the ^1H NMR spectrum shows two hydride signals at -9.7 and -9.9 ppm and a broad resonance at -2.6 ppm which is attributed to a H_2 ligand (Figure 4.2). The two main species in solution are therefore tentatively assigned to *syn* and *anti* isomer (orientation of the N-H proton with respect to the hydride) of *trans* hydride dihydrogen complex **89**. This suggestion is backed up by the fact that its spectral features resemble the similar complex $[(\text{CH}_2\text{Ph})\text{PNP}^{\text{Ph}}]\text{RuH}(\text{H}_2)\text{CO}]\text{BARF}_4$ ($(\text{CH}_2\text{Ph})\text{PNP}^{\text{Ph}} = (\text{CH}_2\text{Ph})\text{N}(\text{CH}_2\text{CH}_2\text{PPh}_2)_2$).^[160] Interestingly, exchange of the solvent with $\text{THF-}d_8$ restores **87** indicating a strong solvent dependence of the chloride abstraction equilibrium.



Scheme 4.2 Reaction of **87** with NaBARF_4 . Structures in brackets can exist as *syn* or *anti* isomer (orientation of the NH proton with respect to the hydride) and are proposed based on ^1H and $^{31}\text{P}\{^1\text{H}\}$ NMR data.

4 Hydrogenolysis of Chlorosilanes

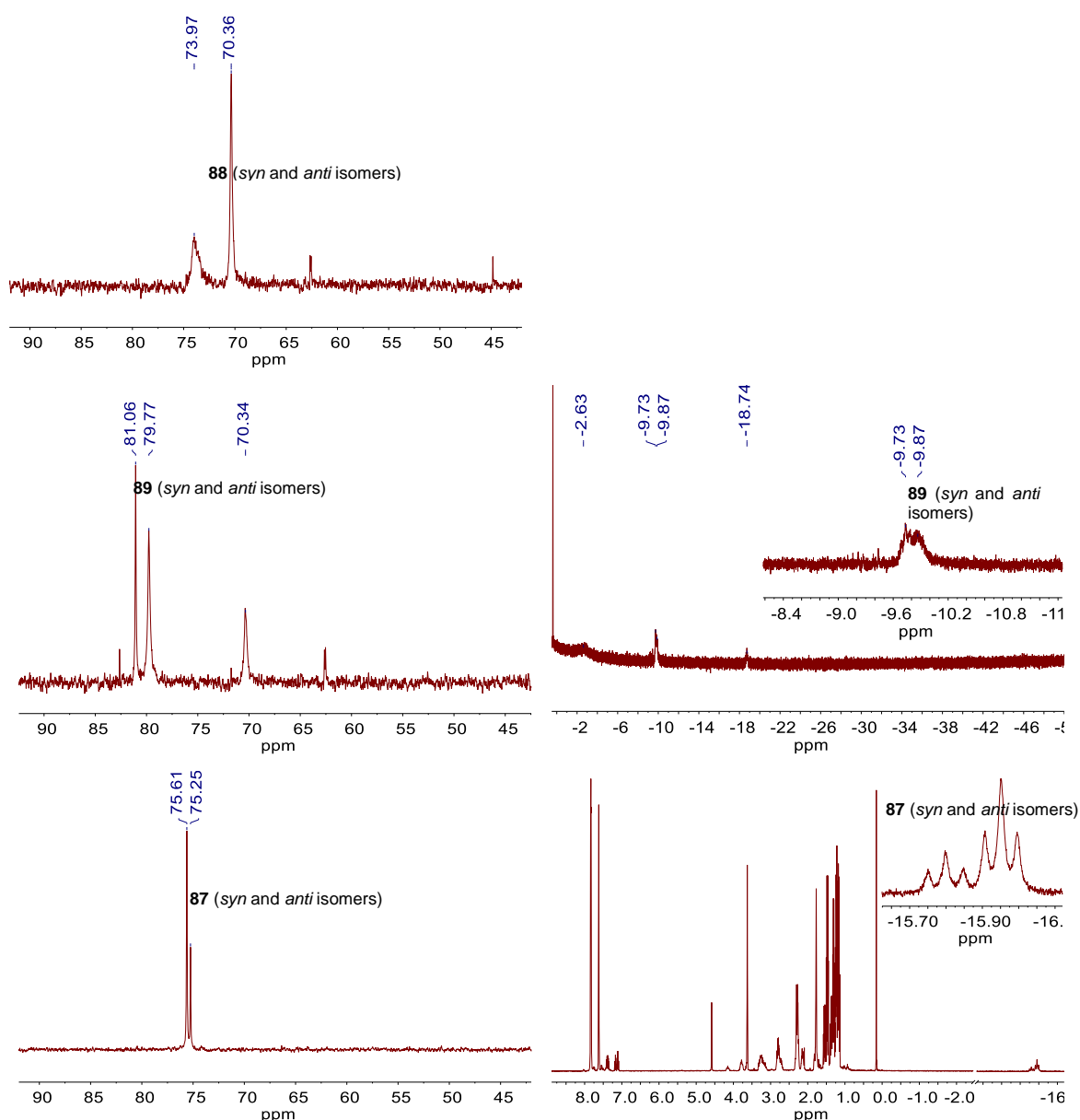


Figure 4.2 Top: ³¹P{¹H} NMR spectrum of the mixture of NaBARF₄ and **87** in PhF. Middle: ³¹P{¹H} (left) and ¹H (right) NMR spectra after introduction of H₂. Bottom: ³¹P{¹H} (left) and ¹H (right) NMR spectra of the mixture after evaporation of the solvent and redissolution in THF-*d*₈ indicate restorage of **87** (syn and anti isomers).

Chlorosilane hydrogenolysis (4 bar H₂, r.t.) with **82** (1 mol-%) as catalyst was therefore examined in the presence of stoichiometric amounts of NaBARF₄ and NEt₃ as base in PhF. Trimethylchlorosilane hydrogenolysis (Table 4.1, Entry 1) requires relatively long reaction times giving spectroscopic yields in Me₃SiH around 50 % after about a week and full conversion with 61 % yield after 4 weeks. It should be noted that (Me₃Si)₂O is the major byproduct, suggesting higher yields under vigorously H₂O/O₂ free conditions.^[161] In contrast, hydrogenolysis of Me₂SiCl₂ (with 2 eq NaBARF₄) to Me₂SiH₂ proceeds at a much faster rate within a day in yields up to around 80 % under otherwise identical conditions (Entry 2), presumably due to the higher electrophilicity of the substrate. With only 1 eq NaBARF₄ (Entry 3), Me₂SiH₂ remains the preferred product, leaving almost

4 Hydrogenolysis of Chlorosilanes

half of the substrate unreacted. Choice of base is crucial as hydrogenolysis with 2,6-lutidine (lut) as base did not yield product despite high conversion (Entry 4).

Table 4.1 Catalytic hydrogenolysis of chlorosilanes with **82**.^[a]

$$\text{Me}_{4-n}\text{SiCl}_n + n \text{NaBARF}_4 \xrightarrow[\text{- [H-base]BARF}_4]{\text{H}_2, \text{base, PhF, r.t., [82] (1 mol-\%)}} \text{Me}_{4-n}\text{SiH}_n$$

$n = 1, 2$
 $\text{- } n \text{NaCl}$

Entry	Substrate	Base	NaBARF ₄ (eq)	Conv. ^[b]	Product (Yield ^[b])	Reaction time
1	Me ₃ SiCl	NEt ₃	1.1	77 % ^[c]	Me ₃ SiH (51 %)	195 h
2	Me ₂ SiCl ₂	NEt ₃	2.0	100 %	Me ₂ SiH ₂ (75 %)	24 h
3	Me ₂ SiCl ₂	NEt ₃	1.1	59 %	Me ₂ SiH ₂ (37 %)	20 h
4	Me ₂ SiCl ₂	lut	1.1	85 %	Me ₂ SiH ₂ (0 %)	6 d

[a] General conditions: 0.027 mmol chlorosilane, 0.03 or 0.054 mmol NaBARF₄, 0.26 μmol **82**, 0.36 mmol NEt₃ or 1 mmol 2,6-lutidine, 0.5 mL PhF, 4 bar H₂, r.t. [b] Conversions/yields were determined by ¹H NMR (relative integration of all signals in the Me_xSi region around 0 ppm vs. 1,2,4,5-tetramethylbenzene (TMB) as internal standard). [c] Conversion of intermediate [Me₃SiNMe₃]⁺ is given.

Table 4.2 Attempts for chlorosilane hydrogenolysis with several salts of weakly coordinating anions (M[WCA]) other than NaBARF₄.^[a]

$$\text{Me}_{4-n}\text{SiCl}_n + \text{M[WCA]} \xrightarrow[\text{- [HNEt}_3\text{][WCA]}]{\text{H}_2, \text{NEt}_3, \text{PhF, r.t., [82] (1 mol-\%)}} \text{Me}_{4-n}\text{SiH}_n$$

$n = 1, 2$
 - MCl

M[WCA] (amount in mmol)	Substrate (amount in mmol)	Catalyst loading	p (H ₂)	Conversion ^[b]	Yield ^[b]	Reaction time
NaBPh ₄ (0.017)	Me ₂ SiCl ₂ (0.0082)	3.5 mol-%	4 bar	100 %	No Si-H detected	26h
NaBF ₄ (0.020)	Me ₃ SiCl (0.016)	6 mol-%	1.2 bar	65 %	<2 % ^[c]	6h
NaSbF ₆ (0.014)	Me ₃ SiCl (0.012)	8 mol-%	1.2 bar	100 %	No Si-H detected	22h
KPF ₆ (0.028)	Me ₃ SiCl (0.028)	4 mol-%	1.2 bar	8 %	<4 %	5h
NaOTf (0.016)	Me ₃ SiCl (0.016)	9 mol-%	1.2 bar	7 %	<5 %	22h

[a] General conditions: 0.05 mL (0.36 mmol) NEt₃, 0.5 - 0.6 mL PhF, 0.001 mmol **82**. [b] Conversions/yields were determined by ¹H NMR (relative integration of all signals in the Me_xSi region around 0 ppm). [c] 60 % Me₃SiF is formed.

Catalytic attempts with other alkaline metal salts of weakly coordinating anions (M[WCA]) only gave (sub-)stoichiometric hydrosilane yields with respect to catalyst loading. Two cases can be distinguished: i) no conversion presumably due to low solubility (NaOTf, KPF₆) ii) high conversion to (unidentified) products (NaBPh₄, NaSbF₆ or NaBF₄). To clarify the role of the WCA, the catalytic reaction with NaBARF₄ was monitored by NMR spectroscopy. The experiment revealed the presence

4 Hydrogenolysis of Chlorosilanes

of an intermediate with a ^{29}Si resonance of 47.5 ppm, i.e. characteristic for base stabilized silyl cations (Figure 4.3 top left).^[162] The same species is obtained upon mixing Me_3SiCl with $\text{NaBAR}_4^{\text{F}}$ and NEt_3 in PhF in the absence of catalyst and H_2 . Furthermore, NEt_3 coordination to silicon is evidenced by a cross peak of the amine methylene protons with the ^{29}Si resonance in the ^1H - ^{29}Si HMBC spectrum (Figure 4.3 top right). These results suggest that *in situ* formed $[\text{Me}_3\text{SiNEt}_3]^+$ is the actual hydrogenolysis substrate, which is sufficiently stabilized by the $\text{BAR}_4^{\text{F}-}$ anion under catalytic conditions.^[163,164]

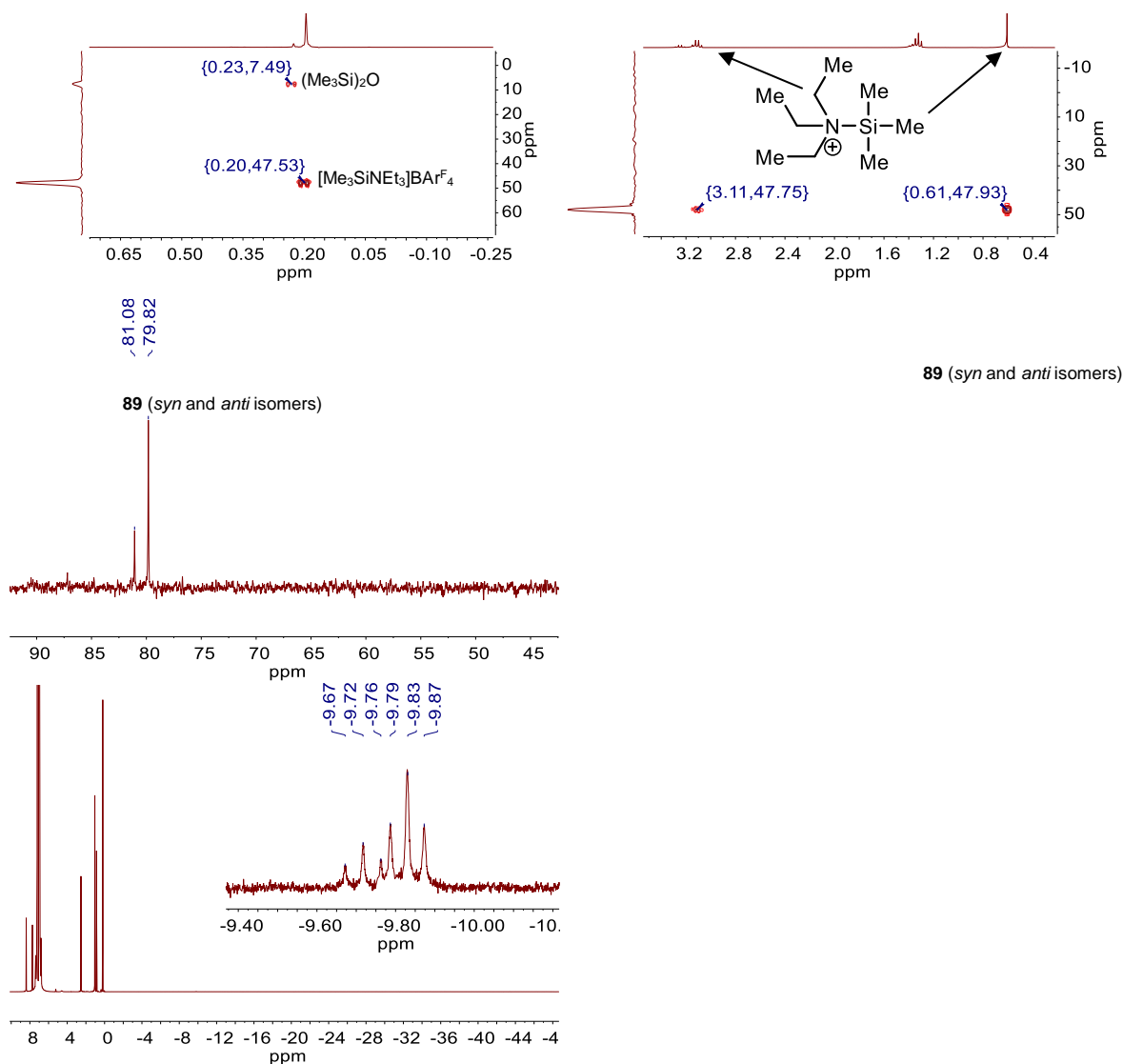
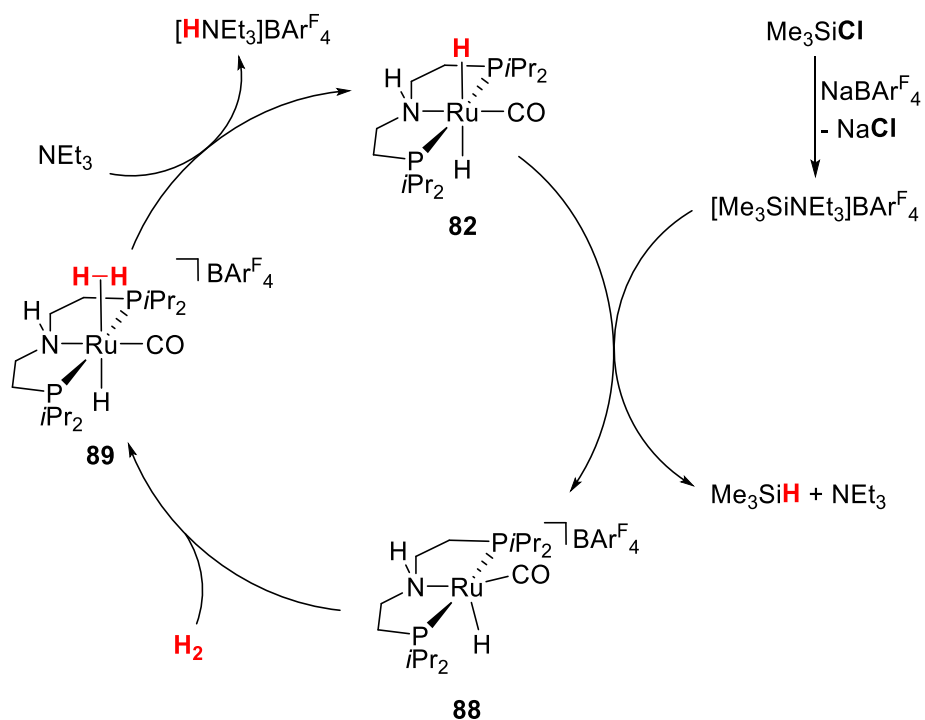


Figure 4.3 Top: ^1H - ^{29}Si HMBC spectrum in the initial phase of a catalytic run in PhF (left) and from the product of the reaction of Me_3SiCl with $\text{NaBAR}_4^{\text{F}}$ and NEt_3 in CD_2Cl_2 (right). Bottom: $^{31}\text{P}\{^1\text{H}\}$ (left) and ^1H (right) NMR spectra during a catalytic run.

Monitoring of a catalytic run by $^{31}\text{P}\{^1\text{H}\}$ NMR reveals the resting state to be the same specie(s) that resulted from simple mixing of **87** and $\text{NaBAR}_4^{\text{F}}$ in PhF under H_2 atmosphere (vide supra) which was tentatively assigned to *syn* and *anti* isomers of the hydride hydrogen complex **89**.



Scheme 4.3 Proposed catalytic cycle for the hydrogenolysis of chlorosilanes with **82** as catalyst and stoichiometric amounts of NaBARF₄.

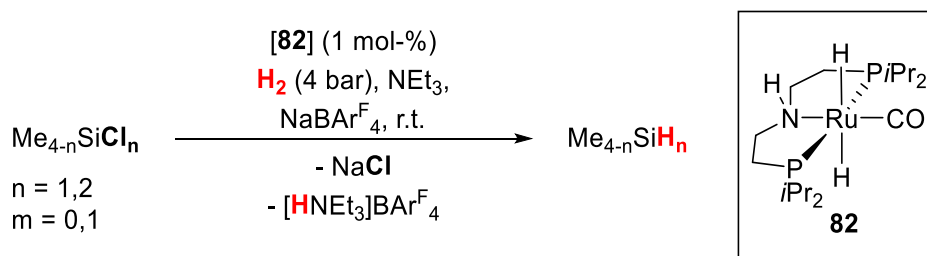
Based on the aforementioned results, a catalytic cycle is proposed in which **82** transfers a hydride to [Me₃SiNEt₃]⁺ to give Me₃SiH upon release of NEt₃ (Scheme 4.3). The resulting five coordinate cationic ruthenium complex **88** readily reacts with H₂ to the resting state hydride dihydrogen complex **89**. Subsequent deprotonation reforms dihydride **82** to close the catalytic cycle.

4 Hydrogenolysis of Chlorosilanes

4.3 Summary

Hydrogenolysis of chlorosilanes with bifunctional ruthenium dihydride catalyst **82** and “superbase” **VB^{Pr}** was estimated to be approx. thermoneutral or exergonic but did not give turnover, presumably due to unfavorable kinetics for regeneration of active dihydride **82** from inactive hydride-chloride complex **87**.

In contrast, chloride precipitation using NaBAR^F₄ in PhF as solvent enables facile catalytic chlorosilane hydrogenolysis. In fact, NaCl formation delivers enough driving force to facilitate catalysis with a much weaker base such as NEt₃. Ruthenium catalyst **82** is highly active at low loadings (1 mol-%) and mild conditions (r.t., 4 bar H₂). Hydrogenolysis of Me₃SiCl only gave moderate yield (51 %) after long reaction times (1 week), but Me₂SiCl₂ (2 eq NaBAR^F₄) was converted within one day in high yield (75 %), presumably due to a combination of decreased steric hindrance and increased electrophilicity of the silicon. Mixed hydrochlorosilanes are not accessible as hydrogenolysis of Me₂SiCl₂ with only one eq NaBAR^F₄ resulted in ca. 50% conversion to Me₂SiH₂. Mechanistic investigations indicate that base stabilized silyl cations are the actual hydrogenation substrate. A combination of stoichiometric experiments and *in situ* NMR monitoring during catalysis allowed for postulation of a preliminary catalytic cycle with cationic hydride dihydrogen complex **89** as resting state.



Scheme 4.4 Catalytic hydrogenolysis of chlorosilanes was achieved under mild conditions using NaBAR^F₄ to add driving force via chloride precipitation.

5 Hydrogenolysis of Silyl Triflates

Results of this chapter have been published recently (A. Glüer, J. I. Schweizer, U. S. Karaca, C. Würtele, M. Diefenbach, M. C. Holthausen, S. Schneider, *Inorg. Chem.* **2018**, **2018**, 57, 13822) and parts of this work have been adapted from this publication with permission from ACS.^[74] Copyright 2018 American Chemical Society.

5.1 Introduction

(Organo)hydrochlorosilane building blocks $\text{SiH}_x\text{Cl}_y\text{R}_z$ enable the orthogonal synthesis of branched polysiloxanes and self-healing silicones by sequential polycondensation and cross-linking via hydrosilylation as used e.g. for the fabrication of release coatings, moldings and adhesives.^[84–86] Some of these precursors, like MeSiCl_2H , are conveniently obtained as a byproduct of the Müller-Rochow process. However, Me_2SiClH synthesis suffers from low crude yields (0.01 - 0.5 %) and challenging separation procedures, necessitating alternative synthetic routes to hydrochlorosilanes from chlorosilanes.^[88] Hydrosilanes can be prepared by salt metathesis from chlorosilanes with LiAlH_4 (see chapter 1.3.1). However, besides the low atom economy that is associated with the use of complex hydride reagents, this approach is not commonly applicable for the synthesis of hydrochlorosilanes due to overreduction.^[134] As an alternative, hydrogenolysis of chlorosilanes with H_2 as hydrogen source is reported in this thesis (see chapter 4), but hydrochlorosilanes were not obtained via this route.

Thus, hydrogenolysis of silyl triflates was evaluated as an alternative to obtain hydro(chloro)silanes via H_2 heterolysis. Supposedly, hydrochlorosilanes $\text{SiH}_x\text{Cl}_y\text{R}_z$ are accessible from chlorosilyl triflate precursors $\text{SiOTf}_x\text{Cl}_y\text{R}_z$ via selective Si-OTf hydrogenolysis. Yet, hydrochlorosilane synthesis via this route is unprecedented and hydrogenolysis of silyl triflates in general is rare. Hydrogenation of silyl triflates typically requires high iridium catalyst loadings (5 - 10 mol-%) and long reaction times (usually days).^[91,94] Additionally, hydrogenolysis of bistriflate $\text{Me}_2\text{SiOTf}_2$ is challenging and proceeds in low yields ($\approx 50\%$).^[94] Thus, new catalysts are required to enhance both activity and selectivity of silyl triflate hydrogenolysis. Bifunctional ruthenium PNP pincer catalyst **82** demonstrated high activity for organochlorosilane hydrogenolysis with NaBARF_4 as additive (chapter 4), suggesting that kinetics for silyl triflate hydrogenolysis are also favorable. Thus, **82** is targeted as potential catalyst for hydrogenolysis of organo silyl triflates.

5.2 Results and Discussion

A stoichiometric reaction of **82** with Me_3SiOTf in C_6D_6 gave selective conversion (97%) to Me_3SiH as evidenced by ^1H NMR (Figure 5.1, bottom left). Additionally, a new metal complex was detected which featured a hydride shift of $\delta_{\text{H}} = -20.9$ ppm and a $^{31}\text{P}\{^1\text{H}\}$ resonance at $\delta_{\text{P}} = 73.8$ ppm (Figure 5.1, bottom right). It was independently prepared from **82** and HOTf and fully characterized as $[(\text{HPNP}^R)\text{RuH}(\text{OTf})\text{CO}]$ (**90**; $\text{H}(\text{PNP}^R) = \text{HN}(\text{CH}_2\text{CH}_2\text{PR}_2)_2$), (see chapter 7.3.1.3).

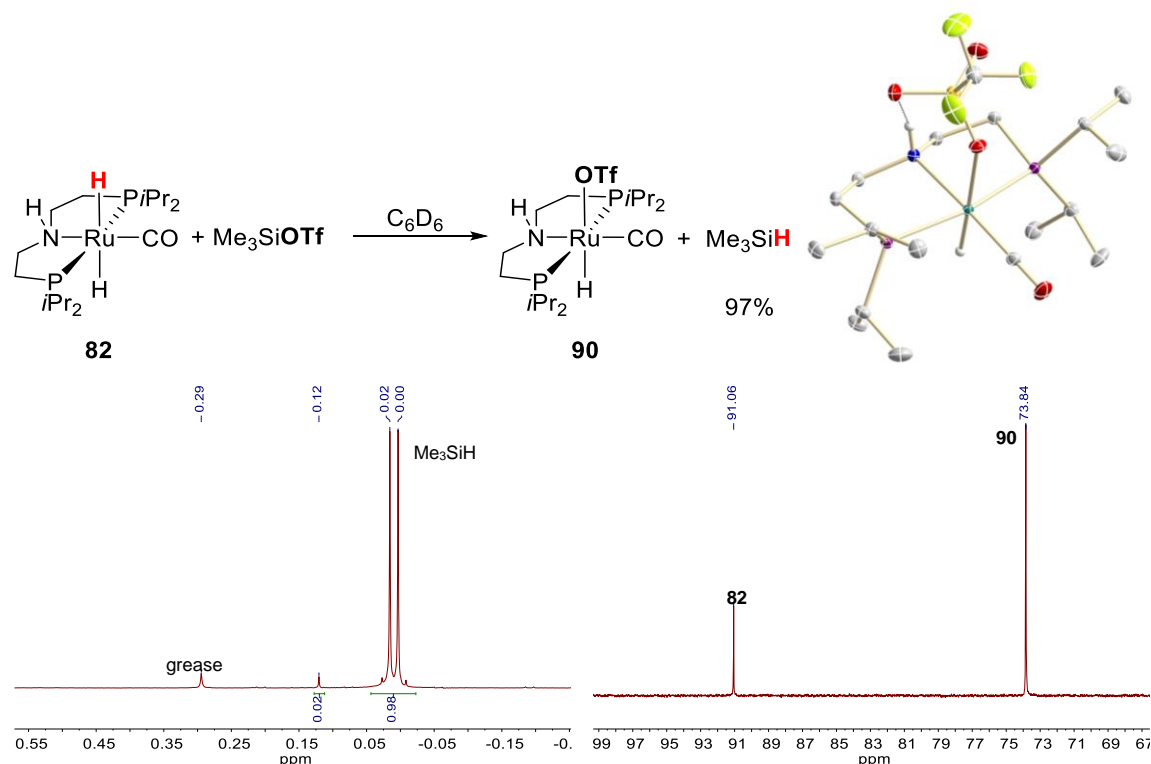


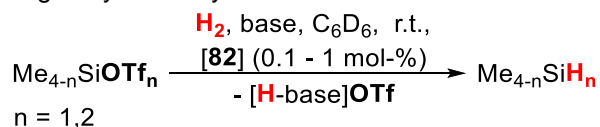
Figure 5.1 Bottom: ^1H NMR (left) and $^{31}\text{P}\{^1\text{H}\}$ NMR spectrum (right) of the reaction depicted on the top left after 1 h. Top right: Thermal ellipsoid plot of **90** with the anisotropic displacement parameters drawn at the 50% probability level. The asymmetric unit contains one complex molecule. The N-H and Ru-H hydrogen atoms were found from the residual density map and isotropically refined. A N-H...O hydrogen bond is shown ($d(\text{H}\cdots\text{O}) = 2.62(2)$ Å). Carbon bound hydrogens are omitted for clarity. Color code: turquoise: Ru, red: O, blue: N, purple: P, yellow: S, grey: C, white: H.

Dissociation of OTf^- , coordination of H_2 and deprotonation of the resulting cationic H_2 -complex would regenerate **82** to close a catalytic cycle. However, mixing of **90** with excess NEt_3 under H_2 atmosphere resulted in no reaction. Nevertheless, catalytic hydrogenolysis of Me_3SiOTf using NEt_3 as base gave selective formation of Me_3SiH (85 %) overnight using 1 mol-% **82** at room temperature and 1 or 4 bar H_2 (Table 5.1, Entry 1 and 2), suggesting that exergonic H^-/OTf^- exchange of **82** with Me_3SiOTf (vide supra) drives the overall reaction. Almost the same yield (82 %) is obtained after 46 h with catalyst loadings as low as 0.1 mol-% (Entry 3). $t\text{BuMe}_2\text{SiOTf}$ is not hydrogenated, pointing towards a sterically crowded rate limiting transition state (Entry 4). In contrast, hydrogenation of the bistriflate $\text{Me}_2\text{SiOTf}_2$ is extremely facile with full conversion after 1 h (Entry 5).

5 Hydrogenolysis of Silyl Triflates

Highly selective semihydrogenolysis is obtained within the same time (Entry 6) using one eq of base to give Me₂SiHOTf in 82 % yield.

Table 5.1 Catalytic hydrogenolysis of silyl triflates with **82**.^[a]



Entry	Substrate	Base (eq)	H ₂ pressure	Conv. ^[b]	Product (Yield ^[b])	Rxn. time
1	Me ₃ SiOTf	NEt ₃ (1.1)	4 bar	99 %	Me ₃ SiH (85 %)	18 h
2	Me ₃ SiOTf	NEt ₃ (1.0)	1.2 bar	90 %	Me ₃ SiH (85 %)	26 h
3 ^[c]	Me ₃ SiOTf	NEt ₃ (1.1)	4 bar	92 %	Me ₃ SiH (82 %)	46 h
4	<i>t</i> BuMe ₂ SiOTf	NEt ₃ (1.1)	1.2 bar	3 %	< 1 %	7 d
5	Me ₂ SiOTf ₂	NEt ₃ (2.2)	4 bar	100 %	Me ₂ SiH ₂ (82 %)	1 h
6	Me ₂ SiOTf ₂	NEt ₃ (1.0)	4 bar	99 %	Me ₂ SiHOTf (82 %) Me ₂ SiH ₂ (4 %)	1 h

[a] General conditions: 0.1 mmol substrate, 1 μmol **82**, 4 bar H₂, 0.5 ml C₆D₆, r.t. [b] Conversions/yields were determined by ¹H NMR (relative integration of all signals in the Me_xSi region around 0 ppm vs. TMB as internal standard). [c] 0.1 μmol **82** (0.1 mol-%).

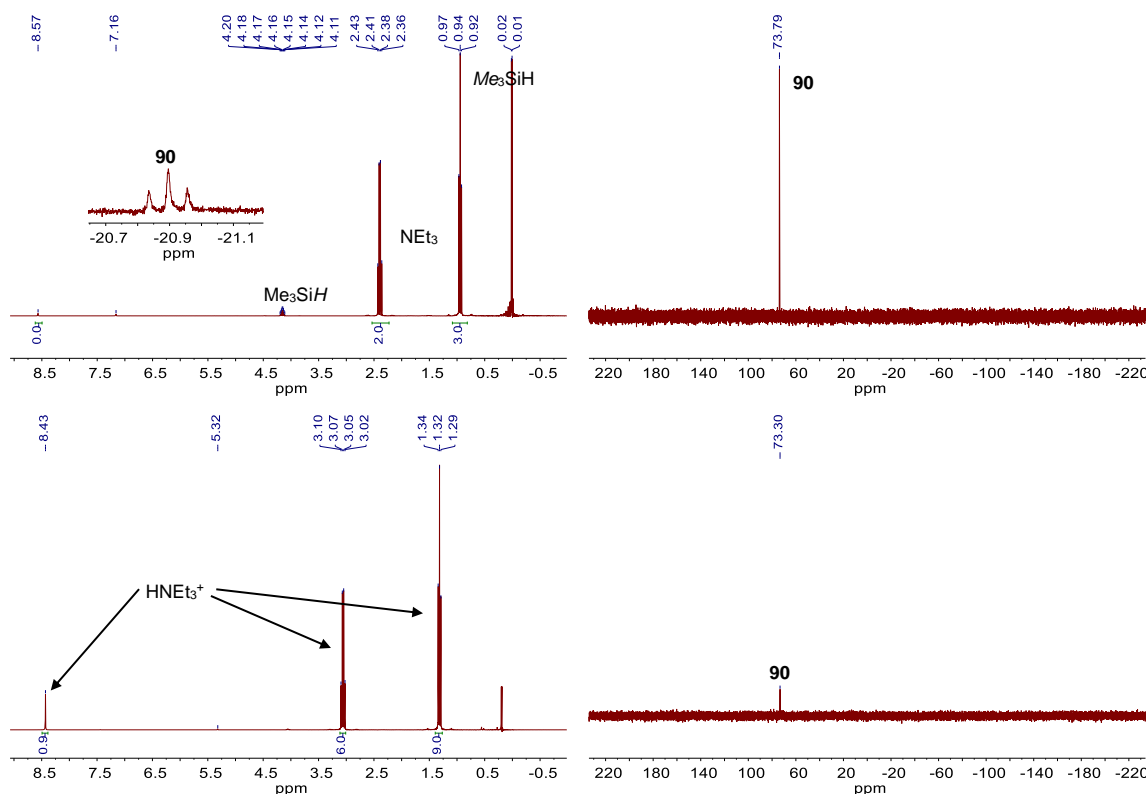


Figure 5.2 Top: ¹H NMR (left) and ³¹P{¹H} NMR (right) of the “upper” C₆D₆ phase. Bottom: ¹H NMR (left) and ³¹P{¹H} NMR (right) of the “lower” ionic liquid phase ([HNEt₃]OTf). Small amounts of Me₃SiH and **90** are present in the ionic liquid phase due to pollution with the C₆D₆ phase.

5 Hydrogenolysis of Silyl Triflates

Interestingly, 2 phases are being formed during catalysis, indicating formation of the ionic liquid $[\text{HNEt}_3][\text{OTf}]$. Separate analysis of both phases after a catalytic run confirmed that the upper (C_6D_6) phase contains silane, NEt_3 and **90**, while the lower phase indeed mostly consists of $[\text{HNEt}_3][\text{OTf}]$ (Figure 5.2).

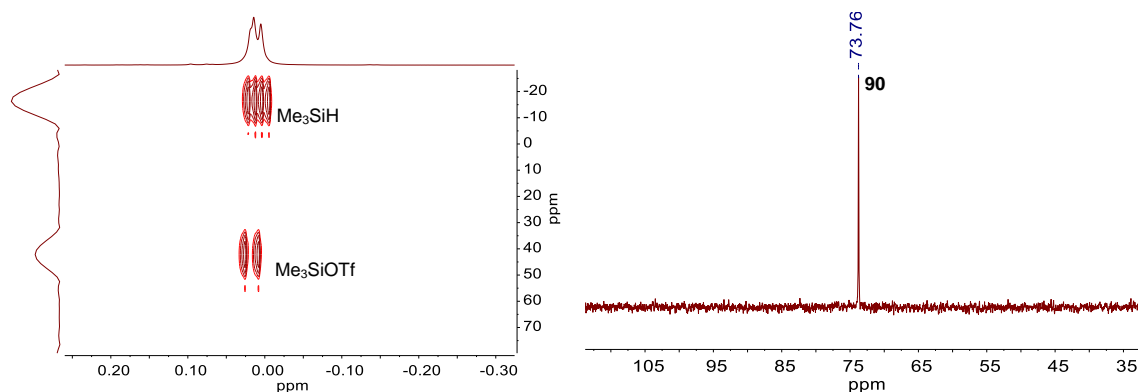
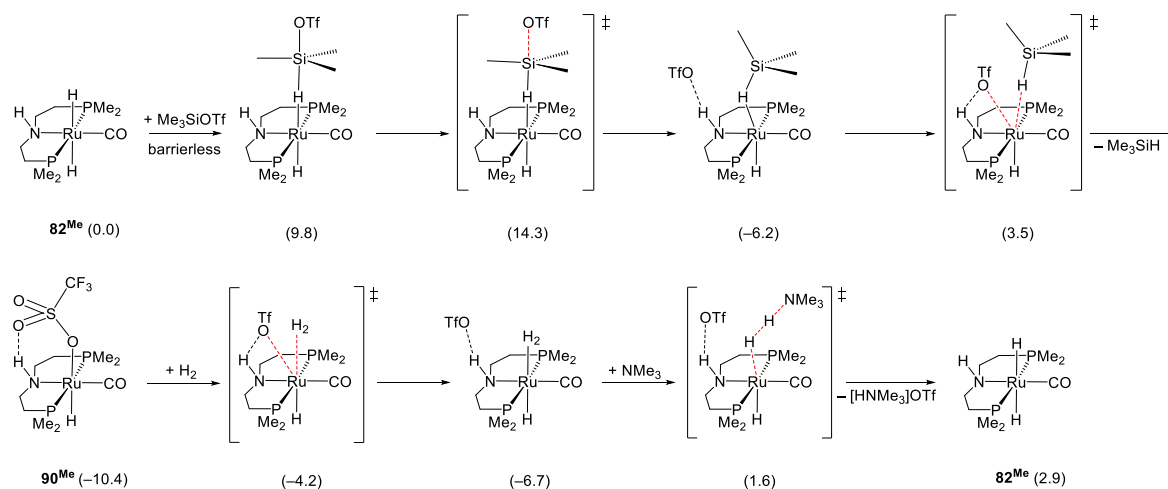


Figure 5.3 ^1H - ^{29}Si HMBC (left) and $^{31}\text{P}\{^1\text{H}\}$ NMR (right) spectrum during catalysis.

Monitoring of catalysis by ^1H and $^{31}\text{P}\{^1\text{H}\}$ NMR revealed **90** as the only ruthenium containing species, suggesting it as the resting state (Figure 5.3). To gain deeper insight into the reaction mechanism, DFT calculations were performed by Umut S. Karaca and Julia I. Schweizer supervised by Max C. Holthausen (University of Frankfurt) for the PMe_2 -truncated model system **82^{Me}** with NMe_3 as base (Scheme 5.1).^[74]



Scheme 5.1 Computed pathway for the hydrogenolysis of Me_3SiOTf using **82^{Me}**; ΔG° in kcal mol^{-1} by Umut S. Karaca and Julia I. Schweizer supervised by Max C. Holthausen from the University of Frankfurt (SMD-PBE0-D3/def2-TZVP//RI-PBE-D3/def2-SVP).^[74]

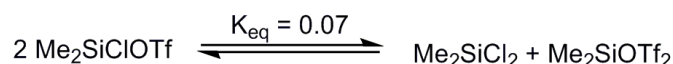
Two points should be noted:

i) The overall reaction is computed to be slightly endergonic ($2.9 \text{ kcal mol}^{-1}$) due to the fact that $[\text{HNMe}_3]\text{OTf}$ is treated as isolated contact ion pair. However, $[\text{HNMe}_3]\text{OTf}$ forms a separate ionic liquid phase (vide supra), therefore exhibiting additional stabilization from ionic interactions. Thus, the overall reaction free energy is disregarded in the calculation of the effective activation barrier of

24.7 kcal mol⁻¹. This value is in agreement with a reaction proceeding at room temperature.

ii) **90**^{Me} is the lowest energy species ($\Delta G^\circ = -10.4$ kcal mol⁻¹) in agreement with experimental results (see above) and its calculated NH...O hydrogen bond is confirmed by X-ray structure analysis of **90** (see chapter 9.1). Resting state destabilization by prevention of hydrogen bonding might enable faster catalysis. Therefore, *N*-methylated analogon [(MePNP^{Pr})RuH(OTf)CO] (**92**, MePNP^{Pr} = MeN(CH₂CH₂P(*i*Pr)₂)₂) was synthesized and employed for hydrogenolysis of Me₃SiOTf with NEt₃ as base. Indeed, activity is slightly increased (91 % conversion after 130 min) compared to **90** (81 % conversion after 135 min) under identical conditions.

As stated above, the bifunctional chlorohydrosilane Me₂SiClH is a valuable reagent for silicone industry. Selective chlorosilyl triflate Si-OTf semihydrogenolysis could be an attractive route for direct synthesis of Me₂SiClH from Me₂SiClOTf. Me₂SiClOTf can be obtained from Me₂SiCl₂ or Me₂SiClPh with 1 eq HOTf as main product according to *in situ* NMR examination. However, isolation attempts by distillation lead to chloride/triflate dismutation (Scheme 5.2). Equilibration is slow at room temperature (ca. 4 d), but considerably accelerated by addition of amines (NEt₃ and 2,6-lutidine) or **82** (ca. 1 h).^l For these mixtures, the ¹⁹F NMR spectra collapse to a singlet, indicating fast triflate exchange on the NMR timescale. In contrast, all species are distinguishable by ¹H and ¹H-²⁹Si HMBC with ²⁹Si NMR chemical shifts identical to the pure substances, indicating that triflate is still bound to silicon and no pentacoordinate species are present.



Scheme 5.2 Redistribution of chlorosilanes/silyl triflates.

Since Me₂SiClOTf remains the main species (66 %) after isomerization according to Scheme 5.2, attempts were made to hydrogenate the mixture. Unexpectedly, hydrogenolysis with NEt₃ as base selectively yielded the doubly hydrogenated Me₂SiH₂ as main product (36 %, i.e. 72 % in Si-H bonds) with concomitant formation of Me₂SiCl₂ and only minor amounts of Me₂SiClH (5 %, Table 5.2, Entry 6). Selectivity is invariant to the nature of the catalyst, as ^tBu(POCOP)IrH₂ (**6**, ^tBuPOCOP = κ³-C₆H₃-2,6-[OP(^tBu)₂]₂), ^{Pr}(HPNP)FeH(Cl)CO (**91**), ^{Pr}(MePNP)RuH(OTf)CO (**92**) and ^tBu(HPNP)RuH(Cl)CO (**93**, ^tBuHPNP = HN(CH₂CH₂P(^tBu)₂)₂) all give similar results (Table 5.2, Entries 1 - 4; see Figure 5.4 for catalyst depictions).^m Likewise, change of solvent to Et₂O did not significantly affect the selectivity (Entry 5). As computational^[74] and experimental^[165] evaluation of the Me₂SiCl₂/Me₂SiH₂ dismutation equilibrium call for higher Me₂SiClH yields (Me₂SiCl₂ + Me₂SiH₂ → 2 Me₂SiClH; $\Delta G_{\text{R}}^\circ_{\text{calc}} = -0.7$ kcal mol⁻¹; $\Delta G_{\text{R}}^\circ_{\text{exp}} \approx -1.3$ kcal mol⁻¹), weaker bases were screened to maintain thermodynamic control. Indeed, change of the base to 2,6-lutidine (1 eq, pK_{a,MeCN} (H-lut⁺) = 14.13)^[166] compared to pK_{a,MeCN} (HNEt₃⁺) = 18.82^[90]) inverted the selectivity, giving Me₂SiClH as main product (Me₂SiClH/Me₂SiH₂ = 10, Entry 8).

^l **82** is converted to **90** under these conditions.

^m For this purpose, ^{Pr}(MePNP)RuHOTfCO (**92**) was synthesized and fully characterized (chapter 7.3.1.4) including X-ray structure analysis (chapter 9.2).

and H₂, Figure 5.5).

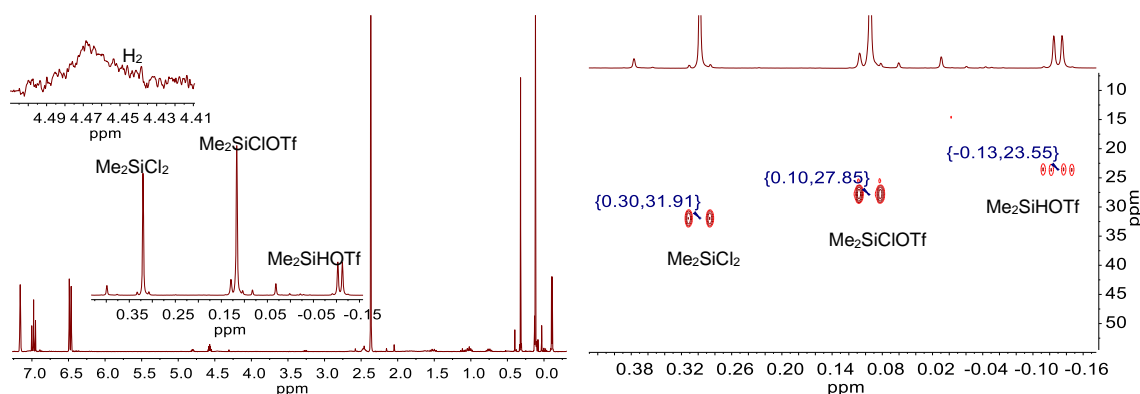


Figure 5.5 *In situ* ¹H NMR (left) and ¹H-²⁹Si HMBC (right) spectra of the reaction of Me₂SiClH with [H-lut]OTf in C₆D₆ indicate conversion to silyl triflates and H₂.

In order to maximize the selectivity for Me₂SiClH over Me₂SiH₂, the equilibrium in Scheme 5.2 was exploited to increase the concentration of Me₂SiClOTf with respect to Me₂SiOTf₂ by addition of excess Me₂SiCl₂. As expected, when 5 or 10 eq Me₂SiCl₂ were mixed with 1 eq Me₂SiOTf₂, Me₂SiClOTf was virtually the only triflate containing species (>97%) as evidenced by ¹H NMR. Subsequent hydrogenolysis of the mixture did in fact increase the yield for Me₂SiClH to 44% and 51%, respectively after one week (Table 5.2, Entry 9 and 10). Notably, the reaction gets slower for higher Me₂SiClOTf/Me₂SiOTf₂ ratios, suggesting that hydrogenolysis of Me₂SiClOTf is significantly slower than of Me₂SiOTf₂.

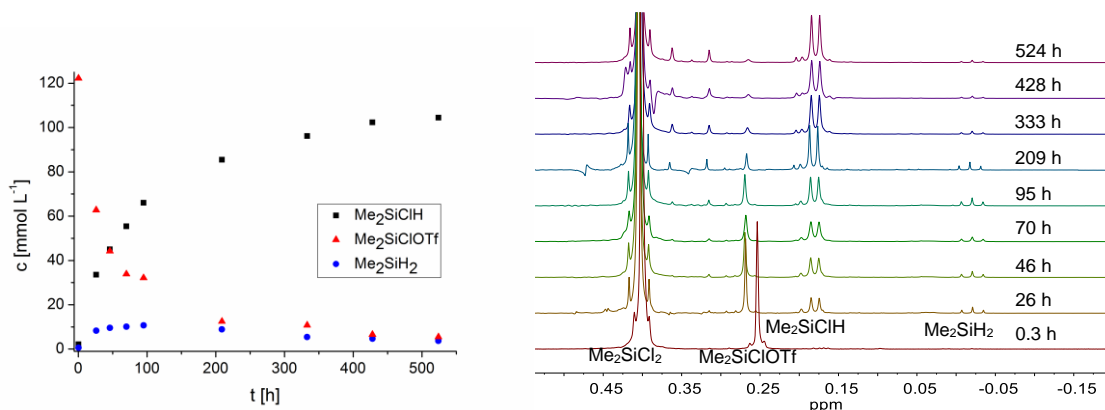
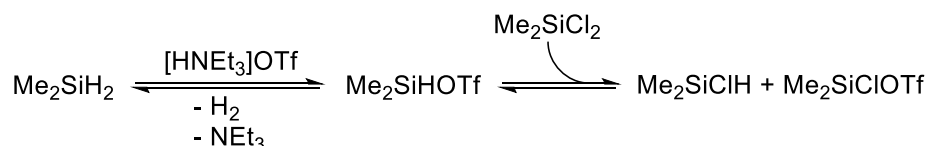


Figure 5.6 Time dependent concentration profiles (left) and corresponding stacked ¹H NMR spectra (right) of the reaction depicted in Table 5.2, Entry 12.

Monitoring of catalysis by ¹H NMR revealed that Me₂SiH₂ is built up in the initial phase of catalysis (up to ≈100 h), whereas its consumed at long reaction times (200 - 500 h). As hydrogenolysis is almost thermoneutral (*vide supra*), it is hypothesized that Me₂SiH₂ is dehydrogenated to Me₂SiHOTf, which would subsequently scramble (*vide supra*) with excess Me₂SiCl₂ to Me₂SiClH and Me₂SiClOTf (Scheme 5.3).

5 Hydrogenolysis of Silyl Triflates



Scheme 5.3 Hypothesized explanation for the consumption of Me_2SiH_2 at long reaction times.

5.2.1 Attempted Hydrogenolysis of Silyl Sulfonic Acids

Hydrogenolysis of silyl sulfonic acids might be a more ecologically benign alternative to the hydrogenolysis of silyl triflates. As with silyl triflates, synthesis of $\text{Me}_3\text{SiOSO}_2\text{Me}$ is facile, as it was prepared by neat reaction of methylsulfonic acid and Me_3SiCl with HCl as only byproduct. A stoichiometric reaction of **82** with $\text{Me}_3\text{SiOSO}_2\text{Me}$ gave Me_3SiH in 97 % yield. Additionally, a new ruthenium species was formed which is characterized by a signal at 75.1 ppm in the $^{31}\text{P}\{^1\text{H}\}$ NMR and a hydride shift of -19.8 ppm indicative of a weak *trans* ligand (Figure 5.7).

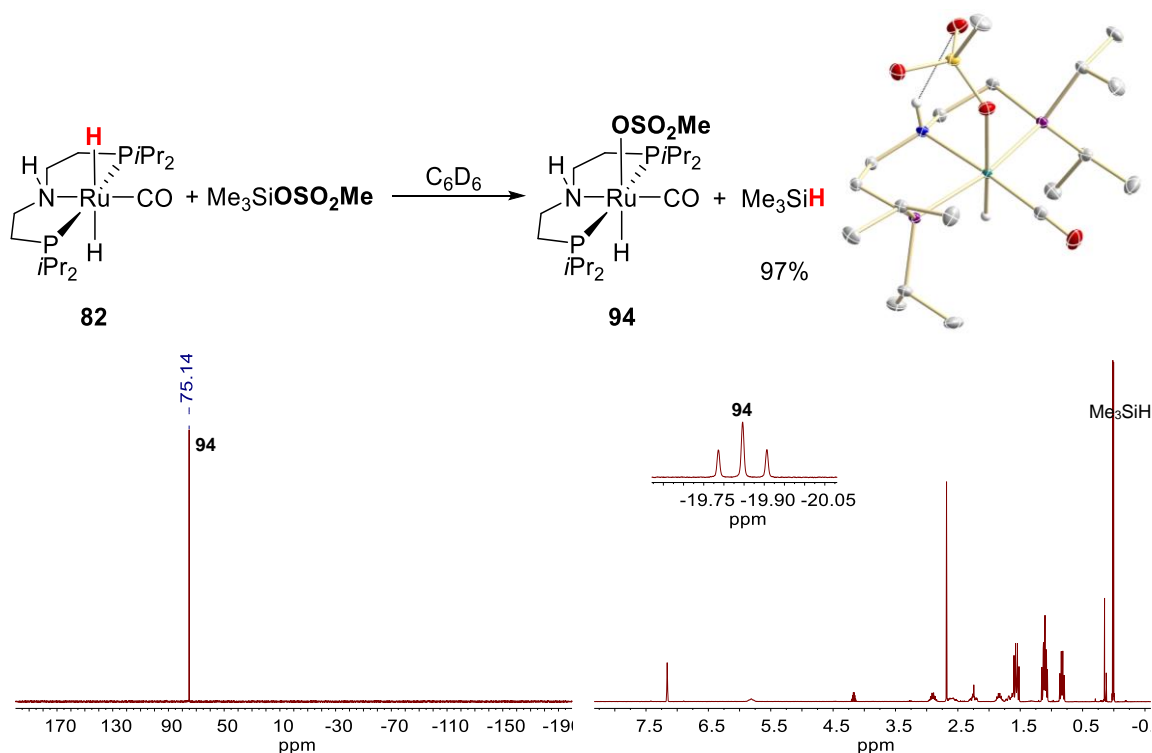


Figure 5.7 $^{31}\text{P}\{^1\text{H}\}$ (bottom left) and ^1H NMR (bottom right) from the reaction of **82** with $\text{Me}_3\text{SiOSO}_2\text{Me}$ (top left). Top right: Thermal ellipsoid plot of **94** with the anisotropic displacement parameters drawn at the 50% probability level. The asymmetric unit contains one complex molecule. The N-H and Ru-H hydrogen atoms were found from the residual density map and isotropically refined. A N-H...O hydrogen bond is shown ($d(\text{H}\cdots\text{O}) = 2.455(17)$ Å). Carbon bound hydrogens are omitted for clarity. Turquoise: Ru, red: O, blue: N, purple: P, yellow: S, grey: C, white: H.

X-ray diffraction establishes formation of $(\text{HPNP}^{\text{Pr}})\text{RuH}(\text{OSO}_2\text{Me})\text{CO}$ (**94**, Figure 5.7 top right) and reveals a hydrogen bond of an oxygen atom and the NH proton ($2.455(17)$ Å) which is considerably shorter than the analogous hydrogen bond in **90** ($2.62(2)$ Å, Table 5.3, Entry 1). Additionally, the O-

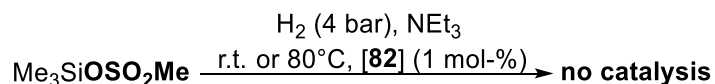
5 Hydrogenolysis of Silyl Triflates

Ru bond in **94** (2.2883(10) Å) is shorter than in **90** (2.2957(11) Å, Entry 2). These features are a direct result of the greater +I effect of hydrogen as compared to fluorine which is propagated through the molecule. Consequently, the oxygen atoms in $^-OSO_2Me$ are stronger donors than in $^-OSO_2CF_3$. LIFDI-MS of **94** shows two species: i) $[M]^+$ with an intensity of 100 a.u. and ii) $[M-OSO_2Me]^+$ with an intensity of 30 a.u., suggesting that $^-OSO_2Me$ is split off during the ionization process (Entry 3). In line with stronger anion binding in **94**, LIFDI-MS of **90** exhibits higher intensity for the $[M-OSO_2CF_3]^+$ signal (80 a.u, Entry 3).

Table 5.3 Selected spectral features for complexes of type $(HPNP^{Pr})RuH(OSO_2R)CO$.

Entry	Feature	90 (R = CF ₃)	94 (R = CH ₃)
1	NH...OSO ₂ R H-bridge distance	2.62(2) Å	2.455(17) Å
2	Ru-O bond length	2.2957(11) Å	2.2883(10) Å
3	LIFDI-MS: <i>m/z</i> (%)	[90]⁺ (100), [90-OSO₂R]⁺ (80)	[94]⁺ (100), [94-OSO₂R]⁺ (30)

A subsequent attempt to hydrogenate Me₃SiOSO₂Me catalytically with 1 mol-% **82** and NEt₃ as base failed at r.t. and 80 °C using 4 bar H₂. Two reasons may be accountable: i) Overstabilization of resting state analog **94** by stronger O→Ru donation and stronger O→HN hydrogen bonds. ii) A stronger Si-O bond in Me₃SiOSO₂Me renders hydrogenolysis endergonic.



Scheme 5.4 Attempted catalytic hydrogenolysis of Me₃SiOSO₂Me failed.

5 Hydrogenolysis of Silyl Triflates

5.2.2 Side note on the Purity of 2,6-Lutidine

NMR monitoring of initial attempts to hydrogenate silyl triflates with **82** and 2,6-lutidine as base (1000 eq with respect to catalyst, dried over CaH_2 and distilled) revealed the formation of several metal complexes as evidenced by multiple hydride and phosphorous signals in the $^1\text{H}\{^{31}\text{P}\}$ and $^{31}\text{P}\{^1\text{H}\}$ spectra respectively. The same complexes were obtained upon simple mixing of **90** with 1000 eq 2,6-lutidine (i.e. the amount that was also used for catalysis) in C_6D_6 but not upon mixing of **90** with 1 eq 2,6-lutidine.

As detailed NMR analysis was hampered by an intense signal for undeuterated 2,6-lutidine and the multitude of signals, crystals were grown by diffusion of pentane into a saturated solution of **90** in 2,6-lutidine. Two types of crystals can be distinguished with the microscope: i) colorless blocks suitable for X-ray diffraction ii) small colorless needles not suitable for X-ray diffraction. The diffraction data for the crystalline blocks reveal formation of 4-methylpyridine complex **95**, suggesting contamination of the 2,6-lutidine batch.ⁿ In fact, 4-methylpyridine and 3-methylpyridine are common impurities in 2,6-lutidine as they possess identical boiling points within ± 1 °C.^[167]

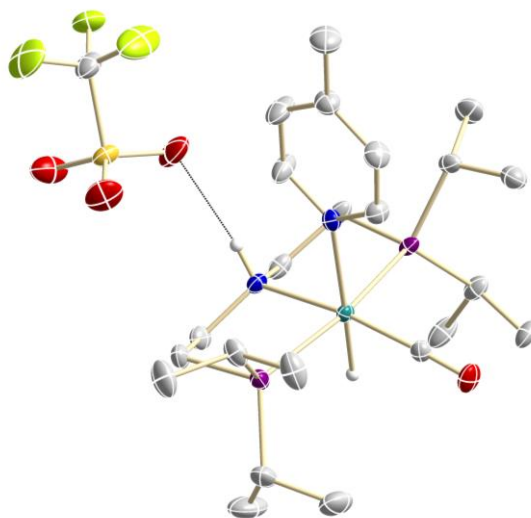


Figure 5.8 Thermal ellipsoid plot of $[(\text{HPNP}^{\text{Pr}})\text{RuH}(\text{lut})\text{CO}]\text{OTf}$ (**95**) with the anisotropic displacement parameters drawn at the 50% probability level. The asymmetric unit contains one complex molecule, one CF_3SO_3^- anion and a half disordered pentane solvent molecule. The N-H and Ru-H hydrogen atoms were found from the residual density map and isotropically refined. Carbon bound hydrogens and cocrystallized *n*-pentane are omitted for clarity. Turquoise: Ru, red: O, blue: N, purple: P, yellow: S, grey: C, white: H.

Subsequent NMR analysis of the crystalline blocks revealed a species as main compound that is characterized by a phosphorous resonance of 71.0 ppm and a hydride resonance of -15.81 ppm, i.e. indicative of a weak *trans*-ligand (Figure 5.1 bottom). Furthermore, two doublets in the aromatic region ($\delta_{\text{H}} = 6.9$ ppm and 8.8 ppm) that integrate to two with identical coupling constant of 8.5 Hz

ⁿ As no impurities were detected by ^1H NMR and GC-MS of the 2,6-lutidine batch, it can be assumed that the impurities amount to less than the detection limit i.e. $<0.1\%$.

5 Hydrogenolysis of Silyl Triflates

are observed, confirming 4-methylpyridine binding (Figure 5.1 top). Evidently, steric shielding prevents coordination of 2,6-lutidine to **90**, but the triflate ligand is readily exchanged by coordinating molecules. Due to the huge excess (1000 eq) of 2,6-lutidine, trace impurities can be stoichiometric with respect to ruthenium. As a consequence, 2,6-lutidine was dried over AlCl_3 and distilled to remove trace impurities of 4-methylpyridine and 3-methylpyridine.^[167] Indeed, when **90** was treated with this batch of 2,6-lutidine (1000 eq) in C_6D_6 no pincer species other than **90** were observed confirming the absence of coordinating species. Of course, all catalytic experiments described in this thesis were performed using properly purified 2,6-lutidine, leading to **90** as the only ruthenium species during catalysis.

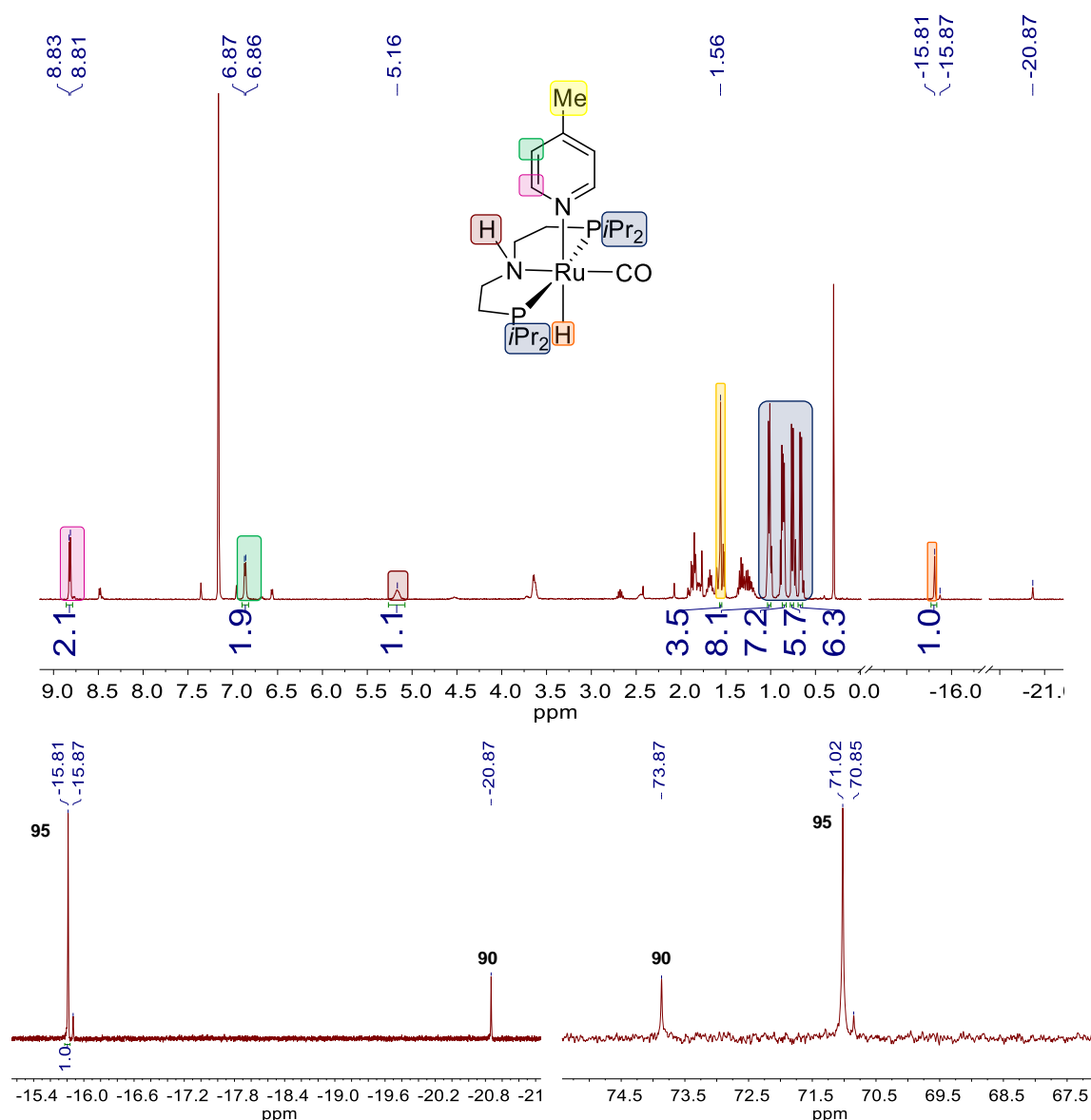
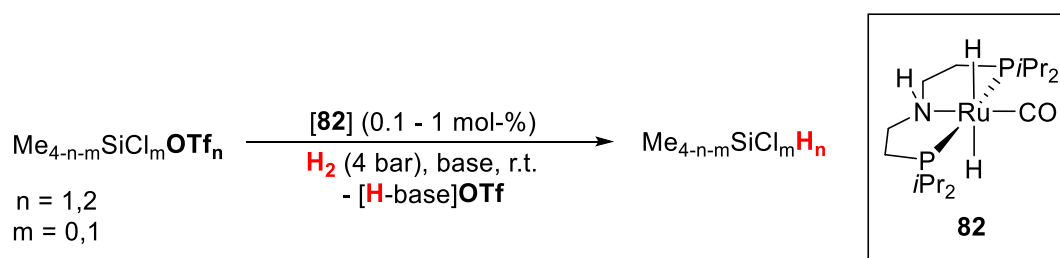


Figure 5.9 $^1\text{H}\{^{31}\text{P}\}$ NMR (top), expansion of the hydride region (bottom left) and $^{31}\text{P}\{^1\text{H}\}$ NMR (bottom right) of the crystalline blocks of **95** in C_6D_6 .

5 Hydrogenolysis of Silyl Triflates

5.3 Summary

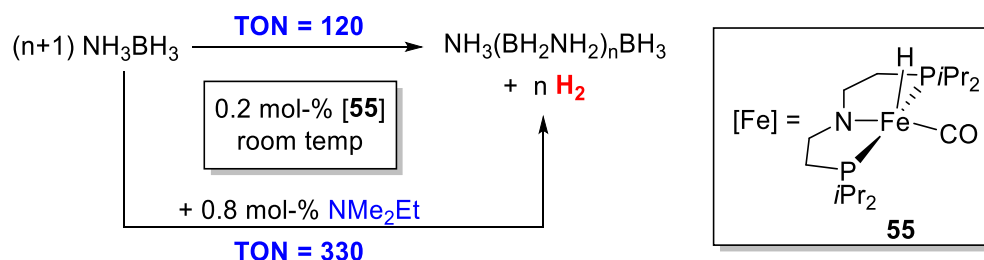
To sum up, efficient hydrogenolysis of Me_3SiOTf and $\text{Me}_2\text{SiOTf}_2$ to the corresponding hydrosilanes was presented using **82** as catalyst (0.1 - 1 mol-%) under mild conditions (4 bar H_2 , r.t.). Depending on the equivalents of base (NEt_3), full or semihydrogenolysis to Me_2SiH_2 or Me_2SiHOTf was achieved in high yields (>80 %) and low reaction times (1 h). It should be noted that **82** is a more active and durable catalyst than the previously reported iridium catalysts **28** and **29** for the same transformation (chapter 1.3.3).^[91,94] Especially, hydrogenolysis of bistriflate $\text{Me}_2\text{SiOTf}_2$ is extremely facile, contrasting with the previous reports. Experimental and computational evaluation support a catalytic cycle involving outer-sphere hydride transfer and H_2 heterolysis. Additionally, chloride/triflate dismutation equilibria were investigated and exploited to give mixed hydrochlorosilane Me_2SiClH in good yield (>50 %) from hydrogenolysis of $\text{Me}_2\text{SiCl}_2/\text{Me}_2\text{SiOTf}_2$ mixtures with 2,6-lutidine as base.



Scheme 5.5 Hydrogenolysis of silyl triflates was achieved under mild conditions. Hydrochlorosilanes were obtained by hydrogenolysis of chlorosilane/silyl triflate mixtures.

6 Conclusion

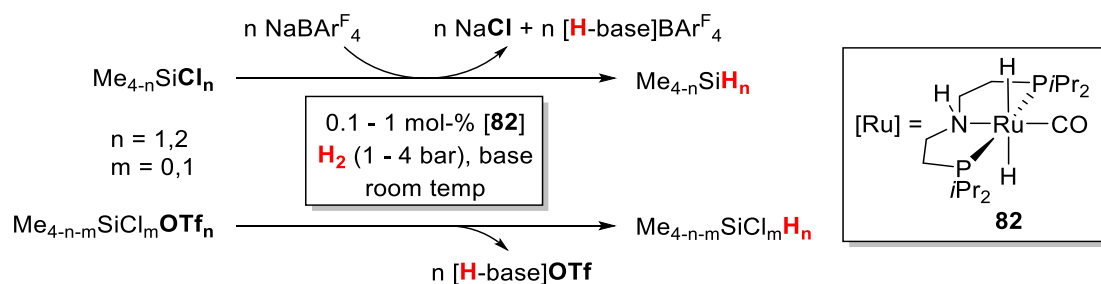
Ammonia borane dehydrocoupling to linear polyaminoborane mediated by bifunctional iron complex **55** (0.1 - 1 mol-%) at room temperature was achieved with an unprecedented TON/TOF for well-defined base metal catalysts. Evaluation of the reaction mechanism and deactivation pathway enabled a rationale to slow down catalyst deactivation by addition of substoichiometric amounts of a simple amine, thereby tripling the TON from 120 to 330 (Scheme 6.1). Importantly, the same effect was also observed with ruthenium and iridium pincer complexes **9** and **6**, pointing towards a general rationale.



Scheme 6.1 Ammonia borane dehydrocoupling with **55**. Addition of substoichiometric amounts of an amine triples the TON to 330, i.e. unprecedented for a well defined base metal catalyst.

Rare hydrogenolysis of chlorosilanes and silyl triflates $\text{Me}_{4-n}\text{SiX}_n$ ($X = \text{Cl}, \text{OTf}$) was achieved using bifunctional ruthenium catalyst **82** (0.1 - 1 mol-%) at mild conditions (r.t., 1 - 4 bar H_2).

Endergonic chlorosilane hydrogenolysis with NEt_3 as base was enabled using $\text{NaBAR}^{\text{F}_4}$ as chloride abstractor. Catalysis was shown to proceed via base stabilized silyl cations such as $[\text{Me}_3\text{SiNEt}_3]^+$. In contrast, hydrogenolysis of silyl triflates proceeded without additive giving high yields (>80 %) of MeSiH_3 , Me_2SiH_2 and Me_2SiHOTf with NEt_3 as base. Hydrogenolysis of chlorosilane/silyl triflate mixtures was optimized with 2,6-lutidine as base to give valuable Me_2SiClH in yields over 50%.



Scheme 6.2 Hydrogenolysis of chlorosilanes and silyl triflates mediated by **82**.

This thesis substantiates the remarkable activity of bifunctional PNP iron and ruthenium catalysts for (de-)hydrogenation reactions of inorganic substrates. While metal-ligand cooperativity via hydrogen bonding of the substrate to the NH proton of the ligand plays a crucial role in ammonia borane dehydrocoupling with iron complex **55**, it was shown to be detrimental for hydrogenolysis of silyl triflates mediated by **82**.

7 Experimental Part

Parts of this chapter have been published ([A. Glüer](#), M. Förster, V. R. Celinski, J. Schmedt auf der Günne, M. C. Holthausen, S. Schneider, *ACS Catal.* **2015**, *5*, 7214 and [A. Glüer](#), J. I. Schweizer, U. S. Karaca, C. Würtele, M. Diefenbach, M. C. Holthausen, S. Schneider, *Inorg. Chem.* **2018**, *57*, 13822) and parts of this work have been adapted from these publications with permission from ACS.^[42,74] Copyright 2015/2018 American Chemical Society.

7.1 General Methods

All experiments were carried out under argon (linde, quality 5.0) atmosphere using Schlenk or glove-box techniques (O₂, H₂O below 0.1 ppm). All glassware (except quartz NMR tubes) was heated in vacuum prior to use. Glassware used for experiments with chlorosilanes or silyl triflates was silanized with Me₂SiCl₂ prior to use. Solvents were bought in HPLC grade and dried by passing through columns packed with activated alumina (Et₂O (stabilized with 8 ppm 2,6-Di-*tert*-butyl-4-methylphenol), THF, C₆H₆, pentane). Fluorobenzene was degassed and dried over molecular sieves (4 Å). Deuterated solvents were dried over Na/K (C₆D₆, THF-*d*₈) or CaH₂ (CD₂Cl₂) and trap-to-trap transfer in vacuo. NEt₃ was dried over KOH, distilled and stored over molecular sieves (4 Å). 2,6-lutidine was purchased from Sigma Aldrich, dried over AlCl₃,^o distilled and stored over molecular sieves (4 Å). Me₃SiCl, Me₂SiCl₂, Me₂SiClH, Me₃SiOTf and MeOTf were degassed and distilled prior to use. 1,2,4,5-tetramethylbenzene (TMB) and KO^tBu were sublimed prior to use. NaBPh₄, NaBF₄, NaSbF₆, KPF₆ and NaOTf were dried *in vacuo* prior to use. Cyclohexene was dried over molecular sieves and distilled. NH₃BH₃ and NMe₃BH₃ were sublimed prior to use. NMe₂Et was dried over CaH₂ and distilled. HOTf was purchased from ABCR and used without further purification. H₂ (quality 6.0) was purchased from Linde and dried by passing through a spiral cooling system which was immersed in N₂ (l). NaBARF₄,^[168] 2,6-lutidinium triflate,^[169] **6**,^[63] **8**^[170], **51**^[140,148], **82**,^[170,171] **87**,^[170] **91**^[148] and **93**^[171] were prepared following published procedures. **9**, **53** and **55** were freshly prepared prior to every experiment following published procedures.^[10,65] All reactions involving hydrogen evolution (except those in NMR tubes) were carried out using overpressure valves to allow pressure equilibration.

Solution NMR spectra were recorded on Bruker Avance III 300, Avance III HD 300, Avance III 400, Avance III HD 400, or Avance III HD 500 spectrometers with a Prodigy broadband cryoprobe and calibrated to the residual proton resonance of the solvent (C₆D₆: δ_H = 7.16 ppm; δ_C = 128.06 ppm, THF-*d*₈: δ_H = 1.72 ppm / 3.58 ppm; δ_C = 25.31 ppm / 67.21 ppm, CD₂Cl₂: δ_H = 5.32 ppm; δ_C = 53.84 ppm) or the solvent itself when undeuterated solvents were used (PhF: δ_{H, ortho/para} = 7.00 ppm). ³¹P, ²⁹Si and ¹¹B NMR chemical shifts are calibrated to the proton resonance of SiMe₄ according to their Δ values^[172] and reported relative to phosphoric acid (δ_P = 0.0 ppm), SiMe₄ (δ_{Si} = 0.0 ppm) and BF₃·Et₂O (15 % in CDCl₃; δ_B = 0.0 ppm), respectively. LIFDI (Linden CMS) mass spectra were measured on a Joel AccuTOF spectrometer under inert conditions by the Zentrale

^o this treatment is necessary to remove trace impurities of 4- and 3-methylpyridine which would coordinate to **90** (see chapter 5.2.2).

7 Experimental Part

Massenabteilung, Fakultät für Chemie, Georg-August-Universität Göttingen. Elemental analyses were obtained from the Analytisches Labor, Georg-August-Universität Göttingen using an Elementar Vario EL 3 analyzer. IR spectra were recorded as powder on a Bruker ALPHA FT-IR spectrometer with Platinum ATR module. Suitable single crystals for X-ray structure determination were selected from the mother liquor under an inert gas atmosphere and transferred in protective perfluoro polyether oil on a microscope slide. The selected and mounted crystals were transferred to the cold gas stream on the diffractometer. The diffraction data were obtained at 100 K on a Bruker D8 three-circle diffractometer, equipped with a PHOTON 100 CMOS detector and an INCOATEC microfocus source with Quazar mirror optics (Mo-K α radiation, $\lambda = 0.71073 \text{ \AA}$).

The data obtained were integrated with SAINT and a semi-empirical absorption correction from equivalents with SADABS was applied. The structures were solved and refined using the Bruker SHELX 2014 software package.^[173–176] All non-hydrogen atoms were refined with anisotropic displacement parameters. All C-H hydrogen atoms were refined isotropically on calculated positions by using a riding model with their U_{iso} values constrained to 1.5 U_{eq} of their pivot atoms for terminal sp^3 carbon atoms and 1.2 times for all other atoms.

7.2 Experimental Part for Ammonia Borane Dehydrocoupling

7.2.1 Synthetic Procedures

7.2.1.1 Catalytic Protocol

In a typical experiment, a stock solution (400 μL) of **55** in THF was quickly added to a solution of NH_3BH_3 in THF (5.6 mL) via syringe. In kinetic experiments hydrogen gas evolution was monitored volumetrically using a gas-burette filled with water. Back diffusion of water was prevented with a mercury filled bubbler between reaction vessel and burette. The amount of H_2 generated was calculated using ideal gas law. Substrate conversion was calculated from: $n(\text{AB}) = n(\text{AB}_0) - n(\text{H}_2)$, neglecting a small error as a result of borazine and polyborazylene formation. However, spectroscopic monitoring showed that these products are formed at later stages of catalysis, leaving initial rates unaffected. The yield of PAB (90%) from typical catalytic runs was derived by isolation of the precipitated solid as described below (chapter 7.2.2.1).

7.2.1.2 Mercury Poisoning Experiment

A stock solution (400 μL) of **55** (0.0802 mol/L, 0.0321 mmol, 0.00991 eq) in THF was quickly added to a suspension of NH_3BH_3 (100 mg, 3.24 mmol, 1.00 eq) and Hg (7.95 g, 39.6 mmol, 12.2 eq) in THF (5.6 mL) via syringe. Evolution of hydrogen gas was monitored as described in chapter 7.2.1.1.

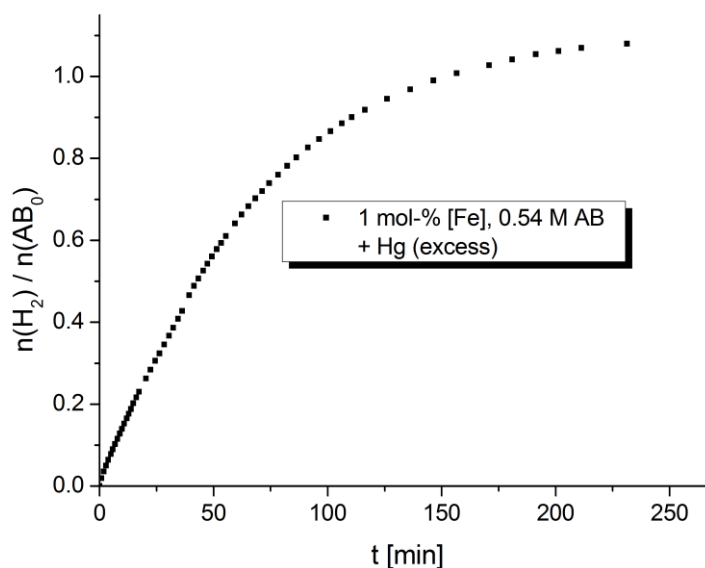


Figure 7.1 Mercury test run.

7.2.1.3 Dehydrocoupling with Ruthenium Catalyst **9**

A stock solution (200 μL) of **9** (0.0016 mol/L, 0.00032 mmol, 0.0001 eq) in THF was quickly added to a solution of NH_3BH_3 (99.8 mg, 3.23 mmol, 1.00 eq) in THF (5.8 mL) via syringe (Figure 3.7) and evolution of hydrogen gas was monitored as described in chapter 7.2.1.1.

7 Experimental Part

7.2.1.4 Catalysis with added Amine

7.2.1.4.1 Amine Addition after Catalyst Deactivation

A stock solution (400 μL) of **55** (0.016 mol/L, 0.0064 mmol, 0.002 eq) in THF was quickly added to a solution of NH_3BH_3 (100 mg, 3.24 mmol, 1.00 eq) in THF (5.6 mL) via syringe. After 4 h a solution (50 μL) of NMe_2Et in THF (3.3 mol/L, 0.016 mmol, 0.005 eq) was quickly added via syringe and evolution of hydrogen gas was monitored as described in chapter 7.2.1.1.

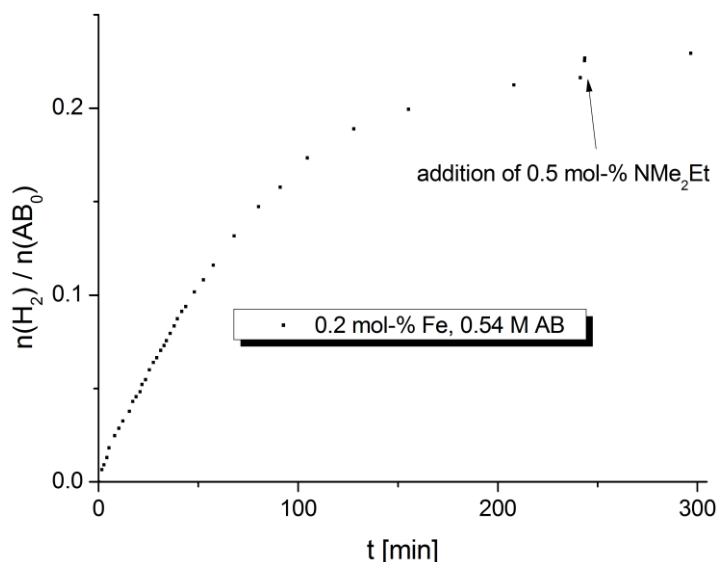


Figure 7.2 Time-conversion plot of a catalytic run with addition of amine after 250 h.

7.2.1.4.2 Addition of Amine prior to Catalysis (Catalyst **55**)

A stock solution (0.20 mL) of NMe_2Et in THF (0.130 mol/L, 0.026 mmol, 0.008 eq) was directly added to a solution of NH_3BH_3 (100.4 mg, 3.25 mmol, 1.00 eq) in THF (5.4 mL). A stock solution (400 μL) of **55** in THF (0.016 mol/L, 0.0065 mmol, 0.002 eq) was quickly added and gas evolution monitored as described in chapter 7.2.1.1 (Figure 3.1). After 10 h another portion of NMe_2Et in THF (200 μL , 0.130 mol/L, 0.026 mmol, 0.080 eq) was added without further increase of H_2 evolution. After catalysis stopped completely (total H_2 yield = 85 %), the yield of PAB (75 %) was derived by isolation of the precipitated product as described below (Chapter 7.2.2.1).

7.2.1.4.3 Addition of Amine prior to Catalysis (Catalyst **9**)

A stock solution (200 μL) of NMe_2Et in THF (0.130 mol/L, 0.026 mmol, 0.008 eq) was added to a solution of NH_3BH_3 (99.8 mg, 3.23 mmol, 1.00 eq) in THF (5.6 mL). A stock solution (200 μL) of **9** in THF (0.0016 mol/L, 0.00032 mmol, 0.0001 eq) was quickly added and gas evolution was monitored as described in chapter 7.2.1.1 (Figure 3.7).

7.2.2 Spectroscopic Examinations

7.2.2.1 Solid State NMR of PAB

After a typical catalytic run (0.54 mol/L AB; 1 mol-% **55**) the precipitated, colorless product was filtered off, washed with THF and pentanes and dried *in vacuo*. The resulting solid was analyzed by ^{11}B MQMAS NMR (Figure 3.2; measured and interpreted by Vinicius R. Celinski and Jörn Schmedt auf der Günne).^[42]

7.2.2.2 NMR Examination of Catalytic Runs

For *in situ* monitoring, AB (10.0 mg, 0.324 mmol, 1.00 eq) was dissolved in THF- d_8 (400 μL) in a quartz NMR tube. A stock solution of **55** in THF- d_8 (200 μL , 0.017 mol/L, 0.01 eq) was quickly added via syringe through the cap and after shaking, the tube was immediately introduced into the NMR spectrometer. ^{11}B NMR spectra (720 scans) were recorded every 15 min over a period of 17 h without sample spinning (Figure 3.6). The same products as in the NMR-tube experiment were observed upon taking an aliquot from a catalytic run in a glass vessel (AB: 50.0 mg, 1.62 mmol, 1.00 eq in 3 mL THF; **55**: 0.0811 mol/L; 0.0162 mmol; 0.01 eq in 200 μL THF; Figure 7.3).

In a similar experiment, AB (8.2 mg, 0.27 mmol, 1.0 eq) and **55** (5.4 mmol/L, 0.01 eq) were dissolved in THF- d_8 (490 μL) in a Young NMR tube and shaken. The mixture was analyzed by $^{31}\text{P}\{^1\text{H}\}$ and ^1H NMR spectroscopy (Figure 3.4). Signals were assigned by comparison to literature.^[17,49,50,141,149,177]

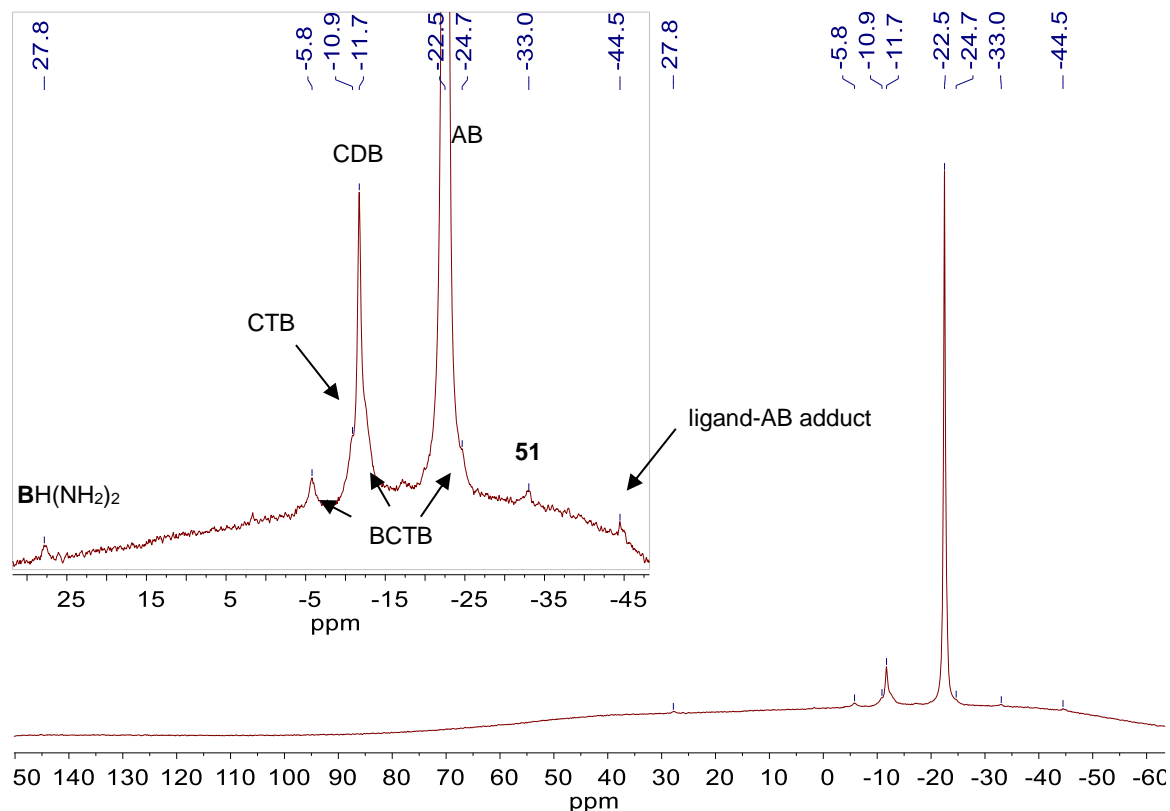


Figure 7.3 $^{11}\text{B}\{^1\text{H}\}$ NMR spectrum (THF- d_8) of a catalytic run (1 mol-% **55**) after 5 h.^[17,49,50,149,177]

7 Experimental Part

7.2.2.2.1 NMR Examination of a Catalytic Run (Catalyst **51**)

AB (10.1 mg, 0.327 mmol, 1.00 eq) was dissolved in THF- d_8 (0.4 mL) in a quartz NMR tube. A stock solution (200 μ L) of **51** (1.6 mmol/L, 3.3 mmol 0.01 eq) was added via syringe through the cap of the NMR tube. After shaking once, the sample was directly introduced into the NMR machine. ^{11}B NMR spectra were measured every 15 min. Quantitative comparison of spectra after 15 min and 11 h indicated 9 % conversion after 11 h.

7.2.2.2.2 NMR Examination of a Catalytic Run (11 mol-% **55**)

A Young NMR tube was charged with **55** (12.1 mg, 0.0311 mmol, 0.11 eq) and NH_3BH_3 (9.0 mg, 0.29 mmol, 1.0 eq) and cooled to 77 K ($\text{N}_2(l)$). THF- d_8 was added at 77 K, thus instantly freezing. Directly after the tube was warmed to room temperature and shaken, it was introduced into the NMR machine and measured. After 1 h, AB was completely consumed (Figure 7.4 left). The dihydrides **53a/b** are the only species detected by $^{31}\text{P}\{^1\text{H}\}$ NMR during a period of 3 h (Figure 7.4 right). Note that the lock signal was unstable due to gas evolution and solid precipitation.

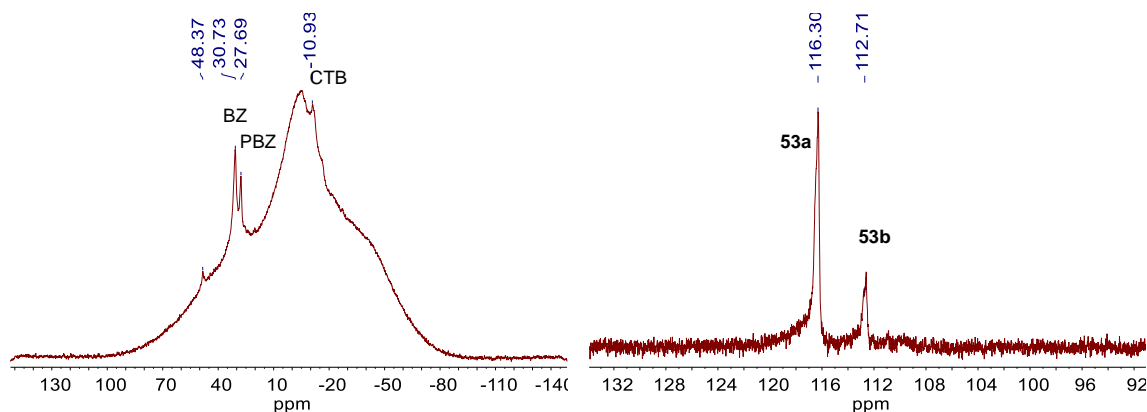


Figure 7.4 *In situ* $^{11}\text{B}\{^1\text{H}\}$ (left) and $^{31}\text{P}\{^1\text{H}\}$ (right) NMR after 1h.

7.2.2.3 Aminoborane Trapping

AB (49.8 mg, 1.61 mmol, 1.00 eq) and cyclohexene (1.0 mL, 0.81 g, 9.9 mmol, 6.1 eq) were dissolved in THF (2.0 mL). A stock solution (200 μ L) of **55** (0.081 mol/L, 0.016 mmol, 0.01 eq) in THF was quickly added via syringe. After 4 h an aliquot was transferred to a quartz NMR tube and examined by $^{11}\text{B}\{^1\text{H}\}$ NMR spectroscopy (Figure 7.5).

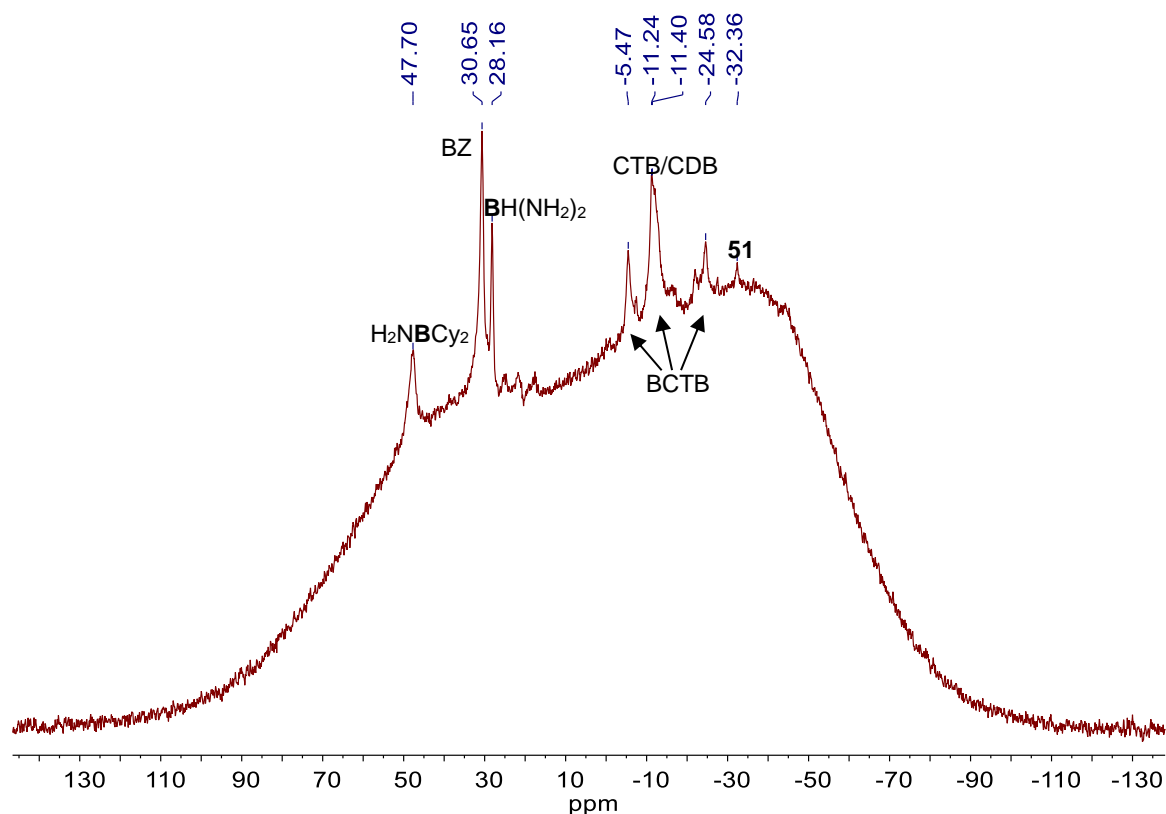


Figure 7.5 Trapping experiment of free NH_2BH_2 with cyclohexene.^[17,49,50,149,177]

7.2.2.4 Catalyst Deactivation

7.2.2.4.1 Examination of Catalyst Deactivation

After completion (5.5 h) of a catalytic run with incomplete substrate conversion (AB: 100 mg, 3.24 mmol, 1.00 eq in 5.6 mL THF; **55**: 0.0062 mol/L, 0.0025 mmol, 0.002 eq in 400 μL THF) the yellow solution was filtered off and all volatiles removed *in vacuo*. The residue was dissolved in $\text{THF-}d_8$ and examined by $^{31}\text{P}\{^1\text{H}\}$ and ^1H NMR spectroscopy (Figure 7.6).

Catalyst deactivation was also monitored by *in situ* $^{31}\text{P}\{^1\text{H}\}$ NMR spectroscopy:

AB (9.8 mg, 0.32 mmol, 1.0 eq) was dissolved in $\text{THF-}d_8$ (400 μL) in a Young NMR tube. A stock solution (200 μL) of **55** in $\text{THF-}d_8$ (0.0032 mol/L, 0.64 μmol , 0.002 eq) was quickly added and the NMR tube subsequently frozen in liquid nitrogen. After thawing to room temperature, the sample was directly introduced into the NMR spectrometer and several $^{31}\text{P}\{^1\text{H}\}$ NMR spectra (3040 scans) were recorded over a period of 12 h without sample spinning (Figure 3.8 left).

7 Experimental Part

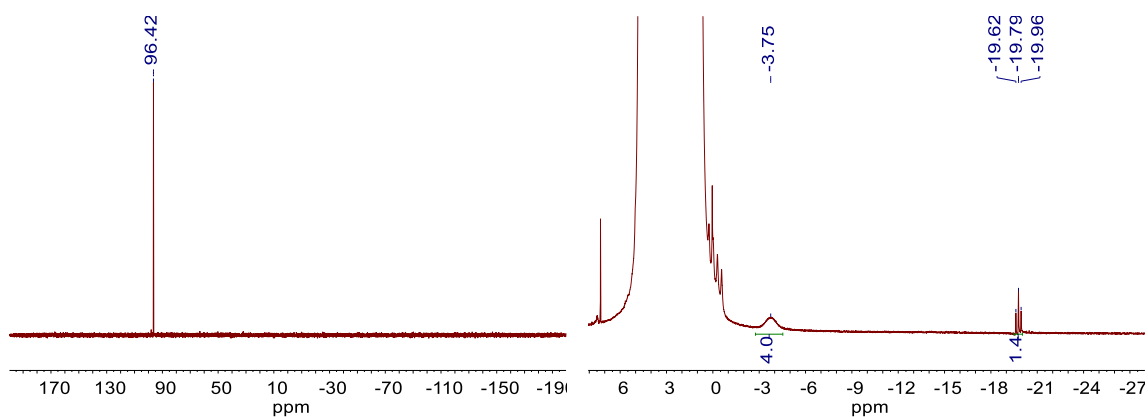


Figure 7.6 Crude $^{31}\text{P}\{^1\text{H}\}$ (left) and ^1H (right) NMR spectra of catalyst deactivation product **51**.^[140,141]

7.2.2.4.2 Examination of Catalyst Deactivation in the Presence of Amine

AB (10.0 mg, 0.324 mmol, 1.00 eq) was dissolved in THF- d_8 (350 μL) in a quartz NMR tube and a stock solution (50 μL) of NMe_2Et (0.052 mol/L, 0.0026 mmol, 0.008 eq) in THF- d_8 was added. Another stock solution (200 μL) of **55** in THF- d_8 (0.0032 mol/L, 0.002 eq) was quickly added via syringe through the cap and after shaking the tube was immediately introduced into the NMR spectrometer. Several $^{31}\text{P}\{^1\text{H}\}$ (3040 scans, Figure 3.8 right) and $^{11}\text{B}\{^1\text{H}\}$ NMR spectra (720 scans, Figure 7.7) were recorded over a period of 13.5 h without sample spinning.

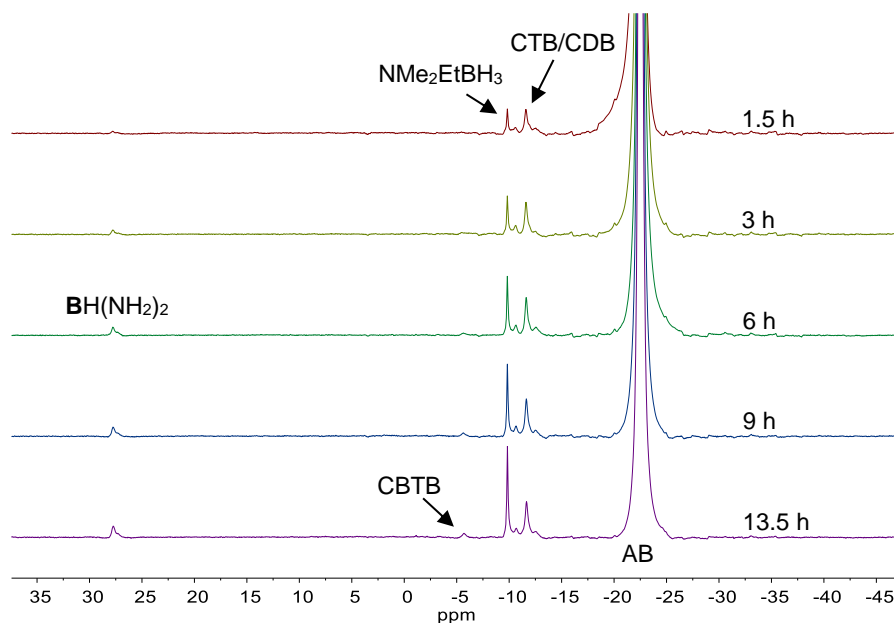


Figure 7.7 $^{11}\text{B}\{^1\text{H}\}$ spectra during catalysis with added amine.

7.2.2.4.3 Control Experiment of **53a/b** with Me_3NBH_3

A solution of **55** (7 mg, 0.02 mmol, 1 eq) in $\text{THF-}d_6$ (0.5 mL) in a Young NMR tube was set under dried dihydrogen (1.1 bar) by two freeze-pump-thaw cycles and backfilling with H_2 . After shaking for 20 min, conversion of **55** to **53a/b** was complete. Me_3NBH_3 (19 mg, 0.26 mmol, 13 eq) was sublimed into the NMR tube. After backfilling with dihydrogen (1.1 bar) the solution was thawed, shaken for 14 h and analyzed by NMR spectroscopy (Figure 7.8).

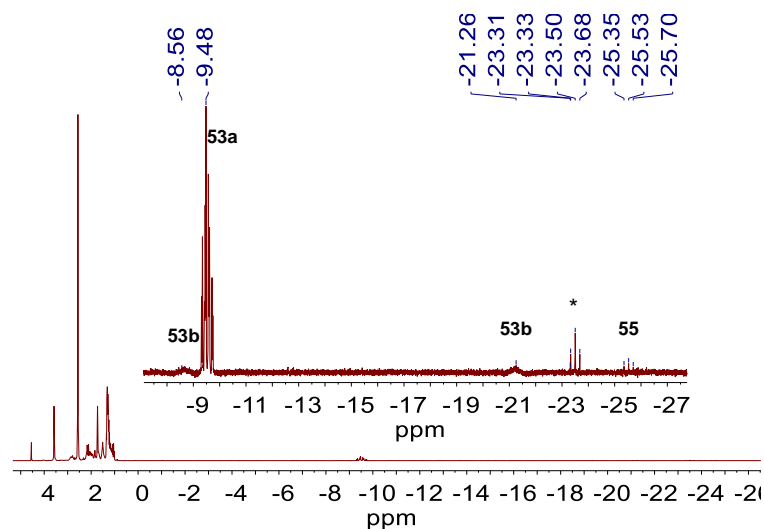


Figure 7.8 ^1H NMR spectrum ($\text{THF-}d_6$) of a mixture of **53a/b** and Me_3NBH_3 under H_2 after 14 h (* the small impurity $H(\text{PNP}^{\text{Pr}})\text{FeH}(\text{Cl})\text{CO}$ (**91**) was already present before addition of Me_3NBH_3).

7.3 Experimental Part for Hydrogenolysis of Chlorosilanes and Silyl Triflates

7.3.1 Synthetic Procedures

7.3.1.1 Synthesis of Me₂SiOTf₂

Me₂SiCl₂ (6.0 mL, 0.050 mol, 1.0 eq) was cooled to 0 °C and HOTf (12.5 mL, 0.14 mol, 2.8 eq) was added in one portion via syringe under stirring. The mixture was heated to 60 °C for 2 d during which time the HCl atmosphere was occasionally removed by a stream of Argon. Excess acid was neutralized by careful addition of NEt₃ (8 mL, 0.07 mol, 1.4 eq) at 0 °C. Removal of volatiles *in vacuo* and distillation (0.3 mbar, 37 °C) gave Me₂SiOTf₂ as a colorless oil (9 mL, 0.04 mol, 79 %) in 97 % purity according to ¹H and ¹⁹F NMR.

¹H NMR (300.13 MHz, C₆D₆, 300K): δ (ppm) = -0.01 (s, CH₃).

¹⁹F NMR (282.37 MHz, C₆D₆, 298K): δ (ppm) = -76.66 (s, CF₃).

²⁹Si NMR (59.63 MHz, C₆D₆, 298K): δ (ppm) = -14.6 (s) (determined by ¹H-²⁹Si HMBC).

7.3.1.2 Synthesis of Me₃SiOSO₂Me

Methylsulfonic acid (2.5 mL, 3.7 g, 0.039 mol, 1 eq) was added dropwise to Me₃SiCl (5 mL, 4.3 g, 0.039 mol, 1 eq) under stirring. The mixture was heated to 60 °C for 3 d and the HCl atmosphere occasionally removed. Excess acid was neutralized with NEt₃ (4 mL) and the mixture fractionally distilled *in vacuo* (> 8·10⁻³ mbar; oil bath set to 40 °C) to give Me₃SiOSO₂Me as colorless oil.

¹H NMR (300.13 MHz, C₆D₆, 301K): δ (ppm) = 2.26 (s, 3H, SCH₃), 0.15 (s, 9H, SiCH₃).

¹³C NMR (75.48 MHz, C₆D₆, 301K): δ (ppm) = -39.2 (s, SCH₃), 0.2 (s, SiCH₃).

²⁹Si NMR (59.63 MHz, C₆D₆, 301K): δ (ppm) = 29.7 (s).

7.3.1.3 Synthesis of (HPNP^{iPr})RuH(OTf)CO (90)

(HPNP^{iPr})Ru(H)₂(CO) (**82**) (100 mg, 0.23 mmol, 1.0 eq) was dissolved in Et₂O (6 mL) in a Young flask and HOTf (20 μL, 0.23 mmol, 1.0 eq) was added. The product precipitated and the volume was reduced to 5 mL *in vacuo*. The flask was transferred to a glove box and the supernatant solution was carefully removed via pipette. The solid was washed with pentane (3 x 3 mL) and dried *in vacuo* to give (HPNP^{iPr})RuH(OTf)CO (**90**) (80 mg, 0.14 mmol, 60%) as white solid with 0.5% impurity of yellow (HPNP^{iPr})Ru(H)₂CO (**82**) according to ¹H NMR. The solid was lyophilized from benzene and stirred in Et₂O (0.5 mL) over night. The supernatant yellow solution was removed via pipette and the residue was dried *in vacuo* to give (HPNP^{iPr})RuH(OTf)CO (**90**) as white solid (75 mg, 0.13 mmol, 56 %). Crystals suitable for X-ray crystallography were obtained by cooling a saturated Et₂O solution to -40 °C. An aliquot of the crystals was used for NMR characterization.

¹H{³¹P} NMR (500.25 MHz, C₆D₆, 298K): δ (ppm) = 4.52 (t (br), ³J_{HH} = 11.3 Hz, 1H, NH), 2.68 (sept, ³J_{HH} = 7.3 Hz, 2H, CH^{syn}), 2.44 (m, 2H, NCH₂^{syn}), 1.88 (m, 2H, PCH₂^{syn}), 1.78 (sept, ³J_{HH} = 6.9 Hz, 2H, CH^{anti}), 1.55 (m, 4H, superposition of PCH₂^{anti} and NCH₂^{anti}), 1.52 (d, ³J_{HH} = 7.3 Hz, 6H, CH₃^{syn}), 1.03 (d, ³J_{HH} = 6.9 Hz, 6H, CH₃^{anti}), 1.00 (d, ³J_{HH} = 7.3 Hz, 6H, CH₃^{syn}), 0.73 (d, ³J_{HH} = 6.9 Hz, 6H,

$\text{CH}_3^{\text{anti}}$, -20.9 (s, 1H, Ru-H^{anti} ($^2J_{\text{HP}} = 18.0$ Hz determined by ^1H NMR)).

$^{13}\text{C}\{^1\text{H}\}$ NMR (125.80 MHz, C_6D_6 , 298K): δ (ppm) = 205.5 (t, $^2J_{\text{CP}} = 11.5$ Hz, CO), 120.2 (signal was not observed directly due to low concentration/high multiplicity but proven by ^{19}F - ^{13}C HSQC), 54.0 (vt, N = $|^1J_{\text{CP}} + ^3J_{\text{CP}}| = 8.8$ Hz, NCH₂), 29.6 (vt, N = $|^2J_{\text{CP}} + ^3J_{\text{CP}}| = 18.5$ Hz, PCH₂), 28.1 (vt, N = $|^1J_{\text{CP}} + ^3J_{\text{CP}}| = 21.6$ Hz, CH^{syn}), 23.9 (vt, N = $|^1J_{\text{CP}} + ^3J_{\text{CP}}| = 26.1$ Hz, CH^{anti}), 20.7 (vt, N = $|^2J_{\text{CP}} + ^4J_{\text{CP}}| = 6.5$ Hz, CH₃^{syn}), 20.1 (vt, N = $|^2J_{\text{CP}} + ^4J_{\text{CP}}| = 6.5$ Hz, CH₃^{anti}), 18.7 (vt, br, N = $|^2J_{\text{CP}} + ^4J_{\text{CP}}| = 1.9$ Hz, CH₃^{anti}), 16.9 (vt, N = $|^2J_{\text{CP}} + ^4J_{\text{CP}}| = 3.5$ Hz, CH₃^{syn}).

syn and *anti* refer to the orientation of the proton/carbon with respect to the NH proton (i.e. above or below the pincer plane). Assignments were confirmed by 2D-NMR.

$^{31}\text{P}\{^1\text{H}\}$ NMR (202.52 MHz, C_6D_6 , 298K): δ (ppm) = 73.8 (s).

^{19}F NMR (470.67 MHz, C_6D_6 , 298K): δ (ppm) = -77.6 (s).

^1H - ^{15}N HSQC revealed a ^{15}N -signal at -331.2 ppm.

LIFDI-MS: m/z (%) = 585.0 (100) [M]⁺, 436.1 (80) [M-OTf]⁺.

IR: ν (cm⁻¹): 3248 (N-H), 2934, 2871, 2035 (Ru-H), 1920 (C≡O), 1879, 1468, 1278, 1231, 1221, 1214, 1188, 1164, 1025, 829, 636, 622.

Anal. Calcd for $\text{C}_{18}\text{H}_{38}\text{F}_3\text{NO}_4\text{P}_2\text{RuS}$: C, 36.98; H, 6.55; N, 2.40. Found: C, 37.13; H, 6.42; N, 2.34.

7.3.1.4 Synthesis of (MePNP^{P_r})RuH(OTf)CO (92)

(HPNP^{P_r})RuH(Cl)CO (87) (35.3 mg, 0.0743 mmol, 1.0 eq) and KO^tBu (10.1 mg, 0.0900 mmol, 1.2 eq) were suspended in Et₂O (2 mL) and stirred for 3 h at r.t. The mixture was filtered through a fritted funnel and the resulting yellow solution was dried *in vacuo*. Extraction with pentane (4x; 4 mL total) gave (PNP^{P_r})RuH(CO) as intermediate product.

MeOTf (8.4 μL , 0.077 mmol, 1.0 eq) was added to this solution to precipitate the product. After filtration and washing with pentane (3 x 1.5 mL) the solid was extracted with benzene (3 x 0.5 mL). Evaporation of the solvent *in vacuo* yielded (MePNP^{P_r})RuH(OTf)CO (92) as a white powder (33 mg, 74 %).

Crystals suitable for X-ray crystallography were obtained from a saturated solution of Et₂O at -40 °C.

$^1\text{H}\{^{31}\text{P}\}$ NMR (500.25 MHz, C_6D_6 , 298K): δ (ppm) = 2.69 (sept, $^3J_{\text{HH}} = 7.2$ Hz, 2H, CH^{syn}), 2.06 (s, 3H, NCH₃), 1.91-1.82 (m, 4H, NCH₂^{syn/anti} superposition), 1.79 (sept, $^3J_{\text{HH}} = 6.9$ Hz, 2H, CH^{anti}), 1.60 (d, $^3J_{\text{HH}} = 7.2$ Hz, 6H, CH₃^{syn}), 1.59-1.51 (m, 2H, PCH₂^{syn}), 1.43-1.38 (m, 2H, PCH₂^{anti}), 1.06 (d, $^3J_{\text{HH}} = 6.9$ Hz, 6H, CH₃^{anti}), 0.97 (d, $^3J_{\text{HH}} = 7.2$ Hz, 6H, CH₃^{syn}), 0.73 (d, $^3J_{\text{HH}} = 6.9$ Hz, 6H, CH₃^{anti}), -20.56 (s, 1H, Ru-H^{anti} ($^2J_{\text{HP}} = 19.0$ Hz determined by ^1H NMR)).

$^{13}\text{C}\{^1\text{H}\}$ NMR (125.80 MHz, C_6D_6 , 298K): δ (ppm) = 205.8 (t, $^2J_{\text{CP}} = 12.1$ Hz, CO), 121.0 (q, $^1J_{\text{CF}} = 320.1$ Hz, CF₃), 65.1 (vt, N = $|^2J_{\text{CP}} + ^3J_{\text{CP}}| = 9.0$ Hz, NCH₂), 45.6 (s, NCH₃), 29.9 (vt, N = $|^1J_{\text{CP}} + ^3J_{\text{CP}}| = 20.5$ Hz, CH^{syn}), 28.1 (vt, N = $|^1J_{\text{CP}} + ^3J_{\text{CP}}| = 18.0$ Hz, PCH₂), 24.3 (vt, N = $|^1J_{\text{CP}} + ^3J_{\text{CP}}| = 26.6$ Hz, CH^{anti}), 20.9 (superposition of two vts appears as a quartet), N = $|^2J_{\text{CP}} + ^4J_{\text{CP}}| = 6.0$ Hz, CH₃^{syn/anti}), 19.2 (s, CH₃^{anti}), 17.1 (vt, N = $|^2J_{\text{CP}} + ^4J_{\text{CP}}| = 3.5$ Hz, CH₃^{syn}).

syn and *anti* refer to the orientation of the proton/carbon with respect to the NCH₃ methyl group (i.e.

7 Experimental Part

above or below the pincer plane). Assignments were confirmed by 2D-NMR.

$^{31}\text{P}\{^1\text{H}\}$ NMR (202.52 MHz, C_6D_6 , 298K): δ (ppm) = 68.8 (s).

^{19}F NMR (470.67 MHz, C_6D_6 , 298K): δ (ppm) = -77.5 (s).

LIFDI-MS: m/z (%) = 599.1 (4) $[\text{M}]^+$, 450.2 (100) $[\text{M-OTf}]^+$.

IR: ν (cm^{-1}): 2960, 2932, 2873, 2056 (Ru-H), 1917 ($\text{C}\equiv\text{O}$), 1460, 1295, 1235, 1220, 1155, 1032, 882, 821, 695, 633, 518.

Anal. Calcd for $\text{C}_{19}\text{H}_{40}\text{F}_3\text{NO}_4\text{P}_2\text{RuS}$: C, 38.12; H, 6.74; N, 2.34. Found: C, 38.05; H, 6.72; N, 2.33.

Compound contained 2% unmethylated (HPNP^{Pr}) $\text{RuH}(\text{CO})(\text{OTf})$ as evidenced by ^1H NMR and LIFDI-MS.

7.3.2 Catalytic Protocols

7.3.2.1 General Catalytic Protocol for Hydrogenolysis of Chlorosilanes

$\text{NaBAR}^{\text{F}_4}$, **82** and base were dissolved in PhF in a Young NMR tube, and the solution was frozen in N_2 (l). Chlorosilane was condensed onto the mixture in static vacuum and the headspace was refilled with H_2 (1.2 bar). The sample was thawed and immediately shaken. When 4 bar pressure was used, the NMR tube was nearly completely immersed in N_2 (l) for 1 min during addition of H_2 before the tube was closed (only the top part with teflon sealing remained at room temperature). After warming to room temperature, the H_2 pressure is at ≈ 4 bar according to ideal gas law.

Products were identified by ^1H NMR and ^1H - ^{29}Si HMBC. As no deuterated solvent was used, samples were measured without lock and shimmed manually. Conversions/yields were determined by relative integration of all signals in the Me_xSi region around 0 ppm vs. 1,2,4,5-tetramethylbenzene as internal standard (Table 4.1).

7.3.2.2 General Catalytic Protocol for Hydrogenolysis of Pure Silyl Triflates

In a Young NMR tube, silyl triflate, **82** and base were dissolved in C_6D_6 . The mixture was frozen in N_2 (l), the headspace was evacuated, and refilled with H_2 (1.2 bar). The tube was closed, warmed to room temperature and shaken. When 4 bar pressure was used, the NMR tube was nearly completely immersed in N_2 (l) for 1 min during addition of H_2 before the tube was closed (only the top part with teflon sealing remained at room temperature). After warming to room temperature, the H_2 pressure should be at ≈ 4 bar according to ideal gas law. Products were identified by ^1H NMR and ^1H - ^{29}Si HMBC. Conversions/yields were determined by relative integration of all signals in the Me_xSi region around 0 ppm vs. 1,2,4,5-tetramethylbenzene as internal standard (Table 5.1).

7.3.2.3 General Catalytic Protocol for Hydrogenolysis of Silyl Chloride/Triflate Mixtures

In a Young NMR tube 1,2,4,5-tetramethylbenzene as internal standard, $\text{Me}_2\text{SiOTf}_2$, Me_2SiCl_2 and catalyst were dissolved in C_6D_6 and shaken for 1.5 h in order to isomerize the mixture (cf. chapter 7.3.3.13). Base was added, and the mixture was frozen in N_2 (l) in a way that most of the tube was covered with N_2 (l) and only the top part with teflon sealing remained at room temperature. The headspace was evacuated, H_2 (1.2 bar) was introduced and cooled for 1 min. The tube was closed

and warmed to room temperature. Thus, according to ideal gas law the pressure in the tube was approx. 4 bar. The mixture was shaken, and products were identified by ^1H NMR and ^1H - ^{29}Si HMBC. Conversions/yields were determined by relative integration of all signals in the Me_xSi region around 0 ppm vs. 1,2,4,5-tetramethylbenzene as internal standard (Table 5.2). When 2,6-lutidine was used as base, the NMR tube was cautiously warmed to room temperature from top to bottom, to avoid cracking of NMR tubes.

7.3.3 Spectroscopic Characterizations

7.3.3.1 Reaction of Me_3SiCl and $(\text{HPNP}^{\text{Pr}})\text{Ru}(\text{H})_2\text{CO}$ (**82**)

$(\text{HPNP}^{\text{Pr}})\text{Ru}(\text{H})_2\text{CO}$ (**82**) (3.6 mg, 0.0082 mmol, 1.1 eq) was dissolved in C_6D_6 (0.55 mL) in a Young NMR tube and cooled in the glovebox-freezer to $-40\text{ }^\circ\text{C}$. Me_3SiCl (1 μL , 0.078 mmol, 1 eq) was added and the tube was shaken for 20 h and analyzed by ^1H and $^{31}\text{P}\{^1\text{H}\}$ NMR (Figure 3.2).

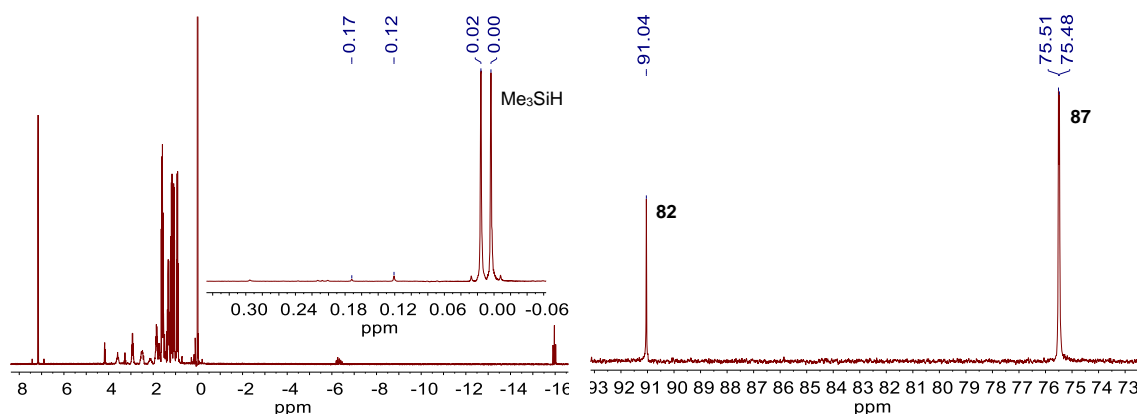


Figure 7.9 ^1H NMR (left) and $^{31}\text{P}\{^1\text{H}\}$ NMR (right) of the mixture after 1 h (18% excess **82** is present as determined by relative integration of hydride signals).

7.3.3.2 Reaction of Me_3SiOTf and $(\text{HPNP}^{\text{Pr}})\text{Ru}(\text{H})_2\text{CO}$ (**82**)

$(\text{HPNP}^{\text{Pr}})\text{Ru}(\text{H})_2\text{CO}$ (**82**) (2.9 mg, 0.0066 mmol, 1.0 eq) was dissolved in C_6D_6 in a Young NMR tube. Me_3SiOTf (1.0 μL , 0.0055 mmol, 0.8 eq) was added via microliter syringe and the resulting mixture was analyzed by ^1H and $^{31}\text{P}\{^1\text{H}\}$ NMR after 1 h (Figure 5.1).

7.3.3.3 Reaction of $\text{Me}_3\text{SiOSO}_2\text{Me}$ and $(\text{HPNP}^{\text{Pr}})\text{Ru}(\text{H})_2\text{CO}$ (**82**)

$(\text{HPNP}^{\text{Pr}})\text{Ru}(\text{H})_2(\text{CO})$ (**82**, 5 mg, 0.011 mmol, 1 eq) was dissolved in C_6D_6 (0.5 mL) and $\text{Me}_3\text{SiOSO}_2\text{CH}_3$ (1.8 μL , 2.0 mg, 0.012 mmol, 1.1 eq) was added dropwise. The mixture was analyzed by ^1H - ^{29}Si HMBC and ^1H and $^{31}\text{P}\{^1\text{H}\}$ NMR and subsequently lyophilized, washed with pentane (3 x 0.3 mL) and dried *in vacuo* to afford **94** as white powder. Crystals suitable for X-ray diffraction were obtained from a saturated solution in Et_2O at $-40\text{ }^\circ\text{C}$.

^1H NMR (300.12 MHz, C_6D_6 , 300K): δ (ppm) = 5.81 (t, $^3J_{\text{HH}} = 11.1$ Hz, 1H, NH), 2.98-2.83 (m, 2H), 2.68 (s, 3H, SCH_3), 2.67-2.49 (m, 2H), 2.33-1.17 (m, 2H), 1.92-1.77 (m, 2H), 1.75-1.51 (m, 10H), 1.10 (m, 12H, $2\times\text{CH}_3$), 0.83 (m, 6H, CH_3), -19.85 (t, $^2J_{\text{HP}} = 18.0$ Hz, 1H, Ru-H).

$^{31}\text{P}\{^1\text{H}\}$ NMR (121.49 MHz, C_6D_6 , 300K): δ (ppm) = 75.1 (s).

7 Experimental Part

LIFDI-MS: m/z (%) = 531.1 (100) $[M]^+$, 436.2 (30) $[M-OSO_2CH_3]^+$.

7.3.3.4 Reaction of $(HPNP^{Pr})RuH(OTf)CO$ (**90**) with NEt_3 under H_2 Atmosphere

$(HPNP^{Pr})RuH(OTf)CO$ (**90**; 3 mg, 0.005 mmol, 1 eq) was dissolved in C_6D_6 (0.5 mL) in a Young NMR tube and NEt_3 (24 μ L, 0.17 mmol, 34 eq) was added. The NMR tube was frozen in N_2 (l) in a way that only the Teflon sealing remained at room temperature and evacuated. H_2 (1.2 bar) was introduced, the tube closed, warmed to room temperature and shaken. Thus, the pressure in the tube is \approx 4 bar according to ideal gas law.

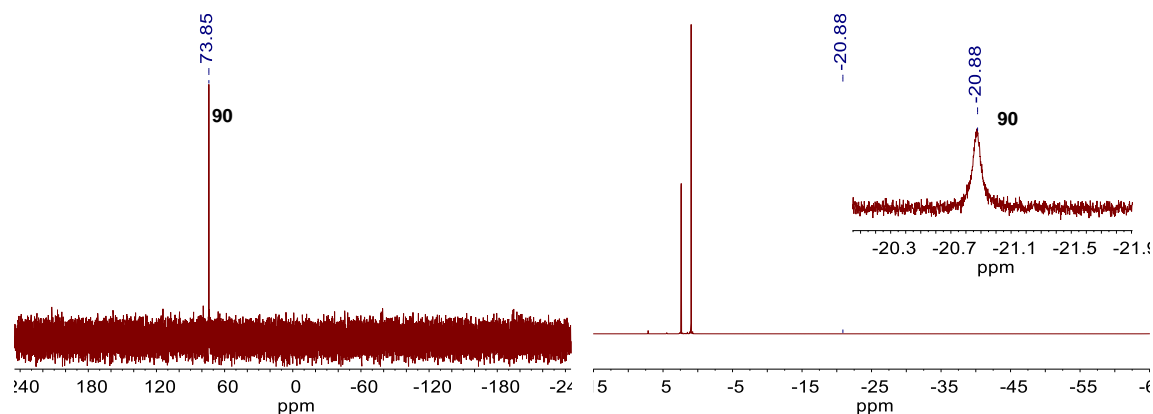


Figure 7.10 $^{31}P\{^1H\}$ (left) and $^1H\{^{31}P\}$ (right) NMR of the mixture after 1 d.

7.3.3.5 Reaction of $(HPNP^{Pr})RuH(Cl)CO$ (**87**) and VB^{Pr} under H_2 Atmosphere

$(HPNP^{Pr})RuH(Cl)CO$ (**87**) (2.4 mg, 0.0055 mmol, 1 eq) and VB^{Pr} (2.4 mg, 0.007 mmol, 1.3 eq) were dissolved in C_6D_6 (0.20 mL) and transferred to a high pressure NMR-tube. H_2 (8.8 bar) was introduced at r.t. and conversion of **87** to **82** was monitored by ^{31}P (ig) and 1H NMR (Figure 4.1).

7.3.3.6 Reaction of $(HPNP^{Pr})RuH(Cl)CO$ (**87**) with $NaBAR^F_4$

$NaBAR^F_4$ (8.6 mg, 0.0097 mmol, 1.0 eq) and $(HPNP^{Pr})RuH(Cl)CO$ (**87**) (4.4 mg, 9.4 μ mol, 1.0 eq) were dissolved in PhF (0.55 mL). A white solid ($NaCl$) precipitated from the resulting yellow solution. The suspension was transferred to a Young quartz NMR tube and analyzed by NMR spectroscopy. After introduction of H_2 (2.5 bar) the solution turned colorless and was analyzed by NMR spectroscopy again. After evaporation of the solvent *in vacuo*, the solid was dissolved in $THF-d_8$ and analyzed by NMR spectroscopy a third time (Figure 4.2).

In a similar experiment, **87** (23 mg, 0.049 mmol, 1.0 eq) and $NaBAR^F_4$ (45 mg, 0.051 mmol, 1.0 eq) were dissolved in PhF (1 mL). A white solid ($NaCl$) precipitated from the resulting orange solution. The solution was filtered, and the solvent was removed *in vacuo*. The remaining solid was dissolved in $THF-d_8$ and analyzed by 1H and $^{31}P\{^1H\}$ NMR (Figure 7.11) as well as LIFDI mass spectrometry (Figure 7.12).

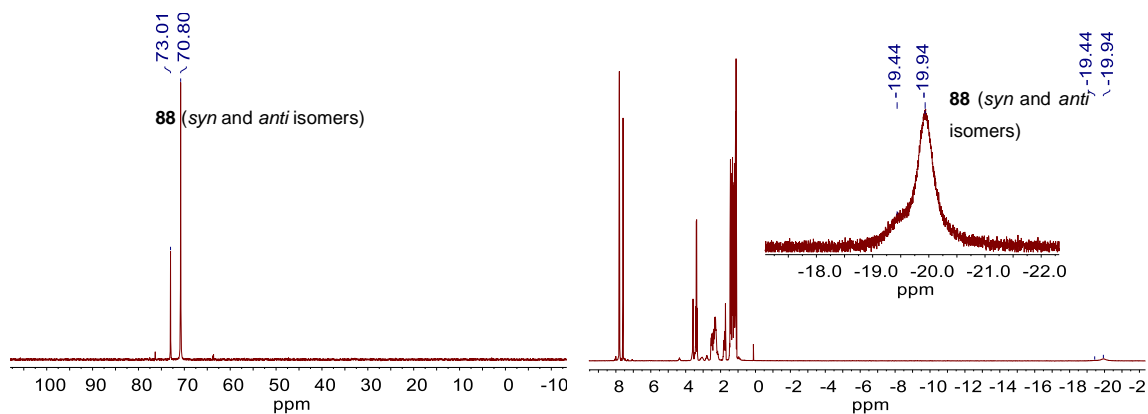


Figure 7.11 $^{31}\text{P}\{^1\text{H}\}$ (left) and ^1H NMR (right) of the crude product after removal of NaCl in THF- d_6 .

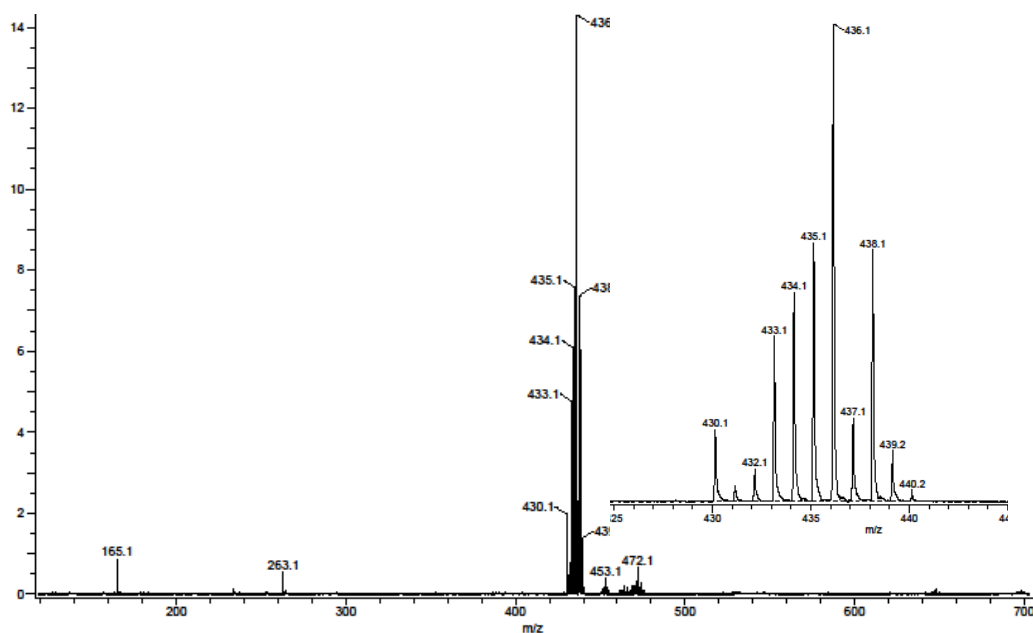


Figure 7.12 LIFDI mass spectrum of the crude product after removal of NaCl. The isotopic pattern of the signals at $m/z = 436.1$ is consistent with formation of $[(\text{HPNP})\text{RuHCO}]^+$.

7.3.3.7 Characterization of $[\text{Me}_3\text{SiNEt}_3]\text{BAR}^{\text{F}_4}$

$\text{NaBAR}^{\text{F}_4}$ (35 mg, 0.039 mmol, 1 eq) was dissolved in PhF (1.5 mL) and NEt_3 (0.25 mL, 1.8 mmol, 46 eq) and Me_3SiCl (5 μL , 0.039 mmol, 1 eq) were added. After stirring for 2 h and filtration, the solvent was removed *in vacuo* and the resulting solid was washed with pentane (3 x 1 mL). After removal of the solvent *in vacuo*, the solid was dissolved in CD_2Cl_2 and analyzed by NMR spectroscopy (Figure 7.13).

^1H NMR (300.13 MHz, CD_2Cl_2 , 300K): δ (ppm) = 7.73 (m, 8H, CH^{ortho}), 7.58 (s, 4H, CH^{para}), 3.11 (q, $^3J_{\text{HH}} = 7.3$ Hz, 6H, CH_2), 1.32 (t, $^3J_{\text{HH}} = 7.3$ Hz, 9H, CH_2CH_3), 0.61 (s, 9H, SiCH_3).

^{13}C NMR (75.48 MHz, CD_2Cl_2 , 300K): δ (ppm) = 162.2 (q, $^1J_{\text{CB}} = 49.9$ Hz, BC), 135.2 (s, CH^{ortho}), 129.3 (qq, $^2J_{\text{CF}} = 31.5$ Hz, $J = 2.8$ Hz, CCF_3), 125.0 (q, $^1J_{\text{CF}} = 272.5$ Hz, CF_3), 117.9 (sept, $^3J_{\text{CF}} = 4.0$ Hz, CH^{para}), 51.5 (s, CH_2CH_3), 9.4 (s, CH_2CH_3), 0.5 (s, SiCH_3).

^{11}B NMR (96.29 MHz, CD_2Cl_2 , 300K): δ (ppm) = 6.60 (s).

7 Experimental Part

^{29}Si NMR (59.63 MHz, CD_2Cl_2 , 300K): δ (ppm) = 47.9 (s) (determined by ^1H - ^{29}Si HMBC).

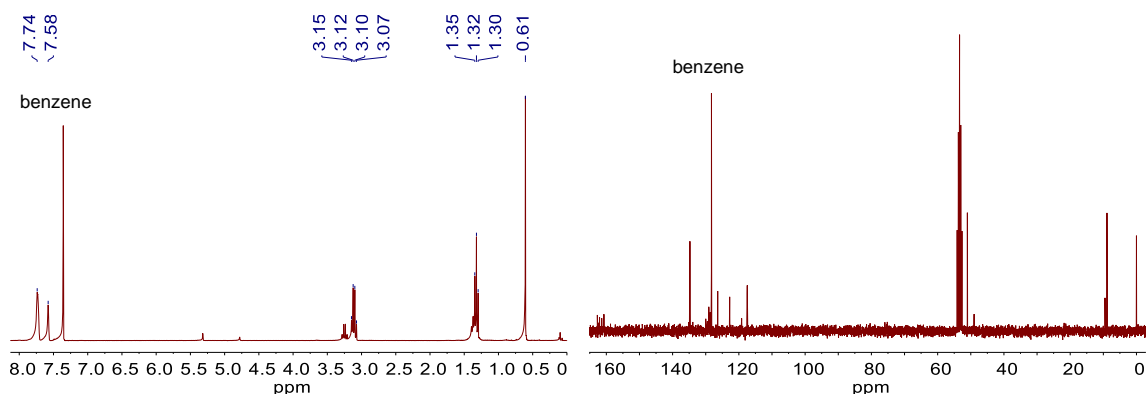


Figure 7.13 ^1H NMR (left) and $^{13}\text{C}\{^1\text{H}\}$ NMR (right) of $[\text{Me}_3\text{SiNEt}_3]\text{BARF}_4$ in CD_2Cl_2 .

7.3.3.8 Catalytic Hydrogenolysis of Chlorosilanes with NEt_3 as Base

NaBARF_4 (14 mg, 0.016 mmol, 1.0 eq) and **82** (0.4 mg, 0.9 μmol , 0.06 eq) were dissolved in PhF (0.6 mL) in a Young NMR tube. NEt_3 (4.4 μL , 0.032 mmol, 2.0 eq) was added via syringe and Me_3SiCl (2 μL , 0.016 mmol, 1.0 eq) was condensed onto the mixture. The atmosphere was backfilled with H_2 (1.2 bar) and the solution allowed to thaw. After shaking, the mixture was analyzed by NMR spectroscopy (Figure 4.3).

7.3.3.9 Catalytic Hydrogenolysis of Silyl Triflates with NEt_3 as Base

7.3.3.9.1 Catalytic Hydrogenolysis with $(\text{HPNP}^{\text{Pr}})\text{Ru}(\text{H})_2(\text{CO})$ (**82**)

A catalytic run with Me_3SiOTf (18 μL , 0.1 mmol), was monitored by ^1H / $^{31}\text{P}\{^1\text{H}\}$ NMR and ^1H - ^{29}Si HMBC (Figure 5.3) (see section 7.3.2.2 for general catalytic protocol; NEt_3 (140 μL , 1.01 mmol), **82** (0.9 μmol , 1 mol-%), 1.2 bar H_2 , 0.5 mL C_6D_6).

7.3.3.9.2 Separation of Phases

After a catalytic run, the upper phase was carefully removed via syringe and diluted with 0.2 mL C_6D_6 (see section 7.3.2.2; Me_3SiOTf (50 μL , 0.28 mmol), NEt_3 (70 μL , 0.51 mmol), **82** (4.6 μmol , 1.6 mol-%), H_2 (4 bar), C_6D_6 (0.5 mL). The lower phase was dissolved in CD_2Cl_2 (0.4 mL). Both phases were analyzed by NMR spectroscopy separately (Figure 5.2).

7.3.3.9.3 Catalytic Hydrogenolysis with $(\text{MePNP}^{\text{Pr}})\text{RuH}(\text{OTf})\text{CO}$ (**92**) and $(\text{HPNP}^{\text{Pr}})\text{RuH}(\text{OTf})\text{CO}$ (**90**)

Two catalytic runs only differing in the catalyst were conducted simultaneously. A stock solution (0.50 mL) of **92** or **90** (2.0 mmol/L, 1.0 μmol , 0.01 eq) was added to Me_3SiOTf (18 μL , 0.10 mmol, 1 eq) in a Young NMR tube. NEt_3 (16 μL , 0.12 mmol, 1.2 eq) was added and the atmosphere exchanged for H_2 (4 bar, cf. chapter 7.3.2.2). After 130 and 135 min, respectively, the mixtures were analyzed by ^1H NMR and ^1H - ^{29}Si HMBC (Figure 7.14).

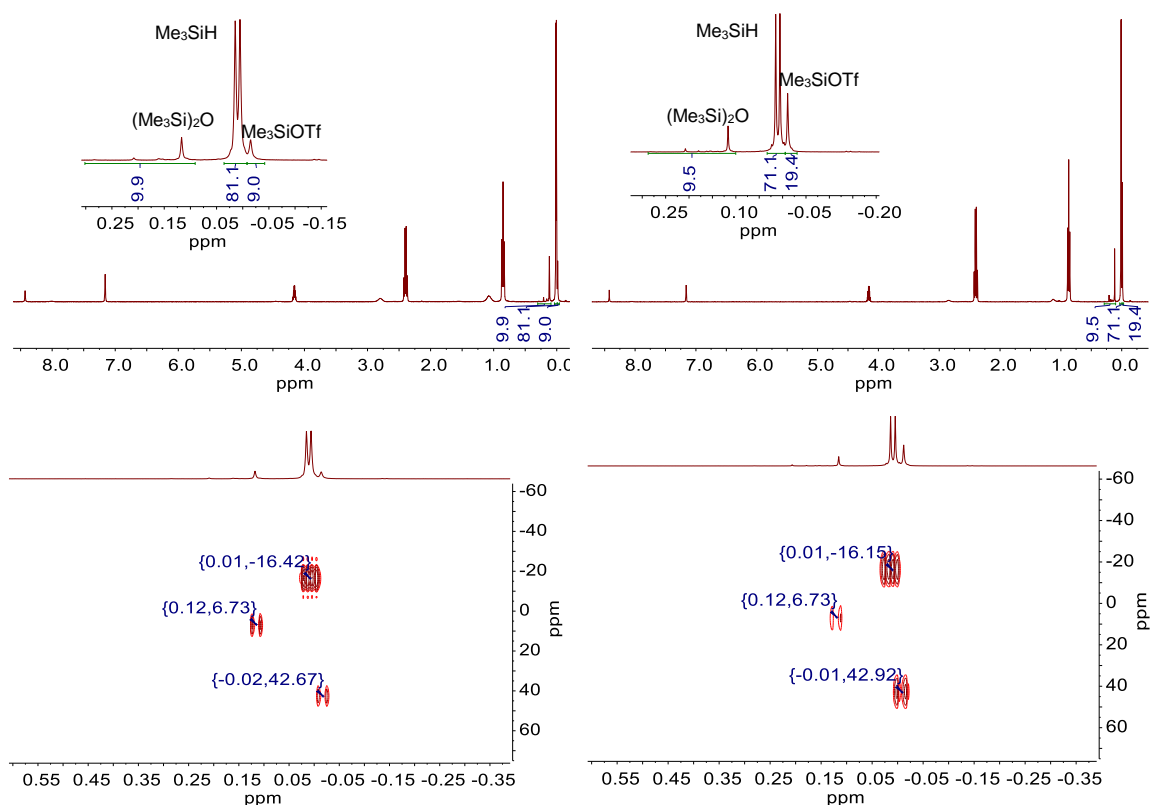


Figure 7.14 Top: ^1H NMR spectra of catalytic mixtures with **92** after 130 min (left) and **90** after 135 min (right). Bottom: corresponding ^1H - ^{29}Si HMBC spectra.

7.3.3.10 Catalytic Hydrogenolysis of Silyl Triflates with 2,6-Lutidine as Base

7.3.3.10.1 Catalytic Run with 1 eq 2,6-Lutidine

A catalytic run with 2,6-lutidine (14 μL , 0.12 mmol, 1.2 eq with respect to silicon/triflate) was analyzed by ^1H NMR spectroscopy after 94 h and 189 h (see section 7.3.2.2; Me_2SiCl_2 (6 μL , 0.05 mmol), $\text{Me}_2\text{SiOTf}_2$ (11.1 μL , 0.05 mmol), **82** (1 μmol , 1 mol-%), H_2 (4 bar), C_6D_6 (0.5 mL)).

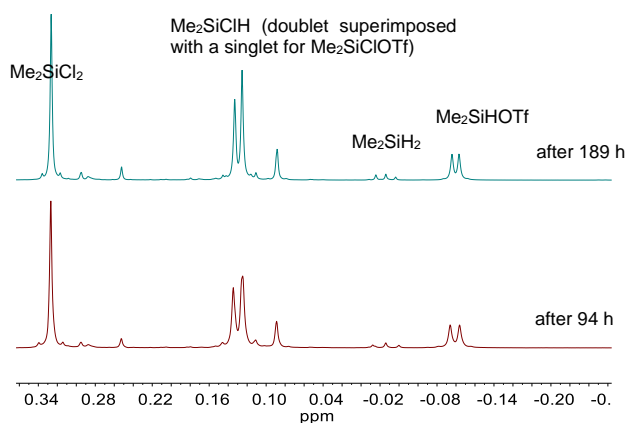


Figure 7.15 Stacked excerpts of ^1H NMR spectra in C_6D_6 after 94 h and 189 h (assignments were confirmed by ^1H - ^{29}Si HMBC).

7 Experimental Part

Table 7.1 Yields of dimethylsilyl species.^[a]

	Me ₂ SiCl ₂	Me ₂ SiClH	Me ₂ SiH ₂	Me ₂ SiHOTf	Me ₂ SiClOTf	Conv. ^[a]	Combined Yield ^[a] in Si-H bonds
After 94 h	30 %	31 %	2 %	13 %	5 %	82 %	48 %
After 189 h	29 %	31 %	2 %	12 %	5 %	83 %	47 %

[a] Conversions/yields are given with respect to 0.1 mmol silicon/triflate and were determined by ¹H NMR (integration vs. 1,2,4,5-tetramethylbenzene as internal standard).

7.3.3.11 Catalytic Run with 2 eq 2,6-Lutidine

A catalytic run with 2,6-lutidine (26 μL, 0.22 mmol, 2.2 eq with respect to silicon/triflate), was analyzed by NMR spectroscopy after 94 h and 189 h (see section 7.3.2.3; Me₂SiCl₂ (6 μL, 0.05 mmol), Me₂SiOTf₂ (11.1 μL, 0.05 mmol), **82** (5 μmol, 5 mol-%), H₂ (4 bar), C₆D₆ (0.5 mL).

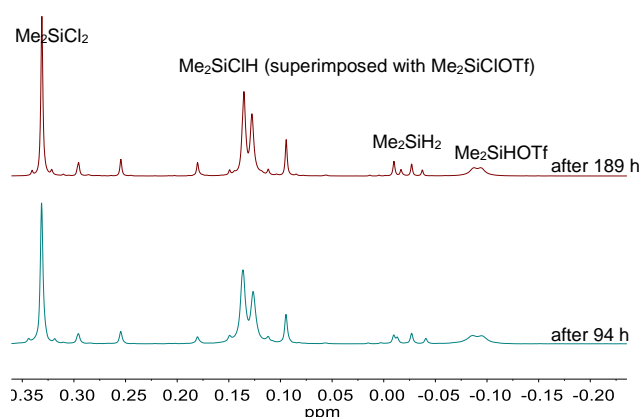


Figure 7.16 Stacked excerpts of ¹H NMR spectra in C₆D₆ after 94 h and 189 h (assignments were confirmed by ¹H-²⁹Si HMBC).

Table 7.2 Yields of dimethylsilyl species relative to internal standard derived from Figure 7.16.^[a]

	Me ₂ SiCl ₂	Me ₂ SiClH	Me ₂ SiH ₂	Me ₂ SiHOTf	Me ₂ SiClOTf	Conv. ^[a]	Combined Yield in Si-H bonds
After 94 h	26 %	32 %	4 %	8 %	4 %	88 %	48 %
After 189 h	25 %	32 %	4 %	8 %	4 %	88 %	48 %

[a] Conversions/yields are given with respect to 0.1 mmol silicon/triflate and were determined by ¹H NMR (integration vs. 1,2,4,5-tetramethylbenzene as internal standard).

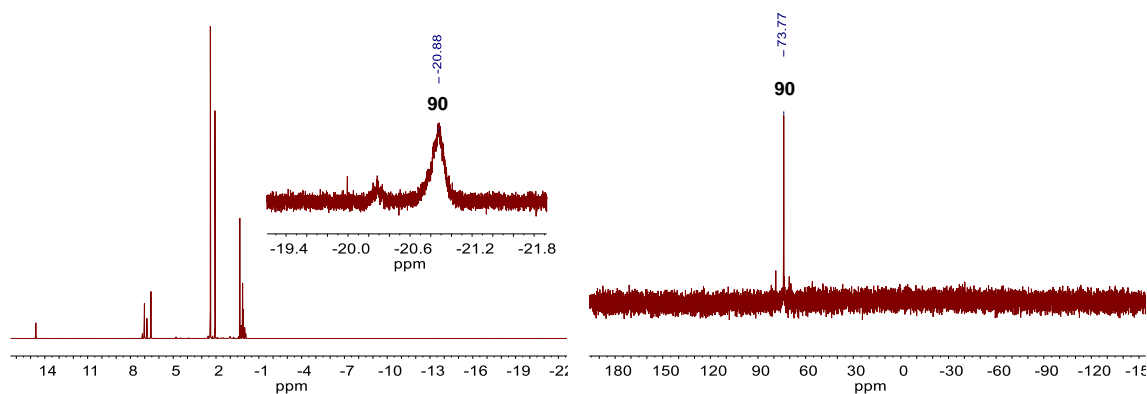


Figure 7.17 ¹H (left) and ³¹P{¹H} NMR (right) spectra of the mixture in C₆D₆ after 189 h.

7.3.3.11.1 Catalytic Run with 10 eq 2,6-Lutidine

A catalytic run was monitored by ^1H , $^1\text{H}\{^{31}\text{P}\}$ and $^{31}\text{P}\{^1\text{H}\}$ NMR and ^1H - ^{29}Si HMBC (see section 7.3.2.3; 2,6-lutidine (120 μL , 1.0 mmol), Me_2SiCl_2 (30 μL , 0.25 mmol), $\text{Me}_2\text{SiOTf}_2$ (11.1 μL , 0.05 mmol), **82** (1 μmol), H_2 (4 bar), C_6D_6 (0.4 mL)).

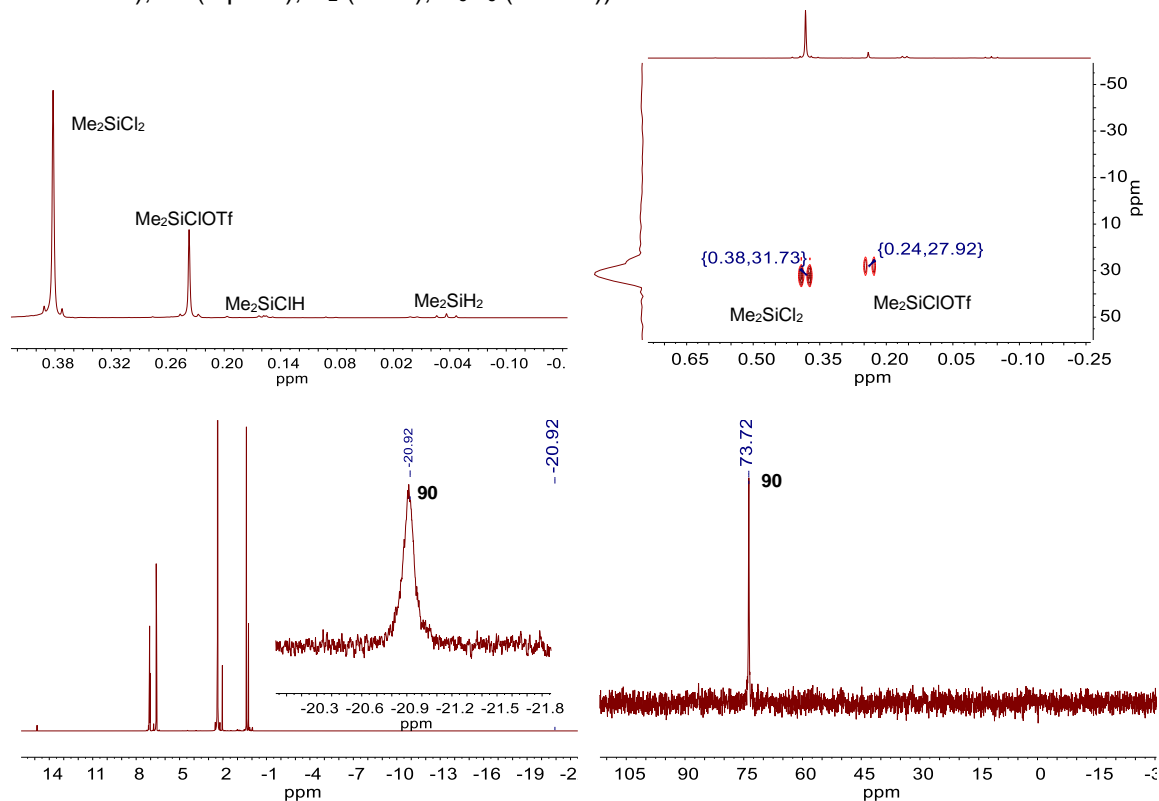


Figure 7.18 Top: ^1H NMR (left) and ^1H - ^{29}Si HMBC spectrum (right) in the initial phase of catalysis. Bottom: $^1\text{H}\{^{31}\text{P}\}$ (left) and $^{31}\text{P}\{^1\text{H}\}$ NMR spectrum (right).

7.3.3.11.2 Monitoring of a Catalytic Run with Excess Me_2SiCl_2

A catalytic run was monitored by ^1H NMR (Figure 5.6) (see section 7.3.2.3; 120 μL 2,6-lutidine, 0.25 mmol Me_2SiCl_2 , 0.05 mmol $\text{Me}_2\text{SiOTf}_2$, 1 μmol **82**, H_2 (4 bar), C_6D_6 (0.4 mL)).

7.3.3.12 Attempted Hydrogenolysis of $\text{Me}_3\text{SiOSO}_2\text{Me}$

$\text{Me}_3\text{SiOSO}_2\text{Me}$ (16.8 mg, 0.0998 mmol, 1 eq), NEt_3 (15 μL , 11 mg, 0.011 mmol, 1.1 eq) and a solution of **82** (1 μmol) in C_6D_6 (2.0 mmol/L, 0.5 mL) were mixed in a Young NMR tube. The NMR tube was frozen in N_2 (l) in a way that only the Teflon sealing remained at room temperature and evacuated. H_2 (1.2 bar) was introduced, the tube closed, warmed to room temperature and shaken. Thus, the pressure in the tube is ≈ 4 bar according to ideal gas law.

7 Experimental Part

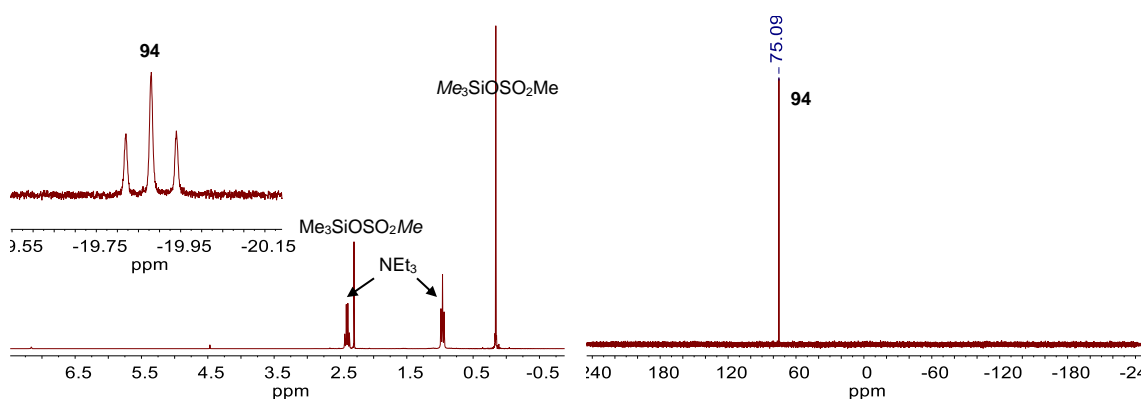


Figure 7.19 ^1H (left) and $^{31}\text{P}\{^1\text{H}\}$ (right) NMR of the mixture after 1d.

7.3.3.13 Comproportionation equilibrium of Me_2SiCl_2 and $\text{Me}_2\text{SiOTf}_2$ to $\text{Me}_2\text{SiClOTf}$

7.3.3.13.1 Uncatalyzed Comproportionation

$\text{Me}_2\text{SiOTf}_2$ (10 μL , 0.044 mmol, 1.0 eq) was dissolved in C_6D_6 (0.5 mL) in a Young NMR tube. Me_2SiCl_2 (5.4 μL , 0.044 mmol, 1.0 eq) was added and shaken. The mixture was daily analyzed by ^1H NMR (Table 7.3).

Table 7.3 Relative ratios of chlorosilanes and silyl triflates after Cl/OTf dismutation.

Reaction time (h)	Me_2SiCl_2 / $\text{Me}_2\text{SiClOTf}$ / $\text{Me}_2\text{SiOTf}_2$
28	30 : 41 : 28
43	24 : 54 : 22
63.5	19 : 63 : 18
95	17 : 67 : 16
116.5	17 : 67 : 16

7.3.3.13.2 Comproportionation Catalyzed by **82**

$\text{Me}_2\text{SiOTf}_2$ (11 μL , 0.048 mmol, 1.0 eq) was dissolved in C_6D_6 (0.5 mL) in a Young NMR tube. Me_2SiCl_2 (6.0 μL , 0.049 mmol, 1.0 eq) and **82** (0.4 mg, 0.0009 mmol, 0.002 eq) were added and shaken for 35 min. ^1H NMR indicated a distribution of Me_2SiCl_2 / $\text{Me}_2\text{SiClOTf}$ / $\text{Me}_2\text{SiOTf}_2$ = 21:55:24, i.e. equilibrium (67 % $\text{Me}_2\text{SiClOTf}$) was nearly established. ^1H and ^{31}P NMR after 11 h indicated quantitative conversion of **82** to **90**.

7.3.3.13.3 Comproportionation Catalyzed by NEt_3

$\text{Me}_2\text{SiOTf}_2$ (10 μL , 0.044 mmol, 1.0 eq) was dissolved in C_6D_6 (0.5 mL) in a Young NMR tube. Me_2SiCl_2 (5.4 μL , 0.044 mmol, 1.0 eq) and NEt_3 (14 μL , 0.12 mmol, 2.6 eq) was added and shaken for 40 min. ^1H NMR indicated a distribution of Me_2SiCl_2 / $\text{Me}_2\text{SiClOTf}$ / $\text{Me}_2\text{SiOTf}_2$ = 18:64:18, i.e. equilibrium (67 % $\text{Me}_2\text{SiClOTf}$) was nearly established.

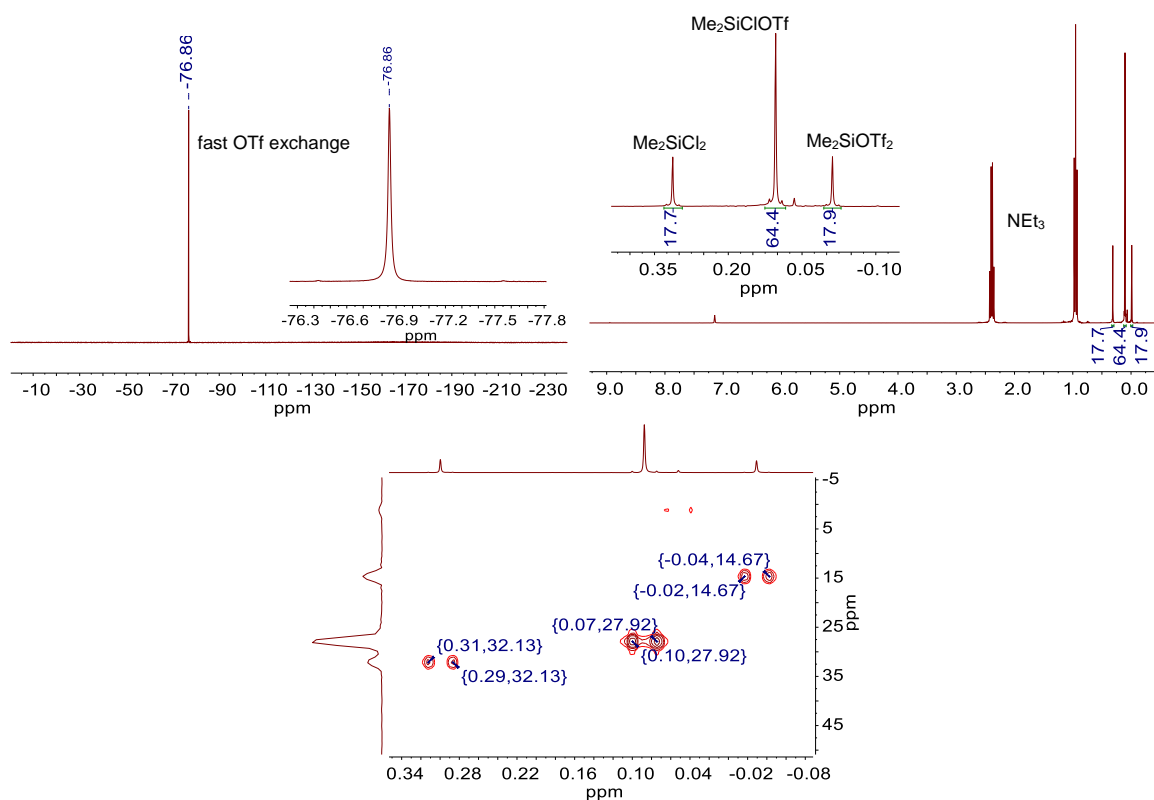


Figure 7.20 Top: ^{19}F NMR (left) and ^1H NMR spectrum (right) of the mixture. Bottom: Corresponding ^1H - ^{29}Si HMBC spectrum.

7.3.3.13.4 Comproportionation Catalyzed by 2,6-Lutidine

$\text{Me}_2\text{SiOTf}_2$ (11.1 μL , 0.049 mmol, 1.0 eq) was dissolved in C_6D_6 (0.5 mL) in a Young NMR tube. Me_2SiCl_2 (6.0 μL , 0.049 mmol, 1.0 eq) and 2,6-lutidine (6.0 μL mg, 0.052 mmol, 1.1 eq) were added and shaken. ^1H NMR spectra after 40 min and 1.5 h indicated a distribution of Me_2SiCl_2 / $\text{Me}_2\text{SiClOTf}$ / $\text{Me}_2\text{SiOTf}_2$ = 22:58:20 and 18:67:15, respectively. Heating the sample to 65 $^\circ\text{C}$ for 40 min in the NMR machine shifted all signals to lower field but only slightly changed the equilibrium distribution to 19:65:16. The ^{19}F NMR collapsed into a singlet.

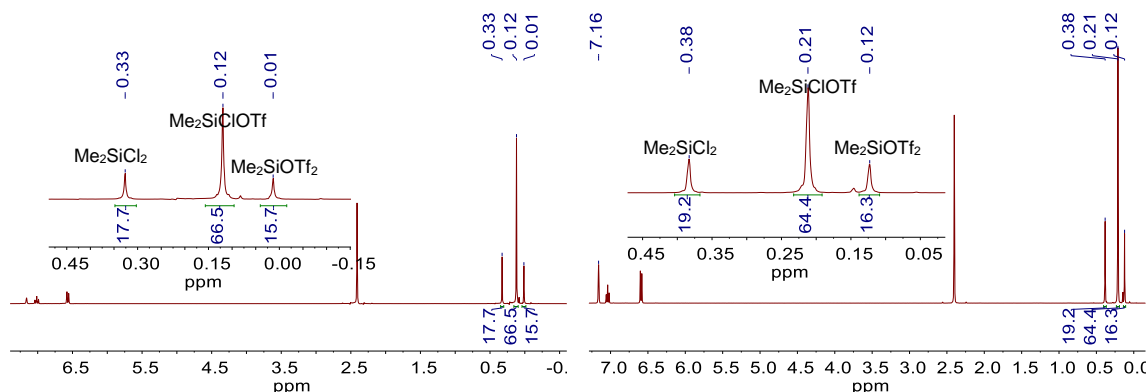


Figure 7.21 ^1H NMR spectra of the mixture after 1.5 h at r.t. (left) and at 65 $^\circ\text{C}$ (right).

7.3.3.13.5 Shifting the Equilibrium with Excess Me_2SiCl_2

1,2,4,5-Tetramethylbenzene (2.1 mg, 0.016 mmol, 3.1 eq) as internal standard and $\text{Me}_2\text{SiOTf}_2$

7 Experimental Part

(11 μL , 0.049 mmol, 1.0 eq) were added to a Young NMR tube and dissolved in a stock solution (0.50 mL) of **82** (2.0 mmol/L, 0.99 μmol , 0.02 eq) in C_6D_6 . Me_2SiCl_2 (30 μL , 0.25 mmol, 5.1 eq) was added, the mixture was left for isomerization (1.5 h) and analyzed by ^1H NMR and $^{31}\text{P}\{^1\text{H}\}$ NMR spectroscopy (Figure 7.22).

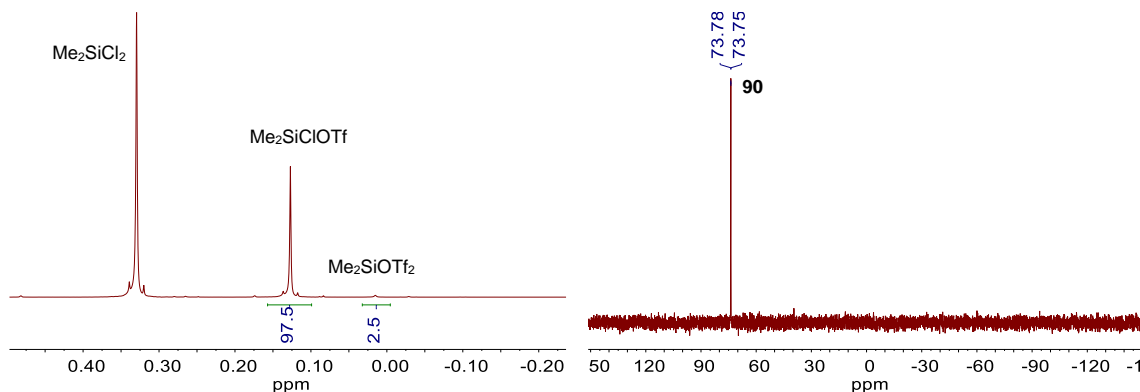


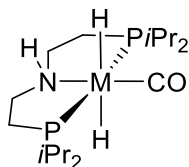
Figure 7.22 ^1H NMR (left) and $^{31}\text{P}\{^1\text{H}\}$ NMR (right) spectrum of the mixture in C_6D_6 after 1.5 h (spectra did not change after additional 15 min).

7.3.3.14 Reaction of Lutidinium Triflate with Me_2SiClH to Silyl Triflates and H_2

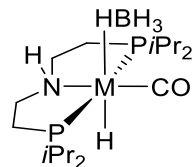
Lutidinium triflate (30.9 mg, 0.12 mmol, 1.2 eq) and **82** (0.4 mg, 0.9 μmol , 0.8 eq) were suspended in C_6D_6 in a Young NMR tube. Me_2SiClH was added and the two-phasic mixture was heated to $60\text{ }^\circ\text{C}$ for 7 d (Figure 5.5).

8 Structures

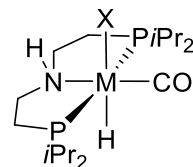
8.1 Structures of Complexes



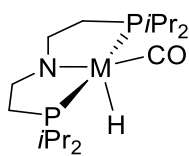
1



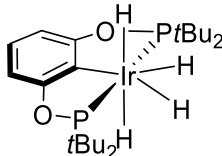
2



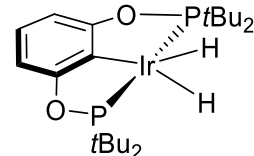
3



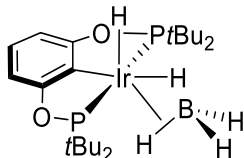
4



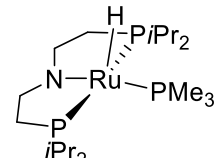
5



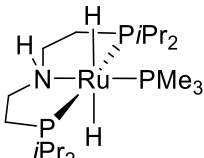
6



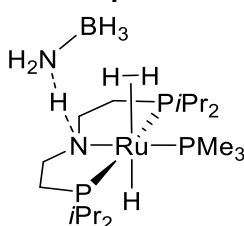
7



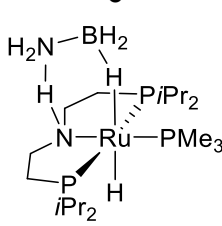
8



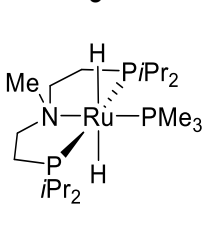
9



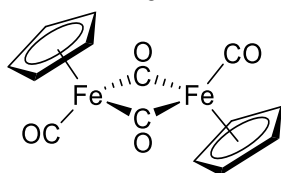
10



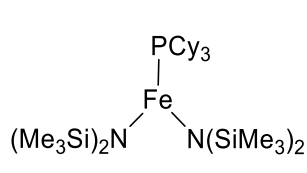
11



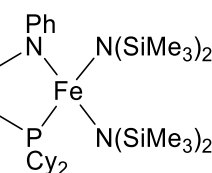
12



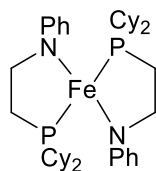
13



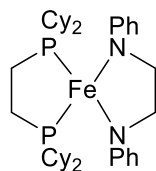
14



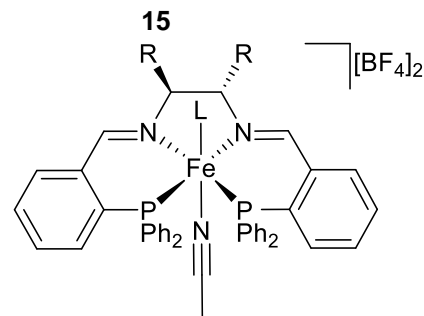
15



16



17



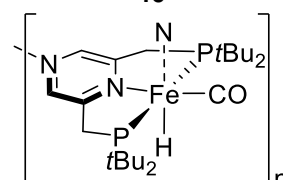
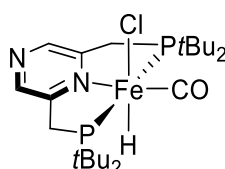
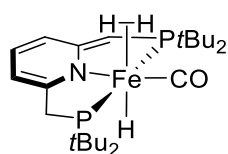
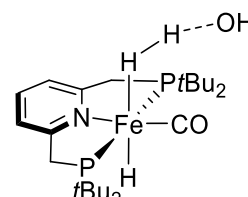
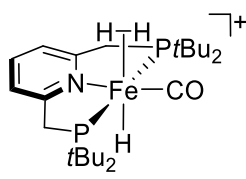
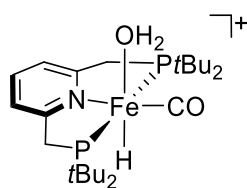
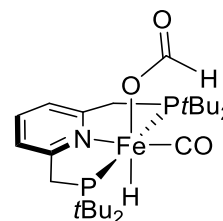
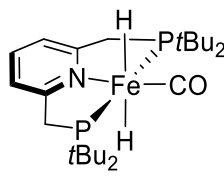
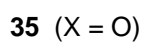
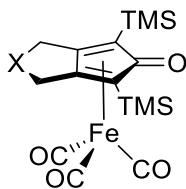
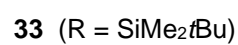
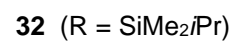
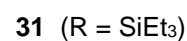
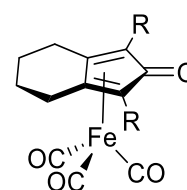
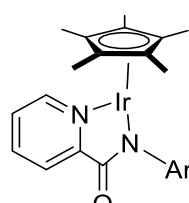
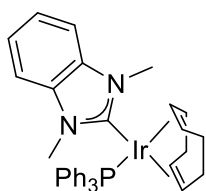
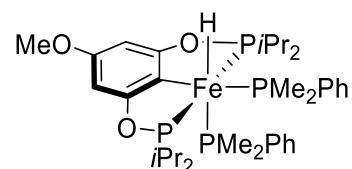
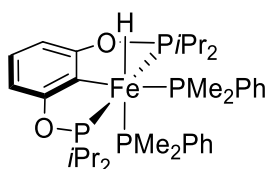
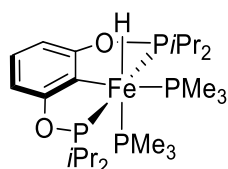
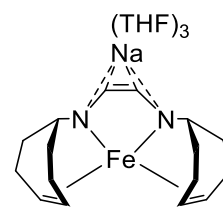
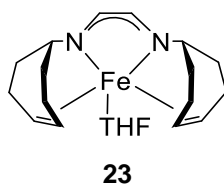
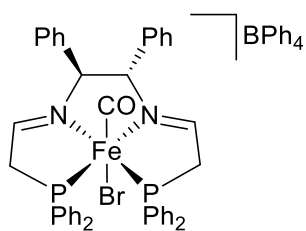
18 (L = MeCN, R = H)

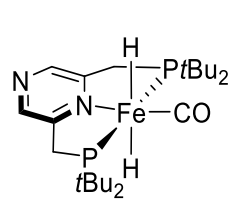
19 (L = CO, R = H)

20 (L = MeCN, R = Ph)

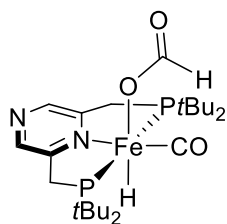
21 (L = CO, R = Ph)

8 Structures

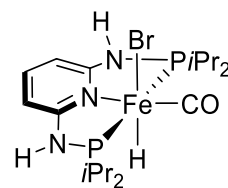




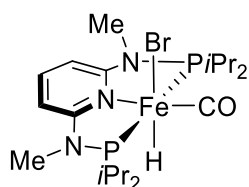
44



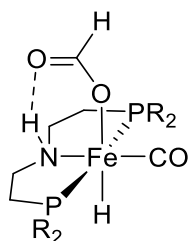
45



46



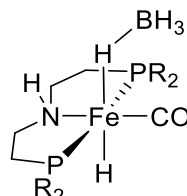
47



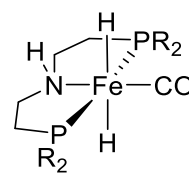
48 (R = Me)

49 (R = *i*Pr)

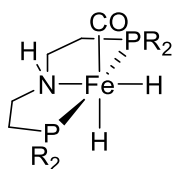
50 (R = Cy)

51 (R = *i*Pr)

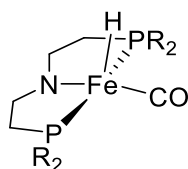
52 (R = Cy)

53a (R = *i*Pr)

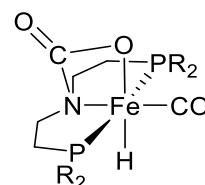
54a (R = Cy)

53b (R = *i*Pr)

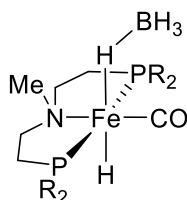
54b (R = Cy)

55 (R = *i*Pr)

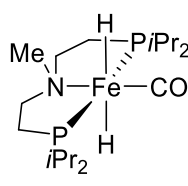
56 (R = Cy)

57 (R = *i*Pr)

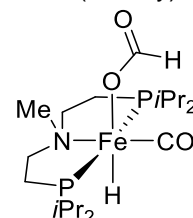
58 (R = Cy)



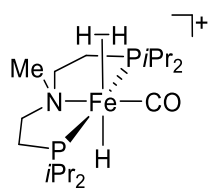
59



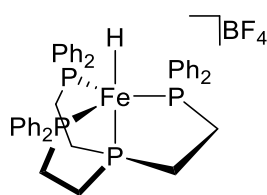
60



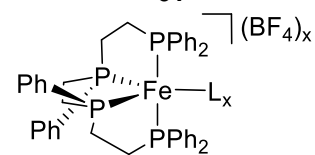
61



62



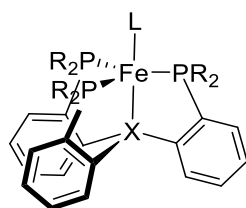
63

64 (L = F-BF₃, x = 1)

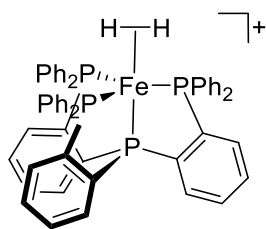
65 (L = NCMe, x = 2)

66 (L = Cl, X = Si, R = *i*Pr)

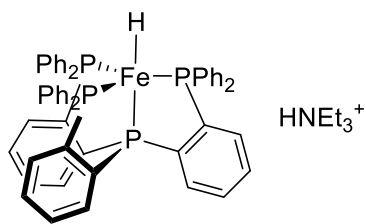
67 (L = Cl, X = Si, R = Ph)

68 (L = Cl, X = BPh, R = *i*Pr)69 (L = Cl, X = C, R = *i*Pr)70 (L = OCHO, X = Si, R = *i*Pr)71 (L = N₂, X = Si, R = *i*Pr, counterion: BAr^F₄)72 (L = F, X = Si, R = Ph, counterion: BF₄)

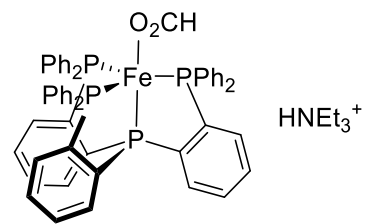
8 Structures



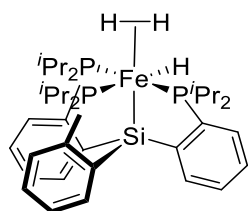
73



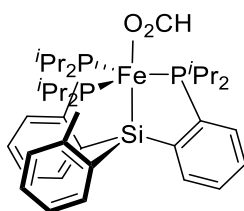
74



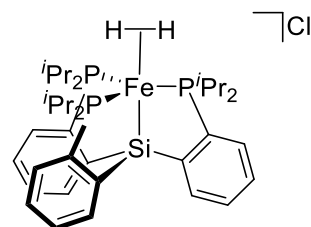
75



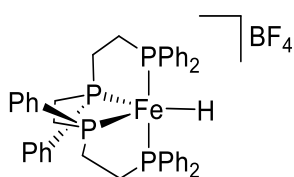
76



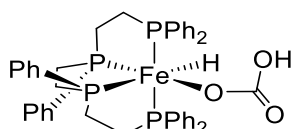
77



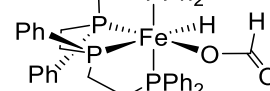
78



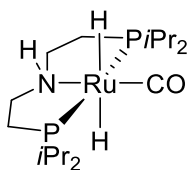
79



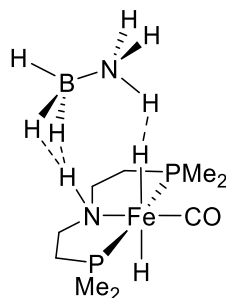
80



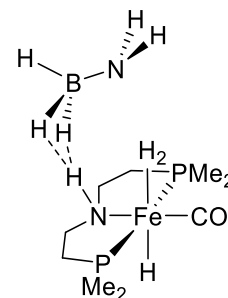
81



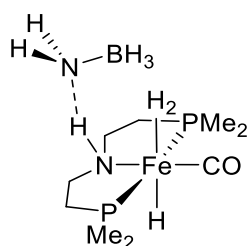
82



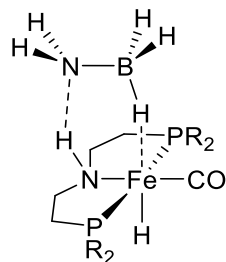
83^{Me}



84^{Me}

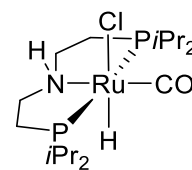


85^{Me}

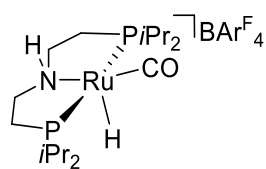


86^{Me} (R = Me)

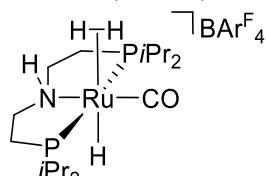
86 (R = *i*Pr)



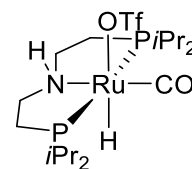
87



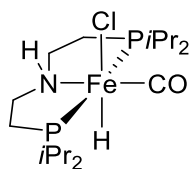
88



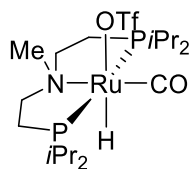
89



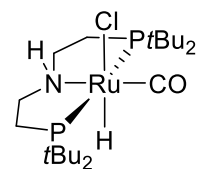
90



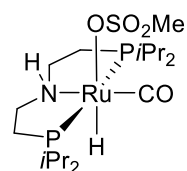
91



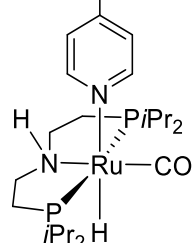
92



93

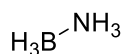
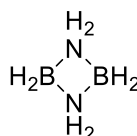
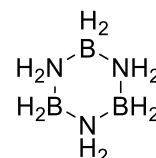
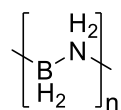
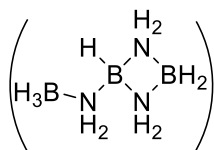
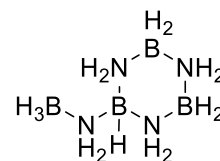
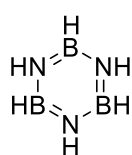
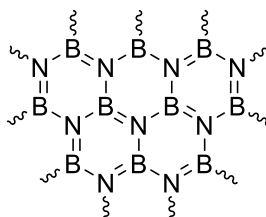
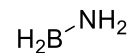


94

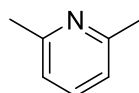
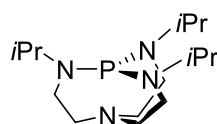
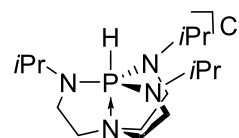


95

8.2 Structures other Compounds

ammonia borane
(AB)cyclodiaminoborane
(CDB)cyclotriaminoborane
(CTB)polyaminoborane
(PAB)B-(cyclodiborazanyl)amine-
borane (BCDB)B-(cyclotriborazanyl)amine-
borane (BCTB)borazine
(BZ)polyborazylene
(PBZ)

aminoborane

2,6-lutidine
(lut)2,8,9-Triisopropyl-2,5,8,9-
tetraaza-1-phosphabicyclo
[3,3,3]undecane (VB^{iPr})[H-VB^{iPr}]Cl

9 Appendix – Crystal Structures

Results of this chapter have been published recently (A. Glüer, J. I. Schweizer, U. S. Karaca, C. Würtele, M. Diefenbach, M. C. Holthausen, S. Schneider, *Inorg. Chem.* **2018**, *57*, 13822) and parts of this work have been adapted from this publication with permission from ACS.^[74] Copyright 2018 American Chemical Society.

9.1 Single-Crystal Structure Analysis of (HPNP^{Pr})RuH(OTf)CO (90)

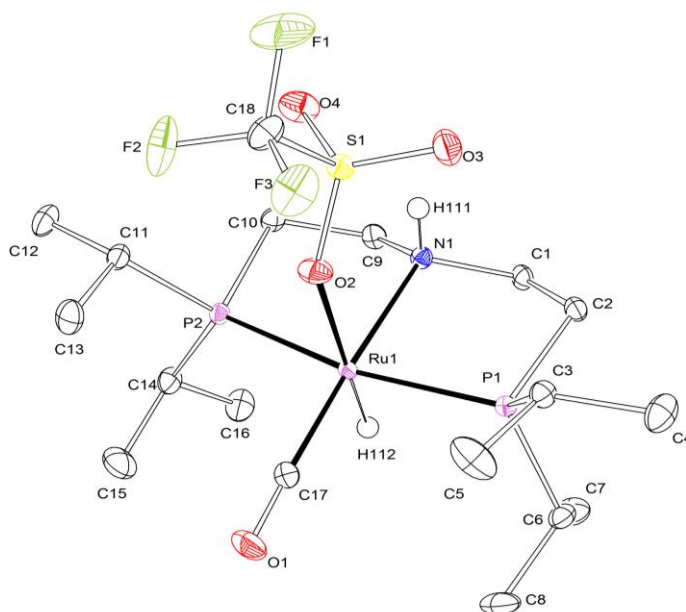


Figure 9.1 Thermal ellipsoid plot of (HPNP^{Pr})RuH(OTf)CO (**90**) with the anisotropic displacement parameters drawn at the 50% probability level. The asymmetric unit contains one complex molecule. The N-H and Ru-H hydrogen atoms were found from the residual density map and isotropically refined.

Table 9.1 Crystal data and structure refinement for (HPNP^{Pr})RuH(OTf)CO (**90**).

Identification code	mo_CW_AG_061017_0m_a (AG387-1a)	
Empirical formula	C ₁₈ H ₃₈ F ₃ NO ₄ P ₂ RuS	
Formula weight	584.56	
Temperature	105(2) K	
Wavelength	0.71073 Å	
Crystal system	Monoclinic	
Space group	P2 ₁ /c	
Unit cell dimensions	a = 10.3328(13) Å	α = 90°
	b = 14.992(2) Å	β = 92.901(6)°
	c = 16.370(3) Å	γ = 90°
Volume	2532.6(7) Å ³	
Z	4	
Density (calculated)	1.533 Mg/m ³	

9 Appendix – Crystal Structures

Absorption coefficient	0.873 mm ⁻¹	
F(000)	1208	
Crystal size	0.499 x 0.322 x 0.266 mm ³	
Crystal shape and color	Block,	clear colourless
Theta range for data collection	2.396 to 30.663°	
Index ranges	-14<=h<=14, -21<=k<=21, -22<=l<=23	
Reflections collected	119725	
Independent reflections	7828 [R(int) = 0.0722]	
Completeness to theta = 25.242°	100.0 %	
Refinement method	Full-matrix least-squares on F ²	
Data / restraints / parameters	7828 / 0 / 287	
Goodness-of-fit on F ²	1.068	
Final R indices [I>2sigma(I)]	R1 = 0.0250,	wR2 = 0.0513
R indices (all data)	R1 = 0.0374,	wR2 = 0.0554
Largest diff. peak and hole	0.537 and -0.665 eÅ ⁻³	

Table 9.2 Bond lengths [Å] and angles [°] for (HPNP^{Pt})RuH(OTf)CO (**90**).

Ru(1)-C(17)	1.8320(16)
Ru(1)-N(1)	2.1969(13)
Ru(1)-O(2)	2.2957(11)
Ru(1)-P(1)	2.3195(4)
Ru(1)-P(2)	2.3276(5)
Ru(1)-H(112)	1.52(2)
S(1)-O(4)	1.4365(12)
S(1)-O(3)	1.4365(12)
S(1)-O(2)	1.4534(11)
S(1)-C(18)	1.8214(17)
P(1)-C(2)	1.8446(15)
P(1)-C(6)	1.8451(15)
P(1)-C(3)	1.8471(15)
P(2)-C(14)	1.8428(16)
P(2)-C(11)	1.8436(15)
P(2)-C(10)	1.8444(15)
F(1)-C(18)	1.329(2)
F(2)-C(18)	1.320(2)
F(3)-C(18)	1.3197(19)
O(1)-C(17)	1.1539(19)
N(1)-C(9)	1.4861(19)
N(1)-C(1)	1.4899(18)
N(1)-H(111)	0.88(2)
C(1)-C(2)	1.518(2)
C(3)-C(5)	1.522(2)
C(3)-C(4)	1.527(2)
C(6)-C(7)	1.524(2)
C(6)-C(8)	1.527(2)
C(9)-C(10)	1.519(2)
C(11)-C(12)	1.527(2)
C(11)-C(13)	1.530(2)
C(14)-C(15)	1.525(2)
C(14)-C(16)	1.527(2)
C(17)-Ru(1)-N(1)	175.11(6)
C(17)-Ru(1)-O(2)	94.02(6)
N(1)-Ru(1)-O(2)	90.82(4)
C(17)-Ru(1)-P(1)	96.25(5)

9 Appendix – Crystal Structures

N(1)-Ru(1)-P(1)	82.88(3)
O(2)-Ru(1)-P(1)	92.13(3)
C(17)-Ru(1)-P(2)	97.63(5)
N(1)-Ru(1)-P(2)	82.79(3)
O(2)-Ru(1)-P(2)	92.79(3)
P(1)-Ru(1)-P(2)	164.903(14)
C(17)-Ru(1)-H(112)	87.6(8)
N(1)-Ru(1)-H(112)	87.6(7)
O(2)-Ru(1)-H(112)	178.3(8)
P(1)-Ru(1)-H(112)	88.3(8)
P(2)-Ru(1)-H(112)	86.3(8)
O(4)-S(1)-O(3)	115.41(8)
O(4)-S(1)-O(2)	114.24(7)
O(3)-S(1)-O(2)	114.27(7)
O(4)-S(1)-C(18)	104.97(8)
O(3)-S(1)-C(18)	104.63(8)
O(2)-S(1)-C(18)	101.19(7)
C(2)-P(1)-C(6)	106.20(7)
C(2)-P(1)-C(3)	101.35(7)
C(6)-P(1)-C(3)	107.02(7)
C(2)-P(1)-Ru(1)	102.30(5)
C(6)-P(1)-Ru(1)	119.02(5)
C(3)-P(1)-Ru(1)	118.54(5)
C(14)-P(2)-C(11)	106.62(7)
C(14)-P(2)-C(10)	104.37(7)
C(11)-P(2)-C(10)	101.85(7)
C(14)-P(2)-Ru(1)	121.01(5)
C(11)-P(2)-Ru(1)	118.02(5)
C(10)-P(2)-Ru(1)	102.08(5)
S(1)-O(2)-Ru(1)	130.60(7)
C(9)-N(1)-C(1)	110.41(11)
C(9)-N(1)-Ru(1)	112.11(9)
C(1)-N(1)-Ru(1)	112.95(9)
C(9)-N(1)-H(111)	106.8(13)
C(1)-N(1)-H(111)	107.9(13)
Ru(1)-N(1)-H(111)	106.3(13)
N(1)-C(1)-C(2)	110.44(12)
C(1)-C(2)-P(1)	109.81(10)

C(5)-C(3)-C(4)	111.54(14)
C(5)-C(3)-P(1)	113.19(11)
C(4)-C(3)-P(1)	113.48(11)
C(7)-C(6)-C(8)	109.56(13)
C(7)-C(6)-P(1)	112.54(11)
C(8)-C(6)-P(1)	110.22(11)
N(1)-C(9)-C(10)	110.38(12)
C(9)-C(10)-P(2)	109.51(10)
C(12)-C(11)-C(13)	111.67(13)
C(12)-C(11)-P(2)	114.11(11)
C(13)-C(11)-P(2)	113.33(11)
C(15)-C(14)-C(16)	110.60(14)
C(15)-C(14)-P(2)	111.43(12)
C(16)-C(14)-P(2)	111.89(11)
O(1)-C(17)-Ru(1)	177.89(15)
F(3)-C(18)-F(2)	107.95(15)
F(3)-C(18)-F(1)	107.67(14)
F(2)-C(18)-F(1)	108.31(14)
F(3)-C(18)-S(1)	111.36(11)
F(2)-C(18)-S(1)	111.41(12)
F(1)-C(18)-S(1)	110.01(12)

9 Appendix – Crystal Structures

Table 9.3 Torsion angles [°] for (*HPNP*^{Pr})RuH(OTf)CO (**90**).

O(4)-S(1)-O(2)-Ru(1)	59.27(11)
O(3)-S(1)-O(2)-Ru(1)	-76.72(11)
C(18)-S(1)-O(2)-Ru(1)	171.47(9)
C(9)-N(1)-C(1)-C(2)	-175.29(12)
Ru(1)-N(1)-C(1)-C(2)	-48.87(14)
N(1)-C(1)-C(2)-P(1)	50.03(14)
C(6)-P(1)-C(2)-C(1)	97.53(11)
C(3)-P(1)-C(2)-C(1)	-150.81(10)
Ru(1)-P(1)-C(2)-C(1)	-27.96(11)
C(2)-P(1)-C(3)-C(5)	167.48(13)
C(6)-P(1)-C(3)-C(5)	-81.47(14)
Ru(1)-P(1)-C(3)-C(5)	56.60(14)
C(2)-P(1)-C(3)-C(4)	-64.08(13)
C(6)-P(1)-C(3)-C(4)	46.96(13)
Ru(1)-P(1)-C(3)-C(4)	-174.96(10)
C(2)-P(1)-C(6)-C(7)	-49.55(13)
C(3)-P(1)-C(6)-C(7)	-157.21(11)
Ru(1)-P(1)-C(6)-C(7)	64.96(13)
C(2)-P(1)-C(6)-C(8)	-172.18(11)
C(3)-P(1)-C(6)-C(8)	80.17(12)
Ru(1)-P(1)-C(6)-C(8)	-57.66(13)
C(1)-N(1)-C(9)-C(10)	178.11(12)
Ru(1)-N(1)-C(9)-C(10)	51.23(14)
N(1)-C(9)-C(10)-P(2)	-51.18(14)
C(14)-P(2)-C(10)-C(9)	-99.58(11)
C(11)-P(2)-C(10)-C(9)	149.60(11)
Ru(1)-P(2)-C(10)-C(9)	27.21(11)
C(14)-P(2)-C(11)-C(12)	-42.96(13)
C(10)-P(2)-C(11)-C(12)	66.14(13)
Ru(1)-P(2)-C(11)-C(12)	176.87(9)
C(14)-P(2)-C(11)-C(13)	86.36(12)
C(10)-P(2)-C(11)-C(13)	-164.54(11)
Ru(1)-P(2)-C(11)-C(13)	-53.81(12)
C(11)-P(2)-C(14)-C(15)	-71.59(13)
C(10)-P(2)-C(14)-C(15)	-178.91(11)
Ru(1)-P(2)-C(14)-C(15)	67.13(13)
C(11)-P(2)-C(14)-C(16)	164.01(11)

9 Appendix – Crystal Structures

C(10)-P(2)-C(14)-C(16)	56.69(13)
Ru(1)-P(2)-C(14)-C(16)	-57.27(13)
O(4)-S(1)-C(18)-F(3)	177.78(12)
O(3)-S(1)-C(18)-F(3)	-60.30(14)
O(2)-S(1)-C(18)-F(3)	58.69(14)
O(4)-S(1)-C(18)-F(2)	57.20(14)
O(3)-S(1)-C(18)-F(2)	179.12(12)
O(2)-S(1)-C(18)-F(2)	-61.88(13)
O(4)-S(1)-C(18)-F(1)	-62.93(13)
O(3)-S(1)-C(18)-F(1)	59.00(13)
O(2)-S(1)-C(18)-F(1)	177.99(12)

9 Appendix – Crystal Structures

Table 9.4 Hydrogen bonds for (*HPNP*^{Pr})RuH(OTf)CO (**90**) [Å and °].

D-H...A	d(D-H)	d(H...A)	d(D...A)	<(DHA)
N(1)-H(111)...O(3)	0.88(2)	2.96(2)	3.6697(18)	138.7(16)
N(1)-H(111)...O(4)	0.88(2)	2.62(2)	3.3664(18)	143.4(16)

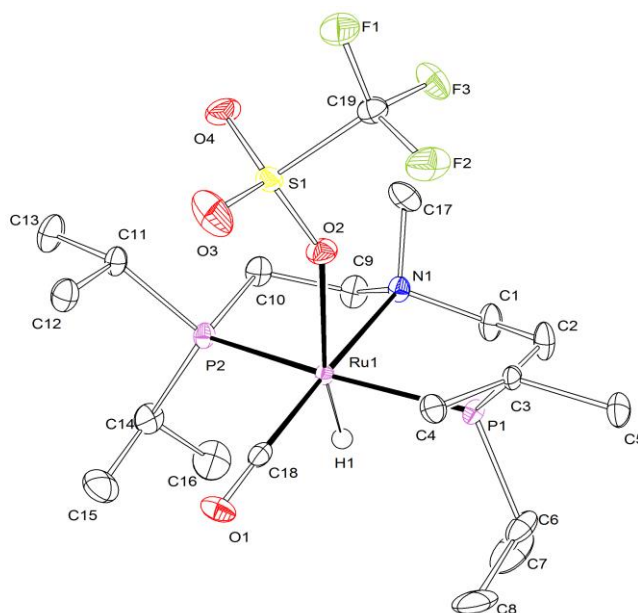
9.2 Single-Crystal Structure Analysis of (*MePNP^{Pr}*)RuH(OTf)CO (**92**)

Figure 9.2 Thermal ellipsoid plot of (*MePNP^{Pr}*)RuH(OTf)CO (**92**) with the anisotropic displacement parameters drawn at the 50% probability level. The asymmetric unit contains one complex molecule. The Ru-H hydrogen atom was found from the residual density map and isotropically refined.

Table 9.5 Crystal data and structure refinement for (*MePNP^{Pr}*)RuH(OTf)CO (**92**).

Identification code	mo_CV_AG_171017_0m_a (AG403-1a)	
Empirical formula	C ₁₉ H ₄₀ F ₃ NO ₄ P ₂ RuS	
Formula weight	598.59	
Temperature	101(2) K	
Wavelength	0.71073 Å	
Crystal system	Monoclinic	
Space group	P2 ₁ /n	
Unit cell dimensions	a = 8.2824(5) Å	α = 90°
	b = 25.0810(14) Å	β = 99.556(3)°
	c = 13.0543(8) Å	γ = 90°
Volume	2674.2(3) Å ³	
Z	4	
Density (calculated)	1.487 Mg/m ³	
Absorption coefficient	0.829 mm ⁻¹	
F(000)	1240	
Crystal size	0.324 x 0.213 x 0.110 mm ³	
Crystal shape and color	Plate, clear colourless-yellow	
Theta range for data collection	2.267 to 28.352°	
Index ranges	-11 ≤ h ≤ 11, -33 ≤ k ≤ 33, -17 ≤ l ≤ 17	

9 Appendix – Crystal Structures

Reflections collected	91419	
Independent reflections	6669 [R(int) = 0.1682]	
Completeness to theta = 25.242°	100.0 %	
Refinement method	Full-matrix least-squares on F ²	
Data / restraints / parameters	6669 / 0 / 293	
Goodness-of-fit on F ²	1.008	
Final R indices [I>2sigma(I)]	R1 = 0.0396,	wR2 = 0.0587
R indices (all data)	R1 = 0.0780,	wR2 = 0.0667
Largest diff. peak and hole	0.509 and -0.480 eÅ ⁻³	

Table 9.6 Bond lengths [Å] and angles [°] for (MePNP^{Pr})RuH(OTf)CO (**92**).

C(1)-N(1)	1.489(3)
C(1)-C(2)	1.530(4)
C(2)-P(1)	1.842(3)
C(3)-C(5)	1.528(4)
C(3)-C(4)	1.532(3)
C(3)-P(1)	1.846(3)
C(6)-C(8)	1.530(4)
C(6)-C(7)	1.531(4)
C(6)-P(1)	1.844(3)
C(9)-N(1)	1.494(3)
C(9)-C(10)	1.523(4)
C(10)-P(2)	1.844(3)
C(11)-C(13)	1.527(4)
C(11)-C(12)	1.528(4)
C(11)-P(2)	1.844(3)
C(14)-C(15)	1.526(4)
C(14)-C(16)	1.528(4)
C(14)-P(2)	1.852(3)
C(17)-N(1)	1.488(3)
C(18)-O(1)	1.158(3)
C(18)-Ru(1)	1.831(3)
C(19)-F(2)	1.327(3)
C(19)-F(1)	1.332(3)
C(19)-F(3)	1.333(3)
C(19)-S(1)	1.837(3)
N(1)-Ru(1)	2.222(2)
O(2)-S(1)	1.4507(19)
O(2)-Ru(1)	2.3337(18)
O(3)-S(1)	1.430(2)
O(4)-S(1)	1.430(2)
P(1)-Ru(1)	2.3203(7)
P(2)-Ru(1)	2.3264(7)
Ru(1)-H(1)	1.42(3)
N(1)-C(1)-C(2)	112.6(2)
C(1)-C(2)-P(1)	109.62(19)
C(5)-C(3)-C(4)	112.4(2)

9 Appendix – Crystal Structures

C(5)-C(3)-P(1)	114.59(18)
C(4)-C(3)-P(1)	110.78(17)
C(8)-C(6)-C(7)	110.2(3)
C(8)-C(6)-P(1)	111.9(2)
C(7)-C(6)-P(1)	111.6(2)
N(1)-C(9)-C(10)	112.1(2)
C(9)-C(10)-P(2)	109.62(19)
C(13)-C(11)-C(12)	111.6(2)
C(13)-C(11)-P(2)	114.8(2)
C(12)-C(11)-P(2)	112.8(2)
C(15)-C(14)-C(16)	110.1(3)
C(15)-C(14)-P(2)	112.0(2)
C(16)-C(14)-P(2)	111.7(2)
O(1)-C(18)-Ru(1)	179.0(2)
F(2)-C(19)-F(1)	107.8(2)
F(2)-C(19)-F(3)	107.3(2)
F(1)-C(19)-F(3)	107.4(2)
F(2)-C(19)-S(1)	111.60(19)
F(1)-C(19)-S(1)	111.09(19)
F(3)-C(19)-S(1)	111.45(19)
C(17)-N(1)-C(1)	108.6(2)
C(17)-N(1)-C(9)	107.9(2)
C(1)-N(1)-C(9)	107.4(2)
C(17)-N(1)-Ru(1)	112.75(16)
C(1)-N(1)-Ru(1)	110.18(16)
C(9)-N(1)-Ru(1)	109.81(16)
S(1)-O(2)-Ru(1)	151.53(12)
C(2)-P(1)-C(6)	103.98(14)
C(2)-P(1)-C(3)	103.94(13)
C(6)-P(1)-C(3)	105.16(13)
C(2)-P(1)-Ru(1)	102.27(9)
C(6)-P(1)-Ru(1)	121.66(10)
C(3)-P(1)-Ru(1)	117.49(9)
C(11)-P(2)-C(10)	102.81(13)
C(11)-P(2)-C(14)	107.46(13)
C(10)-P(2)-C(14)	103.86(14)
C(11)-P(2)-Ru(1)	117.80(9)
C(10)-P(2)-Ru(1)	102.82(9)

C(14)-P(2)-Ru(1)	119.56(10)
C(18)-Ru(1)-N(1)	176.67(10)
C(18)-Ru(1)-P(1)	95.78(8)
N(1)-Ru(1)-P(1)	83.97(6)
C(18)-Ru(1)-P(2)	96.66(8)
N(1)-Ru(1)-P(2)	83.07(6)
P(1)-Ru(1)-P(2)	164.50(3)
C(18)-Ru(1)-O(2)	95.16(9)
N(1)-Ru(1)-O(2)	88.15(7)
P(1)-Ru(1)-O(2)	88.43(5)
P(2)-Ru(1)-O(2)	99.60(5)
C(18)-Ru(1)-H(1)	93.1(10)
N(1)-Ru(1)-H(1)	83.6(10)
P(1)-Ru(1)-H(1)	84.5(10)
P(2)-Ru(1)-H(1)	85.6(10)
O(2)-Ru(1)-H(1)	169.6(10)
O(3)-S(1)-O(4)	116.50(14)
O(3)-S(1)-O(2)	114.66(13)
O(4)-S(1)-O(2)	114.89(12)
O(3)-S(1)-C(19)	103.41(13)
O(4)-S(1)-C(19)	103.30(12)
O(2)-S(1)-C(19)	101.18(12)

9 Appendix – Crystal Structures

Table 9.7 Torsion angles [°] for (MePNP^{Pr})RuH(OTf)CO (**92**).

N(1)-C(1)-C(2)-P(1)	50.0(3)
N(1)-C(9)-C(10)-P(2)	-49.1(3)
C(2)-C(1)-N(1)-C(17)	74.7(3)
C(2)-C(1)-N(1)-C(9)	-168.9(2)
C(2)-C(1)-N(1)-Ru(1)	-49.3(3)
C(10)-C(9)-N(1)-C(17)	-70.9(3)
C(10)-C(9)-N(1)-C(1)	172.2(2)
C(10)-C(9)-N(1)-Ru(1)	52.4(3)
C(1)-C(2)-P(1)-C(6)	101.9(2)
C(1)-C(2)-P(1)-C(3)	-148.3(2)
C(1)-C(2)-P(1)-Ru(1)	-25.6(2)
C(8)-C(6)-P(1)-C(2)	175.6(2)
C(7)-C(6)-P(1)-C(2)	-60.3(3)
C(8)-C(6)-P(1)-C(3)	66.7(2)
C(7)-C(6)-P(1)-C(3)	-169.3(2)
C(8)-C(6)-P(1)-Ru(1)	-70.1(2)
C(7)-C(6)-P(1)-Ru(1)	53.9(3)
C(5)-C(3)-P(1)-C(2)	-70.2(2)
C(4)-C(3)-P(1)-C(2)	161.39(19)
C(5)-C(3)-P(1)-C(6)	38.8(2)
C(4)-C(3)-P(1)-C(6)	-89.6(2)
C(5)-C(3)-P(1)-Ru(1)	177.69(16)
C(4)-C(3)-P(1)-Ru(1)	49.3(2)
C(13)-C(11)-P(2)-C(10)	61.0(2)
C(12)-C(11)-P(2)-C(10)	-169.6(2)
C(13)-C(11)-P(2)-C(14)	-48.2(2)
C(12)-C(11)-P(2)-C(14)	81.2(2)
C(13)-C(11)-P(2)-Ru(1)	173.12(18)
C(12)-C(11)-P(2)-Ru(1)	-57.5(2)
C(9)-C(10)-P(2)-C(11)	144.9(2)
C(9)-C(10)-P(2)-C(14)	-103.2(2)
C(9)-C(10)-P(2)-Ru(1)	22.1(2)
C(15)-C(14)-P(2)-C(11)	-74.6(2)
C(16)-C(14)-P(2)-C(11)	161.4(2)
C(15)-C(14)-P(2)-C(10)	176.9(2)
C(16)-C(14)-P(2)-C(10)	52.9(3)
C(15)-C(14)-P(2)-Ru(1)	63.2(2)

9 Appendix – Crystal Structures

C(16)-C(14)-P(2)-Ru(1)	-60.9(2)
Ru(1)-O(2)-S(1)-O(3)	70.3(3)
Ru(1)-O(2)-S(1)-O(4)	-68.7(3)
Ru(1)-O(2)-S(1)-C(19)	-179.2(2)
F(2)-C(19)-S(1)-O(3)	55.8(2)
F(1)-C(19)-S(1)-O(3)	-64.5(2)
F(3)-C(19)-S(1)-O(3)	175.76(19)
F(2)-C(19)-S(1)-O(4)	177.67(19)
F(1)-C(19)-S(1)-O(4)	57.3(2)
F(3)-C(19)-S(1)-O(4)	-62.4(2)
F(2)-C(19)-S(1)-O(2)	-63.2(2)
F(1)-C(19)-S(1)-O(2)	176.49(18)
F(3)-C(19)-S(1)-O(2)	56.8(2)

9.3 Single-Crystal Structure Analysis of $(\text{HPNP}^{i\text{Pr}})\text{RuH}(\text{OSO}_2\text{Me})\text{CO}$ (**94**)

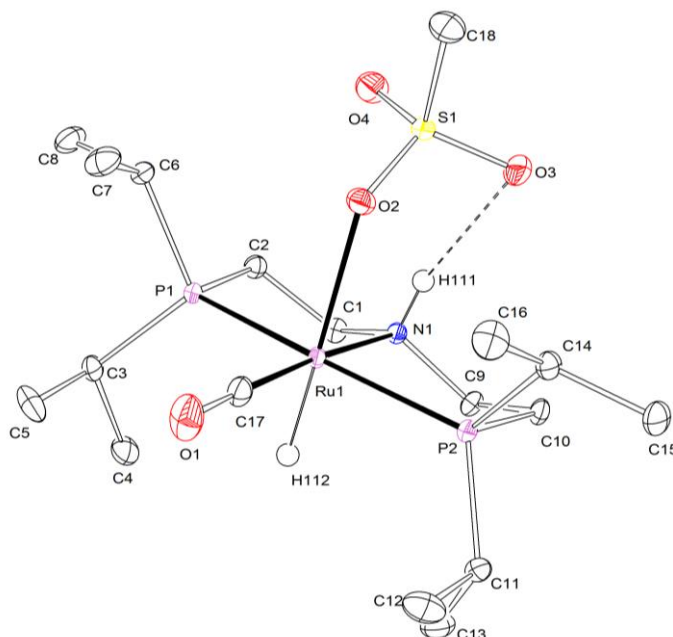


Figure 9.3 Thermal ellipsoid plot of $(\text{HPNP}^{i\text{Pr}})\text{RuH}(\text{CO})(\text{OSO}_2\text{Me})$ (**94**) with the anisotropic displacement parameters drawn at the 50% probability level. The asymmetric unit contains one complex molecule. The N-H and Rh-H hydrogen atoms were found from the residual density map and isotropically refined.

Table 9.8 Crystal data and structure refinement for $(\text{HPNP}^{i\text{Pr}})\text{RuH}(\text{OSO}_2\text{Me})\text{CO}$ (**94**).

Identification code	mo_CW_AG_091017_0m_a (AG384-1a)	
Empirical formula	$\text{C}_{18}\text{H}_{41}\text{NO}_4\text{P}_2\text{RuS}$	
Formula weight	530.59	
Temperature	116(2) K	
Wavelength	0.71073 Å	
Crystal system	Monoclinic	
Space group	$\text{P}2_1/\text{c}$	
Unit cell dimensions	$a = 10.2265(12)$ Å	$\alpha = 90^\circ$
	$b = 15.051(2)$ Å	$\beta = 91.287(4)^\circ$
	$c = 16.114(19)$ Å	$\gamma = 90^\circ$
Volume	$2479.2(6)$ Å ³	
Z	4	
Density (calculated)	1.422 Mg/m ³	
Absorption coefficient	0.867 mm ⁻¹	
F(000)	1112	
Crystal size	$0.865 \times 0.712 \times 0.392$ mm ³	
Crystal shape and color	Block, clear colourless	

9 Appendix – Crystal Structures

Theta range for data collection	2.408 to 33.273°
Index ranges	-15<=h<=15, -23<=k<=23, -24<=l<=24
Reflections collected	99773
Independent reflections	9499 [R(int) = 0.0746]
Completeness to theta = 25.242°	99.9 %
Refinement method	Full-matrix least-squares on F ²
Data / restraints / parameters	9499 / 0 / 261
Goodness-of-fit on F ²	1.036
Final R indices [I>2sigma(I)]	R1 = 0.0268, wR2 = 0.0536
R indices (all data)	R1 = 0.0402, wR2 = 0.0577
Largest diff. peak and hole	0.699 and -0.799 eÅ ⁻³

Table 9.9 Bond lengths [Å] and angles [°] for (HPNP^{Pr})RuH(OSO₂Me)CO (**94**).

Ru(1)-C(17)	1.8353(14)
Ru(1)-N(1)	2.2052(12)
Ru(1)-O(2)	2.2883(10)
Ru(1)-P(1)	2.3243(4)
Ru(1)-P(2)	2.3300(4)
Ru(1)-H(112)	1.499(19)
S(1)-O(3)	1.4517(11)
S(1)-O(4)	1.4525(11)
S(1)-O(2)	1.4736(11)
S(1)-C(18)	1.7673(16)
P(1)-C(6)	1.8482(14)
P(1)-C(3)	1.8483(13)
P(1)-C(2)	1.8506(14)
P(2)-C(14)	1.8464(14)
P(2)-C(11)	1.8471(14)
P(2)-C(10)	1.8492(14)
O(1)-C(17)	1.1590(18)
N(1)-C(9)	1.4879(17)
N(1)-C(1)	1.4906(17)
N(1)-H(111)	0.836(17)
C(1)-C(2)	1.5200(18)
C(3)-C(4)	1.528(2)
C(3)-C(5)	1.530(2)
C(6)-C(7)	1.529(2)
C(6)-C(8)	1.5309(19)
C(9)-C(10)	1.5243(19)
C(11)-C(12)	1.529(2)
C(11)-C(13)	1.530(2)
C(14)-C(15)	1.5304(19)
C(14)-C(16)	1.534(2)
C(17)-Ru(1)-N(1)	174.68(5)
C(17)-Ru(1)-O(2)	94.11(5)
N(1)-Ru(1)-O(2)	91.21(4)
C(17)-Ru(1)-P(1)	96.91(4)
N(1)-Ru(1)-P(1)	82.79(3)
O(2)-Ru(1)-P(1)	91.80(3)
C(17)-Ru(1)-P(2)	97.16(4)

9 Appendix – Crystal Structures

N(1)-Ru(1)-P(2)	82.66(3)
O(2)-Ru(1)-P(2)	92.92(3)
P(1)-Ru(1)-P(2)	164.795(13)
C(17)-Ru(1)-H(112)	86.6(7)
N(1)-Ru(1)-H(112)	88.1(7)
O(2)-Ru(1)-H(112)	178.6(7)
P(1)-Ru(1)-H(112)	87.0(7)
P(2)-Ru(1)-H(112)	88.2(7)
O(3)-S(1)-O(4)	113.09(7)
O(3)-S(1)-O(2)	112.25(6)
O(4)-S(1)-O(2)	112.65(6)
O(3)-S(1)-C(18)	107.24(8)
O(4)-S(1)-C(18)	106.77(8)
O(2)-S(1)-C(18)	104.12(8)
C(6)-P(1)-C(3)	106.75(6)
C(6)-P(1)-C(2)	101.37(6)
C(3)-P(1)-C(2)	105.80(6)
C(6)-P(1)-Ru(1)	118.14(4)
C(3)-P(1)-Ru(1)	119.81(5)
C(2)-P(1)-Ru(1)	102.46(4)
C(14)-P(2)-C(11)	106.68(6)
C(14)-P(2)-C(10)	101.70(6)
C(11)-P(2)-C(10)	103.79(6)
C(14)-P(2)-Ru(1)	117.58(5)
C(11)-P(2)-Ru(1)	121.60(5)
C(10)-P(2)-Ru(1)	102.45(4)
S(1)-O(2)-Ru(1)	127.89(6)
C(9)-N(1)-C(1)	110.28(10)
C(9)-N(1)-Ru(1)	111.83(8)
C(1)-N(1)-Ru(1)	112.88(8)
C(9)-N(1)-H(111)	106.8(11)
C(1)-N(1)-H(111)	108.9(12)
Ru(1)-N(1)-H(111)	105.8(12)
N(1)-C(1)-C(2)	110.78(11)
C(1)-C(2)-P(1)	109.61(9)
C(4)-C(3)-C(5)	109.91(12)
C(4)-C(3)-P(1)	112.51(9)
C(5)-C(3)-P(1)	110.51(10)

9 Appendix – Crystal Structures

C(7)-C(6)-C(8)	111.93(12)
C(7)-C(6)-P(1)	113.00(10)
C(8)-C(6)-P(1)	114.00(10)
N(1)-C(9)-C(10)	110.60(11)
C(9)-C(10)-P(2)	109.27(9)
C(12)-C(11)-C(13)	110.77(12)
C(12)-C(11)-P(2)	111.47(11)
C(13)-C(11)-P(2)	111.56(10)
C(15)-C(14)-C(16)	111.90(12)
C(15)-C(14)-P(2)	114.25(10)
C(16)-C(14)-P(2)	113.30(10)
O(1)-C(17)-Ru(1)	177.74(14)

9 Appendix – Crystal Structures

Table 9.10 Torsion angles [°] for (HPNP^{Pr})RuH(OSO₂Me)CO (**94**).

O(3)-S(1)-O(2)-Ru(1)	-55.03(10)
O(4)-S(1)-O(2)-Ru(1)	74.00(9)
C(18)-S(1)-O(2)-Ru(1)	-170.70(8)
C(9)-N(1)-C(1)-C(2)	174.74(11)
Ru(1)-N(1)-C(1)-C(2)	48.84(12)
N(1)-C(1)-C(2)-P(1)	-49.89(13)
C(6)-P(1)-C(2)-C(1)	150.22(9)
C(3)-P(1)-C(2)-C(1)	-98.53(10)
Ru(1)-P(1)-C(2)-C(1)	27.74(9)
C(6)-P(1)-C(3)-C(4)	160.89(11)
C(2)-P(1)-C(3)-C(4)	53.49(12)
Ru(1)-P(1)-C(3)-C(4)	-61.38(12)
C(6)-P(1)-C(3)-C(5)	-75.83(11)
C(2)-P(1)-C(3)-C(5)	176.76(10)
Ru(1)-P(1)-C(3)-C(5)	61.89(11)
C(3)-P(1)-C(6)-C(7)	84.99(11)
C(2)-P(1)-C(6)-C(7)	-164.50(10)
Ru(1)-P(1)-C(6)-C(7)	-53.57(11)
C(3)-P(1)-C(6)-C(8)	-44.29(12)
C(2)-P(1)-C(6)-C(8)	66.23(11)
Ru(1)-P(1)-C(6)-C(8)	177.16(9)
C(1)-N(1)-C(9)-C(10)	-178.31(11)
Ru(1)-N(1)-C(9)-C(10)	-51.82(12)
N(1)-C(9)-C(10)-P(2)	50.82(13)
C(14)-P(2)-C(10)-C(9)	-148.16(9)
C(11)-P(2)-C(10)-C(9)	101.19(10)
Ru(1)-P(2)-C(10)-C(9)	-26.16(10)
C(14)-P(2)-C(11)-C(12)	68.82(12)
C(10)-P(2)-C(11)-C(12)	175.77(10)
Ru(1)-P(2)-C(11)-C(12)	-69.93(11)
C(14)-P(2)-C(11)-C(13)	-166.77(10)
C(10)-P(2)-C(11)-C(13)	-59.82(11)
Ru(1)-P(2)-C(11)-C(13)	54.48(12)
C(11)-P(2)-C(14)-C(15)	42.41(12)
C(10)-P(2)-C(14)-C(15)	-66.02(12)
Ru(1)-P(2)-C(14)-C(15)	-176.91(9)
C(11)-P(2)-C(14)-C(16)	-87.34(11)

9 Appendix – Crystal Structures

C(10)-P(2)-C(14)-C(16)	164.22(10)
Ru(1)-P(2)-C(14)-C(16)	53.34(12)

9 Appendix – Crystal Structures

Table 9.11 Hydrogen bonds for (*HPNP*^{Pr})RuH(OSO₂Me)CO (**94**) [Å and °].

D-H...A	d(D-H)	d(H...A)	d(D...A)	<(DHA)
N(1)-H(111)...O(3)	0.836(17)	2.455(17)	3.1789(16)	145.5(15)
N(1)-H(111)...O(4)	0.836(17)	2.885(17)	3.5455(16)	137.4(14)

9.4 Single-Crystal Structure Analysis of $[(HPNP^{iPr})RuH(lut)CO]OTf$ (**95**)

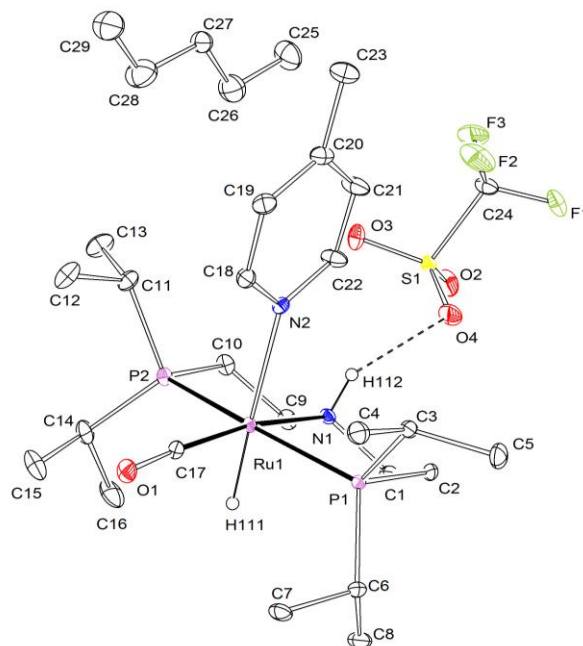


Figure 9.4 Thermal ellipsoid plot of $[(HPNP^{iPr})RuH(lut)CO]OTf$ (**95**) with the anisotropic displacement parameters drawn at the 50% probability level. The asymmetric unit contains one complex molecule, one $CF_3SO_3^-$ anion and a half disordered pentane solvent molecule. The disorder was refined using PART –1 command. The N-H and Ru-H hydrogen atoms were found from the residual density map and isotropically refined.

Table 9.12 Crystal data and structure refinement for $[(HPNP^{iPr})RuH(lut)CO]OTf$ (**95**).

Identification code	mo_CW_AG_200218_0m_a (AG455-1)	
Empirical formula	$C_{24}H_{45}N_2P_2Ru$ $CF_3SO_3^-$ * $\frac{1}{2}$ C_5H_{12}	
Formula weight	713.76	
Temperature	101(2) K	
Wavelength	0.71073 Å	
Crystal system	Triclinic	
Space group	P-1	
Unit cell dimensions	$a = 11.8278(6)$ Å	$\alpha = 68.706(2)^\circ$
	$b = 11.8751(6)$ Å	$\beta = 73.819(2)^\circ$
	$c = 13.7569(7)$ Å	$\gamma = 79.132(2)^\circ$
Volume	$1720.75(15)$ Å ³	
Z	2	
Density (calculated)	1.378 Mg/m ³	
Absorption coefficient	0.657 mm ⁻¹	
F(000)	746	
Crystal size	$0.368 \times 0.342 \times 0.272$ mm ³	

9 Appendix – Crystal Structures

Crystal shape and color	Block, clear colourless
Theta range for data collection	2.311 to 33.308°
Index ranges	-18<=h<=18, -18<=k<=18, -21<=l<=21
Reflections collected	121672
Independent reflections	13272 [R(int) = 0.0765]
Completeness to theta = 25.242°	99.9 %
Refinement method	Full-matrix least-squares on F ²
Data / restraints / parameters	13272 / 0 / 398
Goodness-of-fit on F ²	1.057
Final R indices [I>2sigma(I)]	R1 = 0.0398, wR2 = 0.0737
R indices (all data)	R1 = 0.0683, wR2 = 0.0834
Largest diff. peak and hole	1.411 and -0.892 eÅ ⁻³

Table 9.13 Bond lengths [Å] and angles [°] for [(HPNP^{Pr})RuH(lut)CO]OTf (**95**).

C(25)-C(26)	1.463(8)
C(26)-C(27)	1.484(9)
C(27)-C(28)	1.453(9)
C(28)-C(29)	1.491(10)
C(1)-N(1)	1.491(2)
C(1)-C(2)	1.518(3)
C(2)-P(1)	1.8408(18)
C(3)-C(5)	1.529(3)
C(3)-C(4)	1.529(3)
C(3)-P(1)	1.8538(19)
C(6)-C(8)	1.527(3)
C(6)-C(7)	1.531(3)
C(6)-P(1)	1.8475(19)
C(9)-N(1)	1.486(2)
C(9)-C(10)	1.523(3)
C(10)-P(2)	1.8395(19)
C(11)-C(13)	1.527(3)
C(11)-C(12)	1.531(3)
C(11)-P(2)	1.846(2)
C(14)-C(16)	1.515(3)
C(14)-C(15)	1.531(3)
C(14)-P(2)	1.847(2)
C(17)-O(1)	1.153(2)
C(17)-Ru(1)	1.8294(18)
C(18)-N(2)	1.343(2)
C(18)-C(19)	1.378(3)
C(19)-C(20)	1.377(3)
C(20)-C(21)	1.378(3)
C(20)-C(23)	1.501(3)
C(21)-C(22)	1.380(3)
C(22)-N(2)	1.341(2)
C(24)-F(3)	1.315(3)
C(24)-F(1)	1.327(3)
C(24)-F(2)	1.336(3)
C(24)-S(1)	1.816(2)
N(1)-Ru(1)	2.1962(15)
N(1)-H(112)	0.87(2)

9 Appendix – Crystal Structures

N(2)-Ru(1)	2.2527(15)
O(2)-S(1)	1.4327(17)
O(3)-S(1)	1.4312(16)
O(4)-S(1)	1.4306(17)
P(1)-Ru(1)	2.3220(5)
P(2)-Ru(1)	2.3261(5)
Ru(1)-H(111)	1.53(2)

C(25)-C(26)-C(27)	117.7(6)
C(28)-C(27)-C(26)	119.4(5)
C(27)-C(28)-C(29)	119.6(7)
N(1)-C(1)-C(2)	109.39(15)
C(1)-C(2)-P(1)	109.41(12)
C(5)-C(3)-C(4)	110.62(17)
C(5)-C(3)-P(1)	114.13(15)
C(4)-C(3)-P(1)	112.22(13)
C(8)-C(6)-C(7)	109.05(16)
C(8)-C(6)-P(1)	112.24(14)
C(7)-C(6)-P(1)	111.22(13)
N(1)-C(9)-C(10)	109.48(15)
C(9)-C(10)-P(2)	109.81(13)
C(13)-C(11)-C(12)	111.17(18)
C(13)-C(11)-P(2)	114.75(15)
C(12)-C(11)-P(2)	111.86(15)
C(16)-C(14)-C(15)	108.8(2)
C(16)-C(14)-P(2)	111.37(15)
C(15)-C(14)-P(2)	111.74(15)
O(1)-C(17)-Ru(1)	175.87(17)
N(2)-C(18)-C(19)	123.96(18)
C(20)-C(19)-C(18)	120.26(19)
C(19)-C(20)-C(21)	116.39(19)
C(19)-C(20)-C(23)	121.6(2)
C(21)-C(20)-C(23)	122.0(2)
C(20)-C(21)-C(22)	120.3(2)
N(2)-C(22)-C(21)	123.89(19)
F(3)-C(24)-F(1)	107.53(18)
F(3)-C(24)-F(2)	107.9(2)
F(1)-C(24)-F(2)	106.7(2)

F(3)-C(24)-S(1)	111.98(17)
F(1)-C(24)-S(1)	111.54(15)
F(2)-C(24)-S(1)	110.91(15)
C(9)-N(1)-C(1)	110.83(14)
C(9)-N(1)-Ru(1)	112.32(11)
C(1)-N(1)-Ru(1)	112.21(11)
C(9)-N(1)-H(112)	105.6(14)
C(1)-N(1)-H(112)	103.5(14)
Ru(1)-N(1)-H(112)	111.9(14)
C(22)-N(2)-C(18)	115.24(16)
C(22)-N(2)-Ru(1)	126.02(13)
C(18)-N(2)-Ru(1)	118.63(12)
C(2)-P(1)-C(6)	106.75(9)
C(2)-P(1)-C(3)	102.48(9)
C(6)-P(1)-C(3)	105.77(9)
C(2)-P(1)-Ru(1)	101.73(6)
C(6)-P(1)-Ru(1)	120.14(7)
C(3)-P(1)-Ru(1)	117.87(6)
C(10)-P(2)-C(11)	102.50(9)
C(10)-P(2)-C(14)	105.97(9)
C(11)-P(2)-C(14)	106.32(10)
C(10)-P(2)-Ru(1)	101.67(6)
C(11)-P(2)-Ru(1)	116.93(7)
C(14)-P(2)-Ru(1)	121.11(7)
C(17)-Ru(1)-N(1)	169.74(7)
C(17)-Ru(1)-N(2)	96.18(7)
N(1)-Ru(1)-N(2)	94.08(6)
C(17)-Ru(1)-P(1)	96.74(6)
N(1)-Ru(1)-P(1)	82.88(4)
N(2)-Ru(1)-P(1)	91.68(4)
C(17)-Ru(1)-P(2)	96.53(6)
N(1)-Ru(1)-P(2)	82.89(4)
N(2)-Ru(1)-P(2)	93.39(4)
P(1)-Ru(1)-P(2)	165.191(17)
C(17)-Ru(1)-H(111)	86.3(9)
N(1)-Ru(1)-H(111)	83.4(9)
N(2)-Ru(1)-H(111)	177.4(9)
P(1)-Ru(1)-H(111)	87.2(9)

9 Appendix – Crystal Structures

P(2)-Ru(1)-H(111)	87.1(9)
O(4)-S(1)-O(3)	114.09(11)
O(4)-S(1)-O(2)	115.24(12)
O(3)-S(1)-O(2)	115.02(11)
O(4)-S(1)-C(24)	103.21(11)
O(3)-S(1)-C(24)	104.53(11)
O(2)-S(1)-C(24)	102.52(10)

Table 9.14 Torsion angles [°] for $[(HPNP^{Pr})RuH(lut)CO]OTf$ (**95**).

C(25)-C(26)-C(27)-C(28)	179.4(7)
C(26)-C(27)-C(28)-C(29)	178.1(7)
N(1)-C(1)-C(2)-P(1)	53.12(17)
N(1)-C(9)-C(10)-P(2)	-52.28(18)
N(2)-C(18)-C(19)-C(20)	0.4(3)
C(18)-C(19)-C(20)-C(21)	0.1(3)
C(18)-C(19)-C(20)-C(23)	-180.0(2)
C(19)-C(20)-C(21)-C(22)	-0.3(3)
C(23)-C(20)-C(21)-C(22)	179.7(2)
C(20)-C(21)-C(22)-N(2)	0.1(4)
C(10)-C(9)-N(1)-C(1)	177.55(14)
C(10)-C(9)-N(1)-Ru(1)	51.15(17)
C(2)-C(1)-N(1)-C(9)	-177.69(14)
C(2)-C(1)-N(1)-Ru(1)	-51.23(16)
C(21)-C(22)-N(2)-C(18)	0.3(3)
C(21)-C(22)-N(2)-Ru(1)	-175.78(18)
C(19)-C(18)-N(2)-C(22)	-0.6(3)
C(19)-C(18)-N(2)-Ru(1)	175.82(16)
C(1)-C(2)-P(1)-C(6)	96.69(14)
C(1)-C(2)-P(1)-C(3)	-152.37(13)
C(1)-C(2)-P(1)-Ru(1)	-30.03(13)
C(8)-C(6)-P(1)-C(2)	-42.04(17)
C(7)-C(6)-P(1)-C(2)	-164.53(14)
C(8)-C(6)-P(1)-C(3)	-150.67(14)
C(7)-C(6)-P(1)-C(3)	86.84(16)
C(8)-C(6)-P(1)-Ru(1)	72.81(15)
C(7)-C(6)-P(1)-Ru(1)	-49.68(17)
C(5)-C(3)-P(1)-C(2)	-49.91(16)
C(4)-C(3)-P(1)-C(2)	-176.76(13)
C(5)-C(3)-P(1)-C(6)	61.76(16)
C(4)-C(3)-P(1)-C(6)	-65.10(15)
C(5)-C(3)-P(1)-Ru(1)	-160.56(12)
C(4)-C(3)-P(1)-Ru(1)	72.59(14)
C(9)-C(10)-P(2)-C(11)	150.12(14)
C(9)-C(10)-P(2)-C(14)	-98.61(15)
C(9)-C(10)-P(2)-Ru(1)	28.82(14)
C(13)-C(11)-P(2)-C(10)	49.02(19)

9 Appendix – Crystal Structures

C(12)-C(11)-P(2)-C(10)	176.85(15)
C(13)-C(11)-P(2)-C(14)	-61.99(19)
C(12)-C(11)-P(2)-C(14)	65.84(17)
C(13)-C(11)-P(2)-Ru(1)	159.20(15)
C(12)-C(11)-P(2)-Ru(1)	-72.98(16)
C(16)-C(14)-P(2)-C(10)	43.8(2)
C(15)-C(14)-P(2)-C(10)	165.75(18)
C(16)-C(14)-P(2)-C(11)	152.40(18)
C(15)-C(14)-P(2)-C(11)	-85.69(19)
C(16)-C(14)-P(2)-Ru(1)	-70.89(19)
C(15)-C(14)-P(2)-Ru(1)	51.0(2)
F(3)-C(24)-S(1)-O(4)	-179.49(17)
F(1)-C(24)-S(1)-O(4)	59.93(18)
F(2)-C(24)-S(1)-O(4)	-58.8(2)
F(3)-C(24)-S(1)-O(3)	-59.88(19)
F(1)-C(24)-S(1)-O(3)	179.54(15)
F(2)-C(24)-S(1)-O(3)	60.8(2)
F(3)-C(24)-S(1)-O(2)	60.46(19)
F(1)-C(24)-S(1)-O(2)	-60.12(18)
F(2)-C(24)-S(1)-O(2)	-178.89(18)

Table 9.15 Hydrogen bonds for [(HPNP^{Pr})RuH(lut)CO]OTf (**95**) [Å and °].

D-H...A	d(D-H)	d(H...A)	d(D...A)	<(DHA)
N(1)-H(112)...O(4)	0.87(2)	2.20(2)	2.968(2)	147.5(19)

10 References

- [1] A. Kumar, T. M. Bhatti, A. S. Goldman, *Chem. Rev.* **2017**, *117*, 12357.
- [2] F. Meemken, A. Baiker, *Chem. Rev.* **2017**, *117*, 11522.
- [3] J. Artz, T. E. Müller, K. Thenert, J. Kleinekorte, R. Meys, A. Sternberg, A. Bardow, W. Leitner, *Chem. Rev.* **2018**, *118*, 434.
- [4] K. Sordakis, C. Tang, L. K. Vogt, H. Junge, P. J. Dyson, M. Beller, G. Laurenczy, *Chem. Rev.* **2018**, *118*, 372.
- [5] J. R. Khusnutdinova, D. Milstein, *Angew. Chemie Int. Ed.* **2015**, *54*, 12236.
- [6] G. A. Filonenko, R. van Putten, E. J. M. Hensen, E. A. Pidko, *Chem. Soc. Rev.* **2018**, *47*, 1459.
- [7] S. Schneider, J. Meiners, B. Askevold, *Eur. J. Inorg. Chem.* **2012**, *2012*, 412.
- [8] E. Peris, R. H. Crabtree, *Chem. Soc. Rev.* **2018**, *47*, 1959.
- [9] H. Li, B. Zheng, K. W. Huang, *Coord. Chem. Rev.* **2015**, *293–294*, 116.
- [10] E. A. Bielinski, P. O. Lagaditis, Y. Zhang, B. Q. Mercado, C. Würtele, W. H. Bernskoetter, N. Hazari, S. Schneider, *J. Am. Chem. Soc.* **2014**, *136*, 10234.
- [11] F. Schneck, J. Ahrens, M. Finger, A. C. Stückl, C. Würtele, D. Schwarzer, S. Schneider, *Nat. Commun.* **2018**, *9*, 1161.
- [12] H. Valdés, M. A. García-Eleno, D. Canseco-Gonzalez, D. Morales-Morales, *ChemCatChem* **2018**, *10*, 3136.
- [13] H. Grützmacher, M. Trincado, *Cooperating Ligands in Catalysis in Cooperative Catalysis: Designing Efficient Catalysts for Synthesis* (Ed.: R. Peters), Wiley-VCH, **2008**, pp. 67.
- [14] H. Grützmacher, *Angew. Chemie Int. Ed.* **2008**, *47*, 1814.
- [15] P. A. Dub, J. C. Gordon, *Dalt. Trans.* **2016**, *45*, 6756.
- [16] P. A. Dub, J. C. Gordon, *ACS Catal.* **2017**, *7*, 6635.
- [17] A. N. Marziale, A. Friedrich, I. Klopsch, M. Drees, V. R. Celinski, J. Schmedt auf der Günne, S. Schneider, *J. Am. Chem. Soc.* **2013**, *135*, 13342.
- [18] N. Gorgas, K. Kirchner, *Well-Defined Iron and Manganese Pincer Catalysts in Pincer Compounds* (Ed.: D. Morales-Morales), Elsevier Inc., **2018**, pp. 19.
- [19] Y. Zhang, A. D. MacIntosh, J. L. Wong, E. A. Bielinski, P. G. Williard, B. Q. Mercado, N. Hazari, W. H. Bernskoetter, *Chem. Sci.* **2015**, *6*, 4291.
- [20] U. Jayarathne, N. Hazari, W. H. Bernskoetter, *ACS Catal.* **2018**, *8*, 1338.
- [21] M. R. Mills, C. L. Barnes, W. H. Bernskoetter, *Inorg. Chem.* **2018**, *57*, 1590.
- [22] C. Gunanathan, D. Milstein, *Chem. Rev.* **2014**, *114*, 12024.
- [23] E. Balaraman, D. Milstein, *Hydrogenation of Polar Bonds Catalysed by Ruthenium-Pincer Complexes in Top Organomet Chem* (Eds.: M. Beller, P.H. Dixneuf, J. Dupont, A. Fürstner, F. Glorius, L.J. Gooßen, S.P. Nolan, J. Oro, M. Willis, Q.-L. Zhou), Springer-Verlag, Berlin Heidelberg, **2014**, pp. 19.
- [24] H. A. Younus, W. Su, N. Ahmad, S. Chen, F. Verpoort, *Adv. Synth. Catal.* **2015**, *357*, 283.
- [25] S. Chakraborty, P. Bhattacharya, H. Dai, H. Guan, *Acc. Chem. Res.* **2015**, *48*, 1995.
- [26] E. A. Bielinski, M. Förster, Y. Zhang, W. H. Bernskoetter, N. Hazari, M. C. Holthausen, *ACS Catal.* **2015**, *5*, 2404.
- [27] G. Bauer, X. Hu, *Inorg. Chem. Front.* **2016**, *3*, 741.
- [28] R. H. Crabtree, *Chem. Rev.* **2017**, *117*, 9228.
- [29] H. A. Younus, N. Ahmad, W. Su, F. Verpoort, *Coord. Chem. Rev.* **2014**, *276*, 112.
- [30] E. S. Wiedner, M. B. Chambers, C. L. Pitman, R. M. Bullock, A. J. M. Miller, A. M. Appel, *Chem. Rev.* **2016**, *116*, 8655.
- [31] S. Qu, H. Dai, Y. Dang, C. Song, Z. X. Wang, H. Guan, *ACS Catal.* **2014**, *4*, 4377.
- [32] R. Xu, S. Chakraborty, S. M. Bellows, H. Yuan, T. R. Cundari, W. D. Jones, *ACS Catal.* **2016**, *6*, 2127.
- [33] A. Staubitz, A. P. M. Robertson, I. Manners, *Chem. Rev.* **2010**, *110*, 4079.
- [34] H. Li, Q. Yang, X. Chen, S. G. Shore, *J. Organomet. Chem.* **2014**, *751*, 60.
- [35] Y.-R. Luo, J. A. Kerr, *Bond Dissociation Energies in CRC Handbook of Chemistry and Physics*, **2012**, pp. 65.
- [36] A. Rossin, M. Peruzzini, *Chem. Rev.* **2016**, *116*, 8848.
- [37] A. Staubitz, A. P. M. Robertson, M. E. Sloan, I. Manners, *Chem. Rev.* **2010**, *110*, 4023.
- [38] E. M. Leitao, T. Jurca, I. Manners, *Nat. Chem.* **2013**, *5*, 817.
- [39] M. G. Hu, R. a. Geanangel, W. W. Wendlandt, *Thermochim. Acta* **1978**, *23*, 249.

10 References

- [40] S. D. Rassat, C. L. Aardahl, T. Autrey, R. S. Smith, *Energy & Fuels* **2010**, *24*, 2596.
- [41] D.-P. Kim, K.-T. Moon, J.-G. Kho, J. Economy, C. Gervais, F. Babonneau, *Polym. Adv. Technol.* **1999**, *712*, 702.
- [42] A. Glüer, M. Förster, V. R. Celinski, J. Schmedt auf der Günne, M. C. Holthausen, S. Schneider, *ACS Catal.* **2015**, *5*, 7214.
- [43] B. L. Davis, D. A. Dixon, E. B. Garner, J. C. Gordon, M. H. Matus, B. Scott, F. H. Stephens, *Angew. Chemie - Int. Ed.* **2009**, *48*, 6812.
- [44] A. D. Sutton, A. K. Burrell, D. A. Dixon, E. B. Garner III, J. C. Gordon, T. Nakagawa, K. C. Ott, J. P. Robinson, M. Vasiliu, *Science* **2011**, *331*, 1426.
- [45] C. Reller, F. O. R. L. Mertens, *Angew. Chemie - Int. Ed.* **2012**, *51*, 11731.
- [46] B. L. Davis, B. D. Rekken, R. Michalczyk, E. B. Garner, D. A. Dixon, H. Kalviri, R. T. Baker, D. L. Thorn, *Chem. Commun.* **2013**, *49*, 9095.
- [47] C. R. Miranda, G. Ceder, *J. Chem. Phys.* **2007**, *126*, 184703.
- [48] V. Pons, R. T. Baker, N. K. Szymczak, D. J. Heldebrant, J. C. Linehan, M. H. Matus, D. J. Grant, D. A. Dixon, *Chem. Commun.* **2008**, 6597.
- [49] H. A. Kalviri, F. Gärtner, G. Ye, I. Korobkov, R. T. Baker, *Chem. Sci.* **2015**, *6*, 618.
- [50] W. J. Shaw, J. C. Linehan, N. K. Szymczak, D. J. Heldebrant, C. Yonker, D. M. Camaioni, R. T. Baker, T. Autrey, *Angew. Chemie - Int. Ed.* **2008**, *47*, 7493.
- [51] P. M. Zimmerman, A. Paul, Z. Zhang, C. B. Musgrave, *Inorg. Chem.* **2009**, *48*, 1069.
- [52] S. Bhunya, T. Malakar, A. Paul, *Chem. Commun.* **2014**, *50*, 5919.
- [53] T. Malakar, S. Bhunya, A. Paul, *Chem. Eur. J.* **2015**, *21*, 6340.
- [54] S. Bhunya, P. M. Zimmerman, A. Paul, *ACS Catal.* **2015**, *5*, 3478.
- [55] C. T. Kwon, H. A. McGee, *Inorg. Chem.* **1970**, *9*, 2458.
- [56] K. A. Erickson, J. L. Kiplinger, *ACS Catal.* **2017**, *7*, 4276.
- [57] H. R. Sharpe, A. M. Geer, T. J. Blundell, F. R. Hastings, M. W. Fay, G. A. Rance, W. Lewis, A. J. Blake, D. L. Kays, *Catal. Sci. Technol.* **2018**, *8*, 229.
- [58] G. Bénac-Lestrille, U. Helmstedt, L. Vendier, G. Alcaraz, E. Clot, S. Sabo-Etienne, *Inorg. Chem.* **2011**, *50*, 11039.
- [59] G. Alcaraz, L. Vendier, E. Clot, S. Sabo-Etienne, *Angew. Chemie - Int. Ed.* **2010**, *49*, 918.
- [60] M. C. Denney, V. Pons, T. J. Hebden, D. M. Heinekey, K. I. Goldberg, *J. Am. Chem. Soc.* **2006**, *128*, 12048.
- [61] B. L. Dietrich, K. I. Goldberg, D. M. Heinekey, T. Autrey, J. C. Linehan, *Inorg. Chem.* **2008**, *47*, 8583.
- [62] A. Paul, C. B. Musgrave, *Angew. Chemie - Int. Ed.* **2007**, *46*, 8153.
- [63] I. Göttker-Schnetmann, P. S. White, M. Brookhart, *Organometallics* **2004**, *23*, 1766.
- [64] T. J. Hebden, M. C. Denney, V. Pons, P. M. B. Piccoli, T. F. Koetzle, A. J. Schultz, W. Kaminsky, K. I. Goldberg, D. M. Heinekey, *J. Am. Chem. Soc.* **2008**, *130*, 10812.
- [65] M. Käß, A. Friedrich, M. Drees, S. Schneider, *Angew. Chemie - Int. Ed.* **2009**, *48*, 905.
- [66] A. Staubitz, M. E. Sloan, A. P. M. Robertson, A. Friedrich, S. Schneider, P. J. Gates, I. Manners, J. Schmedt auf der Guenne, *J. Am. Chem. Soc.* **2010**, *132*, 13332.
- [67] J. R. Vance, A. Schäfer, A. P. M. Robertson, K. Lee, J. Turner, G. R. Whittell, I. Manners, *J. Am. Chem. Soc.* **2014**, *136*, 3048.
- [68] J. R. Vance, A. P. M. Robertson, K. Lee, I. Manners, *Chem. Eur. J.* **2011**, *17*, 4099.
- [69] R. J. Keaton, J. M. Blacquiere, R. T. Baker, *J. Am. Chem. Soc.* **2007**, *129*, 1844.
- [70] J. F. Sonnenberg, R. H. Morris, *ACS Catal.* **2013**, *3*, 1092.
- [71] C. Lichtenberg, M. Adelhardt, T. L. Gianetti, K. Meyer, B. de Bruin, H. Grützmacher, *ACS Catal.* **2015**, *5*, 6230.
- [72] P. Bhattacharya, J. A. Krause, H. Guan, *J. Am. Chem. Soc.* **2014**, *136*, 11153.
- [73] Y. Zhang, Y. Zhang, Z.-H. Qi, Y. Gao, W. Liu, Y. Wang, *Int. J. Hydrogen Energy* **2016**, *41*, 17208.
- [74] A. Glüer, J. I. Schweizer, U. S. Karaca, C. Würtele, M. Diefenbach, M. C. Holthausen, S. Schneider, *Inorg. Chem.* **2018**, *57*, 13822.
- [75] S. Park, S. Chang, *Angew. Chemie - Int. Ed.* **2017**, *56*, 7720.
- [76] M. C. Lipke, A. L. Liberman-Martin, T. D. Tilley, *Angew. Chemie - Int. Ed.* **2017**, *56*, 2260.
- [77] J. V. Obligacion, P. J. Chirik, *Nat. Rev. Chem.* **2018**, *2*, 15.
- [78] R. S. Chay, B. G. M. Rocha, A. J. L. Pombeiro, V. Y. Kukushkin, K. V. Luzyanin, *ACS Omega* **2018**, *3*, 863.
- [79] C. Cheng, J. F. Hartwig, *Chem. Rev.* **2015**, *115*, 8946.

- [80] M. Parasram, V. Gevorgyan, *Acc. Chem. Res.* **2017**, *50*, 2038.
- [81] A. A. Toutov, M. Salata, A. Fedorov, Y.-F. Yang, Y. Liang, R. Cariou, K. N. Betz, E. P. A. Couzijn, J. W. Shabaker, K. N. Houk, et al., *Nat. Energy* **2017**, *2*, 17008.
- [82] F. Gauvin, J. F. Harrod, H.-G. Woo, *Catalytic Dehydrocoupling: A General Strategy for the Formation of Element-Element Bonds in Advances in Organometallic Chemistry* (Eds.: R. West, A. Hill), Vol. 42, Academic Press, **1998**, pp. 363.
- [83] R. Waterman, *Chem. Soc. Rev.* **2013**, *42*, 5629.
- [84] R. D. C. Richards, J. Hollingshurst, J. A. Semlyen, *Polymer* **1993**, *34*, 4965.
- [85] J. Li, P. Ren, C. Zhan, J. Qin, *Polym. Int.* **1999**, *48*, 491.
- [86] P. Cancouët, E. Daudet, G. Héлары, M. Moreau, G. Sauvet, *J. Polym. Sci. Part A Polym. Chem.* **2000**, *38*, 826.
- [87] J. Beckmann, D. Dakternieks, A. Duthie, R. C. Foitzik, *Silicon Chem.* **2004**, *2*, 27.
- [88] W. Kalchauer, B. Pachaly, *Inorganic Reactions: The Direct Process to Methylchlorosilanes (Müller-Rochow Synthesis) in Handbook of Heterogeneous Catalysis* (Eds.: G. Ertl, H. Knözinger, F. Schüth, J. Weitkamp), Wiley- VCH, **2008**, pp. 2635.
- [89] K. Chulsky, R. Dobrovetsky, *Angew. Chemie - Int. Ed.* **2017**, *56*, 4744.
- [90] I. Kaljurand, A. Kütt, L. Sooväli, T. Rodima, V. Mäemets, I. Leito, I. A. Koppel, *J. Org. Chem.* **2005**, *70*, 1019.
- [91] T. Beppu, K. Sakamoto, Y. Nakajima, K. Matsumoto, K. Sato, S. Shimada, *J. Organomet. Chem.* **2018**, *869*, 75.
- [92] E. J. Corey, H. Cho, C. Rücker, D. H. Hua, *Tetrahedron Lett.* **1981**, *22*, 3455.
- [93] K. Matyjaszewski, Y. L. Chen, *J. Organomet. Chem.* **1988**, *340*, 7.
- [94] D. Tsushima, M. Igarashi, K. Sato, S. Shimada, *Chem. Lett.* **2017**, *46*, 1532.
- [95] A. Glüer, S. Schneider, *J. Organomet. Chem.* **2018**, *861*, 159.
- [96] Y.-N. Li, R. Ma, L.-N. He, Z.-F. Diao, *Catal. Sci. Technol.* **2014**, *4*, 1498.
- [97] A. P. C. Ribeiro, L. M. D. R. S. Martins, A. J. L. Pombeiro, *Green Chem.* **2017**, *19*, 4811.
- [98] D. R. Lide, *CRC Handbook of Chemistry and Physics, Internet Version*, CRC Press, **2005**.
- [99] P. G. Jessop, T. Ikariya, R. Noyori, *Chem. Rev.* **1995**, *95*, 259.
- [100] G. Laurenczy, F. Joó, L. Nádasdi, *Inorg. Chem.* **2000**, *39*, 5083.
- [101] Y. Inoue, Y. Sasaki, H. Hashimoto, *J. Chem. Soc. Chem. Commun.* **1975**, 718.
- [102] G. O. Evans, C. J. Newell, *Inorganica Chim. Acta* **1978**, *31*, L387.
- [103] P. G. Jessop, F. Joó, C. C. Tai, *Coord. Chem. Rev.* **2004**, *248*, 2425.
- [104] R. Langer, Y. Diskin-Posner, G. Leitus, L. J. W. Shimon, Y. Ben-David, D. Milstein, *Angew. Chemie - Int. Ed.* **2011**, *50*, 9948.
- [105] F. Bertini, N. Gorgas, B. Stöger, M. Peruzzini, L. F. Veiros, K. Kirchner, L. Gonsalvi, *ACS Catal.* **2016**, *6*, 2889.
- [106] O. Rivada-Wheelaghan, A. Dauth, G. Leitus, Y. Diskin-Posner, D. Milstein, *Inorg. Chem.* **2015**, *54*, 4526.
- [107] F. Bertini, I. Mellone, A. Ienco, M. Peruzzini, L. Gonsalvi, *ACS Catal.* **2015**, *5*, 1254.
- [108] C. Federsel, A. Boddien, R. Jackstell, R. Jennerjahn, P. J. Dyson, R. Scopelliti, G. Laurenczy, M. Beller, *Angew. Chemie - Int. Ed.* **2010**, *49*, 9777.
- [109] H. Fong, J. C. Peters, *Inorg. Chem.* **2014**, *54*, 5124.
- [110] C. T. Saouma, C. C. Lu, M. W. Day, J. C. Peters, *Chem. Sci.* **2013**, *4*, 4042.
- [111] C. Ziebart, C. Federsel, P. Anbarasan, R. Jackstell, W. Baumann, A. Spannenberg, M. Beller, *J. Am. Chem. Soc.* **2012**, *134*, 20701.
- [112] F. Zhu, L. Zhu-Ge, G. Yang, S. Zhou, *ChemSusChem* **2015**, *8*, 609.
- [113] H. Ge, X. Chen, X. Yang, *Chem. Commun.* **2016**, 12422.
- [114] H. Ge, X. Chen, X. Yang, *Chem. Eur. J.* **2017**, *23*, 8850.
- [115] G. J. Kubas, *Chem. Rev.* **2007**, *107*, 4152.
- [116] W. Lubitz, H. Ogata, O. Rüdiger, E. Reijerse, *Chem. Rev.* **2014**, *114*, 4081.
- [117] C. Gunanathan, D. Milstein, *Acc. Chem. Res.* **2011**, *44*, 588.
- [118] C. Gunanathan, D. Milstein, *Science* **2013**, *341*, 249.
- [119] X. Yang, *ACS Catal.* **2011**, *1*, 849.
- [120] D. Benito-Garagorri, E. Becker, J. Wiedermann, W. Lackner, M. Pollak, K. Mereiter, J. Kisala, K. Kirchner, *Organometallics* **2006**, *25*, 1900.
- [121] D. Benito-Garagorri, J. Wiedermann, M. Pollak, K. Mereiter, K. Kirchner, *Organometallics* **2007**, *26*, 217.
- [122] D. Benito-Garagorri, M. Puchberger, K. Mereiter, K. Kirchner, *Angew. Chem.* **2008**, *47*,

10 References

- 9142.
- [123] B. Bichler, C. Holzhaecker, B. Stöger, M. Puchberger, L. F. Veiros, K. Kirchner, *Organometallics* **2013**, *32*, 4114.
- [124] N. Gorgas, B. Stöger, L. F. Veiros, E. Pittenauer, G. Allmaier, K. Kirchner, *Organometallics* **2014**, *33*, 6905.
- [125] B. Bichler, M. Glatz, B. Stöger, K. Mereiter, L. F. Veiros, K. Kirchner, *Dalt. Trans.* **2014**, *43*, 14517.
- [126] I. Mellone, N. Gorgas, F. Bertini, M. Peruzzini, K. Kirchner, L. Gonsalvi, *Organometallics* **2016**, *35*, 3344.
- [127] B. Mondal, F. Neese, S. Ye, *Inorg. Chem.* **2016**, *55*, 5438.
- [128] R. Marcos, L. Xue, R. Sánchez-de-Armas, M. S. G. Ahlquist, *ACS Catal.* **2016**, 2923.
- [129] M. Montandon-Clerc, G. Laurencyzy, *J. Catal.* **2018**, *362*, 78.
- [130] B. Mondal, F. Neese, S. Ye, *Inorg. Chem.* **2015**, *54*, 7192.
- [131] P. Munshi, A. D. Main, J. C. Linehan, C.-C. Tai, P. G. Jessop, *J. Am. Chem. Soc.* **2002**, *124*, 7963.
- [132] Q. Liu, L. Wu, S. Güllak, N. Rockstroh, R. Jackstell, M. Beller, *Angew. Chem.* **2014**, *53*, 7085.
- [133] S. Kar, R. Sen, A. Goepfert, G. K. S. Prakash, *J. Am. Chem. Soc.* **2018**, *140*, 1580.
- [134] B. Arkles, *Silicon Compounds, Silanes in Kirk-Othmer Encyclopedia of Chemical Technology* (Ed.: Kirk-Othmer), John Wiley & Sons, Inc., **2001**.
- [135] N. C. Smythe, J. C. Gordon, *Eur. J. Inorg. Chem.* **2010**, 509.
- [136] X. Zhang, L. Kam, R. Trerise, T. J. Williams, *Acc. Chem. Res.* **2017**, *50*, 86.
- [137] R. T. Baker, J. C. Gordon, C. W. Hamilton, N. J. Henson, P. H. Lin, S. Maguire, M. Murugesu, B. L. Scott, N. C. Smythe, *J. Am. Chem. Soc.* **2012**, *134*, 5598.
- [138] J. A. Buss, G. A. Edouard, C. Cheng, J. Shi, T. Agapie, *J. Am. Chem. Soc.* **2014**, *136*, 11272.
- [139] J. K. Pagano, J. P. W. Stelmach, R. Waterman, *Dalt. Trans.* **2015**, *44*, 12074.
- [140] E. Alberico, P. Sponholz, C. Cordes, M. Nielsen, H.-J. Drexler, W. Baumann, H. Junge, M. Beller, *Angew. Chemie Int. Ed.* **2013**, *52*, 14162.
- [141] S. Chakraborty, H. Dai, P. Bhattacharya, T. F. Neil, M. S. Gibson, J. A. Krause, H. Guan, *J. Am. Chem. Soc.* **2014**, *136*, 7869.
- [142] S. Chakraborty, W. W. Brennessel, W. D. Jones, *J. Am. Chem. Soc.* **2014**, *136*, 8564.
- [143] C. Bornschein, S. Werkmeister, B. Wendt, H. Jiao, E. Alberico, W. Baumann, H. Junge, K. Junge, M. Beller, *Nat. Commun.* **2014**, *5*, 4111.
- [144] S. Chakraborty, P. O. Lagaditis, M. Förster, E. A. Bielinski, N. Hazari, M. C. Holthausen, W. D. Jones, S. Schneider, *ACS Catal.* **2014**, *4*, 3994.
- [145] H. Nöth, H. Vahrenkamp, *Chem. Ber.* **1966**, *99*, 1049.
- [146] S. Bhunya, T. Malakar, G. Ganguly, A. Paul, *ACS Catal.* **2016**, *6*, 7907.
- [147] J. F. Sonnenberg, R. H. Morris, *Catal. Sci. Technol.* **2014**, *4*, 3426.
- [148] I. Koehne, T. J. Schmeier, E. A. Bielinski, C. J. Pan, P. O. Lagaditis, W. H. Bernskoetter, M. K. Takase, C. Würtele, N. Hazari, S. Schneider, *Inorg. Chem.* **2014**, *53*, 2133.
- [149] T. S. Briggs, W. D. Gwinn, W. M. Jolly, L. R. Thorne, *J. Am. Chem. Soc.* **1978**, *100*, 7762.
- [150] Y. Kawano, M. Uruichi, M. Shimoi, S. Taki, T. Kawaguchi, T. Kakizawa, H. Ogino, *J. Am. Chem. Soc.* **2009**, *131*, 14946.
- [151] T.-P. Lin, J. C. Peters, *J. Am. Chem. Soc.* **2013**, *135*, 15310.
- [152] C. Lichtenberg, L. Viciu, M. Adelhardt, J. Sutter, K. Meyer, B. De Bruin, H. Grützmacher, *Angew. Chemie - Int. Ed.* **2015**, *54*, 5766.
- [153] A. Friedrich, M. Drees, S. Schneider, *Chem. Eur. J.* **2009**, *15*, 10339.
- [154] T. M. Douglas, A. B. Chaplin, A. S. Weller, X. Yang, M. B. Hall, *J. Am. Chem. Soc.* **2009**, *131*, 15440.
- [155] C. A. Jaska, T. J. Clark, S. B. Clendenning, D. Grozea, A. Turak, Z. H. Lu, I. Manners, *J. Am. Chem. Soc.* **2005**, *127*, 5116.
- [156] A. P. M. Robertson, R. Suter, L. Chabanne, G. R. Whittell, I. Manners, *Inorg. Chem.* **2011**, *50*, 12680.
- [157] T. Malakar, L. Roy, A. Paul, *Chem. Eur. J.* **2013**, *19*, 5812.
- [158] P. B. Kisanga, J. G. Verkade, *J. Org. Chem.* **2000**, *65*, 5431.
- [159] E. Alberico, A. J. J. Lennox, L. K. Vogt, H. Jiao, W. Baumann, H. J. Drexler, M. Nielsen, A. Spannenberg, M. P. Checinski, H. Junge, et al., *J. Am. Chem. Soc.* **2016**, *138*, 14890.
- [160] A. Ramaraj, K. H. K. Reddy, H. Keil, R. Herbst-Irmer, D. Stalke, E. D. Jemmis, B. R. Jagirdar, *Organometallics* **2017**, *36*, 2736.

- [161] M. Sridhar, B. C. Ramanaiyah, C. Narsaiah, M. Kumara Swamy, B. Mahesh, M. K. Kumar Reddy, *Tetrahedron Lett.* **2009**, 50, 7166.
- [162] J. B. Lambert, S. Zhang, S. M. Ciro, *Organometallics* **1994**, 13, 2430.
- [163] H. Emde, G. Simchen, *Synthesis* **1977**, 9, 636.
- [164] Z. Todorova, N. Koseva, K. Troev, *Eur. Polym. J.* **2015**, 62, 87.
- [165] D. R. Weyenberg, A. E. Bey, P. J. Ellison, *J. Organomet. Chem.* **1965**, 3, 489.
- [166] M. Lökov, S. Tshepelevitsh, A. Heering, P. G. Plieger, R. Vianello, I. Leito, *European J. Org. Chem.* **2017**, 4475.
- [167] W. L. . Armarego, C. L. L. Chai, *Purification of Laboratory Chemicals*, **2009**.
- [168] N. A. Yakelis, R. G. Bergman, *Organometallics* **2005**, 24, 3579.
- [169] J. J. Curley, R. G. Bergman, T. D. Tilley, *Dalt. Trans.* **2012**, 41, 192.
- [170] M. Bertoli, A. Choualeb, A. J. Lough, B. Moore, D. Spasyuk, D. G. Gusev, *Organometallics* **2011**, 30, 3479.
- [171] Z. Han, L. Rong, J. Wu, L. Zhang, Z. Wang, K. Ding, *Angew. Chemie Int. Ed.* **2012**, 51, 13041.
- [172] R. K. Harris, E. D. Becker, S. M. De Cabral Menezes, P. Granger, R. E. Hoffman, K. W. Zilm, *Magn. Reson. Chem.* **2008**, 46, 582.
- [173] APEX2 V2014.9-0 (SAINT/SADABS/SHELXT/SHELXL), Bruker AXS Inc., Madison, WI, USA, **2014**.
- [174] G. M. Sheldrick, *Acta Crystallogr. Sect. A Found. Crystallogr.* **2008**, 64, 112.
- [175] G. M. Sheldrick, *Acta Crystallogr. Sect. C Struct. Chem.* **2015**, 71, 3.
- [176] G. M. Sheldrick, *Acta Crystallogr. Sect. A Found. Adv.* **2015**, 71, 3.
- [177] X. Yang, L. Zhao, T. Fox, Z. X. Wang, H. Berke, *Angew. Chemie - Int. Ed.* **2010**, 49, 2058.
- [178] F. Anke, D. Han, M. Klahn, A. Spannenberg, T. Beweries, *Dalt. Trans.* **2017**, 46, 6843.
- [179] X. Chen, J.-C. Zhao, S. G. Shore, *J. Am. Chem. Soc.* **2010**, 132, 10658.